How fish larvae swim
From motion to mechanics

Cees J. Voesenek

How fish larvae swim
From motion to mechanics

Cees J. Voesenek

Thesis
submitted in fulfilment of the requirements for the degree of doctor
at Wageningen University
by the authority of the Rector Magnificus,
Prof. Dr A. P. J. Mol,
in the presence of the
Thesis Committee appointed by the Academic Board
to be defended in public
on Wednesday 12 June 2019
at 4 p.m. in the Aula.

Table of contents

Chapter 1
General introduction

Most of the 34,000 currently known fish species swim by undulating their bodies (Froese and Pauly, 2018). Despite the ubiquity of undulatory swimmers among vertebrates, the complex mechanics behind their locomotion is not yet fully understood. This thesis explores the biomechanics of swimming of fish larvae, to come closer to answering the age-old question:

How do fish swim?

This chapter briefly outlines the subject and contents of this thesis and provides background information on commonly used concepts. For more detail, see **chapter 2**, an extensive review of the biomechanics of swimming in developing larval fish.

1.1   The complexity of swimming

Most fish swim by contracting the axial muscles along their bodies, alternating activation between the left and right side (Altringham and Ellerby, 1999; Videler, 1993). This produces a curvature wave along the body, which causes the water around the fish to move. The resulting flow field produces pressure and friction forces on the skin of the fish, creating propulsion in the desired direction (e.g. Li et al., 2012; Lighthill, 1960; Müller et al., 2008). However, the body does not simply move the water; the fluid forces also influence the body deformation (Tytell et al., 2010). In other words: rather than any individual component, the interaction between the water, passive tissues and muscles creates the instantly-recognisable swimming motion employed by many fish. If any of these three contributions is not present, no swimming motion is produced. To illustrate, an eel's muscle activation pattern creates the characteristic body wave when submerged, but when removed from the water it produces an alternating C-shape (Bowtell and Williams, 1991)—without feedback from the fluid, body motion changes drastically. In engineering, this type of phenomenon is commonly known as fluid-structure interaction. These problems are often highly complex to solve, especially when the fluid and structure are strongly coupled (Hou et al., 2012).

Based on the complexity of the physics, one would expect that fish require an advanced control system for their axial muscles. However, the zebrafish (*Danio rerio*) larva, subject of this thesis, seems to be a counterexample to this. Zebrafish larvae hatch at approximately 2–3 days after the eggs have been fertilised (Parichy et al., 2009), and can immediately swim (Müller and Van Leeuwen, 2004). Their brains are far from fully developed at 2 days after fertilisation (Mueller and Wullimann, 2016), and they have had no opportunity to learn how to activate their muscle to produce effective swimming motion because they were enclosed in an egg. Despite this lack of training, the tiny (around 5 mm) larvae are able to escape threats at high speeds (up to 38 body lengths per second; Müller and Van Leeuwen, 2004), and coordinate their muscles to beat their tails up to 80 times per second (Van Leeuwen et al., 2015).

Interestingly, despite the complex, non-linear physics, swimming motion does not appear to place stringent requirements on the control system. Hence, the swimming of zebra-

fish larvae is a suitable model to investigate this subject of great general interest. Often, in both biology and engineering, complex underlying physics are controlled in a (seemingly) simple manner, offloading much of the complexity to passive systems. This thesis focuses on the mechanics of swimming of larval zebrafish, from their motion to their internal mechanics. We aim to understand how the developing larvae swim effectively, despite the complex physics.

1.2 Swimming motion

A logical first step to study undulatory swimming is to look at the motion of the fish. The study of motion is commonly called kinematics and has been an important branch of fish swimming research. The first quantitative studies on the mechanics of swimming were done in the beginning of the 20th century (Breder, 1926; Gray, 1933), and analysed swimming kinematics based on videographs of fish. In the following 80 years, many analyses of swimming kinematics have followed (e.g. Fleuren et al., 2018; Kayan et al., 1978; Müller and Van Leeuwen, 2004; Nursall, 1958), across a wide range of species. These studies showed that many undulatory swimmers have a common motion pattern: the travelling body wave (Gray, 1933). This wave of deformation moves towards the rear of the body to 'push' water backwards, and thus propels the fish forwards (Fig. 1.1A,B,C). The properties of this wave vary across species, sizes, and types of manoeuvre.

   Breder (1926) was the first to classify swimming styles in groups based on the characteristics of the body wave. Swimming motion is broadly divided into two groups: body and caudal fin (BCF) propulsion and median/paired fin (MPF) propulsion (Sfakiotakis et al., 1999). In BCF propulsion, the fish uses their axial muscles to deform the body and move the caudal fin through the water. In MPF propulsion, the fish uses their median and/or paired fins in an undulatory or oscillatory fashion. This thesis concerns itself with BCF propulsion and mostly ignores the median and paired fins, as their motion is relatively unimportant for zebrafish larvae.

   Body and caudal fin propulsion is further subdivided into groups, depending on the fraction of the body that shows lateral excursions during a body wave (Breder, 1926; Sfakiotakis et al., 1999). These groups are named after the most common families that use that specific swimming style. At one extreme is thunniform, where mainly the tail is moved. The intermediate forms carangiform and subcarangiform show deformation of a larger fraction of the body in addition to the caudal fin. Finally, at the other extreme is anguilliform, where a significant part of the body is moved by the body wave. Most fish larvae exhibit anguilliform swimming, including the zebrafish larvae that we study in this thesis (Fig. 1.1A; Müller and Van Leeuwen, 2004).

   Many studies on swimming have been done under the assumption of periodic motion of the body (Blake, 2004; Li et al., 2016; Sfakiotakis et al., 1999; Webb, 1984). This simplification of actual swimming motion allows the calculation of kinematic parameters such as frequency and tail-beat amplitude (**chapter 3**; Bainbridge, 1958; Müller and Van Leeuwen, 2004). However, for many fish, including zebrafish larvae, cyclic swimming is relatively
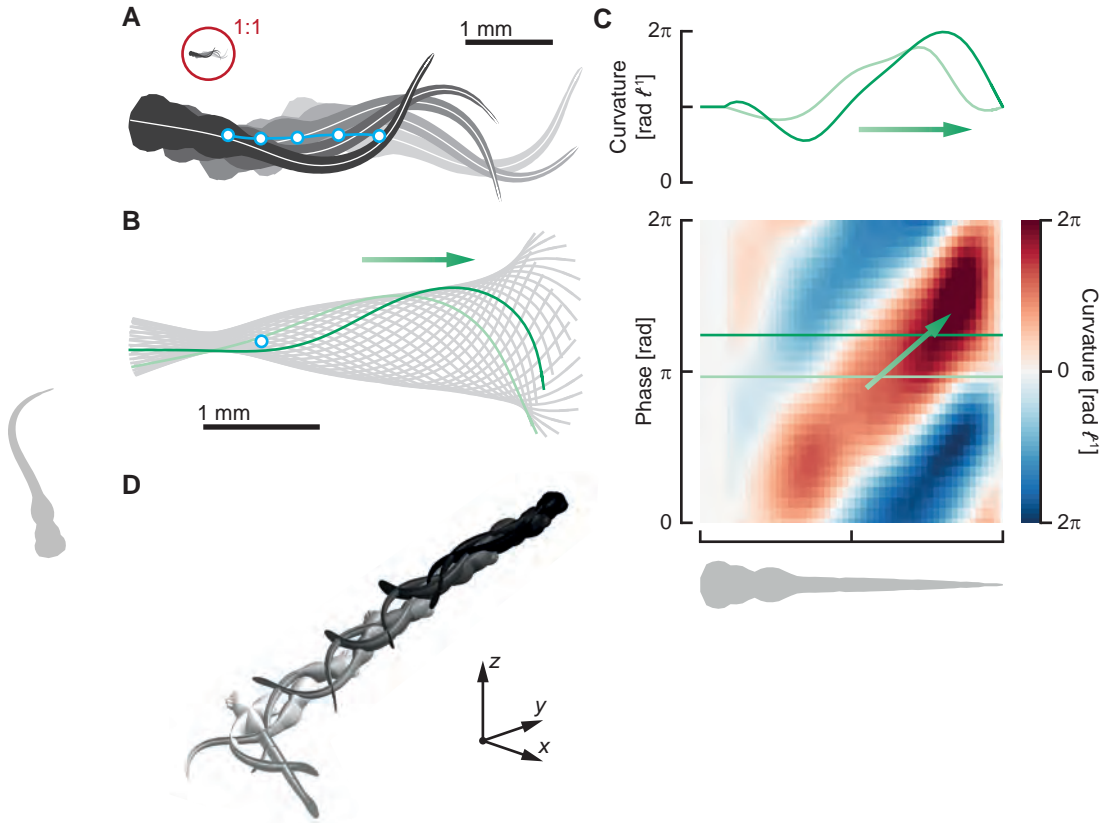
Figure 1.1: Swimming motion of zebrafish larvae. (A) A single cycle of periodic swimming, at 1:1 scale (inset) and enlarged. The centreline of the fish is shown in white. The path of the centre of mass is shown as dots at the time instances where we show the body shape, and with a blue line showing the path in between. (B) The same motion as A, but all centrelines have been moved such that the centre of mass is in the same point. Note that the body wave travels towards the rear of the fish in the two time points highlighted with green lines (also highlighted in C). (C) The curvature of the centreline (colours), along the length of the fish (horizontal), and over the phase (vertical). Above the heat map, highlighted slices along the body at two time points are shown (also highlighted in B). The travelling wave character is also reflected in the curvature. (D) Fast-start motion of a 3 days post fertilisation zebrafish larva, coloured by time (starting from light grey, ending in black), reconstructed three-dimensionally from multi-camera high-speed video.

rare (Sfakiotakis et al., 1999). Zebrafish larvae usually swim in two distinct modes: escape responses and spontaneous swimming motion (Budick and O'Malley, 2000). Both modes involve only a limited number of tail beats before the motion is stopped—during most of the swimming bout, the fish is accelerating or decelerating. The fast start (Fig. 1.1D) is an obvious example of transient swimming behaviour: usually, the fish accelerates strongly from a standstill as a response to a threat, and then decelerates after some tail beats (Domenici and Blake, 1997; Li et al., 2014; Nair et al., 2017). In this thesis, we analyse both periodic (**chapter 3**, **6**) and transient motion (**chapter 4**, **5**, **6**). Studies on periodic motion are valuable despite their real-life rarity, as the simpler analysis makes it easier to observe general

trends and mechanisms. On the other hand, analyses of transient swimming are valuable because they are closer to actual fish motion.

In addition, most of the studies on swimming kinematics have been done assuming that the fish moves in a two-dimensional plane. In some cases, this assumption is valid, e.g. when experiments were done in relatively shallow water tunnels (e.g. Graham et al., 1990; Plaut, 2000), or when only in-plane swimming bouts were analysed (**chapter 3**). However, in many other cases, fish swimming is fundamentally three-dimensional. For example, fish performing escape manoeuvres show a strong vertical motion component (Fleuren et al., 2018; Kasapi et al., 1993; Nair et al., 2015), reef-foraging fish need to perform 3D manoeuvres to navigate in complex environments (Gerstner, 1999), and some species perform diel vertical migration (Neilson and Perry, 1990). Also for zebrafish larvae, the three-dimensional component of their motion is often large (Fig. 1.1D; **chapter 4**, **5**; Nair et al., 2015). Although in-plane motions can be selected to perform two-dimensional analysis (**chapter 3**), three-dimensional analyses are essential to study their full range of behaviour (**chapter 4**, **5**).

1.3 Fluid dynamics of swimming

Fish exist over widely varying scales—from enormous whale sharks of around 10 metres length (Colman, 1997) to tiny fish larvae of only a few millimetres (Parichy et al., 2009). Across this large range of body length, fish swim with body undulations (Gazzola et al., 2014), despite considerable changes in fluid dynamics across length scales. The behaviour of fluids is governed by two main forces: inertia and friction (Anderson, 2001). Inertia is the tendency of mass to keep its velocity, and friction is the resistance of the flow to velocity gradients. Their relative contribution to a fluid-dynamic phenomenon scales with the Reynolds number (e.g. Bainbridge, 1960):

$$\mathrm{Re} = \frac{\rho U L}{\mu},$$ (1.1)

where ρ is the fluid density, U is a characteristic speed, L is a characteristic length, and μ is the dynamic viscosity. Fluid-dynamic phenomena are usually categorised in flow regimes, based on their Reynolds number. Low Reynolds numbers ($\mathrm{Re} \ll 1$) are associated with the viscous flow regime, dominated by friction. At high Reynolds numbers ($\mathrm{Re} \gtrsim 2000$), inertia dominates, although friction may still play an important role to locally shape the flow. In the intermediate regime ($1 \lesssim \mathrm{Re} \lesssim 2000$), both inertia and friction are important. Most adult fish swim in the inertial regime, while most fish larvae swim in the intermediate regime.

This difference in fluid-dynamic regime has profound consequences for the mechanics and energetics of swimming. Adult fish encounter relatively lower drag compared to larval fish, due to the relative importance of friction. Furthermore, because the ratio of inertial to frictional forces changes across the regime, fish must deal with different fluid-dynamic circumstances as they change swimming speed and size. The consequences and challenges of swimming in the intermediate regime are discussed in more detail in **chapter 2**.

Both adult and larval fish leave a vortex wake behind them as they swim, shedding one or more vortices at every tail beat that contribute to the hydrodynamic forces (Müller et al., 1997, 2008; Rosen, 1959). A famous engineering example of a vortex wake is the Von Kármán wake behind a bluff body (Anderson, 2001). The wake behind many fish looks broadly similar, but with the rotation direction of the vortices inverted. This results in an inversion of the jet between them, and therefore the wake produces thrust instead of drag (Lighthill, 1969). In practice, fish wakes often involve a more complex vortex arrangement; the precise topology and complexity of the wake varies across species and motion type (Li et al., 2012, 2014; Triantafyllou et al., 1993), and depends on the body motion. Via pressure and friction forces on the skin, the dynamics of the water are coupled to the internal mechanics of the fish.

1.4 Internal mechanics

Although kinematics and fluid mechanics of swimming are interesting by themselves, they are but a means to an end for the fish. To understand how the fish uses its muscles to propel itself, we need to gain insight into the internal mechanics. For many species, around 50% of the body consists of axial muscle (Graham et al., 1983; Webb, 1978), in most adult fish this mainly consists of white, anaerobic muscle for fast manoeuvres, and a much smaller amount of red, aerobic muscle for cruising (Graham et al., 1983). These muscles are arranged in myomeres, and attach to each other via connective tissue sheets called myosepts, and to the spine (Nursall, 1956).

During swimming, the axial muscles left and right of the spine are activated alternately (Grillner, 1974; Grillner and Kashin, 1976). This asymmetric muscle activation leads to a net bending moment across the spine, that acts to deform it and helps to create the body wave. In many fish, the muscles are activated in a wave travelling backwards along the body, at a speed much higher than the body wave speed (Blight, 1976; Van Leeuwen et al., 1990; Wardle et al., 1995). This difference in wave speeds causes some of the muscle to produce negative work during part of the cycle (Van Leeuwen et al., 1990), which has been suggested to stiffen the body and transfer power to the tail, where a relatively small amount of muscle is located (McHenry et al., 1995).

Most of these studies were done for adult fish, because direct measurements are difficult to perform on free-swimming fish larvae (Buss and Drapeau, 2002; Cho et al., 2015). However, due to the scale differences, and the fact that their muscle system is still in development, we expect differences to exist between larvae and adults (**chapter 2**). Furthermore, as mentioned above, we expect the larvae to have less neural capacity to control their motion. To gain insight into how swimming motion is generated by fish larvae, we would to like examine their internal mechanics.

1.5 Inverse dynamics

Ideally, we wish to investigate the fish larvae's internal mechanics without interfering with its free-swimming behaviour. With direct measurement of the internal mechanics, this is

difficult to achieve. However, swimming kinematics can be measured non-invasively. Filming the fish larvae from multiple angles requires little disturbance of the natural swimming environment of the larvae, nor induces a motion of the water. Therefore, we would like to gather as much information as we can on the internal mechanics of swimming from the kinematics alone.

This approach of reconstructing dynamics from motion is commonly known as inverse dynamics (Knudson, 2007). It is often used in the context of human biomechanics, for example to reconstruct joint moments and -powers from walking kinematics (DeVita and Hortobágyi, 2003; Winter, 1983; Winter and Robertson, 1978). These inverse dynamics analyses are relatively straight-forward in this context, as terrestrial motion generally involves almost-rigid bodies connected by joints, allowing direct computation of joint moments (Hof, 1992). In contrast, fish bodies are far from rigid, and do not only deform at specific joints, but along their entire bodies. This makes inverse dynamics analyses generally more difficult to perform.

In the field of fish biomechanics, an inverse dynamics approach has been used to reconstruct resultant forces and torques from acceleration (**chapter 3**, **4**, **5**; Walker, 2004). According to Newton's laws, the resultant force on the fish's body is equal to the product of its mass and acceleration. Therefore, from the acceleration of the centre of mass and the mass of a body, it is possible to calculate the net force acting upon it: the resultant fluid dynamic force on the fish. Equivalently, we can calculate resultant fluid-dynamic torques from rotational accelerations of the body. This is, however, complicated by the varying body shape. Nevertheless, with a suitable computational method (**chapter 3**), this becomes possible.

We can extract more information from the swimming kinematics if we create models for components of the system. In the case of resultant forces and torques, we only need a model of the mass distribution of the fish. However, if we introduce models on the external fluid dynamics and the internal mechanics, we can reconstruct internal mechanics from kinematics. In this way, Hess and Videler (1984) used a simplified fluid-dynamic and mechanical model of the fish to calculate internal bending moments along the centreline. This model was later refined by Cheng and Blickhan (1994) with a more accurate vortex-panel fluid model, but the same model of the body.

In this thesis, we expand the use of inverse dynamics for fish swimming, reconstructing resultant force and torques, fluid-dynamic forces, and internal bending moments from high-speed video images with unprecedented accuracy. First, we process the high-speed video images to reconstruct 3D kinematics. We use the accelerations of the reconstructed surface of the fish to calculate resultant fluid-dynamic forces and torques. To determine how these forces are produced along the body, we calculate the flow field around the fish by feeding the motion into a computational fluid dynamics (CFD) solver. Finally, we reconstruct internal bending moments based on the motion and the reconstructed fluid forces with a non-linear beam model.

1.6 Aims and content of this thesis

In this thesis, we aim to elucidate the mechanisms behind fish swimming. Specifically, we aim to understand how the zebrafish larvae can swim effectively from a very early stage of development, immediately after hatching. Young fish larvae can perform fast starts to escape from predators, for which they control the speed and direction depending on the threat. These starts are often followed by a swimming bout, where the larvae reach high tail-beat frequencies and speeds. With advanced inverse-dynamics approaches, we examine these motions of zebrafish larvae to help explain how they are able to swim at such an early stage of development.

In **chapter 2**, we review the literature on the swimming of larval fish. Many fish hatch at an early stage of embryonic development, but their survival requires them to swim. Their locomotion system—muscle, brains, skeleton—is being built while remaining operational. Furthermore, their size and speed places them in the intermediate flow regime, where fluid-dynamic forces change rapidly as the fish grow and swim faster. We consider the demands on fish larvae that these unique conditions create, and what solutions have evolved to meet these demands.

In **chapter 3**, we used a two-dimensional inverse-dynamics approach to investigate the cyclic swimming of zebrafish larvae of 2–5 days post fertilisation (dpf). Young larvae swim at lower Reynolds numbers than older larvae, resulting in a relatively higher drag. This requires them to use higher frequencies (f) and tail amplitudes (A) to achieve the same swimming speed (U), as expressed by the Strouhal number (fA/U). The energetically inefficient swimming style of young larvae leads to large yawing amplitudes and high energy losses. This illustrates the challenges of the intermediate flow regime outlined in **chapter 2**—young larvae must expend a relatively large amount of energy on swimming due to the higher contribution of the friction forces.

To make the step to three-dimensional kinematics, we developed a novel method for reconstructing three-dimensional motion, forces and torques of fish from a multi-camera video setup, described in **chapter 4**. For each time point in the video, we fitted a parameterised virtual representation of the fish such that its overlap with the camera views is maximal. In addition, we developed a method to calculate the net forces and torques from the fitted body model. In the remainder of the thesis, this method is used to reconstruct swimming kinematics to be used as input for the inverse-dynamics methods.

The tracking method is applied to fast-starts of fish in **chapter 5**. We used the reconstructed forces and torques to examine how fish larvae meet the functional demands on their fast starts. To escape predators effectively, they need to escape with sufficient speed, and over a wide range of directions. To meet these demands, fish larvae perform C-starts, where the body first bends into a C-shape, and then unfolds rapidly to produce propulsion. We show that most of the reorientation of the body happens in the first stage, which is generally considered 'preparatory'. This is followed by a large propulsion peak in stage 2, resulting in most of the acceleration. Thus, the larvae are able to adjust the speed and direction of the escape mostly independently.

In **chapter 6**, we analysed the internal mechanics of swimming fish larvae across development. We used an advanced inverse-dynamics approach, integrating 3D tracking, numerical solution of the 3D equations of fluid dynamics, and non-linear beam theory to calculate the net bending moments along the fish, including the effects of both active and passive tissues. Comparing the results on a tail-beat by tail-beat basis, we show that the spatiotemporal bending moment patterns are similar across development and swimming speed and acceleration. Our model of how swimming is adjusted reduces to two parameters: the bending moment amplitude and the tail-beat duration. This relative simplicity of control might explain how just-hatched larvae are immediately able to swim effectively: much of the complexity of the physics is taken care of passively.

Finally, in **chapter 7**, I summarise the results of this thesis, and place them in the broader context of swimming research. I examine the strengths and limitations of the novel methods used in this thesis. Furthermore, I hypothesise on the consequences of our results for fish swimming across species and developmental stages. In addition, I give suggestions on how the knowledge from this thesis could contribute to bio-inspired applications. Finally, I suggest directions for future research to further lift the veil on the mysteries of undulatory swimming.

References

Altringham, J. D. and Ellerby, D. J. (1999). Fish swimming: patterns in muscle function. *J. Exp. Biol.* **202**, 3397–3403.

Anderson, J. D. (2001). *Fundamentals of Aerodynamics*. New York City, NY, USA: McGraw-Hill.

Bainbridge, R. (1958). The speed of swimming of fish as related to size and to the frequency and amplitude of the tail beat. *J. Exp. Biol.* **35**, 109–133.

Bainbridge, R. (1960). Speed and stamina in three fish. *J. Exp. Biol.* **37**, 129–153.

Blake, R. W. (2004). Fish functional design and swimming performance. *J. Fish Biol.* **65**, 1193–1222.

Blight, A. R. (1976). Undulatory swimming with and without waves of contraction. *Nature* **264**, 352–354.

Bowtell, G. and Williams, T. L. (1991). Anguilliform body dynamics: modelling the interaction between muscle activation and body curvature. *Philos. Trans. R. Soc., B* **334**, 385–390.

Breder, C. M. J. (1926). The locomotion of fishes. *Zoologica* **4**, 159–297.

Budick, S. A. and O'Malley, D. M. (2000). Locomotor repertoire of the larval zebrafish: swimming, turning and prey capture. *J. Exp. Biol.* **203**, 2565–2579.

Buss, R. R. and Drapeau, P. (2002). Activation of embryonic red and white muscle fibers during fictive swimming in the developing zebrafish. *J. Neurophysiol.* **87**, 1244–1251.

Cheng, J.-Y. and Blickhan, R. (1994). Bending moment distribution along swimming

fish. *J. Theor. Biol.* **168**, 337–348.

Cho, S.-J., Nam, T.-S., Byun, D., Choi, S.-Y., Kim, M.-K. and Kim, S. (2015). Zebrafish needle EMG: a new tool for high-throughput drug screens. *J. Neurophysiol.* **114**, 2065–2070.

Colman, J. G. (1997). A review of the biology and ecology of the whale shark. *J. Fish Biol.* **51**, 1219–1234.

DeVita, P. and Hortobágyi, T. (2003). Obesity is not associated with increased knee joint torque and power during level walking. *J. Biomech.* **36**, 1355–1362.

Domenici, P. and Blake, R. W. (1997). The kinematics and performance of fish fast-start swimming. *J. Exp. Biol.* **200**, 1165–1178.

Fleuren, M., Van Leeuwen, J. L., Quicazan-Rubio, E. M., Pieters, R. P. M., Pollux, B. J. A. and Voesenek, C. J. (2018). Three-dimensional analysis of the fast-start escape response of the least killifish, *Heterandria formosa*. *J. Exp. Biol.* **221**, jeb168609.

Froese, R. and Pauly, D. (2018). *FishBase*.

Gazzola, M., Argentina, M. and Mahadevan, L. (2014). Scaling macroscopic aquatic locomotion. *Nat. Phys.* **10**, 758–761.

Gerstner, C. L. (1999). Maneuverability of four species of coral-reef fish that differ in body and pectoral-fin morphology. *Can. J. Zool.* **77**, 1102–1110.

Graham, J. B., Dewar, H., Lai, N. C., Lowell, W. R. and Arce, S. M. (1990). Aspects of shark swimming performance determined using a large water tunnel. *J. Exp. Biol.* **151**, 175–192.

Graham, J. B., Koehrn, F. J. and Dickson, K. A. (1983). Distribution and relative proportions of red muscle in scombrid fishes: consequences of body size and relationships to locomotion and endothermy. *Can. J. Zool.* **61**, 2087–2096.

Gray, J. (1933). Studies in animal locomotion — I. The movement of fish with special reference to the eel. *J. Exp. Biol.* **10**, 88–104.

Grillner, S. (1974). On the generation of locomotion in the spinal dogfish. *Exp. Brain Res.* **20**, 459–470.

Grillner, S. and Kashin, S. (1976). On the generation and performance of swimming in fish. In *Neural Control of Locomotion* (eds. R. M. Herman, S. Grillner, P. S. G. Stein and D. G. Stuart), pp. 181–201. Berlin, Germany: Springer.

Hess, F. and Videler, J. J. (1984). Fast continuous swimming of saithe (*Pollachius virens*): a dynamic analysis of bending moments and muscle power. *J. Exp. Biol.* **109**, 229–251.

Hof, A. L. (1992). An explicit expression for the moment in multibody systems. *J. Biomech.* **25**, 1209–1211.

Hou, G., Wang, J. and Layton, A. (2012). Numerical methods for fluid-structure interaction — a review. *Commun. Comput. Phys.* **12**, 337–377.

Kasapi, M. A., Domenici, P., Blake, R. W. and Harper, D. (1993). The kinematics and performance of escape responses of the knifefish *Xenomystus nigri*. *Can. J. Zool.* **71**, 189–195.

Kayan, V. P., Kozlov, L. F. and Pyatetskii, V. E. (1978). Kinematic characteristics of the swimming of certain aquatic animals. *Fluid Dyn.* **13**, 641–646.

Knudson, D. (2007). *Fundamentals of Biomechanics*. Berlin, Germany: Springer.

Li, G., Müller, U. K., Van Leeuwen, J. L. and Liu, H. (2012). Body dynamics and hydrodynamics of swimming fish larvae: a computational study. *J. Exp. Biol.* **215**, 4015–4033.

Li, G., Müller, U. K., Van Leeuwen, J. L. and Liu, H. (2014). Escape trajectories are deflected when fish larvae intercept their own C-start wake. *J. R. Soc., Interface* **11**, 20140848–20140848.

Li, G., Müller, U. K., Van Leeuwen, J. L. and Liu, H. (2016). Fish larvae exploit edge vortices along their dorsal and ventral fin folds to propel themselves. *J. R. Soc., Interface* **13**, 20160068.

Lighthill, M. J. (1960). Note on the swimming of slender fish. *J. Fluid Mech.* **9**, 305–317.

Lighthill, M. J. (1969). Hydromechanics of aquatic animal propulsion. *Annu. Rev. Fluid Mech.* **1**, 413–446.

McHenry, M. J., Pell, C. A. and Long, J. H. J. (1995). Mechanical control of swimming speed: stiffness and axial wave form in undulating fish models. *J. Exp. Biol.* **198**, 2293–2305.

Mueller, T. and Wullimann, M. F. (2016). *Atlas of Early Zebrafish Brain Development*. Amsterdam, The Netherlands: Elsevier.

Müller, U. K., Van den Boogaart, J. G. M. and Van Leeuwen, J. L. (2008). Flow patterns of larval fish: undulatory swimming in the intermediate flow regime. *J. Exp. Biol.* **211**, 196–205.

Müller, U. K., Van den Heuvel, B. L. E., Stamhuis, E. J. and Videler, J. J. (1997). Fish foot prints: morphology and energetics of the wake behind a continuously swimming mullet (*Chelon labrosus* Risso). *J. Exp. Biol.* **200**, 2893–2906.

Müller, U. K. and Van Leeuwen, J. L. (2004). Swimming of larval zebrafish: ontogeny of body waves and implications for locomotory development. *J. Exp. Biol.* **207**, 853–868.

Nair, A., Azatian, G. and McHenry, M. J. (2015). The kinematics of directional control in the fast start of zebrafish larvae. *J. Exp. Biol.* **218**, 3996–4004.

Nair, A., Changsing, K., Stewart, W. J. and McHenry, M. J. (2017). Fish prey change strategy with the direction of a threat. *Proc. R. Soc. B* **284**, 20170393.

Neilson, J. D. and Perry, R. I. (1990). Diel vertical migrations of juvenile fish: an obligate or facultative process? In *Advances in Marine Biology* (eds. J. H. S. Blaxter and A. J. Southward), volume 26, pp. 115–168. Amsterdam, The Netherlands: Elsevier.

Nursall, J. R. (1956). The lateral musculature and the swimming of fish. *Proc. Zool. Soc. London* **126**, 127–144.

Nursall, J. R. (1958). A method of analysis of the swimming of fish. *Copeia* **1958**, 136.

Parichy, D. M., Elizondo, M. R., Mills, M. G., Gordon, T. N. and Engeszer, R. E. (2009). Normal table of postembryonic zebrafish development: staging by externally visible anatomy of the living fish. *Dev. Dyn.* **238**, 2975–3015.

Plaut, I. (2000). Effects of fin size on swimming performance, swimming behaviour and routine activity of zebrafish *Danio rerio*. *J. Exp. Biol.* **203**, 813–820.

Rosen, M. W. (1959). *Water flow about a swimming fish*. Master of Science, University of California, Los Angeles.

Sfakiotakis, M., Lane, D. M. and Davies, J. B. C. (1999). Review of fish swimming modes for aquatic locomotion. *IEEE J. Ocean. Eng.* **24**, 237–252.

Triantafyllou, G. S., Triantafyllou, M. S. and Grosenbaugh, M. A. (1993). Optimal thrust development in oscillating foils with application to fish propulsion. *J. Fluids Struct.* **7**, 205–224.

Tytell, E. D., Borazjani, I., Sotiropoulos, F., Baker, T. V., Anderson, E. J. and Lauder, G. V. (2010). Disentangling the functional roles of morphology and motion in the swimming of fish. *Integr. Comp. Biol.* **50**, 1140–1154.

Van Leeuwen, J. L., Lankheet, M. J. M., Akster, H. A. and Osse, J. W. M. (1990). Function of red axial muscles of carp (*Cyprinus carpio*): recruitment and normalized power output during swimming in different modes. *J. Zool.* **220**, 123–145.

Van Leeuwen, J. L., Voesenek, C. J. and Müller, U. K. (2015). How body torque and Strouhal number change with swimming speed and developmental stage in larval zebrafish. *J. R. Soc., Interface* **12**, 20150479.

Videler, J. J. (1993). *Fish Swimming*. Berlin, Germany: Springer.

Walker, J. A. (2004). Dynamics of pectoral fin rowing in a fish with an extreme rowing stroke: the threespine stickleback (*Gasterosteus aculeatus*). *J. Exp. Biol.* **207**, 1925–1939.

Wardle, C. S., Videler, J. J. and Altringham, J. D. (1995). Tuning in to fish swimming waves: body form, swimming mode and muscle function. *J. Exp. Biol.* **198**, 1629–1636.

Webb, P. W. (1978). Fast-start performance and body form in seven species of teleost fish. *J. Exp. Biol.* **74**, 211–226.

Webb, P. W. (1984). Body form, locomotion and foraging in aquatic vertebrates. *Am. Zool.* **24**, 107–120.

Winter, D. A. (1983). Moments of force and mechanical power in jogging. *J. Biomech.* **16**, 91–97.

Winter, D. A. and Robertson, D. G. E. (1978). Joint torque and energy patterns in normal gait. *Biol. Cybern.* **29**, 137–142.
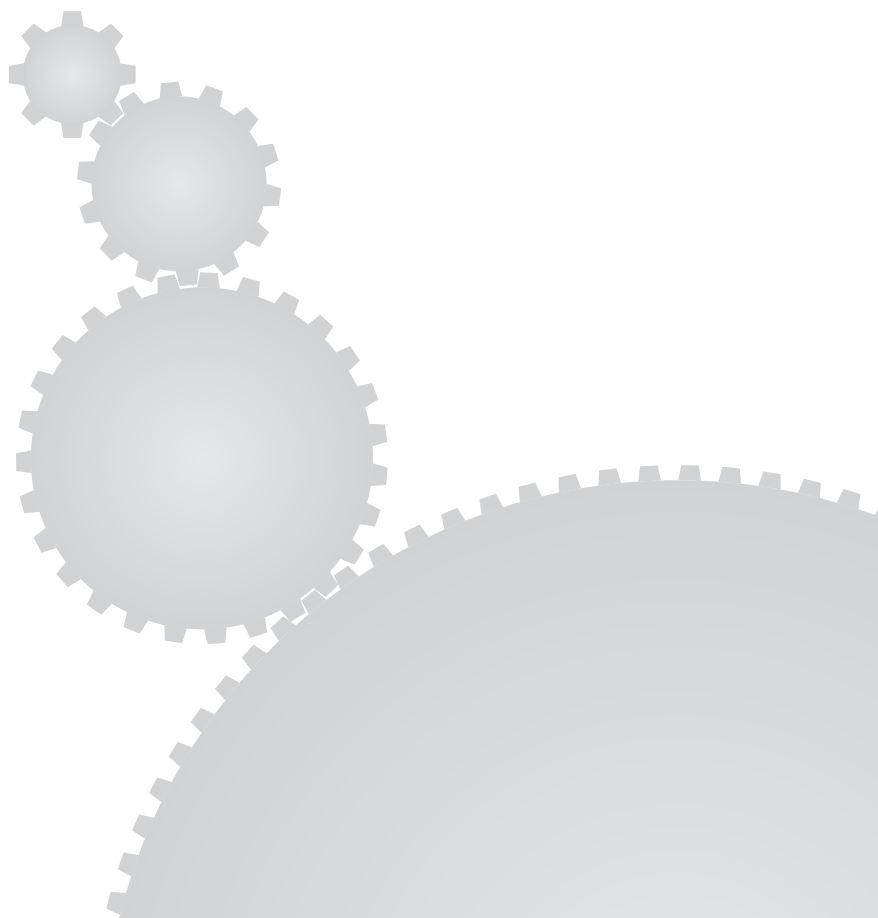
Chapter 2

Biomechanics of swimming in developing larval fish

Cees J. Voesenek[1], Florian T. Muijres[1], Johan L. van Leeuwen[1]

[1] Experimental Zoology Group, Wageningen University & Research, Wageningen, The Netherlands

Abstract

Most larvae of bony fish are able to swim almost immediately after hatching. Their loco-motory system supports several vital functions: fish larvae make fast manoeuvres to escape from predators, aim accurately during suction feeding and may migrate towards suitable future habitats. Owing to their small size and low swimming speed, larval fish operate in the intermediate hydrodynamic regime, which connects the viscous and inertial flow regimes. They experience relatively strong viscous effects at low swimming speeds, and relatively strong inertial effects at their highest speeds. As the larvae grow and increase swimming speed, a shift occurs towards the inertial flow regime. To compensate for size-related lim-itations on swimming speed, fish larvae exploit high tail beat frequencies at their highest speeds, made possible by their low body inertia and fast neuromuscular system. The shifts in flow regime and body inertia lead to changing functional demands on the locomotory system during larval growth. To reach the reproductive adult stage, the developing larvae need to adjust to and perform the functions necessary for survival. Just after hatching, many fish larvae rely on yolk and need to develop their feeding systems before the yolk is exhausted. Furthermore, the larvae need to develop and continuously adjust their sens-ory, neural and muscular systems to catch prey and avoid predation. This Review discusses the hydrodynamics of swimming in the intermediate flow regime, the changing functional demands on the locomotory system of the growing and developing larval fish, and the solu-tions that have evolved to accommodate these demands.

Glossary

Labriform	Swimming mode in which mainly the pectoral fins are used for propulsion.
Lateral line	Sensory organ for flow detection.
Particle image velocimetry (PIV)	Velocity measurement technique based on cross-correlation of particle images.
Particle tracking velocimetry (PTV)	Velocity measurement technique based on tracking of particles in video frames.
Reynolds number (Re)	Ratio between inertial and viscous forces in a fluid (dimensionless number).
Strouhal number (St)	Ratio between average lateral tail speed and forward swimming speed (dimensionless number).
Subcarangiform	Swimming mode between anguilliform and carangiform.
Thunniform	Swimming mode in which undulations are con-fined mostly to the tail.
Undulatory	Using waves of curvature along the body.
Viscosity	Resistance of a fluid to deform under stress.
Viscous flow regime	Hydrodynamic regime where viscosity dominates; $\text{Re} \lesssim 1$.

List of symbols and abbreviations

A	peak-to-peak tail-beat amplitude	PTV	particle tracking velocimetry
CFD	computational fluid dynamics	Re	Reynolds number
CoM	centre of mass	SR	sarcoplasmic reticulum
CoT	cost of transport	St	Strouhal number
$\bar{D}$	cycle-averaged drag	$\bar{T}$	cycle-averaged thrust
dpf	days post-fertilisation	$\bar{v}$	cycle-averaged swimming speed
f	tail-beat frequency	η	Froude efficiency
ℓ	body length	μ	dynamic viscosity
$\bar{P}_{\text{input}}$	cycle-averaged input power	ν	kinematics viscosity
$\bar{P}_{\text{output}}$	cycle-averaged output power	ρ	density of water
PIV	particle image velocimetry		

2.1 Introduction

After hatching from the egg, most bony fish continue life as a larva, a few millimetres in length, that needs to survive autonomously. They have to hunt prey to gather resources for their growth and development, disperse, and escape from predators. This requires the larvae to swim effectively almost immediately after hatching. They generally use an undulatory swimming style (see Glossary), characterised by caudally directed waves of lateral bending of their body and tail. As the fish grow from larvae into juveniles, functional demands on the locomotory system change, requiring larval fish to adapt their locomotory system continuously to these varying requirements.

The fluid-dynamic regimes for swimming fish are defined by the dimensionless Reynolds number (Re; see Glossary) (e.g. Bainbridge, 1960), given by:

$$\text{Re} = \frac{\rho \bar{v} \ell}{\mu} = \frac{\bar{v} \ell}{\nu}, \tag{2.1}$$

where ρ is fluid density, $\bar{v}$ is mean swimming speed, ℓ is body length, μ is dynamic viscosity and ν is kinematic viscosity (see Glossary). The Reynolds number expresses the ratio of contributions of inertial and viscous forces to a fluid-dynamic phenomenon, which is crucial to its dynamics. Viscosity is associated with friction between fluid particles, and inertia (see Glossary) is the tendency of mass to keep the same velocity in the absence of external forces. Very low Re values ($\text{Re} \ll 1$) are associated with the viscous flow regime (see Glossary), where inertia can be ignored. Much larger Re values ($\text{Re} \gtrsim 2000$) indicate that inertia dominates. In the intermediate flow regime ($1 \lesssim \text{Re} \lesssim 2000$) (see Glossary), there is a gradual transition from viscosity-dominated flow at $\text{Re} \approx 1$ to inertia-dominated flow at $\text{Re} \approx 2000$.

Small fish larvae ($\ell \lesssim 5$ mm) operate in the intermediate flow regime over most of their range of swimming speeds, whereas larger fish larvae enter the inertial regime (see Glossary) at their highest swimming speeds (e.g. Fuiman and Webb, 1988; Müller and Van
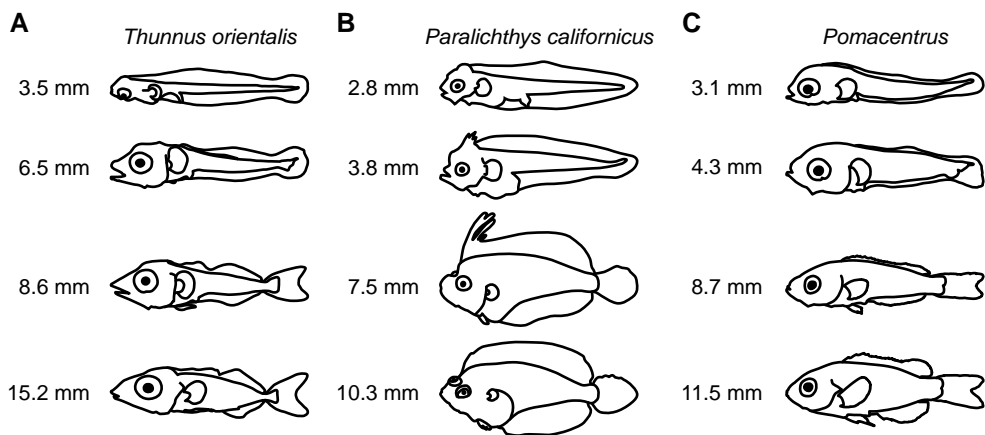
Figure 2.1: Line drawings used to illustrate development of external morphology for different species, from yolk-sac larva to juvenile. (A) Thunniform (see Glossary): Pacific bluefin tuna *Thunnus orientalis*, redrawn from Kaji et al. (1996). (B) Subcarangiform (see Glossary): California halibut *Paralichthys californicus*, redrawn from Gisbert et al. (2002). (C) Labriform (see Glossary): a member of the genus *Pomacentrus*, redrawn from Kavanagh et al. (2000). Note that the fish have initially similar shapes that diverge as they develop into juveniles. The body length of each fish is shown to its left.

Leeuwen, 2004). In the intermediate flow regime, fish larvae have to deal with relatively strong viscous effects at low swimming speeds, whereas, at their highest speeds, inertial effects come to dominate. The changing hydrodynamic circumstances affect the production of fluid-dynamic forces. Hence, demands on the locomotory system change with swimming speed. Because the larvae need to swim throughout a range of speeds, they cannot adapt to a specific hydrodynamic regime and thus need to compromise in morphology, physiology and muscle control to accommodate the varying functional demands.

Bony fish larvae change shape considerably over development (Fig. 2.1), but the morphology of early larval stages of most species is surprisingly similar. When the larvae hatch, they have an elongated body surrounded by a continuous finfold (see Glossary) behind the head and yolk sac (Kendall Jr. et al., 1984). These similarities might indicate adaptations to common developmental constraints and/or common problems in locomotion, feeding and respiration. As the larvae grow and develop into juveniles, the body shapes of the different species diverge to prepare them for their adult lifestyle and swimming styles. For example, flatfish such as halibut change from a yolk-sac-bearing larva to a pelagic suction feeder to an asymmetric benthic flatfish (Fig. 2.1B) (Osse and Van den Boogaart, 1997). In addition to the changing hydrodynamic regime, these changes over the life history of the fish also result in changing functional demands.

This Review addresses the locomotory challenges that larval fish have to cope with, as well as the evolved solutions to the associated functional demands. We discuss the kinematics, fluid dynamics and energetics of swimming, and how the muscles of fish larvae are adapted to power swimming in the intermediate flow regime. Furthermore, we examine the functions supported by the locomotory system and how fish larvae have adapted

A

Functional requirements	Derived requirements
Conserve energy	Minimise cost of transport
	Minimise need for swimming
Cruise and disperse	Swim prolongedly
	Use environmental flow
	Swim sufficiently fast
Escape predators	Respond quickly
	Accelerate strongly
	Control escape angle
	Move unpredictably
Hunt and feed	Control mouth position
	Develop and time suction flow
	Accelerate strongly

B

Specific requirements

External morphology
- Minimise drag
- Generate high thrust
- Generate thrust efficiently

Muscle
- Be useable continuously
- Contract at high frequencies
- Produce sufficient force and power

Control
- Initiate fast starts with minimal delay
- Control swimming muscles accurately
- Sense predators and prey

Behaviour
- Use optimal kinematics
- Move to or stay in suitable habitat

Figure 2.2: Requirements on locomotion for developing fish larvae. (A) General requirements on fish larvae, where functional requirements (depicted by different colours) are connected to derived requirements. (B) Specific requirements on the subsystems of the fish. The functional requirement(s) from A that each specific requirement belongs to is indicated by the small coloured rectangle(s).

to the demands derived from these functions (see Fig. 2.2 for an overview). Cruising is essential for many fish larvae, to disperse or to avoid dispersal caused by environmental flow (discussed in the section Cruising and dispersal). An important factor for survival is escape from predators, requiring the locomotory system to respond quickly and accelerate the fish strongly (discussed in the section Escaping predators). Fish larvae need to swim to find and hunt prey after they exhaust their yolk, which requires accurate control to aim their strikes (discussed in the section Hunting and feeding). Swimming also supports respiration by renewing the diffusive boundary layer of gases and ions (e.g. Green et al., 2011), and helps to maintain and control body orientation (e.g. Ehrlich and Schoppik, 2017); for reasons of space, we do not discuss these two functions. Finally, we provide perspectives for possible future research.

2.2 Body kinematics

Swimming kinematics are produced by a complex interaction between internal body mechanics and fluid mechanics (e.g. McMillen and Holmes, 2006; Tytell et al., 2010). The muscle system of the fish generates forces that cause body deformations. The resulting motion pro-

A — 'True' CoM — 'Stretched-straight' CoM

2 mm

B

C

D

4.8 mm

8.1 mm
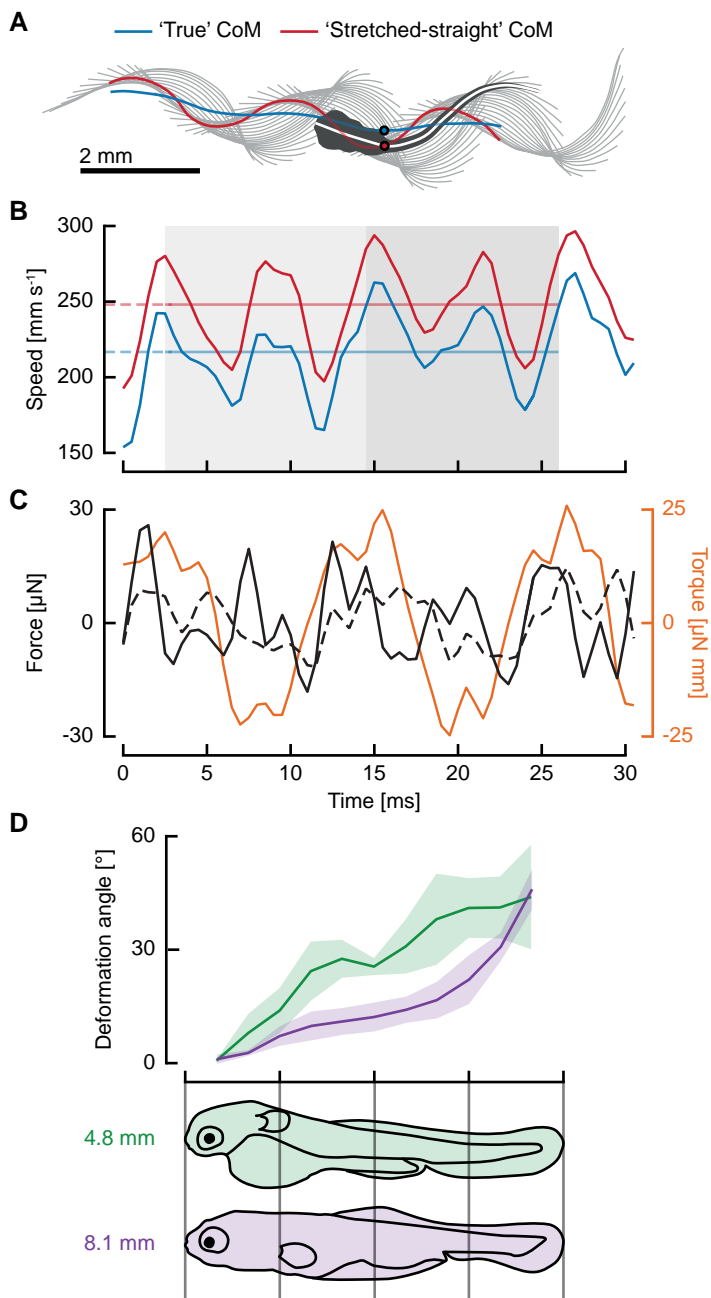
(Caption on the next page.)

Figure 2.3: Swimming kinematics of fish larvae. (A) High-speed-video-derived centreline kinematics (grey), path of the centre of mass (CoM) of a 5 day post-fertilisation (dpf) zebrafish larva based on a body-attached CoM approximation method ('stretched-straight', red), and a more accurate method based on a deforming body model with uniform density ('true', blue). A two-dimensional (2D) projection of the body model is indicated for one time instant, with the two approximations of the CoM indicated with circles. Owing to the large body curvature, the CoM computed with the deforming body model is located outside the body at this instant; the body-attached CoM approximation fails to capture this feature. (B) Speed of the CoM based on the body-attached approximation (red) and the deforming body model (blue). The grey blocks indicate the two swimming cycles, for which the tail-beat averaged speed (horizontal lines) is calculated; this speed is 15% higher for the body-attached approximation (red) than for the deforming body model (blue). (C) Resultant forces (black) and yaw torque (orange) on the CoM, calculated with inverse dynamics. The forces are given in the direction of the instantaneous velocity vector (solid) and perpendicular to it (dashed). Data for A–C are from Van Leeuwen et al. (2015b,a). (D) Change of maximum deformation angle amplitude for two carp larvae, one with a body length of 4.8 mm (green) and the other 8.1 mm (purple). Standard deviations are indicated by the shaded area. The deformation angle is defined as the angle between successive, straight equal-length segments ('virtual body segments') along the central axis. Sketches of larvae are redrawn and data are from Osse and Van den Boogaart (2000).

duces a flow field in the surrounding water, creating a fluid-dynamic force distribution on the skin. In turn, these forces change the loading on the fish, and with it the deformation of the body. Again, this deformation couples back to the fluid forces, creating a loop of interactions between the water and the body of the fish. These mechanical interactions determine the changes in body shape and motion of the fish through the water.

To study these complex interactions, swimming kinematics (i.e. body shape, position and orientation) need to be determined in detail. Historically, this has been performed mostly by tracking the two-dimensional (2D) movements of the body centreline and centre of mass (CoM) in a horizontal plane from a single, vertically oriented movie camera (e.g. Fig. 2.3A; Müller and Van Leeuwen, 2004), but recently more sophisticated multi-camera three-dimensional (3D) tracking systems have been developed (e.g. Butail and Paley, 2012; Voesenek et al., 2016). Results from these new trackers show that swimming motions that appear 2D in a single (bottom or top) camera view often have a large vertical component. For example, a fast-starting larval zebrafish [5 days post-fertilisation (dpf)] produced pitch angles up to 15 deg with respect to the horizontal plane, roll angles up to 30 deg and a considerable vertical speed, demonstrating the necessity of 3D tracking (Voesenek et al., 2016). Also in 3D, kinematics are generally quantified as the movement and lateral curvature of the body centre line, 3D body orientation, and the displacement of the CoM.

The CoM of the fish is important to determine because it is the point that the resultant fluid-dynamic forces and torques act upon (Fig. 2.3A,C; Van Leeuwen et al., 2015b; Voesenek et al., 2016). The CoM depends on the mass distribution of the fish at every point in time, and it changes with deformation of the fish (Tytell and Lauder, 2008; Van Leeuwen et al., 2015b). The position of the CoM along the body axis for a straight fish is often used to define a body- attached point that can be tracked to estimate the CoM movement during swimming. This might be a reasonable approximation for low-amplitude swimming motions (Xiong and Lauder, 2014), but for high-amplitude motions as found in swimming larvae, the difference with the true CoM is large (Fig. 2.3A,B; Van Leeuwen et al., 2015b). Hence, for high-amplitude larval swimming, more sophisticated CoM estimation methods

are required, such as methods based on a 3D model of the deforming body.

Fish locomotion has been divided into cyclic and acyclic swimming. In cyclic swimming, the kinematics repeat themselves and the cycle-averaged speed is constant. In reality, however, variations between the swimming cycles always occur. Acyclic swimming constitutes a large part of natural swimming motion: turns, escape manoeuvres, feeding strikes and burst-and-coast swimming. Many fish switch from (approximately) cyclic swimming to burst-and-coast swimming early in development (Weihs, 1979; Müller and Van Leeuwen, 2004). Much of the work on the fluid mechanics of fish swimming has focused on (near-) cyclic swimming.

During near-cyclic swimming, many teleost larvae employ an anguilliform swimming style (see Glossary), where the majority of the body makes considerable lateral excursions. An example of this motion is shown in (Fig. 2.3A; Van Leeuwen et al., 2015b), which depicts the kinematics of a 5-dpf zebrafish larva swimming at a speed of approximately 50 body lengths s^{-1}. Compared with adults, the larva shows high-amplitude motion of the whole body (peak-to-peak tail-beat amplitude $A \approx 0.44\,\ell$ at the tail) at a high frequency (≈ 85 Hz). This anguilliform swimming mode is relatively rare in most fish species at $\ell > 10$ mm—larvae often change to a more tail-heavy amplitude distribution later in development. Fig. 2.3D (Osse and Van den Boogaart, 2000) shows the amplitude envelope of the deformation angle between successive 'virtual body segments' for a just-hatched carp larva (4.8 mm) and a larger larva (8.1 mm). The just-hatched larva bends strongly along a large part of the body, whereas the older larva confines large amplitudes to the tail.

2.3 Fluid dynamics

Analyses of the hydrodynamic forces on the fish are important for understanding swimming. The flow field surrounding the fish creates time-dependent pressure and shear-stress distributions on the skin. When integrated over the body, these distributions provide a resultant force and torque, resulting in linear and angular accelerations. It is common to divide the resultant force into thrust and drag, where thrust propels the fish, whereas drag opposes its motion. In engineering, drag is defined in the direction of the oncoming flow, and thrust is opposed to it (Anderson, 2001). In many engineering cases, the propulsive system is clearly separate from the body, so drag can easily be distinguished from thrust: drag acts on the body and thrust is produced by the propulsive system. However, for larval fish that undulate their whole body, this distinction is difficult to make (Schultz and Webb, 2002). A large part of the body surface contributes to both forward and backward forces, depending on the phase in the swimming cycle (Fig. 2.4A,B; Li et al., 2016). Almost no part of the body uniquely contributes to thrust or drag over a complete tail beat cycle, except the head, which almost exclusively experiences drag. Efforts were made to define drag and thrust on an undulating body, for example by separating friction forces from inertia forces (Chen et al., 2011), by estimating thrust from the body motion with a fluid-dynamic model (Webb et al., 1984) or by separating forward- and backward-acting forces (Fig. 2.4D–F; Li et al., 2012). The latter approach gives the most robust definition of thrust and drag, but is
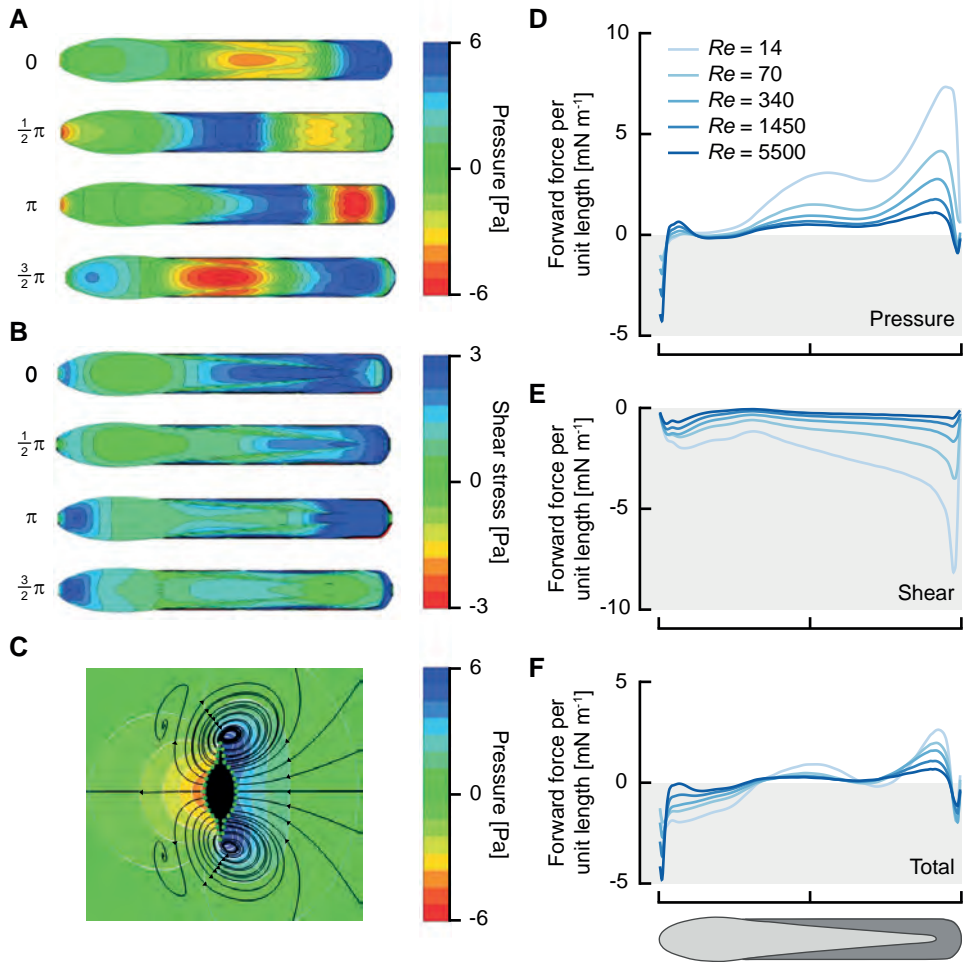
Figure 2.4: Predicted hydrodynamic force generation by a simplified zebrafish larva at different Reynolds numbers (Re**).** These data are from three-dimensional (3D) computational fluid dynamics of a simplified model of a zebrafish larva with dorsoventral symmetry, for which the travelling body waves were prescribed, and the changing body position and yaw were computed from fluid-dynamic forces. (A,B) Surface pressure (A) and shear stress (B) on the left side of the fish at four time instants throughout the cycle; Re = 340. (C) In-plane streamlines (lines) and pressure (contours) in a typical transversal cross-section. (D–F) Cycle-averaged forward component of the pressure force (D), shear force (E) and total force (F) per unit length along the body at different Re. Shear forces contribute almost exclusively to drag, and their relative importance with respect to pressure forces increases with decreasing Re. Adapted from Li et al. (2016).

not generally applicable to measurements on swimming fish because it requires quantitative estimates of fluctuating force distributions along the body.

Many approaches have been used to measure, estimate or calculate the hydrodynamic forces. With an inverse-dynamics approach, resultant forces and torques on the body have been calculated from swimming kinematics of larval zebrafish (2D: Fig. 2.3C; Van Leeuwen et al., 2015b). Particle image velocimetry (PIV; see Glossary) techniques have been used to quantify flow fields around swimming fish larvae (e.g. Müller et al., 2008), allowing the estimation of resultant hydrodynamic forces (Unal et al., 1997; Drucker and Lauder, 1999; Dabiri, 2005). In addition, velocity fields obtained with PIV have been used to estimate pressure fields in a horizontal plane around swimming fish (Dabiri et al., 2013). From the velocity gradient near the body, the shear-stress distribution can be calculated. Therefore, in principle, it is possible to calculate the force distribution on the skin from a velocity field around the fish. In practice, it is difficult to quantify this near-body velocity field with PIV [or with particle tracking velocimetry (PTV; see Glossary)]. Because the flow field around a swimming fish is fundamentally 3D (e.g. Fig. 2.4), 3D PIV/PTV techniques (e.g. Elsinga et al., 2006) are required. These techniques are expensive and still have a relatively low spatial resolution, leading to inaccurate estimations of pressure and shear-stress distributions on the skin. This makes it difficult to obtain reliable force distributions from PIV or PTV.

Force distributions on the fish have been calculated using fluid-dynamic models. In the inertial flow regime, Lighthill's elongated body theory (Lighthill, 1960, 1971) has been used extensively. However, this model is not applicable to the intermediate flow regime because it models only inertial forces and ignores friction (Borazjani and Sotiropoulos, 2009). Simplified fluid-dynamic models have been proposed (Jordan, 1996; Chen et al., 2011) where the force on every segment of the body is calculated based only on the motion of that segment. However, this does not take into account spatial and temporal interactions between segments. Especially for large-amplitude body motion, these assumptions might not hold (Van Leeuwen et al., 2015b). More advanced models have been applied by, for example, (Eloy, 2013), who combined different empirical models to achieve more accurate fluid-dynamic forces. Finally, the full Navier-Stokes equations describing fluid dynamics have been approximated numerically using computational fluid dynamics (CFD) techniques for swimming animals, for example tadpoles (Liu et al., 1997), a modelled eel-like swimmer (Kern and Koumoutsakos, 2006) and zebrafish larvae (Li et al., 2012). This approach has the advantage of capturing the complete fluid dynamics, and may provide accurate force distributions on the skin in the intermediate flow regime. In the inertial flow regime, where turbulence may be important, large-scale differences exist within the flow—from the smallest turbulent vortices to the much larger wake vortices—which makes accurate numerical flow computations challenging with the current technology. In contrast, the scale differences are much smaller in the intermediate flow regime, allowing all scales of the flow to be resolved at achievable computational cost. The calculated flow fields can be validated with flow measurements, for example with planar PIV (Li et al., 2012). We expect that, in the future, a combination of measured kinematics, flow fields and validated CFD will allow accurate estimation of force distributions for arbitrary 3D motion.

Such a CFD approach can help us to answer why small fish larvae show high body curvatures along a large range of the body. For fish swimming in the intermediate flow regime, the relatively high viscous forces result in three negative effects on swimming performance: (1) relatively high skin friction results in a relatively high body drag (Fig. 2.4; Li et al., 2012), (2) thrust is more costly to produce (Najafi and Golestanian, 2004), and (3) the increased amplitudes of the body undulations, necessary to compensate for the relatively high body drag, themselves further increase drag (Van Leeuwen et al., 2015b). Fig. 2.4D–F shows the contribution of pressure and shear (friction) forces to the thrust and drag for a modelled zebrafish larvae swimming at different Re, calculated using CFD (Li et al., 2016). The shear forces contribute almost exclusively to drag (Fig. 2.4E), and their relative importance increases with decreasing Re. For the lowest Re values ($<$ 100), a particularly high contribution to friction drag is present in the posterior region, where relatively strong velocity gradients occur near the skin. Most likely to compensate for the strong friction effects upon drag, the larval fish generates thrust by producing high-amplitude, high-frequency body motions (Verhagen, 2004; Müller and Van Leeuwen, 2004; Van Leeuwen et al., 2015b). This results in a pressure difference across the undulating body (Fig. 2.4D; Li et al., 2016), with large contributions of dorsal- and ventral-edge vortices created at the sharp edges of the finfold (Fig. 2.4C). The highest contribution to thrust is present in the posterior region.

An intriguing experiment with adult African lungfish (*Protopterus annectens*; ℓ = 510–590 mm, two orders larger than larval fish) demonstrated the importance of the Re regime for drag and thrust production (Horner and Jayne, 2008). The viscosity of the surrounding fluid was increased up to three orders of magnitude by adding a polymer to the water, pushing the Reynolds number of the swimming adult fish into the intermediate flow regime. The lungfish swam with increased muscle activity and body curvature in the mid and anterior regions of its trunk, with bending amplitudes (relative to ℓ) approximating those of fish larvae swimming in plain water. The higher drag at a given swimming speed in the more viscous regime presumably required an increased bending effort to generate a similarly higher thrust—the adult lungfish seem to deal with the increased viscous forces similarly to the much smaller larvae. Note that the tail-beat frequency did not reach values similar to larval fish because the much larger body inertia of the lungfish presumably prevented this.

The dimensionless Strouhal number (St; see Glossary) is an important quantity relating tail-beat characteristics and forward velocity and is defined as (Triantafyllou et al., 1993):

$$\text{St} = \frac{fA}{\bar{v}}, \tag{2.2}$$

where f is tail-beat frequency and A is peak-to-peak tail amplitude. The Strouhal number gives an indication of the wake topology; assuming that vortices are shed at the extremes of the lateral tail motion, they are laterally spaced at a distance A and longitudinally at a distance $\bar{v}(2f)^{-1}$ (Fig. 2.5A). The Strouhal number of a swimming fish also defines the
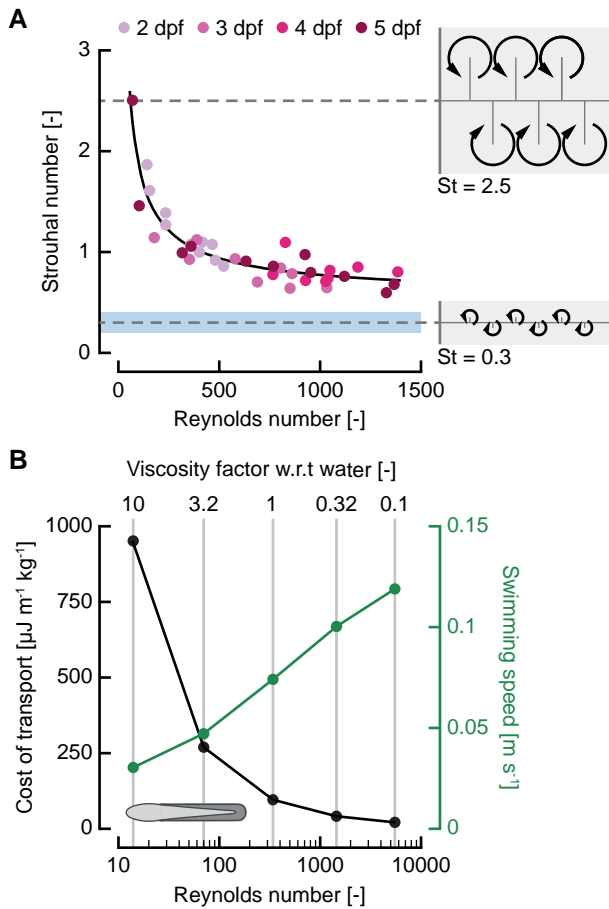
Figure 2.5: Effects of Reynolds number (Re**) on the Strouhal number (**St**) and cost of transport (**CoT**).** (A) St versus Re for zebrafish (*Danio rerio*) larvae of four age classes (colours). Data from Van Leeuwen et al. (2015a,b). The blue region is the suggested optimal St range of 0.2–0.4 from Taylor et al. (2003). Indicated on the right, connected to the dashed lines, are theoretical wake patterns for St = 0.3 and 2.5. (B) CoT (black) and swimming speed (green) versus Re of a simplified computational model of a zebrafish larva swimming in fluids with different viscosities, using the same body curvature fluctuations. Despite the increase in swimming speed with decreasing viscosity, CoT reduces with Re. Data from Li et al. (2016).

ratio between oscillatory flow velocities induced by the beating tail (that scale with fA) and translatory flow velocities (associated with $\bar{v}$). Drag on an animal scales approximately with v^2, whereas thrust scales approximately with $(fA)^2$. A poorly streamlined animal generates relatively high body drag at a given $\bar{v}$ and, thus, to swim periodically, it needs to generate an equally high thrust force, which is achieved by increasing fA. For this reason, poorly streamlined animals need to swim at a relatively high St to produce enough thrust to counter drag, such as crocodiles swimming at $\text{St} = 0.78$ (Eloy, 2012, based on data of Seebacher et al., 2003). For a similar reason, animals that are 'streamlined' but operate at low Re need also to swim at high St (e.g. the lungfish described above) because the relatively strong viscous effects similarly result in increased body drag, which consequently requires an equal increase in thrust production. Owing to this dependency on the friction forces, St varies with Re in the intermediate flow regime (Fig. 2.5A; Kayan et al., 1978; Borazjani and Sotiropoulos, 2009; Van Leeuwen et al., 2015b).

2.4 Energetics

Energy efficiency is important for fish in general, and especially for larvae. Young larvae have a limited amount of energy in their yolk and are not yet able to feed. Because the 'primary goal' of the larva is to reach the reproductive adult stage and produce offspring, they need to use as much of this yolk for growth and development as possible. Because swimming activity can contribute up to 80% of the total metabolism [for larval cod (Ruzicka and Gallager, 2006)], saving energy on locomotion can have a large impact on the total energy budget. Therefore, it is useful to define a measure of swimming energetics for comparison between species and between developmental stages.

Based on the efficiency of thrust production of an oscillating foil in the inertial flow regime, Triantafyllou and colleagues (1993) proposed that optimal efficiency is achieved for St values of 0.25–0.35, where the vortices shed by the fish are optimally reused for thrust production. For the inertial regime, most examined flying and swimming animals have been found to operate in an St range of 0.2–0.4 (Taylor et al., 2003). In contrast, within the intermediate regime, animals tend to operate at higher St than the optimal range for inertia-dominated flows (Fig. 2.5A; Eloy, 2012; Van Leeuwen et al., 2015b). To produce sufficient thrust to overcome the relatively high (viscous) drag at a given swimming speed (see Fluid dynamics section, above), animals swimming in the intermediate Re regime may need to operate at relatively high St. Further research is required to elucidate the link between St value and energy use for the intermediate flow regime.

Another measure often used in the analysis of swimming energetics is the Froude efficiency (η) (Lighthill, 1960), defined as:

$$\eta = \frac{\bar{P}_{\text{output}}}{\bar{P}_{\text{input}}} = \frac{\bar{T}\bar{v}}{\bar{P}_{\text{input}}} = \frac{\bar{D}\bar{v}}{\bar{P}_{\text{input}}}, \tag{2.3}$$

where $\bar{P}_{\text{input}}$ and $\bar{P}_{\text{output}}$ are the cycle-averaged input and output power, respectively. The output power consists of the product of cycle-averaged swimming speed ($\bar{v}$) and magnitude of thrust ($\bar{T}$) or drag ($\bar{D}$), which are equal during cyclic swimming. However, as mentioned above, unambiguously separating drag and thrust requires extensive computational effort, which is not feasible in many cases. But, most importantly, η does not relate to absolute power consumption, a quantity crucial to the fish. To illustrate, consider a high-drag fish and a low-drag fish swimming at the same speed with identical η. The high-drag fish has a higher output power ($\bar{D}\bar{v}$) than the low-drag fish, and therefore requires a higher input power, despite having the same η. In agreement with (Schultz and Webb, 2002), these reasons make Froude efficiency unsuitable as a measure of energetics for whole-body swimmers such as fish larvae.

Instead, a measure of swimming energetics during cruising should give a direct indication of swimming-related power consumption (Schultz and Webb, 2002). Cost of transport (CoT) (Schmidt-Nielsen, 1972) is defined as a locomotion-related energy consump-

tion per unit distance and unit mass:

$$\mathrm{CoT} = \frac{E_{\mathrm{input}}}{dm} = \frac{\bar{P}_{\mathrm{input}}}{\bar{v}m}, \qquad (2.4)$$

where E_{input} is input energy required for locomotion, d is covered distance and m is the mass of the fish. The CoT is directly relevant to the energetics of the animal—minimising CoT at a particular swimming speed is identical to minimising power (and therefore energy) consumption. Furthermore, determining CoT is not burdened by the difficulties associated with separating thrust and drag. The CoT is relevant for cruising fish, swimming either (approximately) cyclically or by burst-and-coast. It is less suitable for motions where maximum acceleration and short response times are paramount, such as fast starts. Here, an efficiency-like quantity could be used, taking for example the ratio of the final kinetic energy to the total invested energy.

To calculate CoT, multiple definitions of the input power are possible, either derived only from the fluid and body dynamics or, better, taking into account all sources of increased energy expenditure due to locomotion, including for example muscles and circulation. The first, which ignores the conversion losses of metabolic energy into muscle work, can be calculated from CFD results (e.g. Li et al., 2012), whereas the latter can be determined from, for example, respiration flow-tunnel experiments (e.g. Madan Mohan Rao, 1971; Palstra et al., 2008). These experiments are, however, challenging for small larval fish because they tend to swim in the (low speed) boundary layer or even adhere to the bottom. Therefore, to measure the swimming speed in a flow tunnel accurately, the flow profile of the tunnel and the position of the larva within it need to be quantified. Note that the locomotion-related energy consumption should be extracted from the respirometry-derived total energy consumption by correcting for the basal metabolic rate.

The body and fluid-dynamic components of the CoT give insight into the energy expended into the flow, but the quantity directly relevant to the fish is the muscle input power—the power that is actually consumed for swimming. Because the muscle efficiency depends on shortening rate and frequency (Curtin and Woledge, 1993), which in turn depend on the motion of the fish, optimal swimming for minimal muscle power presumably needs to compromise between efficient fluid dynamics and optimal muscle shortening rates. Therefore, the optimal swimming motion that minimises fluid-dynamic power will in general not minimise muscle power. Hence, depending on the type of analysis, care should be taken to clearly define the CoT.

Li et al. (2012) studied the effect of swimming speed on (body and fluid-dynamic) power consumption for a simplified model of a zebrafish by varying curvature amplitude. This showed that CoT increases with swimming speed, presumably caused by an increase in drag. Fig. 2.5B shows the swimming speed and (body and fluid-dynamic) CoT for a similar model larva swimming at different viscosities with identical body-curvature fluctuations (Li et al., 2016). Owing to a reduction in viscous forces at a higher Re, thrust and drag are balanced at a higher swimming speed. Despite this higher speed, CoT is lower at a higher Re: the hydrodynamic regime influences CoT strongly.

Fish larvae can actively change their CoT by selecting the speed at which they swim: a lower speed tends to result in a lower CoT (Li et al., 2012). However, constraints often exist on the time spent to cover a distance. The larva needs to compromise between energy consumption and travel time. For example, for a foraging larva, the amount of consumed food tends to increase with the average swimming speed, as does the CoT (i.e. power consumption). In this case, the optimal swimming speed might be the one that leads to the highest net energy gain (energy gained from the food minus the costs for catching and processing), balancing between food intake and energy spent on locomotion (Ware, 1975).

2.5 Muscles

Fish larvae power swimming with their axial muscle system. The varying demands on the muscular system throughout development require continuous molecular changes and spatial rearrangement of muscle fibres, as well as changes in the neural pattern generators that orchestrate the spatiotemporal muscle activation. Given the size and scope of this Review, we do not intend to provide a broad overview of the regulation of muscle development and the molecular changes that occur during the larval phase. Instead, we highlight selected biomechanical challenges that fish larvae need to cope with and point at evolved solutions.

The trunk muscles in bony fish are arranged in two rostrocaudal series of myomeres, one at each side of the body, that power the lateral bending of the body during swimming (Fig. 2.6A). It is advantageous if all muscle fibres in the myomeres can usefully contribute to the mechanical work required to bend the body, and thus power swimming (Alexander, 1969; Van Leeuwen et al., 2008). To achieve this, active muscle fibres need to contract at similar strains, which depend on their lateral position and orientation. Van Leeuwen and colleagues (2008) showed that, in zebrafish, the internal arrangement of the muscle fibres changes over development—they initially have an approximately longitudinal orientation and rearrange over ontogeny to form near-helical muscle-fibre trajectories (Fig. 2.6B). Van Leeuwen et al. (2008) suggested that the fibre reorientation results in reduced variation of the longitudinal muscle-fibre strain over the muscle volume, allowing all muscle fibres to contribute effectively to work production. Although it is still unclear by which mechanism the muscle fibres rearrange, it was shown that larvae that cannot activate their trunk muscles undergo a much-reduced reorientation (Van der Meulen et al., 2005). This suggests that the muscle-fibre forces and the deformation of the trunk are essential for the muscle-fibre rearrangement.

Small fish larvae reach relatively high swimming speeds by beating their tails at high frequencies with large amplitude. Within hours after hatching at 2 dpf, larval zebrafish can swim with tail beat frequencies of ≈ 80 Hz, and 1 or 2 days later even at 90–100 Hz (Müller and Van Leeuwen, 2004; Van Leeuwen et al., 2015b,a), allowing them to reach swimming speeds of ≈ 65 body lengths s^{-1}. To generate these fast motions, the muscle system needs to produce high strain rates, and activate and deactivate at a high frequency. To meet these requirements, bony fish larvae have evolved 'specialised' very fast larval (embryonic) muscle-fibre types that are distinct from the slow (red), intermediate and fast (white) fibres
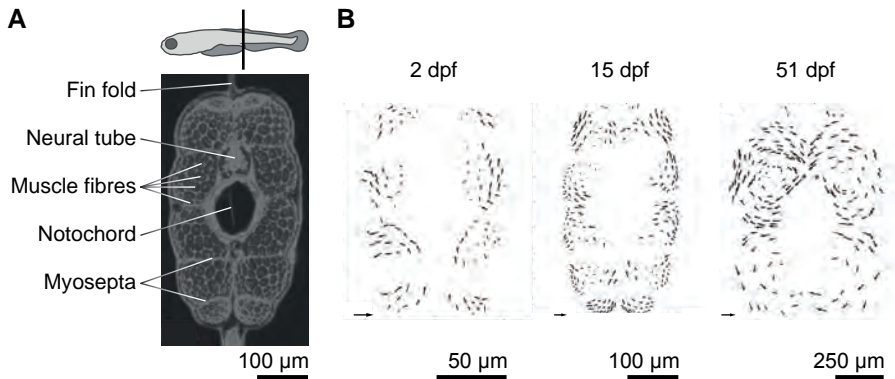
Figure 2.6: Muscle-fibre reorientation during development of zebrafish. (A) Cross-section of the trunk muscle of a 15-dpf zebrafish larva. The diagram at the top indicates the location of the slice, at the anus. Note that only a subset of muscle fibres and myosepta has been labelled. (B) Reorientation of muscle fibres over development of a larval zebrafish, for 2, 15 and 51 dpf. The vectors indicate muscle-fibre directions. Each vector is of unit length (indicated by the reference vector at the bottom left) in 3D. Hence, from the length of each projected vector, the angle with the projection plane can be deduced. Adapted from Van Leeuwen et al. (2008), who used data for 51 dpf larvae from Mos and Van der Stelt (1982).

found in juvenile and adult zebrafish (Buss and Drapeau, 2000). What makes these larval muscle fibres so very fast? They are short [< 200 μm in 7 dpf carp larvae (Alami-Durante et al., 1997)], leading to small activation delays along the fibre. High-frequency contractions require fast release and uptake of Ca^{2+} from the sarcoplasmic reticulum (SR). This is made possible by a relatively large membrane surface of the SR and by short diffusion distances within myofibrils with a comparatively small diameter [≈ 0.3 μm in larval herring (Vieira and Johnston, 1992); ≈ 1–1.2 μm in adult saithe (Patterson and Goldspink, 1976)]. Furthermore, different isotypes of the Ca^{2+}-binding protein parvalbumin are expressed over development (Focant et al., 1992; Huriaux et al., 1996), suggesting specific adaptations to the demands on fast Ca^{2+} release and uptake. In addition, fish larvae have distinct isoforms of myosin heavy chain and myosin light chain proteins compared with those of juveniles and adults (Scapolo et al., 1988; Crockford and Johnston, 1993; Huriaux et al., 1999; Veggetti et al., 1993), which is suggested to correspond to the extreme demands in larvae. Early fish larvae have been observed to have high mitochondrial densities in the muscle (Vieira and Johnston, 1992; Brooks et al., 1995). This, together with the short diffusion distances, suggests that small larvae always swim almost entirely aerobically with their very fast muscle (El-Fiky et al., 1987; Wieser, 1995). As the larvae grow, tail-beat frequencies are decreased owing to the increasing body inertia. At this stage, slower muscle-fibre types appear, suitable for cruising aerobically with higher efficiency than the very fast muscles (Mascarello et al., 1995).

The muscle system needs specific activation patterns to perform effective swimming motion. Muscle activation patterns during swimming are often measured with electromyography (EMG) in adult fish (e.g. Blight, 1976; Van Leeuwen et al., 1990; Horner and

Jayne, 2008). For smaller larval fish, this technique is difficult without strongly disrupting swimming behaviour. Muscle activation patterns were measured in so-called fictive swimming, where a paralysed fish is stimulated to swim and an EMG signal is recorded at the muscles (Buss and Drapeau, 2002). These investigations showed that muscle activation patterns in larval zebrafish are similar to those of the adult fish, with alternating left–right activation of the muscle with a rostrocaudal delay. More recently, a method was proposed to measure muscle activity on a fixed, but non-anaesthetised, zebrafish larva (Cho et al., 2015). However, as far as we are aware, no muscle-activation-pattern measurements have been performed on free- swimming larval fish, limiting our knowledge on the locomotory control in fish larvae.

To drive the very fast muscle system, the neural motor system should be up to the task of generating very fast activation patterns. The motoneurons in the spinal cord of the larval zebrafish that innervate the muscles are arranged in left and right dorsoventral columns (McLean et al., 2007; Fetcho and McLean, 2010). The fastest primary motoneurons lie dorsally and activate high-power, high-frequency motions, whereas the slowest motoneurons lie ventrally and activate finely controlled low-frequency motions. The fastest motoneurons develop first; the slowest motoneurons develop last. Thus, the functionally different motoneurons are spatially segregated and their appearance is shifted in time. McLean and colleagues (2007) suggested that the activation of the motoneurons takes place according to the size principle (Henneman et al., 1965)—the dorsal motoneurons are larger than the ventral ones and more difficult to recruit. In the hindbrain, very large so-called Mauthner (and homologous) neurons are already present in just-hatched larvae. Their axons run along the entire spinal cord and innervate motoneurons. These neurons drive the fast starts by initiating an almost instantaneous activation along one side of the trunk (see Escaping predators section, below). The early presence of the Mauthner neurons and their homologues, and the fastest motoneurons, support fast high-frequency motions from the day of hatching in the larval zebrafish, but fine control is still lacking owing to the absence of functional slower motoneurons, which are still developing. This results in fast but 'visually chaotic' swimming motions of 2-dpf larvae, which seem hard to predict and might still be effective for predator avoidance. Later in development, the response to threats becomes more refined (see also Escaping predators section, below).

2.6 Cruising and dispersal

An obvious reason to swim is to cover distance for migration and dispersal: many fish larvae disperse early in development, travelling long distances (e.g. Sancho et al., 1997; Dudley et al., 2000). For late-stage reef-fish larvae, active swimming might affect dispersion at a magnitude comparable to that of oceanic currents (Fisher, 2005; Huebert and Sponaugle, 2009). These late-stage larvae are relatively large (15–30 mm) and swim at relatively high speeds [≈ 0.2–$0.6\,\mathrm{m\,s^{-1}}$, ≈ 10–20 body lengths$\,\mathrm{s^{-1}}$ (Fisher, 2005)], and so their Re values (3300–$20,000$) are well within the inertial regime. The resulting low CoT allows them to disperse over longer distances, and their relatively high swimming speed allows them

to achieve this within a suitable time window. Even larvae of non-migrating species often need to cruise. Larvae foraging in habitats of low food abundance need to swim relatively long distances to find prey. In addition, in the presence of a prevailing current, larvae need to swim for prolonged periods to remain in their current habitat, unless they have an organ to attach themselves to the substrate (Able et al., 1984; Pottin et al., 2010).

Virtually all bony-fish larvae have a functional finfold when they hatch (Kendall Jr. et al., 1984). To what extent could such a finfold be useful for swimming in the intermediate flow regime? As explained above (see Fig. 2.4), fish larvae swimming in this regime need to produce high thrust to compensate for high drag. To this end, fish larvae adopt an anguilliform swimming style, with a large region along the body that curves substantially and produces thrust. Using CFD, Li and colleagues (2016) showed that production of thrust is enhanced by edge vortices emanating from a sharp edge, making a finfold surrounding a large part of the body an effective adaptation to increase thrust. Keeping the body-curvature fluctuations the same, they also computed that a removal of the finfold, except for the caudal fin, leads to a decrease in swimming speed and fluid-dynamic power input, but with almost the same fluid-dynamic CoT. Thus, compared with the finfold-less larval morph, the morph with finfold covers distance within a shorter time with the same fluid-dynamic costs. This might be advantageous during migration and searching for prey, if the higher power can be delivered with the muscular system. These findings might help to explain the omnipresence of the finfold in larval bony fish.

As the larvae grow, inertia becomes more important during swimming. The associated relative drag reduction allows many fish to shift towards a carangiform swimming mode (see Glossary) by reducing the relative curvature amplitude along their bodies (see Body kinematics section; Osse and Van den Boogaart, 2000). This change in swimming style correlates with development of a separate caudal fin in many species (Osse and Van den Boogaart, 1995). In some species, development of the caudal fin occurs before that of other unpaired fins, presumably because it has the largest contribution to thrust production [black rockfish (Omori et al., 1996), yellow-fin mullet (Kingsford and Tricklebank, 1991)].

2.7 Escaping predators

Predation is an important cause of mortality in fish larvae (Sogard, 1997). Hence, the chances of survival will increase with increasing ability to escape predators. Larval fish generally attempt to escape predators by performing a 'C-start', during which they curl their body into a C-shape, with little movement of the CoM (stage 1, or preparatory stroke), and then uncurl to generate high thrust, and therefore high accelerations of their CoM [stage 2, or propulsive stroke (Müller et al., 2008)]. This motion is often followed by a high-amplitude, high-frequency swimming bout (Müller and Van Leeuwen, 2004). Fig. 2.7A shows an example of a 3D kinematic analysis of a fast-starting zebrafish larva (data in Dataset 1), illustrating the strong body curvature at the end of the C-phase, the subsequent push-off phase with a rapid increase in CoM velocity, and the 3D nature of the motion.
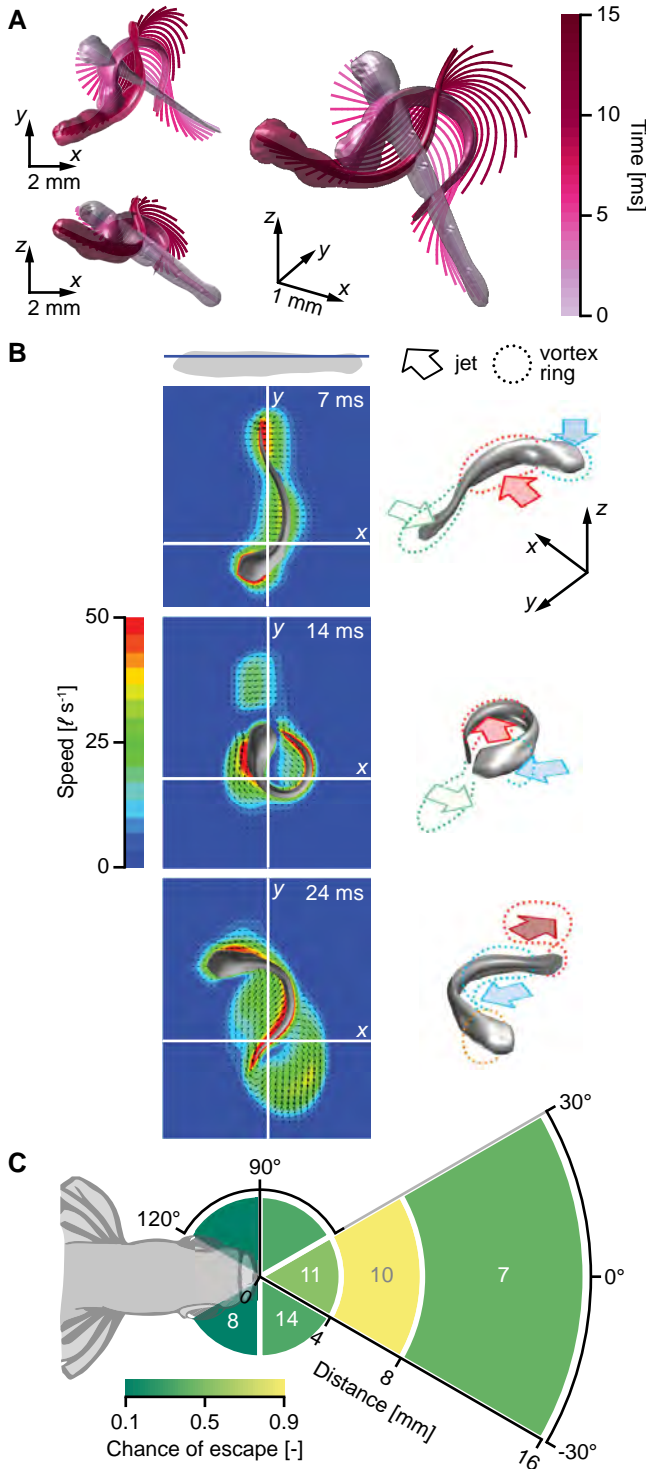
Figure 2.7: Escape responses by larval fish. (A) Fast-start escape response by a 3-dpf zebrafish larva (top view, side view and 3D view) automatically tracked from three synchronised high-speed video cameras at 2000 frames s^{-1} using the setup and method described in Voesenek et al. (2016). Fish midlines are indicated in 3D with lines coloured by time. In all views, three 3D renders are shown: at the start of the escape, at the end of stage 1 and at the end of stage 2. Based on unpublished data by C.J.V., R. P. M. Pieters and J.L.v.L. (B) Contours of velocity magnitude and velocity vectors around a zebrafish larva performing a C-start, simulated with computational fluid dynamics (CFD), along with sketches of the flow illustrating the evolution of jets and vortex rings, at different time instants. The contour plots are shown in the x–y plane, at the height indicated by the blue line over the sketch of the zebrafish. In the sketches at the right, jets (arrows) and vortex rings (dotted lines) with the same colours over multiple time instants indicate that they are the same structure. Adapted from Li et al. (2014). (C) Timing of escape responses is important for survival. The probability of escape depends on distance from the predator's mouth, and the angle with respect to the predator's heading. In the figure, the sketch of the fish head represents the predator; the escape probability is indicated by colour, binned by angle and distance; inside each bin is the number of samples. Adapted from Stewart et al. (2013).

Initiation of the C-start requires fast unilateral activation of the axial muscles [e.g. for adult bluegill sunfish (Jayne and Lauder, 1993)]. Such manoeuvres require concerted actions of the complete locomotory system: the sensory-motor system needs to detect threats reliably, and initiate and control the escape; the muscular system should produce enough force and power at short activation times; and the external morphology needs to support effective hydrodynamic thrust production to maximise acceleration.

2.7.1 Producing high accelerations and velocities

During the preparatory stroke, zebrafish larvae produce a jet flow into the C-form (Fig. 2.7B; Li et al., 2014; Müller et al., 2008). The resulting pressure distribution on the body mainly produces a torque that rotates the larva (Li et al., 2012). In the following propulsive stroke, the jet is reoriented along the body (Fig. 2.7B), where the pressure distribution propels the fish forward and provides a torque that counteracts the angular velocity produced in the preparatory stroke. The relatively high thrust results in high accelerations; for zebrafish, up to $28\,g$ (Müller and Van Leeuwen, 2004). CFD simulations indicate that the typical motions of a C-start in larval fish tend to maximise escape distance (Gazzola et al., 2012). After the propulsive phase, larvae use large-amplitude high-frequency motion, up to ≈ 100 Hz [zebrafish (Müller and Van Leeuwen, 2004; Van Leeuwen et al., 2015b)]. Larval fish increase their fast-start performance over development, decreasing the time spent performing a start and increasing the distance within that time, which is suggested to be associated with an increase in Re [Chinook salmon (Hale, 1996)].

The high-frequency body undulations require the muscle system to operate at the same high frequencies and produce relatively high forces and power within a short time (< 5 ms) to push off against the water with the tail. These short high-amplitude contractions lead to high strain rates, and put high demands on the activation and deactivation systems. This conflicts with the requirement to produce high force: superfast muscle required for high-frequency swimming tends to produce low tensile stresses at low efficiency (Rome et al., 1999). However, because the larvae are small, scaling works in their favour: the produced force is proportional to the muscle physiological cross-section, which scales with ℓ^2, whereas body mass is approximately proportional to the volume, which scales with ℓ^3. The favourable ratio of muscle cross-section to body inertia allows larvae to produce sufficient muscle force to power strong accelerations. Furthermore, fish larvae might employ an elastic mechanism to support swimming at high frequencies (Müller and Van Leeuwen, 2004). For example, larval carp have smaller, stiffer isoforms of titin than adults, suggested to contribute to an increased muscle and body stiffness and possibly elastic energy storage (Spierts, 2001). As fish larvae grow, the required hydrodynamic power for escaping increases but it is compensated by a decrease in the required muscle shortening velocity and an increase in muscle mass, leading to an increase in total muscle force and power [carp (Wakeling et al., 1999)].

2.7.2 Timing and controlling the escape

When attacked by a slow-moving predator, as is often the case for suction-feeding predators (Webb, 1984), fish larvae may reach higher speeds than the predator. In these cases, predator detection rather than locomotor performance has been suggested to be the most important determinant of escape success (Nair et al., 2017). Prey escape success in zebrafish larvae is highest when they respond at an intermediate distance (4–8 mm) from the predator (Fig. 2.7C; Stewart et al., 2013). Larger response distances allow the predator to adjust its intercept course, whereas smaller distances do not give the larvae enough time to escape. This places requirements on the sensing systems, to detect predators sufficiently early, and on the control of the escape, to perform an adequate response.

Flow sensing using the lateral line (see Glossary) plays an important role for predator detection (McHenry et al., 2009). Zebrafish larvae detect the approach of a predator by sensing pressure differences, and escape in the direction away from the fastest flow (Stewart et al., 2014). In Atlantic herring, late-stage larvae make more-sophisticated escape manoeuvres than younger larvae and undergo fewer false alarms (Fuiman, 1993), suggesting that they become better at performing a proportional and well-timed response, presumably owing to learning, and improved sensing and control capabilities.

Fish larvae also use visual cues to detect threats. Zebrafish larvae of 5–6 dpf respond to a growing dark spot (i.e. a looming stimulus) by performing an escape manoeuvre after it has reached a critical size on the retina, suggesting relatively advanced visual processing early in development (Dunn et al., 2016). Herring larvae only show responses to looming stimuli late in development (at 25 mm body length), whereas early larvae do respond to flashing stimuli, indicating that visual processing power increases over development (Batty, 1989). Compared with sound or touch, visual responses result in more escape trajectories directed away from the stimulus. Hence, it is likely that improvements in the sensory systems allow older fish larvae to escape predators more effectively.

Fast reaction times place requirements on the neural control of escape manoeuvres and sensors to detect approaching predators. The fast-start response to stimuli is controlled mainly by the Mauthner neurons and their homologues (Wilson, 1959; Foreman and Eaton, 1993). A group of three reticulospinal neurons—the Mauthner cell, MiD2cm and MiD3cm—initiates escape manoeuvres in zebrafish larvae: the Mauthner cell is involved in responding to tail-directed stimuli, whereas the two other neurons respond to head-directed stimuli (Liu and Fetcho, 1999). This system develops early in zebrafish: larvae show a strong swimming response to touch stimuli after 2 days of development (Eaton and Farley, 1973), allowing them to respond to threats immediately after hatching. The response time to visual stimuli is often much larger than that of acoustic stimuli, and delays in both decrease throughout development [red drum larvae (Fuiman et al., 1999)].

Following an optimal escape trajectory requires precise control of muscle activation patterns. In adult goldfish, the escape trajectory is controlled by the relative magnitude of ipsilateral and contralateral muscle contraction, and by the delay between them (Foreman and Eaton, 1993). Furthermore, fish larvae actively regulate the elevation angle of their fast

starts, likely by separate activation of hypaxial and epaxial muscle [zebrafish (Nair et al., 2015)], and presumably also by using their medial and paired fins. During a strong C-start, an escaping larva can intercept its own wake, which causes a deflection of the escape path of more than 5 deg (Li et al., 2014). For precise control over the final heading of the escape trajectory, this should be taken into account by the neural control system.

2.8 Hunting and feeding

The vast majority of hatched fish larvae die before they reach the juvenile stage, often owing to starvation (Hjort, 1914; Houde, 2002). As soon as larvae exhaust their yolk, they need to hunt prey to meet their energy requirements. Limited energy supply arising from ineffective feeding can cause starvation; in a less extreme case, it can limit the growth rate of the larva (Lee et al., 2010). The resulting smaller size might negatively affect survival owing to increased predation of smaller larvae (Peterson and Wroblewski, 1984). To gather the required food, nearly all teleost fish larvae are pelagic suction feeders preying on zooplankton after they exhaust their yolk sac (Hunter, 1980; Drost, 1987). Suction feeding places requirements on the developing fish: it needs to be able to detect prey, approach it while aiming the mouth, create an accurately timed suction flow, and subsequently swallow and digest the prey (Osse, 1989). The hydrodynamics of suction feeding depends on the Reynolds number. Feeding under relatively viscous conditions generally seems less successful because the prey can more easily escape the suction, requiring smaller forces than in a less viscous flow regime (China and Holzman, 2014). For this reason, larger fish can catch more prey and hence survive longer.

The locomotory system supports suction feeding by allowing the fish to control and time its prey approach for effective capture (Van Leeuwen, 1984). During undulatory swimming, the head oscillates with respect to the path of the CoM (Van Leeuwen et al., 2015b). This makes a precise approach of the feeding apparatus towards the prey difficult, especially without creating large flow disturbances that might be sensed by the prey. The fish require specific adaptations to achieve this, either another means of propulsion (e.g. pectoral fins) or specific control patterns that limit head motion and hydrodynamic disturbances [e.g. a J-turn (Bianco et al., 2011)].

Pectoral fin movement to brake and manoeuvre during suction feeding has been observed in adult (Higham, 2007) and juvenile (Lankheet et al., 2016) fish. Pectoral fins have been suggested to play a respiratory function in larval zebrafish, rather than a locomotory one (Green et al., 2011; Hale, 2014), because genetic elimination of the pectoral fins did not seem to influence slow-swimming performance. However, during feeding, they might play an important role in aligning the head through control of the pitch and yaw angles, as well as contributing to forward acceleration and deceleration. Fig. 2.8A depicts a carp larvae performing a feeding strike (Drost et al., 1987). It beats the pectoral fins to approach the prey, adducts them against the body and then brakes by flapping them forward. Zebrafish larvae beat their pectoral fins to align themselves before a strike, perform an S-start to accelerate and finally brake using forward motion of the pectoral fins (Fig. 2.8B). The S-start produces
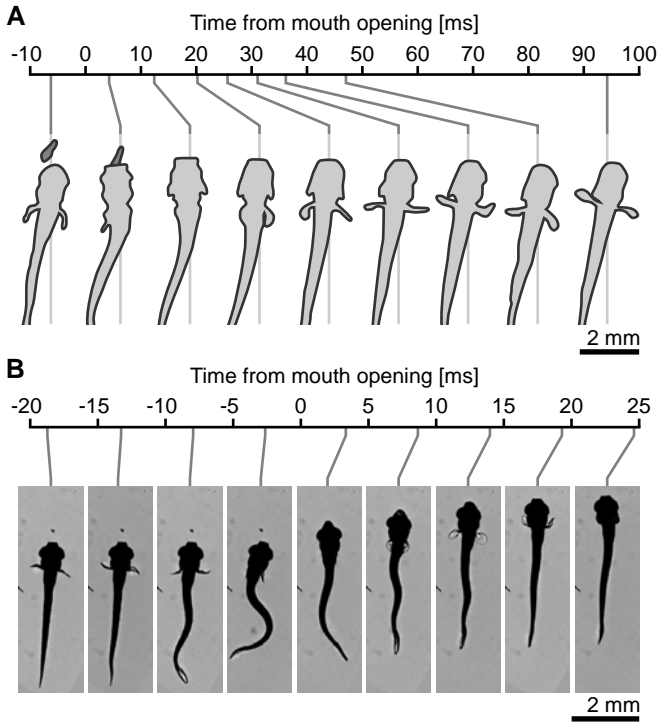
Figure 2.8: Pectoral fin use during feeding of carp and zebrafish larvae. (A) Traces from high-speed-video frames of a 6.5-mm carp (*Cyprinus carpio*; pale grey) larva while sucking prey (*Artemia*; dark grey). Redrawn from (Drost et al., 1987). (B) High-speed video frames of a 5-dpf zebrafish larva performing a feeding strike on a piece of debris. Based on unpublished data by C.J.V., R. P. M. Pieters and J.L.v.L. For both panels, time is relative to the moment of mouth opening, and each drawing/frame connects to the associated point on the time axis.

much lower yaw angles of the head than the C-start, allowing for an accurate alignment of the head.

Newborn juvenile guppies (*Girardinus metallicus*) have a partly 'innate' feeding behaviour, but more advanced eye-fin coordination develops rapidly after birth (Lankheet et al., 2016). Early zebrafish larvae (6–8 dpf) have been suggested to have fine motor control during feeding, showing complex bend-to-bend variation in timing and rostrocaudal location of bending (Borla et al., 2002). Prey tracking in zebrafish larvae is visually guided (McElligott and O'Malley, 2005). Because the eye becomes functional only after hatching (which occurs at 2 dpf) [zebrafish (Glass and Dahm, 2004)], rapid development of the visual processing system is required before the first feeding at approximately 5 dpf.

2.9 Perspectives

Much work on the swimming of fish has been performed under the assumption of periodic motion, although the majority of swimming behaviour of most (larval) fish is aperiodic. With the exception of fast starts, aperiodic motion has been studied much less. Furthermore, owing to technical limitations, much of the analyses have been done in a single plane, even though swimming motion is often highly 3D. Many open questions remain on the kinematics, fluid dynamics and control of complex 3D manoeuvres often performed by the fish during escape or hunting.

Whereas the fluid dynamics of wakes behind swimming fish has received considerable attention, both experimentally and numerically, the resulting force distributions on the skin have not. As demonstrated with dedicated CFD solvers (e.g. Li et al., 2016—see Fluid dynamics section), the fluid dynamics of swimming in the intermediate flow regime and the resulting force distributions can be well modelled using CFD techniques, because the lack of turbulence allows all relevant scales of the flow to be resolved accurately. The advent of open-source fluid-dynamic solvers [e.g. OpenFOAM (Jasak et al., 2007)] make this possible at low cost with comparatively limited programming effort. There are interesting opportunities to numerically investigate force, torque and power production, and 3D manoeuvring, and how these correlate with shifts in the fluid-dynamic regime.

The development and restructuring of the axial muscle of larvae have been investigated in previous studies, but research on the physiological properties and activation patterns of the larval muscle system is relatively limited. Larval fish have adapted to the required high-frequency contractions with specific larval muscle-fibre types, possessing unique properties. Research on these properties could uncover how larval muscle can generate sufficient force at such high frequencies. Furthermore, although many studies have measured muscle activation patterns of swimming adult fish, little is known about these patterns in free-swimming larval fish. These measurements might answer how larvae produce swimming motions with their muscles, how this changes over development and whether muscle control is innate or learned. Owing to the small size of the larvae, both muscle-property and muscle-activation measurements are challenging and will require novel methodologies.

Many studies have addressed different aspects of the biomechanics of larval swimming separately. However, swimming motion is created by a complex interaction between the different components; to understand the system as a whole, the components need to be studied integratively. By combining models and measurements of different systems of the fish, including the neuromuscular system, passive tissues and the fluid dynamics, an *in silico* integrative neuromechanical model of the fish larva can be developed. Although a daunting task, such an approach will allow investigators to study the effect of the variation of a large range of parameters on swimming performance in an unprecedented way, and might therefore answer numerous questions on the locomotory system of larval fish throughout their development.

Acknowledgements

Competing interests

The authors declare no competing or financial interests.

Funding

References

Able, K. W., Markle, D. F. and Fahay, M. P. (1984). Cyclopteridae: development. In *Ontogeny and Systematics of Fishes* (eds. H. G. Moser, W. J. Richards, D. M. Cohen, M. P. Fahay, A. W. Kendall, Jr. and S. L. Richardson), pp. 428–437. Lawrence, KS, USA: American Society of Ichthyologists and Herpetologists.

Alami-Durante, H., Fauconneau, B., Rouel, M., Escaffre, A. M. and Bergot, P. (1997). Growth and multiplication of white skeletal muscle fibres in carp larvae in relation to somatic growth rate. *J. Fish Biol.* **50**, 1285–1302.

Alexander, R. M. (1969). The orientation of muscle fibres in the myomeres of fishes. *J. Mar. Biol. Assoc. U. K.* **49**, 263–290.

Anderson, J. D. (2001). *Fundamentals of Aerodynamics*. New York City, NY, USA: McGraw-Hill.

Bainbridge, R. (1960). Speed and stamina in three fish. *J. Exp. Biol.* **37**, 129–153.

Batty, R. S. (1989). Escape responses of herring larvae to visual stimuli. *J. Mar. Biol. Assoc. U. K.* **69**, 647–654.

Bianco, I. H., Kampff, A. R. and Engert, F. (2011). Prey capture behavior evoked by simple visual stimuli in larval zebrafish. *Front. Syst. Neurosci.* **5**, 1–13.

Blight, A. R. (1976). Undulatory swimming with and without waves of contraction. *Nature* **264**, 352–354.

Borazjani, I. and Sotiropoulos, F. (2009). Numerical investigation of the hydrodynamics of anguilliform swimming in the transitional and inertial flow regimes. *J. Exp. Biol.* **212**, 576–592.

Borla, M. A., Palecek, B., Budick, S. and O'Malley, D. M. (2002). Prey capture by larval zebrafish: evidence for fine axial motor control. *Brain. Behav. Evol.* **60**, 207–229.

Brooks, S., Vieira, V. L. A., Johnston, I. A. and Macheru, P. (1995). Muscle development in larvae of a fast growing tropical freshwater fish, the curimatã-pacú. *J. Fish Biol.* **47**, 1026–1037.

Buss, R. R. and Drapeau, P. (2000). Physiological properties of zebrafish embryonic red and white muscle fibers during early development. *J. Neurophysiol.* **84**, 1545–1557.

Buss, R. R. and Drapeau, P. (2002). Activation of embryonic red and white muscle fibers during fictive swimming in the developing zebrafish. *J. Neurophysiol.* **87**, 1244–1251.

Butail, S. and Paley, D. A. (2012). Three-dimensional reconstruction of the fast-start swimming kinematics of densely schooling fish. *J. R. Soc., Interface* **9**, 77–88.

Chen, J., Friesen, W. O. and Iwasaki, T. (2011). Mechanisms underlying rhythmic locomotion: body-fluid interaction in undulatory swimming. *J. Exp. Biol.* **214**, 561–574.

China, V. and Holzman, R. (2014). Hydrodynamic starvation in first-feeding larval fishes. *Proc. Natl. Acad. Sci. U. S. A.* **111**, 8083–8088.

Cho, S.-J., Nam, T.-S., Byun, D., Choi, S.-Y., Kim, M.-K. and Kim, S. (2015). Zebrafish needle EMG: a new tool for high-throughput drug screens. *J. Neurophysiol.* **114**, 2065–2070.

Crockford, T. and Johnston, I. A. (1993). Developmental changes in the composition of myofibrillar proteins in the swimming muscles of Atlantic herring, *Clupea harengus*. *Mar. Biol.* **115**, 15–22.

Curtin, N. A. and Woledge, R. C. (1993). Efficiency of energy conversion during sinusoidal movement of white muscle fibres from the dogfish *Scyliorhinus canicula. J. Exp. Biol.* **183**, 137–147.

Dabiri, J. O. (2005). On the estimation of swimming and flying forces from wake measurements. *J. Exp. Biol.* **208**, 3519–3532.

Dabiri, J. O., Bose, S., Gemmell, B. J., Colin, S. P. and Costello, J. H. (2013). An algorithm to estimate unsteady and quasi-steady pressure fields from velocity field measurements. *J. Exp. Biol.* **217**, 331–336.

Drost, M. R. (1987). Relation between aiming and catch success in larval fishes. *Can. J. Fish. Aquat. Sci.* **44**, 304–315.

Drost, M. R., Muller, M. and Osse, J. W. M. (1987). Prey capture by fish larvae, water flow patterns and the effect of escape movements of prey. *Neth. J. Zool.* **38**, 23–45.

Drucker, E. G. and Lauder, G. V. (1999). Locomotor forces on a swimming fish: three-dimensional vortex wake dynamics quantified using digital particle image velocimetry. *J. Exp. Biol.* **202**, 2393–2412.

Dudley, B., Tolimieri, N. and Montgomery, J. (2000). Swimming ability of the larvae of some reef fishes from New Zealand waters. *Mar. Freshw. Res.* **51**, 783–787.

Dunn, T. W., Gebhardt, C., Naumann, E. A., Riegler, C., Ahrens, M. B., Engert, F. and Del Bene, F. (2016). Neural circuits underlying visually evoked escapes in larval zebrafish. *Neuron* **89**, 613–628.

Eaton, R. C. and Farley, R. D. (1973). Development of the Mauthner neurons in embryos and larvae of the zebrafish, *Brachydanio rerio. Copeia* **1973**, 673–682.

Ehrlich, D. E. and Schoppik, D. (2017). Control of movement initiation underlies the development of balance. *Curr. Biol.* **27**, 334–344.

El-Fiky, N., Hinterleitner, S. and Wieser, W. (1987). Differentiation of swimming muscles and gills, and development of anaerobic power in the larvae of cyprinid fish (Pisces, Teleostei). *Zoomorphology* **107**, 126–132.

Eloy, C. (2012). Optimal Strouhal number for swimming animals. *J. Fluids Struct.* **30**,

205–218.

Eloy, C. (2013). On the best design for undulatory swimming. *J. Fluid Mech.* **717**, 48–89.

Elsinga, G. E., Scarano, F., Wieneke, B. and Van Oudheusden, B. W. (2006). Tomographic particle image velocimetry. *Exp. Fluids* **41**, 933–947.

Fetcho, J. R. and McLean, D. L. (2010). Some principles of organization of spinal neurons underlying locomotion in zebrafish and their implications. *Ann. N. Y. Acad. Sci.* **1198**, 94–104.

Fisher, R. (2005). Swimming speeds of larval coral reef fishes: impacts on self-recruitment and dispersal. *Mar. Ecol. Prog. Ser.* **285**, 223–232.

Focant, B., Huriaux, F., Vandewalle, P., Castelli, M. and Goessens, G. (1992). Myosin, parvalbumin and myofibril expression in barbel (*Barbus barbus* L.) lateral white muscle during development. *Fish Physiol. Biochem.* **10**, 133–143.

Foreman, M. B. and Eaton, R. C. (1993). The direction change concept for reticulospinal control of goldfish escape. *J. Neurosci.* **13**, 4101–4113.

Fuiman, L. A. (1993). Development of predator evasion in Atlantic herring, *Clupea harengus* L. *Anim. Behav.* **45**, 1101–1116.

Fuiman, L. A., Smith, M. E. and Malley, V. N. (1999). Ontogeny of routine swimming speed and startle responses in red drum, with a comparison of responses to acoustic and visual stimuli. *J. Fish Biol.* **55**, 215–226.

Fuiman, L. A. and Webb, P. W. (1988). Ontogeny of routine swimming activity and performance in zebra danios (Teleostei: Cyprinidae). *Anim. Behav.* **36**, 250–261.

Gazzola, M., Van Rees, W. M. and Koumoutsakos, P. (2012). C-start: optimal start of larval fish. *J. Fluid Mech.* **698**, 5–18.

Gisbert, E., Merino, G., Muguet, J. B., Bush, D., Piedrahita, R. H. and Conklin, D. E. (2002). Morphological development and allometric growth patterns in hatchery-reared California halibut larvae. *J. Fish Biol.* **61**, 1217–1229.

Glass, A. S. and Dahm, R. (2004). The zebrafish as a model organism for eye development. *Ophthalmic Res.* **36**, 4–24.

Green, M. H., Ho, R. K. and Hale, M. E. (2011). Movement and function of the pectoral fins of the larval zebrafish (*Danio rerio*) during slow swimming. *J. Exp. Biol.* **214**, 3111–3123.

Hale, M. E. (1996). The development of fast-start performance in fishes: escape kinematics of the chinook salmon (*Oncorhynchus tshawytscha*). *Am. Zool.* **36**, 695–709.

Hale, M. E. (2014). Developmental change in the function of movement systems: transition of the pectoral fins between respiratory and locomotor roles in zebrafish. *Integr. Comp. Biol.* **54**, 238–249.

Henneman, E., Somjen, G. and Carpenter, D. O. (1965). Functional significance of cell size in spinal motoneurons. *J. Neurophysiol.* **28**, 560–580.

Higham, T. E. (2007). Feeding, fins and braking maneuvers: locomotion during prey capture in centrarchid fishes. *J. Exp. Biol.* **210**, 107–117.

Hjort, J. (1914). Fluctuations in the great fisheries of northern Europe, viewed in the light of biological research. *Rapp. P.-V. Cons. Perm. Int. Explor. Mer* **20**, 1–228.

Horner, A. M. and Jayne, B. C. (2008). The effects of viscosity on the axial motor pattern and kinematics of the African lungfish (*Protopterus annectens*) during lateral undulatory swimming. *J. Exp. Biol.* **211**, 1612–1622.

Houde, E. D. (2002). Mortality. In *Fishery Science: the Unique Contributions of Early Life Stages* (eds. L. A. Fuiman and R. G. Werner), pp. 64–87. Hoboken, NJ, USA: Blackwell Science.

Huebert, K. B. and Sponaugle, S. (2009). Observed and simulated swimming trajectories of late-stage coral reef fish larvae off the Florida Keys. *Aquat. Biol.* **7**, 207–216.

Hunter, J. R. (1980). The feeding behavior and ecology of marine fish larvae. In *Fish Behavior and Its Use in the Capture and Culture of Fishes*, pp. 287–330.

Huriaux, F., Mélot, F., Vandewalle, P., Collin, S. and Focant, B. (1996). Parvalbumin isotypes in white muscle from three teleost fish: characterization and their expression during development. *Comp. Biochem. Physiol., Part B: Biochem. Mol. Biol.* **113**, 475–484.

Huriaux, F., Vandewalle, P., Baras, E., Legendre, M. and Focant, B. (1999). Myofibrillar proteins in white muscle of the developing African catfish *Heterobranchus longifilis* (Siluriforms, Clariidae). *Fish Physiol. Biochem.* **21**, 287–301.

Jasak, H., Jemcov, A. and Tukovic, Ž. (2007). OpenFOAM : A C ++ library for complex physics simulations. In *Proceedings of the International Workshop on Coupled Methods in Numerical Dynamics* (eds. Z. Terze and C. Lacor), pp. 47–66. Zagreb, Croatia: Faculty of Mechanical Engineering and Naval Architecture.

Jayne, B. C. and Lauder, G. V. (1993). Red and white muscle activity and kinematics of the escape response of the bluegill sunfish during swimming. *J. Comp. Physiol., A* **173**, 495–508.

Jordan, C. E. (1996). Coupling internal and external mechanics to predict swimming behavior: a general approach. *Am. Zool.* **36**, 710–722.

Kaji, T., Tanaka, M., Takahashi, Y., Oka, M. and Ishibashi, N. (1996). Preliminary observations on development of pacific bluefin tuna *Thunnus thynnus* (Scombridae) larvae reared in the laboratory, with special reference to the digestive system. *Mar. Freshw. Res.* p. 261.

Kavanagh, K. D., Leis, J. M. and Rennis, D. S. (2000). Pomacentridae (Damselfishes). In *Larvae Indo-Pacific Coastal Fishes: An Identification Guide to Marine Fish Larvae* (eds. J. M. Leis and B. M. Carson-Ewart), pp. 526–535. Leiden, The Netherlands: Brill.

Kayan, V. P., Kozlov, L. F. and Pyatetskii, V. E. (1978). Kinematic characteristics of the

swimming of certain aquatic animals. *Fluid Dyn.* **13**, 641–646.

Kendall Jr., A. W., Ahlstrom, E. H. and Mose, H. G. (1984). Early life. In *Ontogeny and Systematics of Fishes* (eds. H. G. Moser, W. J. Richards, D. M. Cohen, M. P. Fahay, J. A. W. Kendall and S. L. Richardson), pp. 11–22. Lawrence, KS, USA: American Society of Ichthyologists and Herpetologists.

Kern, S. and Koumoutsakos, P. (2006). Simulations of optimized anguilliform swimming. *J. Exp. Biol.* **209**, 4841–4857.

Kingsford, M. J. and Tricklebank, K. A. (1991). Ontogeny and behavior of *Aldrichetta forsteri* (Teleostei, Mugilidae). *Copeia* **1991**, 9–16.

Lankheet, M. J., Stoffers, T., Van Leeuwen, J. L. and Pollux, B. J. A. (2016). Acquired versus innate prey capturing skills in super-precocial live-bearing fish. *Proc. R. Soc. B* **283**, 20160972.

Lee, W.-S., Monaghan, P. and Metcalfe, N. B. (2010). The trade-off between growth rate and locomotor performance varies with perceived time until breeding. *J. Exp. Biol.* **213**, 3289–3298.

Li, G., Müller, U. K., Van Leeuwen, J. L. and Liu, H. (2012). Body dynamics and hydrodynamics of swimming fish larvae: a computational study. *J. Exp. Biol.* **215**, 4015–4033.

Li, G., Müller, U. K., Van Leeuwen, J. L. and Liu, H. (2014). Escape trajectories are deflected when fish larvae intercept their own C-start wake. *J. R. Soc., Interface* **11**, 20140848–20140848.

Li, G., Müller, U. K., Van Leeuwen, J. L. and Liu, H. (2016). Fish larvae exploit edge vortices along their dorsal and ventral fin folds to propel themselves. *J. R. Soc., Interface* **13**, 20160068.

Lighthill, M. J. (1960). Note on the swimming of slender fish. *J. Fluid Mech.* **9**, 305–317.

Lighthill, M. J. (1971). Large-amplitude elongated-body theory of fish locomotion. *Proc. R. Soc. B* **179**, 125–138.

Liu, H., Wassersug, R. and Kawachi, K. (1997). The three-dimensional hydrodynamics of tadpole locomotion. *J. Exp. Biol.* **200**, 2807–2819.

Liu, K. S. and Fetcho, J. R. (1999). Laser ablations reveal functional relationships of segmental hindbrain neurons in zebrafish. *Neuron* **23**, 325–335.

Madan Mohan Rao, G. (1971). Influence of activity and salinity on the weight-dependent oxygen consumption of the rainbow trout *Salmo gairdneri*. *Mar. Biol.* **8**, 205–212.

Mascarello, F., Rowlerson, A., Radaelli, G., Scapolo, P.-A. and Veggetti, A. (1995). Differentiation and growth of muscle in the fish *Sparus aurata* (L): I. Myosin expression and organization of fibre types in lateral muscle from hatching to adult. *J. Muscle Cell Res. Cell Motil.* **16**, 213–222.

McElligott, M. B. and O'Malley, D. M. (2005). Prey tracking by larval zebrafish: axial

kinematics and visual control. *Brain. Behav. Evol.* **66**, 177–196.

McHenry, M. J., Feitl, K. E., Strother, J. A. and Van Trump, W. J. (2009). Larval zebrafish rapidly sense the water flow of a predator's strike. *Biol. Lett.* **5**, 477–479.

McLean, D. L., Fan, J., Higashijima, S., Hale, M. E. and Fetcho, J. R. (2007). A topographic map of recruitment in spinal cord. *Nature* **446**, 71–75.

McMillen, T. and Holmes, P. (2006). An elastic rod model for anguilliform swimming. *J. Math. Biol.* **53**, 843–886.

Mos, W. and Van der Stelt, A. (1982). Efficiency in relation to the design of the segmented body musculature in *Brachydanio rerio*. *Neth. J. Zool.* **32**, 123–143.

Müller, U. K., Van den Boogaart, J. G. M. and Van Leeuwen, J. L. (2008). Flow patterns of larval fish: undulatory swimming in the intermediate flow regime. *J. Exp. Biol.* **211**, 196–205.

Müller, U. K. and Van Leeuwen, J. L. (2004). Swimming of larval zebrafish: ontogeny of body waves and implications for locomotory development. *J. Exp. Biol.* **207**, 853–868.

Nair, A., Azatian, G. and McHenry, M. J. (2015). The kinematics of directional control in the fast start of zebrafish larvae. *J. Exp. Biol.* **218**, 3996–4004.

Nair, A., Changsing, K., Stewart, W. J. and McHenry, M. J. (2017). Fish prey change strategy with the direction of a threat. *Proc. R. Soc. B* **284**, 20170393.

Najafi, A. and Golestanian, R. (2004). Simple swimmer at low Reynolds number: Three linked spheres. *Phys. Rev. E: Stat. Phys., Plasmas, Fluids, Relat. Interdiscip. Top.* **69**, 062901.

Omori, M., Sugawara, Y. and Honda, H. (1996). Morphogenesis in hatchery-reared larvae of the black rockfish, *Sebastes schlegeli*, and its relationship to the development of swimming and feeding functions. *Ichtyological Res.* **43**, 267–282.

Osse, J. W. M. (1989). Form changes in fish larvae in relation to changing demands of function. *Neth. J. Zool.* **40**, 362–385.

Osse, J. W. M. and Van den Boogaart, J. G. M. (1995). Fish larvae, development, allometric growth, and the aquatic environment. *ICES Mar. Sci. Symp.* **201**, 21–34.

Osse, J. W. M. and Van den Boogaart, J. G. M. (1997). Size of flatfish larvae at transformation, functional demands and historical constraints. *J. Sea Res.* **37**, 229–239.

Osse, J. W. M. and Van den Boogaart, J. G. M. (2000). Body size and swimming types in carp larvae; effects of being small. *Neth. J. Zool.* **50**, 233–244.

Palstra, A., Van Ginneken, V. and Van den Thillart, G. (2008). Cost of transport and optimal swimming speed in farmed and wild European silver eels (*Anguilla anguilla*). *Comp. Biochem. Physiol., Part A: Mol. Integr. Physiol.* **151**, 37–44.

Patterson, S. and Goldspink, G. (1976). Mechanism of myofibril growth and proliferation in fish muscle. *J. Cell Sci.* **22**, 607–616.

Peterson, I. and Wroblewski, J. S. (1984). Mortality rate of fishes in the pelagic ecosystem. *Can. J. Fish. Aquat. Sci.* **41**, 1117–1120.

Pottin, K., Hyacinthe, C. and Rétaux, S. (2010). Conservation, development, and function of a cement gland-like structure in the fish *Astyanax mexicanus. Proc. Natl. Acad. Sci. U. S. A.* **107**, 17256–17261.

Rome, L. C., Cook, C., Syme, D. A., Connaughton, M. A., Ashley-Ross, M., Klimov, A., Tikunov, B. and Goldman, Y. E. (1999). Trading force for speed: why superfast crossbridge kinetics leads to superlow forces. *Proc. Natl. Acad. Sci. U. S. A.* **96**, 5826–5831.

Ruzicka, J. J. and Gallager, S. M. (2006). The importance of the cost of swimming to the foraging behavior and ecology of larval cod (*Gadus morhua*) on Georges Bank. *Deep-Sea Res. Part II: Top. Stud. Oceanogr.* **53**, 2708–2734.

Sancho, G., Ma, D. and Lobel, P. S. (1997). Behavioral observations of an upcurrent reef colonization event by larval surgeonfish *Ctenochaetus strigosus* (Acanthuridae). *Mar. Ecol. Prog. Ser.* **153**, 311–315.

Scapolo, P. A., Veggetti, A., Mascarello, F. and Romanello, M. G. (1988). Developmental transitions of myosin isoforms and organisation of the lateral muscle in the teleost *Dicentrarchus labrax* (L.). *Anat. Embryol.* **178**, 287–295.

Schmidt-Nielsen, K. (1972). Locomotion: energy cost of swimming, flying, and running. *Science (80-.).* **177**, 222–228.

Schultz, W. W. and Webb, P. W. (2002). Power requirements of swimming: do new methods resolve old questions? *Integr. Comp. Biol.* **42**, 1018–1025.

Seebacher, F., Elsworth, P. G. and Franklin, C. E. (2003). Ontogenetic changes of swimming kinematics in a semi-aquatic reptile (*Crocodylus porosus*). *Aust. J. Zool.* **51**, 15–24.

Sogard, S. M. (1997). Size-selective mortality in the juvenile stage of teleost fishes: A review. *Bull. Mar. Sci.* **60**, 1129–1157.

Spierts, I. L. Y. (2001). Titin isoforms and kinematics of fast swimming carp larvae (*Cyprinus carpio* L.). *Neth. J. Zool.* **51**, 17–31.

Stewart, W. J., Cardenas, G. S. and McHenry, M. J. (2013). Zebrafish larvae evade predators by sensing water flow. *J. Exp. Biol.* **216**, 388–398.

Stewart, W. J., Nair, A., Jiang, H. and McHenry, M. J. (2014). Prey fish escape by sensing the bow wave of a predator. *J. Exp. Biol.* **217**, 4328–4336.

Taylor, G. K., Nudds, R. L. and Thomas, A. L. R. (2003). Flying and swimming animals cruise at a Strouhal number tuned for high power efficiency. *Nature* **425**, 707–711.

Triantafyllou, G. S., Triantafyllou, M. S. and Grosenbaugh, M. A. (1993). Optimal thrust development in oscillating foils with application to fish propulsion. *J. Fluids Struct.* **7**, 205–224.

Tytell, E. D., Borazjani, I., Sotiropoulos, F., Baker, T. V., Anderson, E. J. and Lauder,

G. V. (2010). Disentangling the functional roles of morphology and motion in the swimming of fish. *Integr. Comp. Biol.* **50**, 1140–1154.

Tytell, E. D. and Lauder, G. V. (2008). Hydrodynamics of the escape response in bluegill sunfish, *Lepomis macrochirus*. *J. Exp. Biol.* **211**, 3359–3369.

Unal, M. F., Lin, J.-C. and Rockwell, D. (1997). Force prediction by PIV imaging: a momentum-based approach. *J. Fluids Struct.* **11**, 965–971.

Van der Meulen, T., Schipper, H., Van Leeuwen, J. L. and Kranenbarg, S. (2005). Effects of decreased muscle activity on developing axial musculature in *nic*^{b107} mutant zebrafish (*Danio rerio*). *J. Exp. Biol.* **208**, 3675–3687.

Van Leeuwen, J. L. (1984). A quantitative study of flow in prey capture by rainbow trout, *Salmo gairdneri* with general consideration of the actinopterygian feeding mechanism. *Trans. Zool. Soc. London* **37**, 171–227.

Van Leeuwen, J. L., Lankheet, M. J. M., Akster, H. A. and Osse, J. W. M. (1990). Function of red axial muscles of carp (*Cyprinus carpio*): recruitment and normalized power output during swimming in different modes. *J. Zool.* **220**, 123–145.

Van Leeuwen, J. L., Van der Meulen, T., Schipper, H. and Kranenbarg, S. (2008). A functional analysis of myotomal muscle-fibre reorientation in developing zebrafish *Danio rerio*. *J. Exp. Biol.* **211**, 1289–1304.

Van Leeuwen, J. L., Voesenek, C. J. and Müller, U. K. Data from: How body torque and Strouhal number change with swimming speed and developmental stage in larval zebrafish.

Van Leeuwen, J. L., Voesenek, C. J. and Müller, U. K. (2015b). How body torque and Strouhal number change with swimming speed and developmental stage in larval zebrafish. *J. R. Soc., Interface* **12**, 20150479.

Veggetti, A., Mascarello, F., Scapolo, P. A., Rowlerson, A. and Candia Carnevali, M. D. (1993). Muscle growth and myosin isoform transitions during development of a small teleost fish, *Poecilia reticulata* (Peters) (Atheriniformes, Poeciliidae): a histochemical, immunohistochemical, ultrastructural and morphometric study. *Anat. Embryol.* **187**, 353–361.

Verhagen, J. H. G. (2004). Hydrodynamics of burst swimming fish larvae; a conceptual model approach. *J. Theor. Biol.* **229**, 235–248.

Vieira, V. L. A. and Johnston, I. A. (1992). Influence of temperature on muscle-fibre development in larvae of the herring *Clupea harengus*. *Mar. Biol.* **112**, 333–341.

Voesenek, C. J., Pieters, R. P. M. and Van Leeuwen, J. L. (2016). Automated reconstruction of three-dimensional fish motion, forces, and torques. *PLoS One* **11**, e0146682.

Wakeling, J. M., Kemp, K. M. and Johnston, I. A. (1999). The biomechanics of fast-starts during ontogeny in the common carp *Cyprinus carpio*. *J. Exp. Biol.* **202**, 3057–3067.

Ware, D. M. (1975). Growth, metabolism, and optimal swimming speed of a pelagic fish.

J. Fish. Res. Board Canada **32**, 33–41.

Webb, P. W. (1984). Body and fin form and strike tactics of four teleost predators attacking fathead minnow (*Pimephales promelas*) prey. *Can. J. Fish. Aquat. Sci.* **41**, 157–165.

Webb, P. W., Kostecki, P. T. and Don Stevens, E. (1984). The effect of size and swimming speed on locomotor kinematics of rainbow trout. *J. Exp. Biol.* **109**, 77–95.

Weihs, D. (1979). Energetic significance of changes in swimming modes during growth of larval anchovy, *Engraulis mordax*. *Fish. Bull.* **77**, 597–604.

Wieser, W. (1995). Energetics of fish larvae, the smallest vertebrates. *Acta Physiol. Scand.* **154**, 279–290.

Wilson, D. M. (1959). Function of giant Mauthner's neurons in the lungfish. *Science* **129**, 841–842.

Xiong, G. and Lauder, G. V. (2014). Center of mass motion in swimming fish: effects of speed and locomotor mode during undulatory propulsion. *Zoology* **117**, 269–281.

2
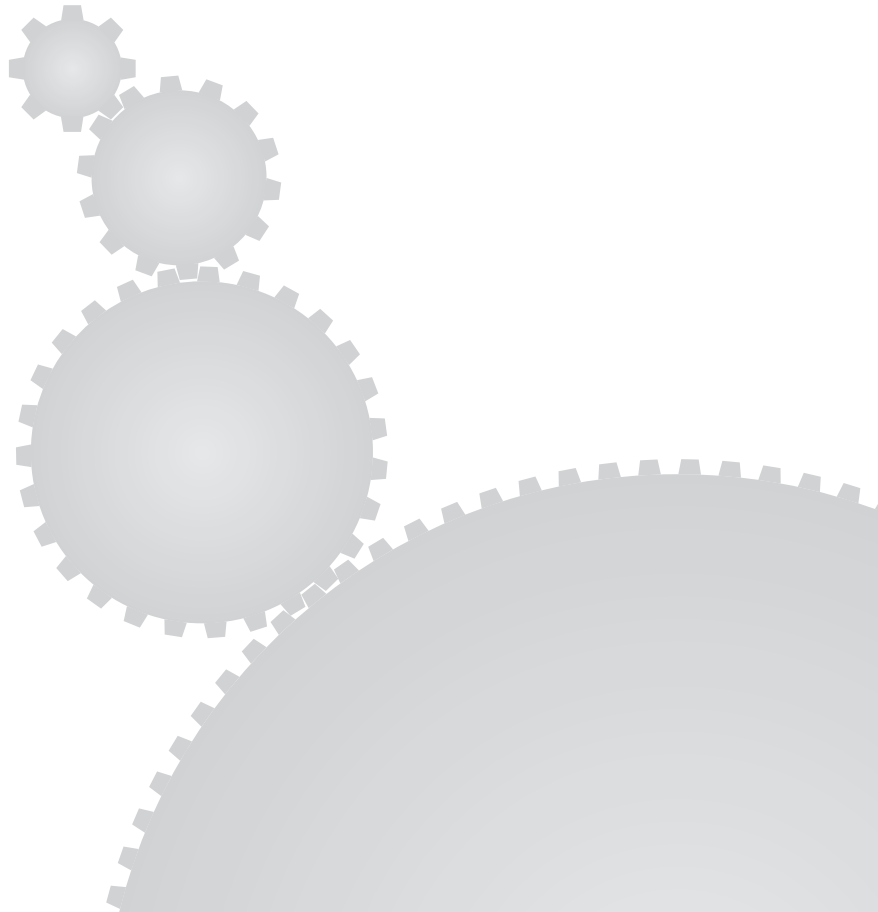
Chapter 3

How body torque and Strouhal number change with swimming speed and developmental stage in larval zebrafish

Johan L. van Leeuwen[1], Cees J. Voesenek[1], Ulrike K. Müller[2]

[1] Experimental Zoology Group, Wageningen University & Research, Wageningen, The Netherlands
[2] Department of Biology, California State University Fresno, Fresno, California, USA

Abstract

Small undulatory swimmers such as larval zebrafish experience both inertial and viscous forces, the relative importance of which is indicated by the Reynolds number (Re). Re is proportional to swimming speed ($\bar{v}_{\text{swim}}$) and body length; faster swimming reduces the relative effect of viscous forces. Compared with adults, larval fish experience relatively high (mainly viscous) drag during cyclic swimming. To enhance thrust to an equally high level, they must employ a high product of tail-beat frequency and (peak-to-peak) amplitude fA_{tail}, resulting in a relatively high $fA_{\text{tail}}/\bar{v}_{\text{swim}}$ ratio (Strouhal number, St), and implying relatively high lateral momentum shedding and low propulsive efficiency. Using kinematic and inverse-dynamics analyses, we studied cyclic swimming of larval zebrafish aged 2–5 days post-fertilization (dpf). Larvae at 4–5 dpf reach higher f (95 Hz) and A_{tail} (2.4 mm) than at 2 dpf (80 Hz, 1.8 mm), increasing swimming speed and Re, indicating increasing muscle powers. As Re increases (60 $\rightarrow$ 1400), St (2.5 $\rightarrow$ 0.72) decreases non-linearly towards values of large swimmers (0.2–0.6), indicating increased propulsive efficiency with v_{swim} and age. Swimming at high St is associated with high-amplitude body torques and rotations. Low propulsive efficiencies and large yawing amplitudes are unavoidable physical constraints for small undulatory swimmers.

3.1 Introduction

Being small has costs and benefits for swimmers and flyers. On the one hand, small swimmers and flyers experience relatively strong viscous forces resulting in high drag, reduced stride length ℓ_{stride} (distance travelled per cycle) and propulsive efficiency (Batty and Blaxter, 1992; Borazjani and Sotiropoulos, 2009b; Chattopadhyay et al., 2006; Fuiman and Batty, 1997; Osse and Van den Boogaart, 1999). On the other hand, they have relatively high muscle strength and low body inertia, affording small flyers and swimmers excellent manoeuvrability—they achieve high rotational accelerations (Fry et al., 2003; Müller and Van Leeuwen, 2004; Verhagen, 2004). Small swimmers often move in the intermediate flow regime, where both viscous and inertial forces play an important role. The ratio of inertial to viscous forces is expressed by the Reynolds number:

$$\text{Re} = \frac{\rho_{\text{water}} \ell_{\text{body}} v_{\text{swim}}}{\mu}, \tag{3.1}$$

with ρ_{water} the density of water, ℓ_{body} the body length of the fish, v_{swim} the swimming speed (defined here as the speed of the centre of mass (CoM)) and μ the dynamic viscosity of water. Symbols and definitions are listed in the electronic supplementary material, Table S3.1.

Fish larvae, compelled to generate high thrust with their posterior body to overcome the high drag on the anterior body (Li et al., 2012), must use high tail-beat frequencies and amplitudes to generate the required high rate of change of momentum of the fluid. Fast, large-amplitude tail beats can cause large lateral forces on the body and large torques around the CoM, in turn causing large yaw accelerations. Large yaw can increase drag, which then

requires more thrust to overcome. The large body deformations should also cause significant fluctuations in the fish's moment of inertia. Furthermore, we expect fluctuations in swimming speed and kinetic energy due to the time-varying nature of thrust production with a flapping propeller that causes large fluctuations in instantaneous force, both in direction and in amplitude. So far, these consequences have not been explored systematically and their relation with swimming speed and Re is unclear. Here, we quantify these aspects in zebrafish larvae using a combined kinematic and inverse-dynamics approach and show how body kinematics and dynamics vary with Re.

Large body undulations affect also the fluid-dynamic efficiency of swimming and cost of transport. Computational studies of larval swimmers have shown that increasing body-wave amplitude steadily increases energy cost per unit distance while propulsive efficiency plateaus at a value just above 0.3 at tail-beat frequency $f = 57$ Hz (Li et al., 2012), suggesting that fish larvae use body-wave amplitudes that maximize fluid-dynamic efficiency at acceptable costs of transport. Nevertheless, swimmers in the viscous and intermediate flow regime (Re < 300) often achieve only low propulsive efficiency (Chattopadhyay et al., 2006; Borazjani and Sotiropoulos, 2009b). Propulsive efficiency in fluids strongly depends on vortex shedding dynamics, which correlates with the Strouhal number:

$$\text{St} = \frac{f A_{\text{tail}}}{\bar{v}_{\text{swim}}}, \tag{3.2}$$

where $\bar{v}_{\text{swim}}$ is the mean swimming speed during cyclic swimming, A_{tail} is the peak-to-peak amplitude of the tail tip. Several studies suggest (Eloy and Schouveiler, 2011; Nudds et al., 2014; Taylor et al., 2003; Triantafyllou et al., 1993) that swimmers in the inertial flow regime swim close to the St that maximizes efficiency (St = 0.25–0.35 for carangiform swimmers and 0.4–0.5 for anguilliform swimmers (Borazjani and Sotiropoulos, 2009b,c, 2010; Eloy, 2012). By contrast, small organisms swimming in the viscous and intermediate flow regimes experience relatively higher drag forces, which reduces relative stride length ($\ell_{\text{stride}}/\ell_{\text{body}}$) and increases St, indicating a high-energy wake with a relatively large component of lateral momentum and thus low efficiency (Borazjani and Sotiropoulos, 2009b; Müller and Van Leeuwen, 2004; Tytell, 2004b). Adult fish increase $\bar{v}_{\text{swim}}$ in proportion to f while keeping A_{tail} nearly constant, implying that St and propulsive efficiency remain nearly constant (Tytell, 2004b; Bainbridge, 1958; Van Weerden et al., 2014). In cyclic swimming, St must increase with decreasing Re if a swimmer is to balance thrust and drag over the tail-beat cycle (Borazjani and Sotiropoulos, 2009c). Fish larvae are particularly interesting because they swim in the critical Re range that corresponds to the transition from high to low St (Borazjani and Sotiropoulos, 2009a,c). As body size and swimming speed increase, Re increases, and so should efficiency.

By changing v_{swim}, larvae change Re and thus the relative influence of inertial and viscous forces. Using $\bar{v}_{\text{swim}}$ to compute Re (electronic supplementary material, Equation S3.3), it follows that St relates to Re as

$$\text{St} = \frac{\rho_{\text{water}} f A_{\text{tail}} \ell_{\text{body}}}{\mu \, \text{Re}} = \frac{\text{Sw}}{\text{Re}}, \tag{3.3}$$

where $\mathrm{Sw} = (\rho_{\mathrm{water}} f A_{\mathrm{tail}} \ell_{\mathrm{body}})/\mu$ is the dimensionless swimming number (introduced by Gazzola et al. (2014)). To explore how St varies with Re, and hence what larval fish can do to increase hydrodynamic efficiency, we determined f and A_{tail} for a range of (nearly) cyclic swimming speeds spanning more than one order of magnitude.

Changes in Re and St are confounded by larval development. We expect developmental stage to profoundly affect swimming performance, because body shape and size as well as sensory, neural and muscular properties change rapidly in the first days of larval development. The changes in muscle size, structure and physiology are expected to provide a higher power output, enabling an increase in f or A_{tail}, or a combination of both.

We aim to quantify the body kinematics and dynamics of larval zebrafish aged 2–5 dpf (days post-fertilization), including body torques and Strouhal number, and their relation with developmental age and swimming speed, which indirectly yields performance requirements for swimming muscles. Our data also provide validation criteria for computational swimming models.

3.2 Material and methods

3.2.1 Animals

Zebrafish larvae (*Danio rerio* Hamilton 1822) were reared in the laboratory from wild-type stock at a water temperature of 28°C and a 12 L : 12 D cycle. We used larvae at age 2, 3, 4 and 5 dpf. Larvae were fed *Paramecium* twice a day at age 5 dpf.

3.2.2 Kinematic analysis and force on centre of mass

We used custom software developed in Matlab R2013a (Mathworks, MA, USA) for our analysis. To collect kinematic data of cyclically swimming larvae, we used three video set-ups recording at 1000–2000 frames s^{-1} (see the electronic supplementary material, §S3.2 for details). We recorded spontaneous and elicited swimming sequences (by approaching individual larvae with a horse hair) and selected 8–11 sequences per age group. We manually digitized 18–25 points on the fish's midline of every video frame, then smoothed and interpolated the midlines to obtain 51 equidistant points (see the electronic supplementary material, §S3.3.1 for details). We defined two Cartesian coordinate systems, an earth-bound frame of reference, XYZ, and a 'fish-bound frame' $X_{\mathrm{mov}} Y_{\mathrm{mov}} Z_{\mathrm{mov}}$ with the origin located at the fish's CoM and axes parallel to XYZ. We selected sequences with a small Z-component, and assumed that fish moved parallel to the XY-plane. To ensure that we include only (near-)cyclic swimming events (a prerequisite for computing Strouhal numbers), we identified 38 close-to-cyclic swimming events by calculating auto-correlation functions of the body wave (expressed as 51 segment angles) for all tail beats of a given event and selected video sequences comprising at least three consecutive tail beats above the normalized auto-correlation threshold of 0.975 and at least two extrema in the body angle (α_{body}).

To determine the body shape of larvae (details in the electronic supplementary mater-

ial, §S3.3.1), we digitized the outline of the fin fold, body, eye and yolksac in dorsal and lateral views of larvae aged 2–5 dpf (five per age group) at 51 equidistant points from snout to tail tip. We selected the larva whose values were closest to the per age average, to represent the body shape of its age group.

We estimated body volume by modelling the fish as a series of 51 segments by fitting ellipses to the head, eyes, fin fold, trunk (excluding fins) and yolk sac (for details, see the electronic supplementary material, §S3.3.1 and Fig. S3.1). We assumed a uniform mass density ($\rho_{\text{fish}} = 1000$ kg m^3) over the entire body. For each segment, we computed volume V_i, mass m_i, and position vector r_i of the local CoM by numerical integration. The average ℓ_{body} for stages 2–5 dpf were 3.39, 3.81, 4.37 and 4.36 mm ($N = 5$ larvae per age group). Body mass m_{body} was computed as the sum of the segmental masses, resulting in 239, 289, 414 and 373 mg for stages 2–5 dpf. These values for ℓ_{body} and m_{body} were used for all subsequent computations.

We then calculated the instantaneous position, velocity, acceleration and force acting on the CoM from the instantaneous positions of the body segments (see electronic supplementary material, §S3.3.1 for details).

3.2.3 Instantaneous moment of inertia, body angle, angular velocity and torque

For each body segment i, we computed the moment of inertia J_i about the segmental vertical centre line and the moment of inertia with respect to the CoM J_{CoM}, i about the vertical Z_{mov}-axis in the fish frame of reference (electronic supplementary material, §S3.3.3 Equations S3.6 and S3.7) to ultimately derive the instantaneous moment of inertia of the body J_{body} with respect to the CoM location (electronic supplementary material, Equation S3.8). We computed the instantaneous body angle α_{body}, angular velocity ω_{body} and angular acceleration $\dot{\omega}_{\text{body}}$ (electronic supplementary material, §S3.3.3). We computed the inertial body torque about the CoM, τ_{body}, as the summation of the contributions of all body segments to the inertial torque about the CoM (electronic supplementary material, §S3.3.3: Equation S3.15).

To explore the spatio-temporal contributions of external fluid forces along the body to the net torque on the body, we computed skin friction-based ($\tau^*_{\text{fric},i}$), dynamic pressure-based ($\tau^*_{\text{dynp},i}$) and acceleration reaction-based ($\tau^*_{\text{acc},i}$) torques per unit length along the fish, which include, respectively, the effects of forces associated with the local velocity components parallel and perpendicular to the body, and the acceleration of an added mass perpendicular to the body, as well as the relevant surface per unit length and position vector from the CoM to the location of interest along the body. The net estimated contributions of the three torque distributions to the external body torque (τ_{fric}, τ_{dynp}, τ_{acc}) were obtained by integration along the fish and compared with the fluctuations in τ_{body}. Computational details are provided in the electronic supplementary material, §S3.3.3.

3.2.4 Kinetic energy and power

We computed the total kinetic energy of the body $E_{\text{kin,body}}$, as well as the kinetic energy associated with translation of the CoM, $E_{\text{tr,CoM}}$, and the kinetic energy due to rotation of the body segments about the CoM, $E_{\text{rot,body}}$. The latter is a close approximation of the internal kinetic energy of the body. We computed also the total power due to kinetic energy changes of the body, $P_{\text{kin,body}}$, the power associated with translation of the CoM, $P_{\text{tr,CoM}}$ and the power associated with rotation of the body about the CoM, $P_{\text{rot,body}}$. Specific energies and powers were computed by dividing the respective values by body mass (designated as E^* and P^*). Details on energy computations are provided in the electronic supplementary material, §S3.3.4.

3.2.5 Dimensionless quantities and trend analyses

We defined dimensionless swimming speed along the path of the CoM as

$$\hat{v}_{\text{swim}} = \frac{v_{\text{swim}}}{f\ell_{\text{body}}}. \tag{3.4}$$

To compute f for (near-)cyclic swimming events, we first determined a series of positive and negative extremes in α_{body} with the 'findpeaks' function of Matlab's Signal Processing toolbox (v. 2013a). Frequency was computed as

$$f = \frac{n-1}{2(t_n - t_1)}, \tag{3.5}$$

where n is the number of extrema in α_{body}, and t_1 and t_n the time, respectively, at the first and last extreme in α_{body}. Dimensionless tail amplitude was computed as

$$\hat{A}_{\text{tail}} = \frac{A_{\text{tail}}}{\ell_{\text{fish}}}. \tag{3.6}$$

Dimensionless body torque was defined as

$$\hat{\tau}_{\text{body}} = \frac{\tau_{\text{body}}}{J_| f^2}, \tag{3.7}$$

where $J_|$ is the value of J_{body} for the straight fish. Details about the computation of Re and St are provided in the electronic supplementary material, §S3.3.2.

We fitted curves to the datasets used for trend analyses (Figs 3.6–3.9) using an optimization procedure with Matlab's 'fminsearch' function. Fitted variables were scaled by their mean value, then we computed for each set of optimized coefficients the perpendicular distance from each data point to the curve (i.e. total least-squares approach for either a line, a parabola, a power curve or a power curve plus a constant). We used the sum of squared distances as the objective function for the optimization and estimated 95% confidence intervals for the coefficients of each curve fit with a Monte Carlo approach (see the

electronic supplementary material, §S3.3.5 for details). We computed the ratio of the root of the sum of squared distances for each nonlinear curve fit and the corresponding linear curve fit. Standard linear regression curve fits were applied for the log transformed data of Sw and Re for a comparison with previous work (Gazzola et al., 2014).

3.3 Results and discussion

3.3.1 Body morphology

During larval development, mass is redistributed within the body as the yolk sac is absorbed and the body grows allometrically (e.g. Müller and Videler, 1996; Fuiman, 1983; electronic supplementary material, Fig. S3.3). Yet, the shift in mass distribution does not affect the location of the CoM along the straight fish (expressed as fraction of total length). At 2 dpf, the CoM is at $0.287\,\ell_{\text{body}}$ from the snout tip, at age 5 dpf at $0.286\,\ell_{\text{body}}$.

3.3.2 Larval fish swim with small centre of mass sideslip and large body angle fluctuations

Fish larvae typically swim with wide body undulations (Müller and Van Leeuwen, 2004) (see Fig. 3.1A,B for an example with $\bar{v}_{\text{swim}}^{*} \approx 50\,\ell_{\text{body}}$ s^{-1}, $f \approx 83$ Hz). Snout tip (Fig. 3.1A: green curve) and tail tip (Fig. 3.1A: red curve) oscillate substantially. While the large-amplitude body undulations do not result in large side-slip (lateral movements of the CoM, Fig. 3.1A: black curve; lateral component of net force with respect to $\dot{\mathbf{r}}_{\text{CoM}}$, Fig. 3.1D: dotted curve), they do cause the CoM to move outside the body (twice per cycle) (Fig. 3.1B). CoM speed (v_{swim}) fluctuates strongly (Fig. 3.1C), a result of the oscillating net force on the body (Fig. 3.1D). The forward speed of the fish fluctuates over the tail-beat cycle in tune to the fore–aft force component (Fig. 3.1C,D).

Body yaw is smaller than head yaw—the peak-to-peak amplitude of the body angle α_{body} is half that of the head angle α_{head} (Fig. 3.2A, for event in Fig. 3.1). Changes in α_{body} are also delayed with respect to α_{head}. Thus, α_{head} is not a valid approximation for α_{body} in undulatory swimming fish larvae. Both ω_{body} and $\dot{\omega}_{\text{body}}$ reach high amplitudes, respectively $\approx 10°$ ms^{-1} and $\approx 5°$ ms^{-2} for the example event (Fig. 3.2B,C); $\dot{\omega}_{\text{body}}$ generally shows a double peak per tail beat.

The undulatory body movements cause the body moment of inertia J_{body} and its rate $\dot{J}_{\text{body}}$ to fluctuate (Fig. 3.2D,E). They also cause J_{body} to be smaller than $J_{|}$ of the straight fish. Furthermore, specific power ($P_{\text{kin,body}}^{*}$) fluctuates due to changes in kinetic energy (up to 20 W kg^{-1} in Fig. 3.2F).

3.3.3 Body dynamics during cyclic swimming: insights from torque

Body torque around the CoM (τ_{body}) fluctuates strongly (Fig. 3.3A), causing large changes in $\dot{\omega}_{\text{body}}, \omega_{\text{body}}$ and α_{body} (Fig. 3.2A–C). Torque τ_{body} oscillates in a non-sinusoidal manner with usually a double peak per tail beat (four peaks per tail-beat cycle; Fig. 3.3A), consist-

A

1 mm

B

1 mm

C

D
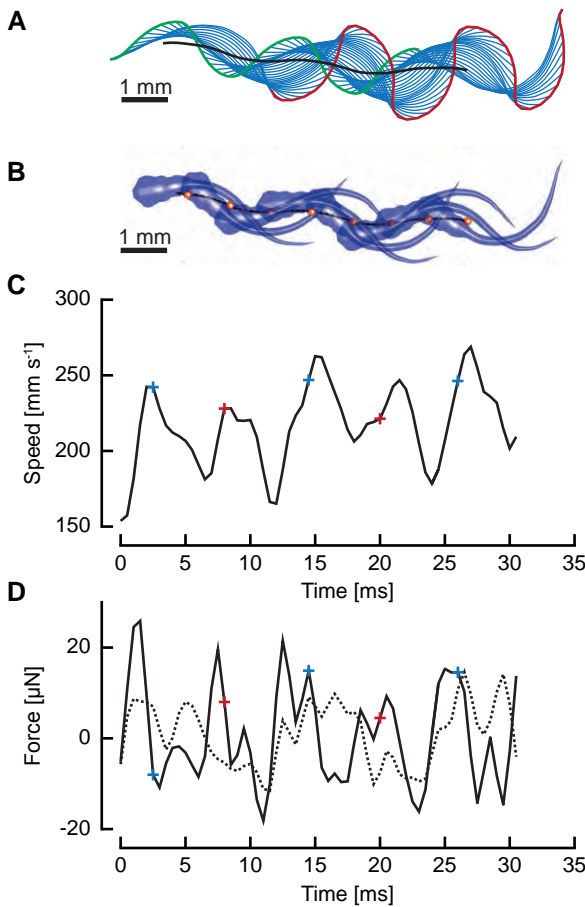
Figure 3.1: A 5 dpf fish larva swimming at approximately 50 ℓ_{body} s^{-1}.
(A) Sequence of body midlines at 0.5 ms intervals (blue); path of snout tip (green), tail tip (red) and CoM (black). (B) Body shape at 3 ms intervals. CoM (red sphere) periodically falls outside the body. (C) Translational speed of CoM and (D) force on CoM in the direction of (continuous curve) and perpendicular to (dotted curve) the instantaneous velocity vector. The blue and red '+' signs in panel C and D correspond to the minima and maxima in α_{body} (Fig. 3.2A). The time between two '+' signs of the same colour represents a full tail-beat cycle.

ent with the double peak in $\dot{\omega}_{\text{body}}$. Body torque is just ahead of the fluctuations in angle-of-attack of the tail with respect to the local velocity vector (β_{tail}), which is also double peaked and deviates considerably from a sine wave (Fig. 3.3B) due to the large-amplitude motion. These observations indicate that the force associated with tail velocity may contribute significantly to τ_{body}.

We will now consider how the segmental contribution to the inertial torque about the CoM varies in time and along the body (derived by an inverse-dynamics analysis; electronic supplementary material, §S3.3.3; note that this is not a distribution of the segmental inertial torque with respect to the segmental CoM). The amplitude of the inertial torque about the CoM per unit length $\tau^*_{\text{body},i}$ is largest at the head and tail, as indicated by the amplitude envelope over a tail-beat cycle (Fig. 3.3C). Although the tail has less mass per unit length than the head, it contributes similar to inertial torque of the body, because the tail is further away from the CoM and moves at higher accelerations. The location of the 'neck' at about $0.28\,\ell_{\text{body}}$ of the envelope corresponds to the caudo-rostral location of the CoM in the straight fish. Inertial torque behaves as a travelling wave along the flexible posterior two-
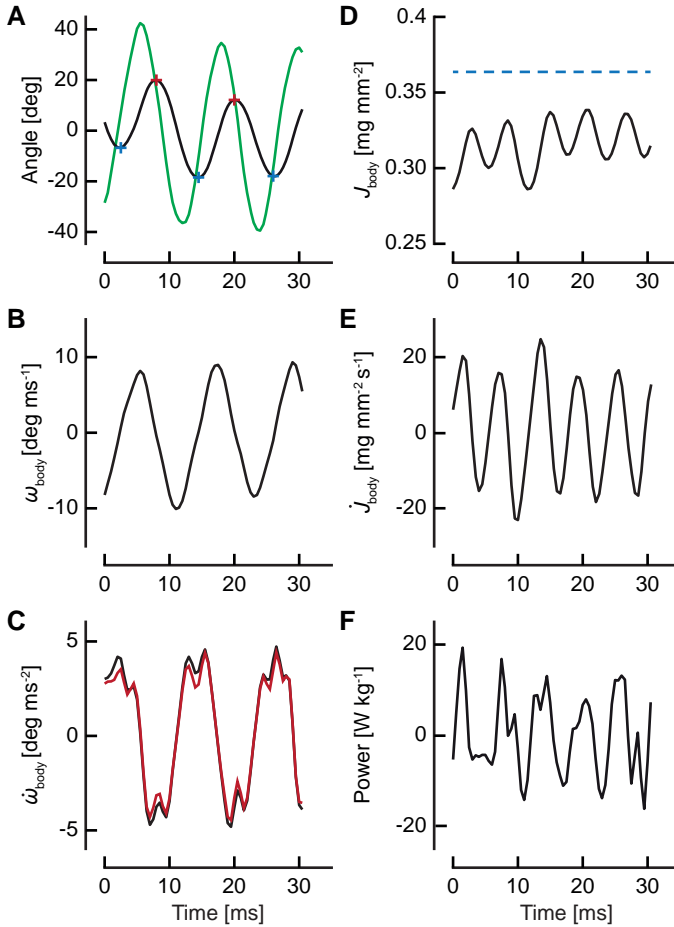
Figure 3.2: Body angle, moment of inertia and power for episode in Fig. 3.1. (A) Instantaneous body angle α_{body} (black; blue and red '+' signs: minima and maxima) and head angle α_{head} (green); (B) body angular velocity ω_{body}; (C) body angular acceleration $\dot{\omega}_{\text{body}}$ (black: by differentiation of ω_{body}; red: according to electronic supplementary material, Equation S3.18); (D) moment of inertia about the CoM J_{body}; dashed blue line shows $J_{\shortparallel}$ (i.e. J_{body} for the straight fish), (E) rate of change of the moment of inertia $\dot{J}_{\text{body}}$; (F) total specific body power $P^*_{\text{kin,body}}$ based on the rate of change of kinetic energy.

thirds of the body and as a standing wave along the stiff head (Fig. 3.4A).

To explore how external forces on the body contribute to the external torque on the body, we estimated $\tau^*_{\text{dynp},i}$ (Fig. 3.4C), $\tau^*_{\text{fric},i}$ (Fig. 3.4D) and $\tau^*_{\text{acc},i}$ (Fig. 3.4F) for the swimming event of Fig. 3.1. Our simplified approach to calculate external torque contributions is useful for our analysis but causes the sum of τ_{dynp}, τ_{fric} and τ_{acc} to not equal the inertial body torque τ_{body}. Torque τ_{dynp} (Fig. 3.4B: green curve) is of similar magnitude and phase as τ_{body} (Fig. 3.4E: black curve). By far the highest $\tau^*_{\text{dynp},i}$ amplitudes are found in the tail region (Fig. 3.4C). By contrast, τ_{fric} contributes little and is shifted forward in phase with respect to τ_{body} (Fig. 3.4E: blue and black curve, respectively), indicating that skin friction has a relatively small effect on body torque. Peak values of $\tau^*_{\text{fric},i}$ are found in the tail region where high velocities occur (Fig. 3.4D). Finally, the estimated contribution of τ_{acc} (Fig. 3.4E: red curve; a fivefold scale reduction was applied to preserve the visible dynamic range of the other curves) is about five times as large in peak amplitude as τ_{body} and almost in counter-phase. From this grossly simplified analysis, we conclude that τ_{dynp} performs remarkably well as an indicator of the external torque on the body, while τ_{fric}
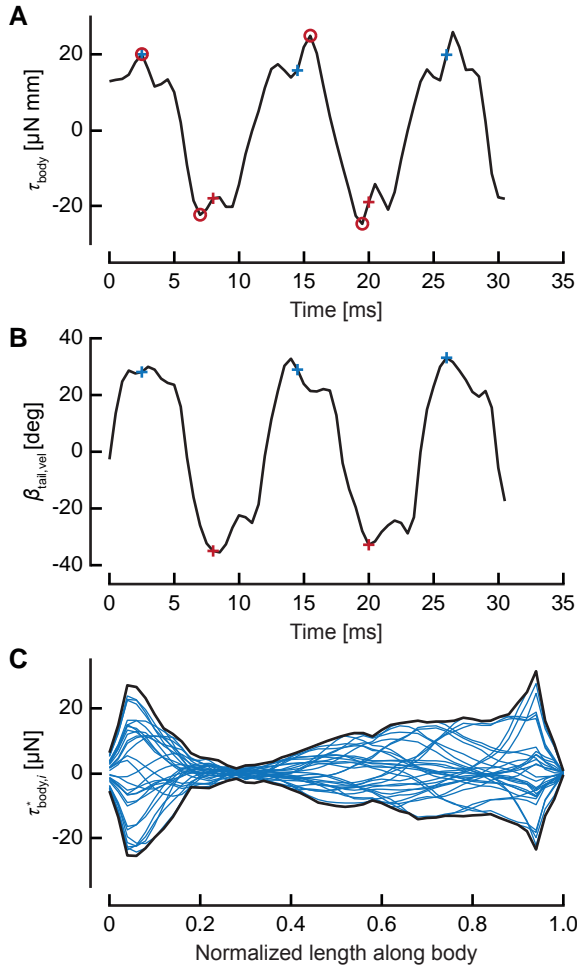
Figure 3.3: Body torque and angle-of-attack of the tail at 0.96 ℓ_{body} for the episode in Fig. 3.1. (A) Instantaneous inertial body torque τ_{body} (circles: selected extrema). (B) Angle-of-attack of the tail with respect to the velocity vector of the tail (β_{tail}). The blue and red '+' signs in panel A and B correspond to the minima and maxima in α_{body} (Fig. 3.2A). The time between two '+' signs of the same colour represents a full tail-beat cycle. (C) Distribution of the contribution to τ_{body} by the 51 body segments expressed as torque per unit length $\tau^*_{\text{body},i}$. Each blue curve represents the torque distribution at a particular instant (at 1 ms intervals). The heavy black curves show the envelope. The narrowest location along of the 'neck' of the envelope corresponds to the location of the straight-body CoM.

is relatively small. The estimate of τ_{acc} deviates significantly in amplitude and phase and should be avoided as an indicator of the external torque on the body. A future computational fluid-dynamics solution may show how pressure and shear-stress distributions on the body contribute to the external torque on the body.

3.3.4 Kinetic energy fluctuations

While cyclic swimming entails no changes in body dynamics between successive cycles, instantaneous values oscillate considerably in fish larvae. Kinetic energy comprises two main contributions: translational kinetic energy of the CoM ($E_{\text{tr,CoM}}$) and rotational energy around the CoM ($E_{\text{rot,body}}$). Translational kinetic energy varies in proportion to v^2_{swim}. Rotational kinetic energy never drops to zero because the body undulates continuously (Fig. 3.5). Kinetic energy fluctuates by a factor of 3 during slow swimming (Fig. 3.5B, $\bar{v}^*_{\text{swim}} \approx 8\,\ell_{\text{body}}\,\text{s}^{-1}$), and less than twofold during fast swimming (Fig. 3.5A, $\bar{v}^*_{\text{swim}} \approx$
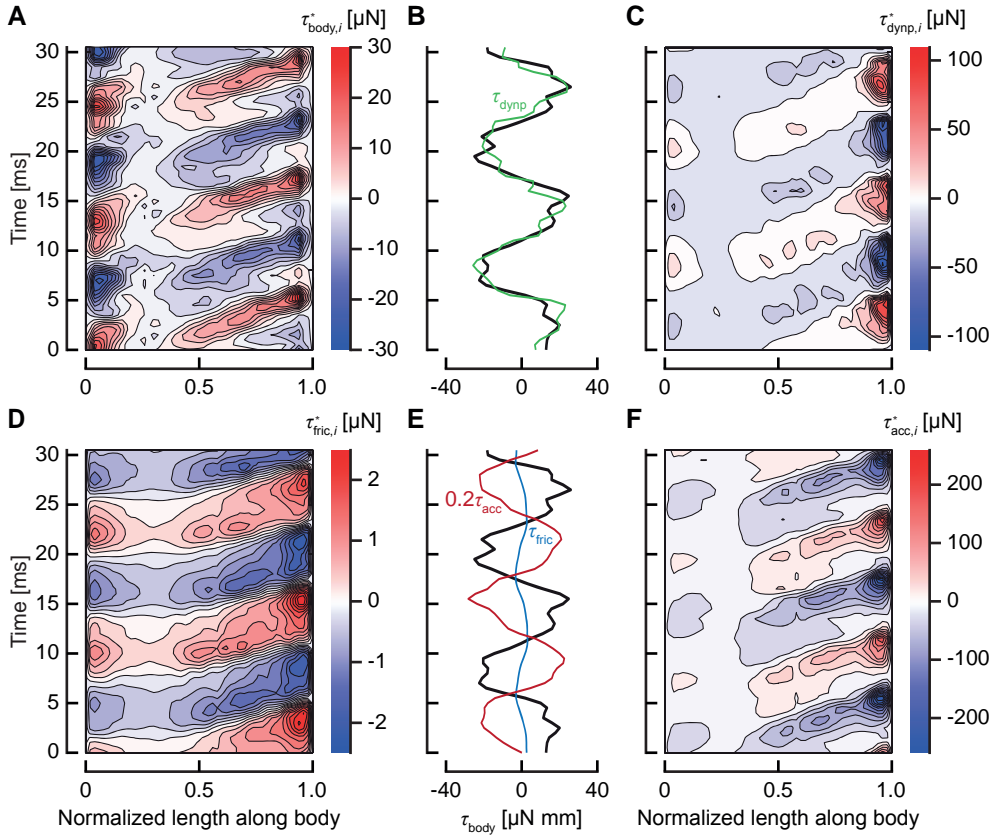
Figure 3.4: Estimated torques. (A) Contour plot of inertial torque per unit length with respect to the CoM against normalized position along the body ($\hat{\ell}$) and time. (B) Inertial body torque τ_{body} against time (black); torque on the body due to dynamic pressure, τ_{dynp} (green). (C) Contour plot of torque on the body per unit length due to dynamic pressure against $\hat{\ell}$ and time. (D) Contour plot of torque on the body per unit length due to shear-force distribution against $\hat{\ell}$ and time. (E) Inertial body torque τ_{body} against time (black); torque on the body torque due to shear-force distribution, τ_{fric} (blue) and acceleration reaction forces $\tau_{\text{acc}} \times 0.2$ (red). (F) Contour plot of torque per unit length on the body due to acceleration reaction forces against $\hat{\ell}$ and time.

$50\,\ell_{\text{body}}\,\text{s}^{-1}$), caused by fluctuations of the net force on the body (F_{CoM}) (Li et al., 2012). Figure 5 shows that instantaneous and mean $E_{\text{tr,CoM}}$ are higher than the corresponding values for $E_{\text{rot,body}}$ at a relatively high swimming speed (Fig. 3.5A), whereas the low-speed example (Fig. 3.5B) shows the reverse, which suggests a lower efficiency at the lower speed. Most of the in-phase reductions of both kinetic energy components over the swimming cycle will be dissipative (without useful conversion into elastic energy). Both translational kinetic energy and rotational kinetic energy fluctuate in phase (Fig. 3.5), mainly due to the varying amplitude and direction of the fluid force on the posterior body that causes oscillations in both F_{CoM} and τ_{body}.
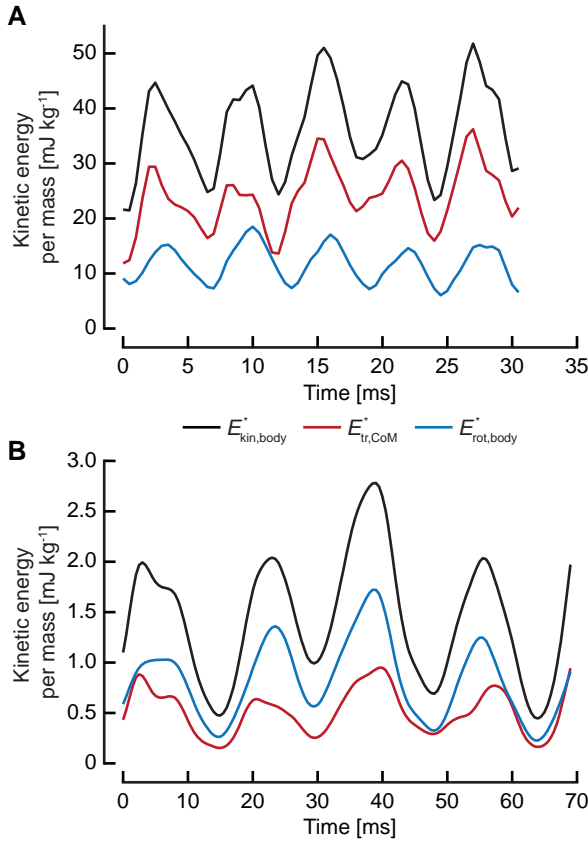
Figure 3.5: Specific kinetic energy for (A) a near-cyclic swimming event at approximately 50 ℓ_{body} s^{-1} (age 5 dpf) (same as Fig. 3.1) and (B) approximately 8 ℓ_{body} s^{-1} (age 3 dpf). Total kinetic energy of the body ($E^*_{kin,body}$; black), kinetic energy due to speed of the CoM ($E^*_{tr,CoM}$; red), and sum of kinetic energy due to rotation of the segmental masses around CoM and rotation of the segments about their central vertical axis ($E^*_{rot,body}$; blue). $E^*_{kin,body} \approx E^*_{tr,CoM} + E^*_{rot,body}$.

3.3.5 Changes in swimming speed and tail-beat amplitude with frequency

To reach higher speeds, fish tend to increase tail-beat frequency f rather than body-wave amplitude (Müller and Van Leeuwen, 2004; Borazjani and Sotiropoulos, 2009c). However, the relationship between f and mean swimming speed $\bar{v}_{swim}$ is not a simple proportionality in larval zebrafish (Fig. 3.6A) during (near-)cyclic swimming. We previously found a decreasing slope with speed (Müller and Van Leeuwen, 2004), based on a small dataset biased towards younger stages. Based on a much larger dataset, this study found that younger larvae swim slower than older larvae at $f > 50$ Hz (Fig. 3.6A). Stage 2 dpf reached frequencies of close to 80 Hz with $\bar{v}^*_{swim} \approx 40$ s^{-1} (Fig. 3.6B). Stages 3–5 dpf top off at about 95 Hz and 60 s^{-1}. The largest improvement in maximum swimming speed occurs between stage 2 and 3 dpf.

Swimming speed depends also on tail-beat amplitude. When looking at the trend of A_{tail} with f within age groups, there is only a weak trend in early larvae (Fig. 3.6C,D blue line: data for 2 and 3 dpf combined). By contrast, A_{tail} increases markedly with frequency in older larvae (Fig. 3.6C,D red-green line: data for 4 and 5 dpf combined). Older larvae use higher amplitudes as $f > 50$ Hz. Correspondingly, for $f > 50$ Hz swim-
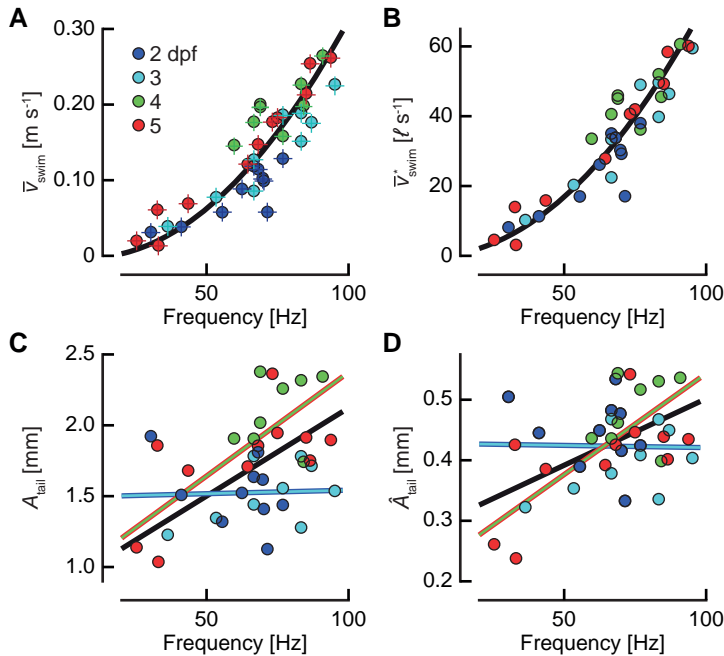
Figure 3.6: Swimming kinematics during (near-)cyclic swimming for 9–11 swimming events per age group (2–5 dpf). (A) Mean swimming speed $\bar{v}_{swim}$ along the path of the CoM (◦) and along a straight line approximation of the path of motion (+) against cycle frequency f. Both speeds differ little, indicating small sideslip. 2, 3 dpf larvae reach lower speeds for a given f than 4, 5 dpf larvae. (B) Specific swimming speed ($\bar{v}^*_{swim} = \bar{v}_{swim}/\ell_{body}$) against f (same dataset as A). (C) Peak-to-peak tail-beat amplitude A_{tail} against f. Data in C and D were fitted by total least squares. In C, the black curve shows the fit for the total dataset. The combined datasets for 2 and 3 dpf (blue-cyan line) and 4 and 5 dpf (red-green line) were fitted also separately. The 4–5 dpf age group tended to use higher A_{tail} than the 2–3 dpf group for $f > 50$ Hz, and they vary A_{tail} more over the frequency range. Panel D shows same data as C for dimensionless tail-beat amplitude ($\hat{A}_{tail} = A_{tail}/\ell_{body}$). Parameter values for each curve fit are given in electronic supplementary material, Table S3.2.

ming speed tends to be higher in older larvae for the same tail-beat frequency (Fig. 3.6A). While younger larvae mainly increase frequency, older larvae increase both frequency and amplitude to swim faster. Increasing both frequency and amplitude requires more muscle power, suggesting that 4–5 dpf larvae have more powerful muscles than younger larvae. Non-dimensionalizing A_{tail} reduces the differences in how much amplitude changes with frequency (Fig. 3.6D), showing the importance of size in between-stage differences.

Plots of $\bar{v}_{swim}$ against fA_{tail} and $\bar{v}^*_{swim}$ against $f\hat{A}_{tail}$ show the expected upward trend (electronic supplementary material, Fig. S3.4), yet the scatter is largest at the highest swimming velocities (caused by a relatively large range of tail-beat amplitudes of the 4–5 dpf larvae and small deviations from an ideal cyclic swimming pattern).

3.3.6 Body torque and yawing angle

Higher swimming speeds imply higher drag and require more thrust, resulting in higher amplitudes of body torques and yaw, because local forces on the body are generally not in line with the CoM (Fig. 3.7A). This trend remains even after removing size effects (Fig. 3.7B). With swimming speed proportional to Re, torque increases with increasing Re (Fig. 3.7C,D). Higher torques at higher speeds result in higher body yaw (despite the decreasing cycle time with increasing $\bar{v}_{\text{swim}}$)—the peak-to-peak amplitude of α_{body} increases with swimming speed (Fig. 3.7E,F), reaching almost $40°$. Head yaw (fluctuation in α_{head}) is twice as large as body yaw (fluctuation in α_{head}; mean $\pm$ s.d. of peak-to-peak ratio of α_{head} over α_{body} is 2.11 ± 0.49), indicating that head yaw is not a valid proxy of body yaw. Maximum τ_{body} increases fivefold from stage 2 to 4 dpf (Fig. 3.7A,C). Maximum torque more than doubles from stage 2 to 3 dpf. Non-dimensionalizing torque reduces these increases (although it increases scatter), showing the important effect of size on torque (Fig. 3.7B,D).

3.3.7 Effects of Reynolds number on Strouhal number and swimming number

The same increase in the product of tail-beat frequency and amplitude causes a larger increase in swimming speed at high than at low swimming speeds (electronic supplementary material, Fig. S3.4A). This larger increase in speed for a given increase in fA_{tail} causes St to drop with increasing Re, which is proportional to $\bar{v}_{\text{swim}}$. The lowest swimming speeds result in Strouhal numbers of up to 2.5; St drops to 0.72 as larvae reach top swimming speeds of nearly 0.30 m s^{-1} or $60 \ell_{\text{body}} \text{ s}^{-1}$ (Fig. 3.7G). The decrease in St is largely explained by the increase in Re: St decreases from 2.5 to 0.72 (with $\approx 0.72/2.5 = 0.29$) at a similar rate as the ratio of the product of tail-beat frequency and amplitude to Re—the product fA_{tail} increases by a factor of ≈ 8 as Re increases by a factor of ≈ 23 ($8/23 \approx 0.30$). More precisely, the St relates to Re as $St = fA_{\text{tail}}\rho_{\text{water}}\ell_{\text{body}}/(\mu\text{Re}) = Sw/\text{Re}$. The St–Re data of larval fish are described well by a (negative) power function plus a constant ($St = c_1\text{Re}^{c_2} + c_3 = 41.29\text{Re}^{-0.741} + 0.525$; Fig. 3.7G, black curve). The youngest larvae of 2 dpf do not reach the high Re–low St combinations exploited by the older larvae. With $St = Sw/\text{Re}$, our curve fit can be rewritten as $Sw = c_1\text{Re}^{c_2} + c_3\text{Re}$, which deviates from a simple power function. When plotted on a double logarithmic scale (Fig. 3.7H) this fit is still curved, the slope decreases with increasing Re.

Our experimental data do not conform with the theoretical prediction of Gazzola et al. (2014), which states that $St \propto \text{Re}^{-0.25}$ and $\text{Re} \propto Sw^{4/3}$ (giving a straight line in a double log Re–Sw plot) based on small-amplitude body undulations and Blasius resistive theory for the laminar swimming regime. The predicted exponent of -0.25 lies outside the 95% confidence interval $[21.250, 20.389]$ of the experimentally obtained exponent of -0.741. A large deviation is to be expected because neither assumption is substantiated by the actual swimming motions of larval fish. To further compare the predicted exponent with our data, we also made linear regressions for $\log \text{Re} = c_2 \log Sw + c_1$. For the full Sw–Re
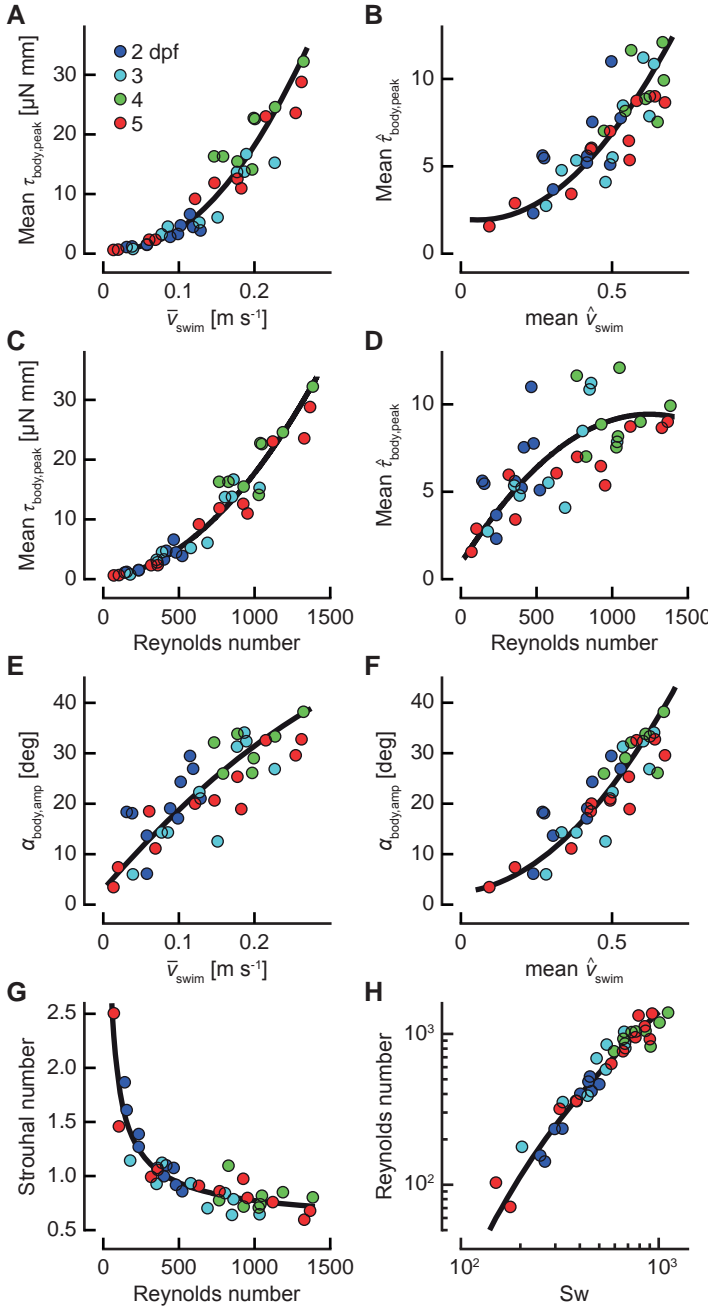
Figure 3.7: Dynamics of (near-)cyclic swimming for same dataset as Fig. 3.6. (A) Amplitude of torque peaks (mean per event, colour code: age 2–5 dpf) over mean swimming speed ($\bar{v}_{swim}$). (B) As A, but non-dimensionalized. (C) Amplitude of torque peaks against Reynolds number (Re). (D) As C but non-dimensionalized. (E) Peak-to-peak amplitude of body angle (mean per event) against $\bar{v}_{swim}$ (F) Idem, but against dimensionless swimming speed. Second-order polynomial curve fits are shown for A–F. (G) St against Re, with a fit of a (negative) power function plus a constant. (H) Re against swimming number Sw (logarithmic scales). The curve fit follows from the fit of St against Re, by using St = Sw/Re. Parameter values for each curve fit are given in electronic supplementary material, Table S3.3.

range in the dataset, we obtained values for c_2 of 1.464 and 1.572 for, respectively, Re and Sw as the dependent variable. Both values are well above $4/3$. Restricting the maximum in Re to 800 (used as upper limit for numerical simulations of the laminar regime in Gazzola), we found corresponding values of 1.614 and 1.710, deviating even more from $4/3$. The higher value of the exponent for the lower Re range is in agreement with the curved shape of the double log Sw–Re fit (Fig. 3.7H).

3.3.8 Kinetic energy and power

Translational and rotational kinetic energy increase nonlinearly with swimming speed (Fig. 3.8A,B). The contribution of translational versus rotational kinetic energy changes with age and swimming speed (Figs 3.5, 3.8A,B). Maximum mass-specific $E^*_{\mathrm{tr,CoM}}$ and $E^*_{\mathrm{rot,body}}$ more than triple between age 2 and 4 dpf. Translational energy outweighs rotational energy in most recorded swimming events (Fig. 3.8C,D) except a few young larvae (age 2 dpf) at low $\bar{v}^*_{\mathrm{swim}}$ ($< 15\, \ell_{\mathrm{body}}\, \mathrm{s}^{-1}$) and high St, when the tail produces a relatively high lateral force component. In general, rotational kinetic energy is a substantial component of the total kinetic energy of the body in larval swimmers.
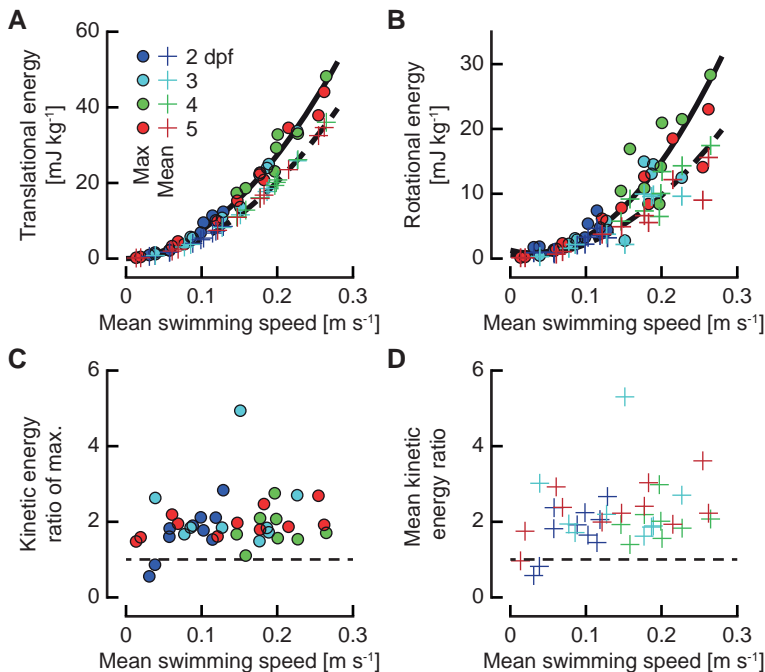
Figure 3.8: Specific kinetic energy due to translation $E^*_{\mathrm{tr,CoM}}$ and rotation $E^*_{\mathrm{rot,body}}$ during (near-)cyclic swimming for the same dataset as Fig. 3.6. (A,B) Maximum (○) and mean (+) values against mean swimming speed $\bar{v}_{\mathrm{swim}}$. Second-order polynomial curve fits for maxima (continuous curve) and mean (dashed curve) are shown in A,B. (C,D) Ratio of the maxima (C) and the means (D) of $E^*_{\mathrm{tr,CoM}}$ and $E^*_{\mathrm{rot,body}}$ over $\bar{v}_{\mathrm{swim}}$. The horizontal dashed line indicates a ratio of 1. Parameter values for each curve fit in A and B are given in electronic supplementary material, Table S3.4.

Maximum specific power due to fluctuations in kinetic energy of the body increases nonlinearly with $\bar{v}_{\mathrm{swim}}$ (Fig. 3.9A). The two main contributors to power are translational and rotational power (Fig. 3.9B). Rotational power exceeds translational power rarely and only at low $\bar{v}_{\mathrm{swim}}$ (Fig. 3.9B). Specific power triples within 3 days of development—peak $P^*_{\mathrm{kin,body}}$ at the highest observed $\bar{v}_{\mathrm{swim}}$ in 5 versus 2 dpf larva is 22 versus 7 W kg^{-1}. These values are much lower than the total power required for swimming, neglecting energy dissipated in the body and power spent on external fluid flow. Assuming that this body kinematics-based motion power is 25% of muscle power, and that 50% of the body is locomotion musculature, and 50% of these contribute at any one time, zebrafish larvae require muscle peak power outputs of 112–352 W kg^{-1} muscle at the respective maximum performance at 2 and 4–5 dpf with contraction frequencies of 80–95 Hz. Given the high maximum tail-beat frequencies, these projected muscle powers match or exceed the currently known maxima for aerobic fast, super-fast and asynchronous muscles (tree frog: 200 W kg^{-1} (peak), 54 W kg^{-1} (average in work loop) at 44 Hz at 25°C (Girgenrath and Marsh, 1999); toadfish: 14 W kg^{-1} (average in workloop) at 22 Hz at 15°C (Young and Rome, 2001); beetle: 200 W kg^{-1} (peak), 127 W kg^{-1} (average in workloop) at 94 Hz at 35°C (Josephson et al., 2000)), but are less than maximum power in anaerobic quail muscles (1121 W kg^{-1} (peak), 390 W kg^{-1} (average during shortening phase in workloop) at 23 Hz at 40°C (Askew et al., 2001)).
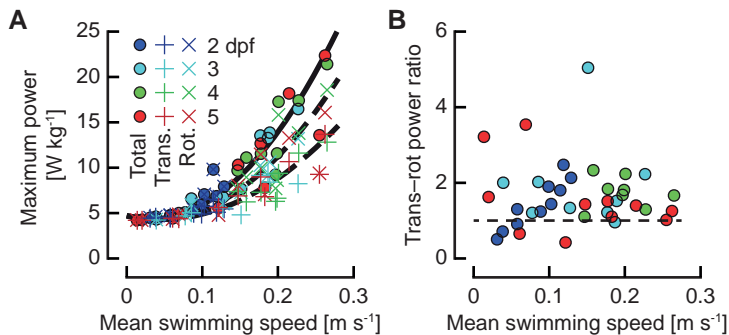
Figure 3.9: Maximum specific power computed as rate of change of kinetic energy of the body per body mass during (near-)cyclic swimming for same dataset as Fig. 3.6. (A) Total (○), translational (×) and rotational (+) power over mean swimming speed. Second-order polynomial curve fits for maximum total (continuous curve), and translational, and rotational (dashed curves) powers are shown. (B) Ratio of maximum translational to rotational power. The horizontal dashed line indicates a ratio of 1. Parameter values of the curve fits in (a) are given in electronic supplementary material, Table S3.4.

3.4 General discussion

3.4.1 Body dynamics of undulatory swimming in larval fish: improving swimming skills within a narrow time window

Using a distributed-mass inverse-dynamics approach, we shed new light on the swimming mechanics of larval fish. Across the observed range of swimming speeds, large body undulations do not cause large sideslip of the CoM, but considerable body yaw. We expect that adult fish, which use narrower, lower frequency body waves, will show considerably lower relative fluctuations in body yaw, torque and moment of inertia.

Comparing within larval stages, swimming performance greatly improves between 2 and 5 dpf. Over this age range, larval fish increasingly favour intermittent over cyclic swimming (Müller and Van Leeuwen, 2004). Yet burst periods are sufficiently long and cyclic to analyse trends that elucidate the physics of swimming in the intermediate Reynolds regime and the development of swimming in larval fish. From 2 to 3 dpf, the larvae increase maximum tail-beat frequency f_{max} from 80 to 95 Hz. The 4 dpf larvae used similar f_{max} as 3 dpf larvae, but generated higher maximum tail-beat amplitudes for frequencies above 50 Hz. The higher tail-beat frequencies and amplitudes lead to higher swimming speeds and indicate that maximum power output of the swimming musculature increases rapidly after hatching. Improving swimming speed reduces the predation risk of larval fish (Fuiman and Magurran, 1994) and enhances their ability to catch prey when they start feeding at 5 dpf. Several other performance criteria require future attention, such as fast-start performance and manoeuvres in three-dimensional space.

3.4.2 Coping with high-friction forces: trading efficiency for thrust

Vortex shedding mechanics (as expressed by St) changes with flow regime (as expressed by Re) in a nonlinear way (Eloy, 2012; Van Weerden et al., 2014; Roshko, 1954). The inverse relationship between St and Re is mapped out by larval fish (Fig. 3.7G). Slow larvae swim at higher St (St $\approx$ 2.5 at Re $=$ 60) than fast larvae (St $\approx$ 0.72 at Re $=$ 1400). Thus, across the examined larval size range (body length 3–4.5 mm), increasing swimming speed by one order of magnitude from 25 to 250 mm s^{-1} causes a drastic, nonlinear drop in St. The Strouhal number remains roughly constant across the typical speed range of adult fish and cetaceans (St $=$ 0.2–0.4 for Re $=$ 10^3–10^5) (Triantafyllou et al., 1993; Eloy, 2012; Van Weerden et al., 2014; Rohr and Fish, 2004). When adult fish increase tail-beat frequency, their swimming speed increases proportionally without increasing tail-beat amplitude, so St drops little with increasing speed (Tytell, 2004a). The Strouhal number reflects differences in vortex shedding mechanics caused by body shape. Swimmers with high aspect-ratio tail fins use lower St values (Eloy, 2012; Rohr and Fish, 2004) than anguilliform swimmers (Eloy, 2012; Tytell, 2004a). Overall, undulatory swimmers operate close to optimal St values, yet optimal Strouhal numbers vary with body shape and swimming speed.

Undulatory swimmers use high Strouhal numbers in high-friction environments. High

Strouhal numbers occur not just at small body sizes, but generally in systems with high body drag, such as adult lungfish moving through highly viscous watery solutions (Horner and Jayne, 2008); sandfish and nematodes moving through granular media (Maladen et al., 2009, 2011; Ding et al., 2012; Jung, 2010); and alligators (data in Gazzola et al., 2014). When facing higher frictional forces, undulatory swimmers swim at lower stride lengths—tail-beat frequency f and amplitude A_{tail} must increase to achieve the same displacement (computational: Borazjani and Sotiropoulos, 2009b,c, 2010; Reid et al., 2012, experimental: Van Weerden et al., 2014; Horner and Jayne, 2008; Kayan et al., 1978; Sznitman et al., 2010). Theoretical studies (Eloy and Schouveiler, 2011; Eloy, 2012) show that maximal efficiency decreases and St increases with decreasing Re. When viscous or other frictional forces become large relative to inertial forces, undulatory swimmers must sacrifice efficiency for higher thrust.

The Strouhal number decreases steeply as undulatory swimmers transition from the viscous to the inertial flow regime (Fig. 3.7G,H), consistent with the inverse relationship between St and Re. As seen in larval fish, swimming at lower Re requires generating relatively higher propulsive forces by increasing f and A_{tail} (Fig. 3.7H). Both increase the torque around the CoM and hence decrease the ratio of translational to rotational kinetic energy. Undulatory swimmers have no known mechanisms to store rotational kinetic energy. Hence, a lower ratio of translational to rotational kinetic energy implies a lower propulsive efficiency, as indicated by a high St value. As Re drops, a given increase in f or A_{tail} causes less of an increase in swimming speed and St increases. By swimming faster, larval fish crank up their Re, which might enable them to increase propulsive efficiency at the expense of higher power expenditure. High swimming speeds require very high tail-beat frequencies, which demand super-fast muscles, which are known to have low efficiencies (Rome, 2006), which counteracts the gain in fluid-dynamic efficiency. In larval zebrafish of 4–5 dpf, this limitation tops off f_{max} at about 100 Hz and Re at about 1400. The general trend of a decreasing St with Re in the intermediate regime has been predicted by CFD studies (e.g. Borazjani and Sotiropoulos, 2009b,c; Gazzola et al., 2014)).

3.4.3 Scaling of the swimming number Sw

We obtained a more complex relationship between Re and the swimming number Sw than suggested by Gazzola et al. (2014). They explored the relation between Re (range 200–20,000) and Sw with CFD simulations. They suggested that the nonlinear Sw–Re relationship can be described by first approximation by two power functions. While the theoretical prediction matches both the CFD and the experimental data on large swimmers, the match is less convincing in the laminar flow regime, where the power exponents predicted using Blasius theory ($\text{Re} \propto \text{Sw}^{1.33}$) and CFD ($\text{Re} \propto \text{Sw}^{1.31}$) are considerably lower than the experimentally observed exponent ($\text{Re} \propto \text{Sw}^{1.52}$, power function fit to zebrafish data over $10 \lesssim \text{Re} \lesssim 1000$) and depend critically on the exact value of transitional Re—Gazzola et al. obtain a good fit between Blasius prediction (exponent 1.33), CFD data (exponent 1.31) and experimental data (exponent 1.33) partly by placing the

transition from the laminar to the turbulent flow regime at different Re and Sw (CFD: Re 800, Sw 2000; experimental data: Re 3000, Sw 10, 000).

The large discrepancy between experimental data on the one hand and theoretical Blasius prediction on the other hand stem from the complex fluid-dynamic effects caused by large-amplitude tail motion. Any high anterior drag must be balanced by high thrust, which the swimmer generates by increasing tail-beat amplitude and frequency, which in turn increase anterior drag by positive feedback on tbody and hence amplitudes of α_{head} and α_{body}. The nature of this feedback depends on Re and body shape. The Blasius prediction of Gazzola et al. is not able to capture this complex feedback, leading them to underestimate drag and hence St.

3.4.4 Swimming performance varies with size and speed

Small organisms ($\ell_{\text{body}} < 10$ mm) operating in the intermediate flow regime ($10^1 <$ Re $< 10^3$) reach not only much higher tail-beat frequencies, but also higher ℓ_{body}-specific swimming speeds than large undulatory swimmers ($\ell_{\text{body}} > 10$ mm). Despite experiencing relatively higher viscous fluid forces and despite a lower swimming efficiency, zebrafish larvae can reach extreme forward speeds of up to $60\ell_{\text{body}}$ s^{-1}, because they can generate relatively high propulsive forces at tail-beat frequencies of up to 95 Hz. By contrast, large undulatory swimmers have considerably lower tail-beat frequencies and ℓ_{body}-specific swimming speeds. And adult fish retain those low values when placed in more viscous flow regimes. Lungfish maintain swimming speeds of 0.15–0.25 ℓ_{body} s^{-1} and tail-beat frequencies of 1–2 Hz over a 1000-fold increase in viscosity (Horner and Jayne, 2008). Sandfish 'swimming' in sand use similar tail-beat frequencies (1–4 Hz) (Maladen et al., 2009). Compared with small undulatory swimmers, which are adapted to the intermediate flow regime, large undulatory swimmers have muscles optimized to operate at low cycle frequencies in order to swim at low Strouhal numbers. Large swimmers cannot adjust to increased friction forces by increasing tail-beat frequency by orders of magnitude, because their axial muscles have a low maximum cycling frequency.

Across body sizes, distance/ℓ_{body} covered per tail beat in the viscous flow regime is low compared with undulatory swimmers in the inertial flow regime: lungfish and sandfish reach 0.1–0.2 ℓ_{body}/tail-beat cycle (Horner and Jayne, 2008; Maladen et al., 2009), zebrafish larvae 0.2–0.6 (Fuiman and Batty, 1997; Müller and Van Leeuwen, 2004), tadpoles 0.3–0.6 (D'Août and Aerts, 1999), insect larvae 0.3 (Brackenbury, 2000). By contrast, adult fish in the inertial flow regime swim at 0.4 (anguilliform swimmers; (Kern and Koumoutsakos, 2006; Gillis, 1998)) to 0.9 ℓ_{body}/tail-beat cycle (carangiform swimmers; (Videler, 1993; Wardle et al., 1995; Müller et al., 2002)) during routine swimming. In summary, during undulatory swimming in systems with high viscous or friction forces, St is high and efficiency is low.

Ethics

The experiments were approved by the Wageningen University Animal Experiments Committee.

Data accessibility

Data available from the Dryad Digital Repository:

```
http://dx.doi.org/10.5061/dryad.r503m
```

Authors' contributions

U.K.M. manually digitized the video data. J.L.v.L. and C.J.V. wrote the Matlab codes used to process and analyse data. J.L.v.L. and U.K.M. wrote most of the paper. All authors participated in experimental design, execution of the experiments, development of concepts, and critical revisions and gave their approval for publication.

Competing interests

We declare we have no competing interests.

Funding

Acknowledgements

References

Askew, G. N., Marsh, R. L. and Ellington, C. P. (2001). The mechanical power output of the flight muscles of blue-breasted quail (*Coturnix chinensis*) during take-off. *J. Exp. Biol.* **204**, 3601–3619.

Bainbridge, R. (1958). The speed of swimming of fish as related to size and to the frequency and amplitude of the tail beat. *J. Exp. Biol.* **35**, 109–133.

Batty, R. S. and Blaxter, J. H. S. (1992). The effect of temperature on the burst swimming of the fish larvae. *J. Exp. Biol.* **170**, 187–201.

Borazjani, I. and Sotiropoulos, F. (2009a). Numerical investigation of the hydrodynamics of anguilliform swimming in the transitional and inertial flow regimes. *J. Exp. Biol.* **212**, 576–592.

Borazjani, I. and Sotiropoulos, F. (2009b). Numerical investigation of the hydrodynamics of carangiform swimming in the transitional and inertial flow regimes. *J. Exp. Biol.* **212**, 1541–1558.

Borazjani, I. and Sotiropoulos, F. (2009c). Vortex-induced vibrations of two cylinders in tandem arrangement in the proximity-wake interference region. *J. Fluid Mech.* **621**, 321–364.

Borazjani, I. and Sotiropoulos, F. (2010). On the role of form and kinematics on the hydrodynamics of self-propelled body/caudal fin swimming. *J. Exp. Biol.* **213**, 89–107.

Brackenbury, J. (2000). Locomotory modes in the larva and pupa of *Chironomus plumosus* (Diptera, Chironomidae). *J. Insect Physiol.* **46**, 1517–1527.

Chattopadhyay, S., Moldovan, R., Yeung, C. and Wu, X. L. (2006). Swimming efficiency of bacterium *Escherichia coli*. *Proc. Natl. Acad. Sci. U. S. A.* **103**, 13712–13717.

D'Août, K. and Aerts, P. (1999). The kinematics of voluntary steady swimming of hatchling and adult axolotls (*Ambystoma mexicanum* Shaw, 1789). *Belgian J. Zool.* **129**, 305–316.

Ding, Y., Sharpe, S. S., Masse, A. and Goldman, D. I. (2012). Mechanics of undulatory swimming in a frictional fluid. *PLoS Comput. Biol.* **8**, e1002810.

Eloy, C. (2012). Optimal Strouhal number for swimming animals. *J. Fluids Struct.* **30**, 205–218.

Eloy, C. and Schouveiler, L. (2011). Optimisation of two-dimensional undulatory swimming at high Reynolds number. *Int. J. Non. Linear. Mech.* **46**, 568–576.

Fry, S. N., Sayaman, R. and Dickinson, M. H. (2003). The aerodynamics of free-flight, maneuvers in *Drosophila*. *Science (80-.).* **300**, 495–498.

Fuiman, L. A. (1983). Growth gradients in fish larvae. *J. Fish Biol.* **23**, 117–123.

Fuiman, L. A. and Batty, R. S. (1997). What a drag it is getting cold: partitioning the physical and physiological effects of temperature on fish swimming. *J. Exp. Biol.* **200**, 1745–1755.

Fuiman, L. A. and Magurran, A. E. (1994). Development of predator defences in fishes. *Rev. Fish Biol. Fish.* **4**, 145–183.

Gazzola, M., Argentina, M. and Mahadevan, L. (2014). Scaling macroscopic aquatic locomotion. *Nat. Phys.* **10**, 758–761.

Gillis, G. B. (1998). Environmental effects on undulatory locomotion in the American eel *Anguilla rostrata*: kinematics in water and on land. *J. Exp. Biol.* **201**, 949–961.

Girgenrath, M. and Marsh, R. L. (1999). Power output of sound-producing muscles in the tree frogs *Hyla versicolor* and *Hyla chrysoscelis*. *J. Exp. Biol.* **202**, 3225–3237.

Horner, A. M. and Jayne, B. C. (2008). The effects of viscosity on the axial motor pattern and kinematics of the African lungfish (*Protopterus annectens*) during lateral undulatory swimming. *J. Exp. Biol.* **211**, 1612–1622.

Josephson, R. K., Malamud, J. G. and Stokes, D. R. (2000). Power output by an asynchronous flight muscle from a beetle. *J. Exp. Biol.* **203**, 2667–2689.

Jung, S. (2010). *Caenorhabditis elegans* swimming in a saturated particulate system. *Phys. Fluids* **22**, 031903.

Kayan, V. P., Kozlov, L. F. and Pyatetskii, V. E. (1978). Kinematic characteristics of the swimming of certain aquatic animals. *Fluid Dyn.* **13**, 641–646.

Kern, S. and Koumoutsakos, P. (2006). Simulations of optimized anguilliform swimming. *J. Exp. Biol.* **209**, 4841–4857.

Li, G., Müller, U. K., Van Leeuwen, J. L. and Liu, H. (2012). Body dynamics and hydrodynamics of swimming fish larvae: a computational study. *J. Exp. Biol.* **215**, 4015–4033.

Maladen, R. D., Ding, Y., Li, C. and Goldman, D. I. (2009). Undulatory swimming in sand: subsurface locomotion of the sandfish lizard. *Science (80-.).* **325**, 314–319.

Maladen, R. D., Ding, Y., Umbanhowar, P. B., Kamor, A. and Goldman, D. I. (2011). Mechanical models of sandfish locomotion reveal principles of high performance subsurface sand-swimming. *J. R. Soc., Interface* **8**, 1332–1345.

Müller, U. K., Stamhuis, E. J. and Videler, J. J. (2002). Riding the waves: the role of the body wave in undulatory fish swimming. *Integr. Comp. Biol.* **42**, 981–987.

Müller, U. K. and Van Leeuwen, J. L. (2004). Swimming of larval zebrafish: ontogeny of body waves and implications for locomotory development. *J. Exp. Biol.* **207**, 853–868.

Müller, U. K. and Videler, J. J. (1996). Inertia as a 'safe harbour': do fish larvae increase length growth to escape viscous drag? *Rev. Fish Biol. Fish.* **6**, 353–360.

Nudds, R. L., John, E. L., Keen, A. N. and Shiels, H. A. (2014). Rainbow trout provide the first experimental evidence for adherence to a distinct Strouhal number during animal oscillatory propulsion. *J. Exp. Biol.* **217**, 2244–2249.

Osse, J. W. M. and Van den Boogaart, J. G. M. (1999). Dynamic morphology of fish larvae, structural implications of friction forces in swimming, feeding and ventilation. *J. Fish Biol.* **55**, 156–174.

Reid, D. A. P., Hildenbrandt, H., Padding, J. T. and Hemelrijk, C. K. (2012). Fluid dynamics of moving fish in a two-dimensional multiparticle collision dynamics model. *Phys. Rev. E - Stat. Nonlinear, Soft Matter Phys.* **85**, 021901.

Rohr, J. J. and Fish, F. E. (2004). Strouhal numbers and optimization of swimming by odontocete cetaceans. *J. Exp. Biol.* **207**, 1633–1642.

Rome, L. C. (2006). Design and function of superfast muscles: new insights into the physiology of skeletal muscle. *Annu. Rev. Physiol.* **68**, 193–221.

3

Roshko, A. (1954). On the development of turbulent wakes from vortex streets. Technical report, California Institute of Technology.

Sznitman, J., Shen, X., Purohit, P. K. and Arratia, P. E. (2010). The effects of fluid viscosity on the kinematics and material properties of *C. elegans* swimming at low Reynolds number. *Exp. Mech.* **50**, 1303–1311.

Taylor, G. K., Nudds, R. L. and Thomas, A. L. R. (2003). Flying and swimming animals cruise at a Strouhal number tuned for high power efficiency. *Nature* **425**, 707–711.

Triantafyllou, G. S., Triantafyllou, M. S. and Grosenbaugh, M. A. (1993). Optimal thrust development in oscillating foils with application to fish propulsion. *J. Fluids Struct.* **7**, 205–224.

Tytell, E. D. (2004a). Kinematics and hydrodynamics of linear acceleration in eels, *Anguilla rostrata*. *Proc. R. Soc. B* **271**, 2535–2540.

Tytell, E. D. (2004b). The hydrodynamics of eel swimming II. Effect of swimming speed. *J. Exp. Biol.* **207**, 3265–3279.

Van Weerden, J. F., Reid, D. A. P. and Hemelrijk, C. K. (2014). A meta-analysis of steady undulatory swimming. *Fish Fish.* **15**, 397–409.

Verhagen, J. H. G. (2004). Hydrodynamics of burst swimming fish larvae; a conceptual model approach. *J. Theor. Biol.* **229**, 235–248.

Videler, J. J. (1993). *Fish Swimming*. Berlin, Germany: Springer.

Wardle, C. S., Videler, J. J. and Altringham, J. D. (1995). Tuning in to fish swimming waves: body form, swimming mode and muscle function. *J. Exp. Biol.* **198**, 1629–1636.

Young, I. S. and Rome, L. C. (2001). Mutually exclusive muscle designs: the power output of the locomotory and sonic muscles of the oyster toadfish (*Opsanus tau*). *Proc. R. Soc. B* **268**, 1965–1970.

Electronic supplementary material

S3.1 Symbols and definitions

Mathematical symbols and abbreviations used in the main manuscript and this electronic supplement are listed in Table S3.1.

Table S3.1: Overview of symbols and abbreviations.

Symbol	Definition	Dimension
A_{tail}	peak-to-peak amplitude in (near) cyclic swimming event	L
$\hat{A}_{\text{tail}}$	dimensionless peak-to-peak amplitude in a (near) cyclic swimming event: $A_{\text{tail}}/\ell_{\text{fish}}$	–
$\mathbf{a}_{\perp,i}$	acceleration perpendicular to fish axis of body segment i	LT^{-2}
c_1; c_2; c_3	constants used to make curve fits for various parameter sets, for specifications and values see Tables S3.2–S3.4	variable
$c_{\text{dynp},i}$; $c_{\text{fric},i}$	constants used to estimate the external torque per unit length on the body due to dynamic pressure and skin friction	–
CoM	centre of mass of the body; the centre of mass of a body segment is indicated as the segmental CoM	–
dpf	days post fertilization	–
$E_{\text{kin,body}}$	total kinetic energy of the body	ML^2T^{-2}
$E_{\text{kin,int}}$	'internal' kinetic energy of the body	ML^2T^{-2}
$E_{\text{tr,CoM}}$	kinetic energy due to CoM translation	ML^2T^{-2}
$E_{\text{rot,body}}$	kinetic energy due to rotation of the body parts around the CoM	ML^2T^{-2}
E^*	specific energy: E/m_{body}	L^2T^{-2}
$\mathbf{F}_{\text{CoM}}$	net force vector on the CoM	MLT^{-2}
$F_{v\perp}$; $F_{v\parallel}$	force components on the CoM, respectively, perpendicular and parallel to the velocity of the CoM (Fig. 3.1D)	MLT^{-2}
f; f_{max}	cycle frequency; maximum cycle frequency	T^{-1}
$J_{\mid}$	moment of inertia of straight fish body with respect to the CoM	ML^2
J_{body}; $\dot{J}_{\text{body}}$	moment of inertia of the body with respect to the CoM and its rate of change	ML^2; ML^2T^{-1}

J_i	moment of inertia of body segment i about its vertical central axis	ML^2
$J_{CoM,i}$; $\dot{J}_{CoM,i}$	moment of inertia of body segment i about about the CoM; time derivative of $J_{CoM,i}$	ML^2
h_i	dorso-ventral height of segment i	L
i	indicator for the number of a body segment	–
$\hat{\ell}$	normalised position along the body (0 at the snout, 1 at the tail tip)	–
ℓ_{body}; ℓ_{stride}	length of the fish body; stride length (distanced travelled per tail-beat cycle)	L
m_{body}	mass of the body	M
m_i	mass of body segment i	M
n	number of extrema in α_{body}	–
N	number of objects	–
$P_{kin,body}$	total kinetic power of the body	ML^2T^{-3}
$P_{tr,CoM}$	power due to translational velocity changes of the CoM	ML^2T^{-3}
$P_{rot,body}$	power due to rotation of body parts around the CoM	ML^2T^{-3}
P^*	specific power: P/m_{body}	L^2T^{-3}
$\mathbf{r}_{CoM}$; $\dot{\mathbf{r}}_{CoM}$; $\ddot{\mathbf{r}}_{CoM}$	position, velocity and acceleration vector of the CoM	L; LT^{-1}; LT^{-2}
$r_{x,CoM}$; $r_{y,CoM}$; $r_{z,CoM}$	components of $\mathbf{r}_{CoM}$, coordinates of the CoM in earth-bound frame	L
$\mathbf{r}_i$; $\dot{\mathbf{r}}_i$; $\ddot{\mathbf{r}}_i$	position, velocity and acceleration vector of segment i	L; LT^{-1}; LT^{-2}
$\mathbf{r}_{mov,i}$; $\dot{\mathbf{r}}_{mov,i}$; $\ddot{\mathbf{r}}_{mov,i}$	idem for segment i in moving frame	L; LT^{-1}; LT^{-2}
$r_{x,mov,i}$; $r_{y,mov,i}$; $r_{z,mov,i}$	components of $\mathbf{r}_{mov,i}$	L
$r_{seg,i}$	distance to central vertical axis through segment i	L
$\mathbf{r}_{tail}$	direction vector of the tail	L
$r_{x,tail}$; $r_{y,tail}$; $r_{z,tail}$	components of $\mathbf{r}_{tail}$	L
Re	Reynolds number	–
s_i	distance of segment i from the the tip of the snout along the axis of the fish	L
S_i	wetted surface of segment i	L^2
St	Strouhal number	–
Sw	Swimming number	–

$t; t_1; t_n$	time; time at first extreme in α_{body}; time at last extreme in α_{body}	T
V_i	volume of body segment i	L^3
$\mathbf{v}_{\parallel,i}; \mathbf{v}_{\perp,i}$	velocity parallel and perpendicular to fish axis of segment i	LT^{-1}
$v_{\text{swim}}; \bar{v}_{\text{swim}}$	swimming speed along path of CoM; idem but mean value	LT^{-1}
$\hat{v}_{\text{swim}}$	dimensionless swimming speed (Equation 3.4)	–
$v_{\text{swim}}^*; \bar{v}_{\text{swim}}^*$	specific swimming speed $(v_{\text{swim}}/\ell_{\text{body}})$; idem but mean value	T^{-1}
$\mathbf{v}_{\text{tail}}; \mathbf{v}_{\perp,\text{tail}}$	velocity of the tail; component of tail velocity perpendicular to local fish axis	LT^{-1}
$v_{x,\text{tail}}; \quad v_{y,\text{tail}}; v_{z,\text{tail}}$	components of $\mathbf{v}_{\text{tail}}$	LT^{-1}
XYZ	earth-bound coordinate system	–
$X_{\text{mov}}Y_{\text{mov}}Z_{\text{mov}}$	moving coordinate system	–
$y(x)$	curve fit y as function of x	–
$\alpha_{0,\text{body}}$	constant used to compute the angle of the body in the XY-plane	–
$\alpha_{0,\text{head}}$	constant used to compute the angle of the head in the XY-plane	–
α_{body}	angle of the body in XY-plane	–
$\alpha_{\text{CoM},i}$	the angle of the position vector from the CoM to the centre of mass of segment i	–
α_{head}	angle of the head in XY-plane	–
β_{tail}	angle of attack of the tail with respect to the local velocity vector of the tail	–
μ	dynamic viscosity of water	ML^{-1}T^{-3}
$\Delta\ell_i$	length of segment i	L
$\rho_{\text{fish}}; \rho_{\text{water}}$	mass density of the body; mass density of water	ML^{-3}
$\tau_{\text{acc}}; \tau_{\text{acc},i}^*$	torque on the body due to acceleration-reaction forces; idem but per unit length along the body	ML^{2}T^{-2}; MLT^{-2}
τ_{body}	net inertial torque of the body	ML^{2}T^{-2}
$\hat{\tau}_{\text{body}}$	dimensionless body torque (Equation 3.7)	–
$\tau_{\text{body},i}^*$	inertial torque per unit length along the body with respect to the CoM	MLT^{-2}
$\tau_{\text{dynp}}; \tau_{\text{dynp},i}^*$	torque on the body due to dynamic pressure, proportional to squared perpendicular velocity component; idem but per unit length along the body	ML^{2}T^{-2}; MLT^{-2}
$\tau_{\text{fric}}; \tau_{\text{fric},i}^*$	torque on the body due the skin friction; idem but per unit length along the body	ML^{2}T^{-2}; MLT^{-2}

3

$\omega_{\text{body}}; \dot{\omega}_{\text{body}}$	angular velocity and angular acceleration of the body	$\mathsf{T}^{-1}; \mathsf{T}^{-2}$
$\omega_{\text{CoM},i}; \dot{\omega}_{\text{CoM},i}$	angular velocity and acceleration in the XY-plane of the position vector from the CoM to the centre of mass of segment i	$\mathsf{T}^{-1}; \mathsf{T}^{-2}$
$\omega_i; \dot{\omega}_i$	angular velocity and acceleration of segment i around the local central axis	$\mathsf{T}^{-1}; \mathsf{T}^{-2}$

S3.2   High-speed video recordings

We used three video setups: a Redlake MotionPro high-speed camera (Redlake, San Diego, CA, USA; 1000 frames s^{-1}, 1280×512 pixels, exposure time 124 μs), recording through a dissection microscope (Zeiss, Sliedrecht, The Netherlands; magnification 0.6–1.6× on the camera chip), for details see Müller and Van Leeuwen (2004); a pco.dimax HS4 high-speed camera (PCO AG, Kelheim, Germany; 2000×2000 pixels, 2000 frames s^{-1}, exposure time of 74 μs); a Photron FASTCAM 1024 PCI (Photron, West Wycombe, UK; 1500 frames s^{-1}, 896×784 pixels, exposure time 124 μs). In the first setup, we filmed from a dorsal viewpoint with background light from below. In the latter two setups, we used a Nikkor 105D macro lens at f2.8 with an extension tube and back-light from above with a nearly parallel beam, and we filmed from a ventral viewpoint. In a few cases, we recorded the fish in water seeded with Nylon particles (diam. 6 μm) with laser sheet illumination (details in Müller et al., 2008). The set up with the pco.dimax HS4 camera provided the best resolution in space and time.

S3.3   Supplementary computations

S3.3.1   Body shape and force components on centre of mass and dimensionless quantities

Using the spline routine package of Woltring (1986), the manually digitised body axes of the larval fish (main text, §3.2.2) were first interpolated with a cubic spline function, providing 51 equidistant axis points along the length of the fish with a straight portion imposed for the head region, then smoothed with a cubic spline function (smoothing factor 10^{-7}). The smoothed body outlines were subsequently smoothed with a quintic spline function as a function of time (using the generalized cross validation criterion). In one video sequence, the tail tip was missing in a single frame (not at the maximum tail amplitude that was used to compute the Strouhal number). The tail-tip position for this frame was estimated manually, followed by a correction of the interpolation with a smoothing spline.

To determine body shape, we photographed (Olympus DP50 digital camera mounted on a Zeiss Stemi SV1 microscope) dorsal and lateral views of larvae aged 2–5 dpf, then digitized the outlines of the main body, dorsal and ventral fin fold, eyes, and yolk sac at 53–55 equidistant points along the body with AnalySIS V3.1 (Soft Imaging System GmbH, Germany) and interpolated with a cubic spline fit to 51 equidistant points from snout to

tail tip for each measurement.
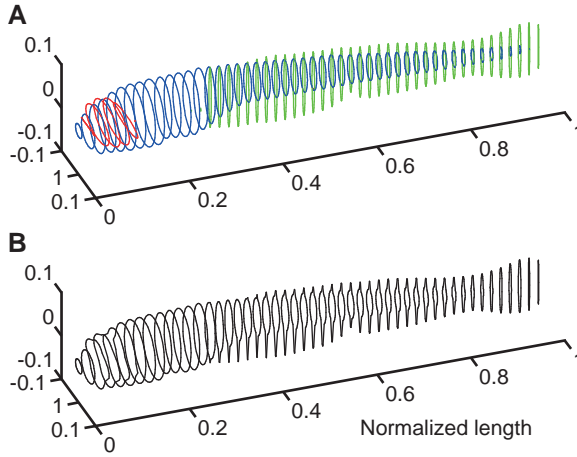
A

B

Normalized length

We estimated body volume by modelling the fish as a series of 51 segments: the first and last segment each of length $\ell_{\text{body}}/100$ and all others of $\ell_{\text{body}}/50$. Ellipses were fitted to the head, eyes, fin fold, trunk (excluding fins) and yolk sac (where present). The circumference of each segment was assumed to be the closed-loop combination of the most peripheral arcs of the intersecting ellipses (Fig. S3.1). We assumed a uniform mass density ($\rho_{\text{fish}} = 1000\,\text{kg m}^{-3}$) over the entire body. For each segment, we computed volume V_i, mass m_i, and position vector $\mathbf{r}_i$ of the local centre of mass by numerical integration. Body mass m_{body} was computed as the sum of the segmental masses, resulting in 239, 289, 414, and 373 µg for stages 2–5 dpf. The average ℓ_{body} for these stages were, respectively, 3.39, 3.81, 4.37 and 4.36 mm. These values for ℓ_{body} and m_{body} were used for all subsequent computations.

The position vector $\mathbf{r}_{\text{CoM}}$ of the CoM of the fish was calculated by dividing the sum of the product of m_i and $\mathbf{r}_i$ by m_{body}:

$$\mathbf{r}_{\text{CoM}} = \sum_i \left(m_i \mathbf{r}_i \right) / m_{\text{body}}, \tag{S3.1}$$

which enabled us to calculate the instantaneous CoM position during swimming. Velocity and acceleration vectors ($\dot{\mathbf{r}}_{\text{CoM}}$ and $\ddot{\mathbf{r}}_{\text{CoM}}$) of the CoM were calculated by (double) differentiation of Equation S3.1. The required segmental velocities $\dot{\mathbf{r}}_i$ and accelerations $\ddot{\mathbf{r}}_i$ were calculated by (double) differentiation of the spline functions describing the fish's midline. Swimming speed was defined as: $v_{\text{swim}} = \dot{r}_{\text{CoM}} = ||\dot{\mathbf{r}}_{\text{CoM}}||$, and the specific swimming speed as: $v_{\text{swim}}^* = v_{\text{swim}}/\ell_{\text{body}}$. The force on the CoM was computed from Newton's second law:

$$\mathbf{F}_{\text{CoM}} = m_{\text{body}} \ddot{\mathbf{r}}_{\text{CoM}}. \tag{S3.2}$$

S3.3.2 Dimensionless quantities

The Reynolds number was computed as

$$\mathrm{Re} = \rho_{\mathrm{water}}\ell_{\mathrm{body}}\bar{v}_{\mathrm{swim}}/\mu, \tag{S3.3}$$

with $\bar{v}_{\mathrm{swim}}$ the mean swimming speed over either a full or half a swimming cycle. We used a full swimming cycle unless only two lateral tail beats of a particular swimming event met the auto-correlation criterion for near cyclic swimming (main text: §3.2.2). We computed $\bar{v}_{\mathrm{swim}}$ as the displacement over the swimming cycle (or half the cycle) divided by the cycle time (or half the cycle time). We used $\rho_{\mathrm{water}} = 996.232$ kg m^{-3} for the density and $\mu = 0.833$ mPa s for the viscosity, i.e. the values for water at 28°C. The Strouhal number was defined as:

$$\mathrm{St} = fA_{\mathrm{tail}}/\bar{v}_{\mathrm{swim}}, \tag{S3.4}$$

where A_{tail} is the peak to peak amplitude of the tail, and $\bar{v}_{\mathrm{swim}}$ the mean swimming speed. The computation of A_{tail} from our selected recordings was complicated by lateral oscillations of the CoM (sideslip), and by unavoidable slight deviations from pure cyclic swimming (in spite of our fairly strict cross-correlation criterion). To address these problems, the average of 2 or 3 tail-beat maxima during the swimming cycle was manually measured from graphs of the paths of the CoM and tail, and doubled to obtain an estimate for A_{tail}. Corrections were applied for slightly curved paths of the CoM.

S3.3.3 Instantaneous values of moment of inertia, body angle, angular velocity and torque

In the fish frame of reference, the position vector of the segment centre i is:

$$\mathbf{r}_{\mathrm{mov},i} = \mathbf{r}_i - \mathbf{r}_{\mathrm{CoM}}. \tag{S3.5}$$

For each segment, the moment of inertia about the segmental vertical centre line as a function of time was obtained by a numerical approximation of:

$$J_i = \int \rho_{\mathrm{fish}} r_{\mathrm{seg},i}^2 \, \mathrm{d}V_i, \tag{S3.6}$$

where $r_{\mathrm{seg},i}$ is the distance to the central vertical axis through segment i. The moment of inertia of segment i with respect to the CoM about the vertical Z_{mov}-axis was computed as:

$$J_{\mathrm{CoM},i} = J_i + m_i r_{\mathrm{mov},i}^2, \tag{S3.7}$$

where $r_{\mathrm{mov},i}$ is the distance of the centre of mass of the segment to the CoM. The time-dependent instantaneous moment of inertia of the body with respect to the instantaneous location of the CoM was computed as the sum of $J_{\mathrm{CoM},i}$ along the body:

$$J_{\mathrm{body}} = \sum_i J_{\mathrm{CoM},i}. \tag{S3.8}$$

The rate of change of J_{body} was computed by a smoothing cubic spline (tolerance value $5 \cdot 10^{-8}$ kg m^2) and a subsequent differentiation with the Matlab routines `spaps` and `fnder`.

The angular velocity of the body ω_{body} can be derived from the momentum equation:

$$J_{\text{body}}\omega_{\text{body}} = \sum_i J_{\text{CoM},i}\,\omega_{\text{CoM},i}, \tag{S3.9}$$

where $\omega_{\text{CoM},i}$ is defined as the angular velocity of the centre of mass of segment i with respect to the CoM. The relatively small contribution of the rotation around the central vertical axis of the segment is ignored here.
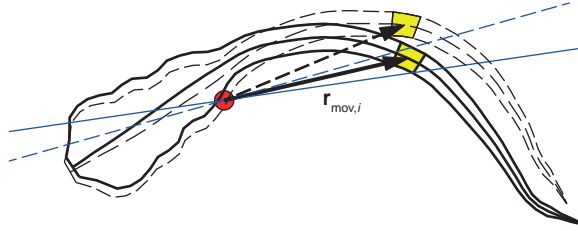
Figure S3.2: Diagram of the shape of the larval body in the moving frame at two different instances (continuous and dashed curves, 1 ms apart), taken from the event of Fig. 3.1 (main text). The red dot indicates the CoM (which is fixed in the moving frame). A segment (yellow) is indicated with its position vector $\mathbf{r}_{\text{mov},i}$. The components of $\mathbf{r}_{\text{mov},i}$ and its derivative are used to compute the angular velocity of the segments about the CoM (Equation S3.10). The continuous and dashed blue lines indicate the computed body orientation at the two instances, which differ considerably from the head orientation. The head rotates slightly clockwise, while the total body rotates counter clockwise.

Angular velocity $\omega_{\text{CoM},i}$ can be calculated by dividing the cross product of $\mathbf{r}_{\text{mov},i}$ and $\dot{\mathbf{r}}_{\text{mov},i}$ by $r^2_{\text{mov},i}$, which for the considered two-dimensional case results in:

$$\omega_{\text{CoM},i} = \frac{\dot{r}_{y,\text{mov},i}\,r_{x,\text{mov},i} - \dot{r}_{x,\text{mov},i}\,r_{y,\text{mov},i}}{r^2_{\text{mov},i}}. \tag{S3.10}$$

During a swimming cycle, the CoM passes twice through the central body axis, leading to very small values of $r_{\text{mov},i}$ in nearby body segments (or even a singular point if the location of the CoM overlaps with the segmental centre). This problem was neutralized by dividing by 10^{-8} m^2 for $r_{\text{mov},i} < 10^{-4}$ m, instead of the computed value of $r^2_{\text{mov},i}$. The angular velocity of the body was obtained from Equation S3.9:

$$\omega_{\text{body}} = \frac{\sum_i J_{\text{CoM},i}\,\omega_{\text{CoM},i}}{J_{\text{body}}}. \tag{S3.11}$$

The body angle α_{body} was derived by integration of ω_{body}:

$$\alpha_{\text{body}} = \int_{t_0}^{t} \omega_{\text{body}}\,\mathrm{d}t - \alpha_{0,\text{body}}. \tag{S3.12}$$

where $\alpha_{0,\text{body}}$ is defined as zero or the mean angle of translation of the CoM over a complete swimming cycle. We approximated the integral by numerical integration with the trapezoidal method [1]. The angular acceleration of the body $\dot{\omega}_{\text{body}}$ was computed by differentiation of ω_{body}.

For the examined (near) cyclic swimming events, we detected the maxima and minima in α_{body} with the Matlab function `findpeaks`. For each of these events, we computed the peak-to-peak amplitude by taking the absolute value of the difference between the second peak and the mean of the first and the third peak. For very short events with only two available peaks in α_{body}, we took the absolute value of the difference between the first and the second peak. This forms the basis for the body angular amplitude data against swimming speed shown in Fig. 3.7E,F.

To enable a comparison with α_{body}, the yaw angle of the head was computed as:

$$\alpha_{\text{head}} = \begin{cases} \arctan\left(\frac{r_{y,\text{mov},1}-r_{y,\text{mov},7}}{r_{x,\text{mov},1}-r_{xmov,7}}\right) & \text{for } r_{x,\text{mov},1}-r_{x,\text{mov},7} > 0 \\ \pi/2 & \text{for } \begin{cases} r_{x,\text{mov},1}-r_{x,\text{mov},7}=0 \\ r_{y,\text{mov},1}-r_{y,\text{mov},7}>0 \end{cases} \\ 3\pi/2 & \text{for } \begin{cases} r_{x,\text{mov},1}-r_{x,\text{mov},7}=0 \\ r_{y,\text{mov},1}-r_{y,\text{mov},7}<0 \end{cases} \\ \arctan\left(\frac{r_{y,\text{mov},1}-r_{y,\text{mov},7}}{r_{x,\text{mov},1}-r_{x,\text{mov},7}}\right)+\pi & \text{for } r_{x,\text{mov},1}-r_{x,\text{mov},7}<0 \end{cases} \quad, \quad \text{(S3.13)}$$

where an unwrapping correction was applied for angular transitions around $3\pi/2$ and the average value resulting from Equation S3.13 during the swimming event ($\alpha_{0,\text{head}}$). The angle of attack of the tail was calculated as:

$$\beta_{\text{tail}} = \begin{cases} \arccos\left(\frac{r_{x,\text{tail}}v_{x,\text{tail}}+r_{y,\text{tail}}v_{y,\text{tail}}}{r_{\text{tail}}v_{\text{tail}}}\right) & \text{if } \mathbf{v}_{\perp,\text{tail}} \text{ points to left} \\ -\arccos\left(\frac{r_{x,\text{tail}}v_{x,\text{tail}}+r_{y,\text{tail}}v_{y,\text{tail}}}{r_{\text{tail}}v_{\text{tail}}}\right) & \text{if } \mathbf{v}_{\perp,\text{tail}} \text{ points to right} \end{cases} \quad, \quad \text{(S3.14)}$$

where $r_{x,\text{tail}}$ and $r_{y,\text{tail}}$ are the components of the direction vector of the tail $\mathbf{r}_{\text{tail}}$, which was defined to point from segmental centre 50 to segmental centre 48. Similarly, $v_{x,\text{tail}}$ and $v_{y,\text{tail}}$ are the components of the velocity vector of the tail $\mathbf{v}_{\text{tail}}$, defined as the velocity

---

[1] Alternatively, we can first expand and rewrite Equation S3.12 before numerical integration: $\alpha_{\text{body}} = \sum_i \int_{t_0}^{t} \frac{J_{\text{CoM},i}}{J_{\text{body}}}\omega_{\text{CoM},i}\,dt - \alpha_{0,\text{body}}$. Integration by parts gives: $\alpha_{\text{body}} = \sum_i \frac{J_{\text{CoM},i}}{J_{\text{body}}}\alpha_{\text{CoM},i} - \sum_i \int_{t_0}^{t} \left(\frac{J_{\text{CoM},i}}{J_{\text{body}}}\right)' \alpha_{\text{CoM},i}\,dt - \alpha_{0,\text{body}}$, where the prime denotes the first derivative with respect to time, and $\alpha_{\text{CoM},i}$ is the integral of $\omega_{\text{CoM},i}$. The equation can be expanded as: $\alpha_{\text{body}} = \sum_i \frac{J_{\text{CoM},i}}{J_{\text{body}}}\alpha_{\text{CoM},i} - \sum_i \int_{t_0}^{t} \alpha_{\text{CoM},i}\frac{\dot{J}_{\text{CoM},i}J_{\text{body}}-J_{\text{CoM},i}\dot{J}_{\text{body}}}{J_{\text{body}}^2}\,dt - \alpha_{0,\text{body}}$. By ignoring the relatively small second term at the right-hand-side, we obtain: $\alpha_{\text{body}} \approx \sum_i \frac{J_{\text{CoM},i}}{J_{\text{body}}}\alpha_{\text{CoM},i} - \alpha_{0,\text{body}}$. With this simplification, the instantaneous body angle α_{body} is computed by dividing the sum of the products of $\alpha_{\text{CoM},i}$ and $J_{\text{CoM},i}$ along the body by J_{body}. Thus, the relative contribution of segment i to α_{body} is proportional to $J_{\text{CoM},i}$. We did not adopt this method because it requires implementation of a relatively cumbersome unwrapping procedure.

of segmental centre 49. Furthermore, $\mathbf{v}_{\perp,\text{tail}}$ is the perpendicular component of $\mathbf{v}_{\text{tail}}$ to $\mathbf{r}_{\text{tail}}$. The words left and right in Equation S3.14 refer to the left and right side of the larva.

Following Newton's second law, body torque about the CoM is equal to the rate of change of angular momentum (Equation S3.15, which was also used to calculate $\dot{\omega}_{\text{body}}$). For the considered planar motions, we computed body torque about the CoM as a summation of the inertial torque components over all body segments:

$$\tau_{\text{body}} = \sum_i \frac{\mathrm{d}\left(J_{\text{CoM},i}\,\omega_{\text{CoM},i}\right)}{\mathrm{d}t} = \sum_i \dot{J}_{\text{CoM},i}\,\omega_{\text{CoM},i} + J_{\text{CoM},i}\,\dot{\omega}_{\text{CoM},i}, \quad \text{(S3.15)}$$

where we ignored the small contribution of the additional rotations of the individual body segments around their vertical central axes. We computed also the inertial torque per unit length along the body (with respect to the CoM) to explore the spatio-temporal contributions to τ_{body} along the body:

$$\tau_{\text{body},i}^* = \sum_i \frac{\dot{J}_{\text{CoM},i}\,\omega_{\text{CoM},i} + J_{\text{CoM},i}\,\dot{\omega}_{\text{CoM},i}}{\Delta\ell_i}, \quad \text{(S3.16)}$$

where $\Delta\ell_i$ is the length of segment i.

The inertial body torque about the CoM can also be written as:

$$\tau_{\text{body}} = \frac{\mathrm{d}\left(J_{\text{body}}\omega_{\text{body}}\right)}{\mathrm{d}t} = J_{\text{body}}\dot{\omega}_{\text{body}} + \omega_{\text{body}}\dot{J}_{\text{body}}. \quad \text{(S3.17)}$$

This torque is equal to the torque exerted on the body by the surrounding fluid. From this equation, we derived the angular acceleration of the body:

$$\dot{\omega}_{\text{body}} = \frac{\tau_{\text{body}} - \omega_{\text{body}}\dot{J}_{\text{body}}}{J_{\text{body}}}. \quad \text{(S3.18)}$$

This approach is an alternative for the computation of the angular acceleration by differentiation of ω_{body} (obtained via Equation S3.11) that might be less prone to errors, because of summation along the body used to obtain τ_{body}.

To explore which portions of the body might contribute most to the net torques on the body, we estimated velocity-based torques per unit length ('dynamic pressure torque') along the body that include the density of water ρ_{water}, the local height of the body h_i, the velocity components perpendicular to the body $\mathbf{v}_{\perp,i}$, and the position vector from CoM to the location of interest along the body:

$$\tau_{\text{dynp},i}^* = \frac{1}{2}\,\rho_{\text{water}}\,c_{\text{dynp},i}\,h_i\,\mathbf{r}_{\text{mov},i} \times \left(-||\mathbf{v}_{\perp,i}||\mathbf{v}_{\perp,i}\right), \quad \text{(S3.19)}$$

where i in the subscript refers to the location on the body. The value of the coefficient $c_{\text{dynp},i}$ was prescribed to increase linearly along the body:

$$c_{\text{dynp},i} = 2.0 + 1.25i/50, \quad \text{(S3.20)}$$

a simplification of Jordan's approach (1992), who made a distinction between cross-sections that are approximately circular in shape and those that are shaped like plates. The simplification appeared to work as well as Jordan's approach, if not better. The contribution to the total body torque was computed by a summation along the fish:

$$\tau_{\text{dynp}} = \sum_{i=2}^{50} \tau_{\text{dynp},i}^* \Delta\ell_i, \tag{S3.21}$$

where the relatively small tip segments were ignored.

Following Jordan (1992), we estimated the torques per unit length due the skin friction:

$$\tau_{\text{fric},i}^* = \frac{1}{2}\rho_{\text{water}}\, c_{\text{fric},i}\, S_i\, \mathbf{r}_{\text{mov},i} \times \left(-||\mathbf{v}_{\|,i}||\mathbf{v}_{\|,i}\right)/\Delta\ell_i, \tag{S3.22}$$

where S_i is the wetted surface of segment i, and $\mathbf{v}_{\|,i}$ the velocity parallel to the fish axis of segment i. We defined $c_{\text{fric},i}$ as:

$$c_{\text{fric},i} = 0.64\mu^{1/2}\left(s_i v_{\|,i}\, \rho_{\text{water}}\right)^{-1/2}, \tag{S3.23}$$

where s_i is the distance along the body axis of segment i from the snout. The contribution to the total body torque due to skin friction of all segments was computed as:

$$\tau_{\text{fric}} = \sum_{i=2}^{50} \tau_{\text{fric},i}^* \Delta\ell_i, \tag{S3.24}$$

where the tip elements were again ignored. Since acceleration-reaction forces might also play a role in the interaction with body and water, we computed the torque per unit length for each of the segments:

$$\tau_{\text{acc},i}^* = \rho_{\text{water}}\pi(0.5h_i)^2\mathbf{r}_{\text{mov},i} \times (-\mathbf{a}_{\perp,i}), \tag{S3.25}$$

where $\mathbf{a}_{\perp,i}$ is the acceleration perpendicular to the fish axis at body segment i. The contribution to the total body torque was computed as:

$$\tau_{\text{acc}} = \sum_{i=2}^{50} \tau_{\text{acc},i}^* \Delta\ell_i, \tag{S3.26}$$

where the small tip elements were ignored.

S3.3.4 Kinetic energy and power of the body

The kinetic energy associated with translation of the CoM was calculated as

$$E_{\text{tr,CoM}} = \frac{1}{2}m_{\text{body}}v_{\text{swim}}^2. \tag{S3.27}$$

The kinetic energy due to rotation of the body segments about the CoM was calculated as

$$E_{\text{rot,body}} = \frac{1}{2} \sum_i \left(J_{\text{CoM},i}\, \omega_{\text{CoM},i}^2 + J_i \omega_i^2 \right), \tag{S3.28}$$

where ω_i is angular velocity of body segment i around the vertical axis through the segmental centre of mass. The first term at the right-hand-side represents rotational energy with respect to the CoM, the second term accounts for rotational energy of the segments about the local vertical axis. This rotational energy of the *deforming* body is a close approximation of what is usually considered internal kinetic energy ($E_{\text{kin,int}} = \frac{1}{2}\sum_i m_i \dot{r}_{\text{mov},i}^2 + J_i\omega_i^2$). The total kinetic energy of the body was calculated as

$$E_{\text{kin,body}} = \frac{1}{2} \sum_i \left(m_i \dot{r}_i^2 + J_i \omega_i^2 \right). \tag{S3.29}$$

The sum of $E_{\text{tr,CoM}}$ and $E_{\text{rot,body}}$ is a close approximation of $E_{\text{kin,body}}$.

The power associated with translation of the CoM was calculated as

$$P_{\text{tr,CoM}} = m_{\text{body}} \ddot{\mathbf{r}}_{\text{CoM}} \cdot \dot{\mathbf{r}}_{\text{CoM}}, \tag{S3.30}$$

which for planar motion reduces to

$$P_{\text{tr,CoM}} = m_{\text{body}} (\ddot{r}_{x,\text{CoM}}\, \dot{r}_{x,\text{CoM}} + \ddot{r}_{y,\text{CoM}}\, \dot{r}_{y,\text{CoM}}). \tag{S3.31}$$

The power associated with rotation of the body about the CoM was calculated as

$$\begin{aligned} P_{\text{rot,body}} &= \sum_i \left\{ \frac{\mathrm{d}\left(J_{\text{CoM},i}\,\omega_{\text{CoM},i}\right)}{\mathrm{d}t} \cdot \omega_{\text{CoM},i} + \frac{\mathrm{d}\left(J_i\omega_i^2/2\right)}{\mathrm{d}t} \right\} \\ &\approx \sum_i \left(\dot{J}_{\text{CoM},i}\,\omega_{\text{CoM},i}^2 + J_{\text{CoM},i}\,\dot{\omega}_{\text{CoM},i} \cdot \omega_{\text{CoM},i} + J_i\dot{\omega}_i \cdot \omega_i \right), \end{aligned} \tag{S3.32}$$

where we ignored the negligibly small term $\sum_i \dot{J}_i\omega_i^2/2$ at the right-hand side of the $\approx$ sign. The total power due to kinetic energy changes of the body was computed as

$$P_{\text{kin,body}} \approx \sum_i \left(m_i \ddot{\mathbf{r}}_i \cdot \dot{\mathbf{r}}_i + J_i \dot{\omega}_i \cdot \omega_i \right) \tag{S3.33}$$

where we again ignored the term $\sum_i \dot{J}_i\omega_i^2/2$. The power of the body $P_{\text{kin,body}} \approx P_{\text{tr,CoM}} + P_{\text{rot,body}}$. Specific energies and powers were computed by dividing the respective values by body mass (designated, respectively, as E^* and P^*).

S3.3.5 Computation of confidence intervals

To calculate confidence intervals for the coefficients from the curve fitting procedure (main text, §3.2.5), we used a Monte Carlo approach implemented in Matlab (see chapter 17 in

(Motulsky and Christopoulos, 2003) for a detailed discussion of this approach). We first performed a scaled total-least-squares-fit to obtain the optimal fit for the data points. We then calculated the standard deviations with respect to the curve for both variables, which were used to generate $10,000$ simulated data sets with the same number of points as the original, and fitted these with the same total-least-squares-procedure. The 2.5^{th} percentile and the 97.5^{th} percentile of the resulting coefficient distributions from all simulated data sets were then selected as the boundaries of the 95% confidence interval, except for constant c_1 in the fit $St = c_1 Re^{c_2} + c_3$ (see data for Fig. 3.7G in Table S3.3), where a single sided 95% confidence interval was applied.

S3.4 Supplementary results

The measured shape of a 2 dpf and a 5 dpf fish larva is shown in Fig. S3.3A,B. The mass of the body increases from 2 to 4 dpf, while the relative position of the CoM along the body is constant (Fig. S3.3C).
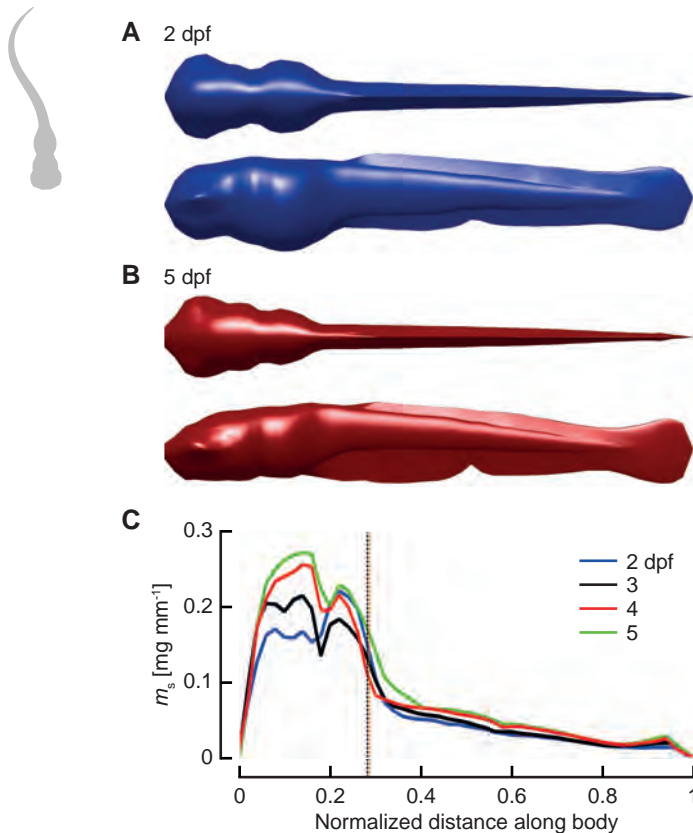
Figure S3.3: Morphology and mass distribution. (A–B) Dorsal and lateral views of reconstructed larval shapes at 2 and 5 dpf. (C) Mass per unit length and position of CoM (dotted vertical lines) along the body of four larval stages.

Fish increase their swimming speed by increasing the product of fA_{tail} as illustrated by the scatter plots of Fig. S3.4.
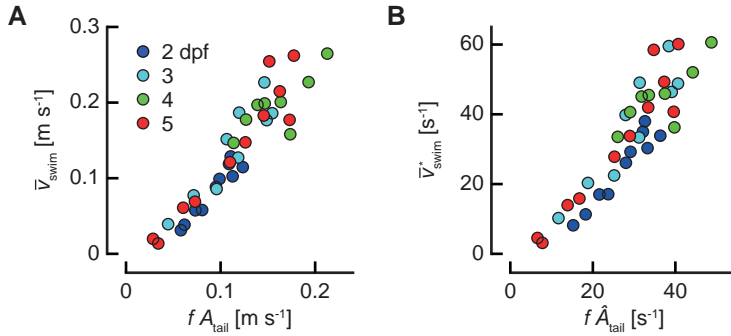
Figure S3.4: (A) Scatter plot of mean swimming velocity $\bar{v}_{\text{swim}}$ against fA_{tail} of fish larvae aged 2–5 dpf. (B) Scatter plot of specific mean swimming velocity $\bar{v}^*_{\text{swim}}$ against $f\hat{A}_{\text{tail}}$.

Two supplementary movies (play back rate 6 frames s^{-1}, original frame rate of high-speed video 1000 frames s^{-1}) illustrate the motion and net torque fluctuations on the body of a 5 dpf fish larva (same event as shown in Fig. 3.1 of the main text; duration of event 31.5 ms). Movie S1 shows the swimming motion in the earth-bound frame and movie S2 shows the same event in the moving frame with a fixed location of the CoM.

Tables S3.2–S3.4 show the values found of the coefficients (including the associated confidence intervals), as well as the ratio of the square root of the sum of the squared perpendicular distances to the fitted curve for the non-linear fit of the curves shown in Figs 3.6–3.9 and a linear fit (where applicable).

Additional data underlying this paper can be found at:

`https://doi.org/10.1371/journal.pone.0146682.s002`

Table S3.2: Values of the coefficients for the linear fits ($y = c_2 x + c_3$) of Fig. 3.6C,D and those for the second order polynomial fits ($y = c_1 x^2 + c_2 x + c_3$) of Fig. 3.6A,B of the main text. The curve fits of Fig. 3.6A,B were constrained to go through the origin. Confidence intervals are indicated by the values between []. Distances were expressed in meters and time in seconds to compute the coefficients. Column 5 shows the ratio of the square root of the sum of squared perpendicular distances to the fitted curve for the non-linear fit and a linear fit (where applicable). The lower the ratio, the more important the non-linear component of the fit. A high scatter in the data (which is partly due to variance in the behaviour of the fish and partly due to measurements errors) may increase the computed ratio.

Figure panel	c_1	c_2	c_3	Ratio
3,6A	$3.7331 \cdot 10^{-5}$ $[2.9158 \cdot 10^{-5}, 4.4634 \cdot 10^{-5}]$	$-6.2132 \cdot 10^{-4}$ $[-1.1201 \cdot 10^{-3}, -5.9165 \cdot 10^{-5}]$	0 $[0,0]$	0.8771
3,6B	$7.8015 \cdot 10^{-3}$ $[6.3010 \cdot 10^{-3}, 9.1511 \cdot 10^{-3}]$	$-5.2255 \cdot 10^{-2}$ $[-1.4578 \cdot 10^{-1}, 5.2535 \cdot 10^{-2}]$	0 $[0,0]$	0.8910
3,6C, total	—	$1.2421 \cdot 10^{-5}$ $[9.4281 \cdot 10^{-6}, 2.2036 \cdot 10^{-5}]$	$8.8016 \cdot 10^{-4}$ $[2.2119 \cdot 10^{-4}, 1.0957 \cdot 10^{-3}]$	—
3,6C, 2 & 3 dpf	—	$5.0497 \cdot 10^{-7}$ $[-7.1788 \cdot 10^{-6}, 8.3690 \cdot 10^{-6}]$	$1.4770 \cdot 10^{-3}$ $[9.5474 \cdot 10^{-4}, 2.0154 \cdot 10^{-3}]$	—
3,6C, 4 & 5 dpf	—	$1.4610 \cdot 10^{-5}$ $[1.0370 \cdot 10^{-5}, 2.1661 \cdot 10^{-5}]$	$9.1177 \cdot 10^{-4}$ $[4.1919 \cdot 10^{-4}, 1.2204 \cdot 10^{-3}]$	—
3,6D, total	—	$2.1980 \cdot 10^{-3}$ $[1.4390 \cdot 10^{-3}, 4.0392 \cdot 10^{-3}]$	$2.8189 \cdot 10^{-1}$ $[1.5715 \cdot 10^{-1}, 3.3486 \cdot 10^{-1}]$	—
3,6D, 2 & 3 dpf	—	$-7.2696 \cdot 10^{-5}$ $[-2.3014 \cdot 10^{-3}, 2.0720 \cdot 10^{-3}]$	$4.2819 \cdot 10^{-1}$ $[2.8104 \cdot 10^{-1}, 5.7989 \cdot 10^{-1}]$	—
3,6D, 4 & 5 dpf	—	$3.3355 \cdot 10^{-3}$ $[2.3667 \cdot 10^{-3}, 4.9440 \cdot 10^{-3}]$	$2.0968 \cdot 10^{-1}$ $[9.7112 \cdot 10^{-2}, 2.8030 \cdot 10^{-1}]$	—

Table S3.3: Values of the coefficients for the St-Re and Sw-Re fits (Fig. 3.7G: $St = c_1 Re^{c_2} + c_3$; Fig. 3.7H: $Sw = c_1 Re^{c_2} + c_3 Re$), and those for the second order polynomial fits ($y = c_1 x^2 + c_2 x + c_3$; Fig. 3.7A–F) of the main text. Confidence intervals are indicated by the values between [ ]. Angles were expressed in radians, distances in meters and time in seconds to compute the coefficients. Column 5 shows the ratio of the square root of the sum of squared perpendicular distances to the fitted curve for the non-linear fit and a linear fit. The lower the ratio, the more important the non-linear component of the fit. A high scatter in the data (which is partly due to variance in the behaviour of the fish and partly due to measurements errors) may increase the computed ratio.

Figure panel	c_1	c_2	c_3	Ratio
3.7A	$5.5768 \cdot 10^{-7}$, $[4.4454 \cdot 10^{-7}, 6.8118 \cdot 10^{-7}]$	$-2.6908 \cdot 10^{-8}$, $[-5.3662 \cdot 10^{-8}, -2.0937 \cdot 10^{-9}]$	$1.1678 \cdot 10^{-9}$, $[1.6300 \cdot 10^{-10}, 2.1881 \cdot 10^{-9}]$	0.6939
3.7B	2.5535×10^{1}, $[1.0552 \times 10^{1}, 3.8976 \times 10^{1}]$	-2.9964, $[-1.2770 \times 10^{1}, 9.0826]$	2.0094, $[-1.7394 \cdot 10^{-1}, 3.6139]$	0.9097
3.7C	$1.5398 \cdot 10^{-14}$, $[1.1841 \cdot 10^{-14}, 1.9493 \cdot 10^{-14}]$	$2.0120 \cdot 10^{-12}$, $[-2.6979 \cdot 10^{-12}, 6.3142 \cdot 10^{-12}]$	$2.5309 \cdot 10^{-10}$, $[-7.0840 \cdot 10^{-10}, 1.2047 \cdot 10^{-9}]$	0.7483
3.7D	$-5.4913 \cdot 10^{-6}$, $[-1.2272 \cdot 10^{-5}, -2.0426 \cdot 10^{-6}]$	$1.3703 \cdot 10^{-2}$, $[9.0251 \cdot 10^{-3}, 2.4130 \cdot 10^{-2}]$	$8.8983 \cdot 10^{-1}$, $[-2.4308, 2.2085]$	0.9498
3.7E	-2.7362, $[-9.1224, 2.9376]$	3.0374, $[1.5548, 4.9574]$	$5.0523 \cdot 10^{-2}$, $[-7.5670 \cdot 10^{-2}, 1.3303 \cdot 10^{-1}]$	0.9953
3.7F	1.2638, $[4.7988 \cdot 10^{-1}, 1.9316]$	$1.0444 \cdot 10^{-1}$, $[-3.8221 \cdot 10^{-1}, 7.4434 \cdot 10^{-1}]$	$4.1930 \cdot 10^{-2}$, $[-7.9665 \cdot 10^{-2}, 1.2225 \cdot 10^{-1}]$	0.9097
3.7G	4.1293×10^{1}, $[-, 3.4060 \times 10^{2}]$	$-7.4121 \cdot 10^{-1}$, $[-1.2502, -3.8940 \cdot 10^{-1}]$	$5.2533 \cdot 10^{-1}$, $[8.7694 \cdot 10^{-2}, 7.0233 \cdot 10^{-1}]$	0.3963
3.7H	4.1293×10^{1}, $[-, 3.4060 \times 10^{2}]$	$2.5879 \cdot 10^{-1}$, $[-2.5020 \cdot 10^{-1}, 6.1060 \cdot 10^{-1}]$	$5.2533 \cdot 10^{-1}$, $[8.7694 \cdot 10^{-2}, 7.0233 \cdot 10^{-1}]$	–

3

Table S3.4: Values of the coefficients for the second order polynomial fits ($y = c_1x^2 + c_2x + c_3$) of Figs 3.8 and 3.9 of the main text. Confidence intervals are indicated by the values between [ ]. Angles were expressed in radians, distances in meters and time in seconds to compute the coefficients. Column 5 shows the ratio of the square root of the sum of squared perpendicular distances to the fitted curve for the non-linear fit and a linear fit (where applicable). The lower the ratio, the more important the non-linear component of the fit. A high scatter in the data (which is partly due to variance in the behaviour of the fish and partly due to measurements errors) may increase the computed ratio.

Figure panel	c_1	c_2	c_3	Ratio
3.8A, max.	$6.0855 \cdot 10^{-1}$ $[5.3999 \cdot 10^{-1},\ 6.8057 \cdot 10^{-1}]$	$1.6375 \cdot 10^{-2}$ $[4.8731 \cdot 10^{-6},\ 3.2099 \cdot 10^{-2}]$	$-2.7306 \cdot 10^{-4}$ $[-9.6686 \cdot 10^{-4},\ 4.1121 \cdot 10^{-4}]$	0.4516
3.8A, mean	$5.0519 \cdot 10^{-1}$ $[4.9969 \cdot 10^{-1},\ 5.1070 \cdot 10^{-1}]$	$3.4114 \cdot 10^{-4}$ $[-9.1169 \cdot 10^{-4},\ 1.5783 \cdot 10^{-3}]$	$-3.0270 \cdot 10^{-6}$ $[-5.1533 \cdot 10^{-5},\ 4.7094 \cdot 10^{-5}]$	0.0475
3.8B, max.	$4.8040 \cdot 10^{-1}$ $[3.5621 \cdot 10^{-1},\ 6.1953 \cdot 10^{-1}]$	$-2.7568 \cdot 10^{-2}$ $[-5.7679 \cdot 10^{-2},\ -1.1980 \cdot 10^{-4}]$	$1.2503 \cdot 10^{-3}$ $[1.0950 \cdot 10^{-4},\ 2.4146 \cdot 10^{-3}]$	0.7372
3.8B, mean	$2.9006 \cdot 10^{-1}$ $[2.2307 \cdot 10^{-1},\ 3.6437 \cdot 10^{-1}]$	$-1.2209 \cdot 10^{-2}$ $[-2.8373 \cdot 10^{-2},\ 2.4745 \cdot 10^{-3}]$	$5.2856 \cdot 10^{-4}$ $[-7.7283 \cdot 10^{-5},\ 1.1486 \cdot 10^{-3}]$	0.7158
3.9A, total	4.1174×10^{2} $[3.2366 \times 10^{2},\ 5.0926 \times 10^{2}]$	-2.7124×10^{1} $[-4.7733 \times 10^{1},\ -8.0980]$	$6.6257 \cdot 10^{-1}$ $[-1.0110 \cdot 10^{-1},\ 1.4420]$	0.6798
3.9A, trans.	3.1958×10^{2} $[2.4056 \times 10^{2},\ 4.0554 \times 10^{2}]$	-2.4722×10^{1} $[-4.2851 \times 10^{1},\ -7.8713]$	$6.2836 \cdot 10^{-1}$ $[-5.8459 \cdot 10^{-2},\ 1.3195]$	0.6739
3.9A, rot.	2.2367×10^{2} $[1.7217 \times 10^{2},\ 2.7734 \times 10^{2}]$	-1.9902×10^{1} $[-3.1253 \times 10^{1},\ -8.5698]$	$6.0527 \cdot 10^{-1}$ $[1.2808 \cdot 10^{-1},\ 1.0595]$	0.6507

References

Jordan, C. E. (1992). A model of rapid-start swimming at intermediate Reynolds number: undulatory locomotion in the chaetognath *Sagitta elegans*. *J. Exp. Biol.* **163**, 119–137.

Motulsky, H. J. and Christopoulos, A. Fitting models to biological data using linear and nonlinear regression. A practical guide to curve fitting. www.graphpad.com.

Müller, U. K., Van den Boogaart, J. G. M. and Van Leeuwen, J. L. (2008). Flow patterns of larval fish: undulatory swimming in the intermediate flow regime. *J. Exp. Biol.* **211**, 196–205.

Müller, U. K. and Van Leeuwen, J. L. (2004). Swimming of larval zebrafish: ontogeny of body waves and implications for locomotory development. *J. Exp. Biol.* **207**, 853–868.

Woltring, H. J. (1986). A Fortran package for generalized, cross-validatory spline smoothing and differentiation. *Adv. Eng. Softw.* **8**, 104–113.

3
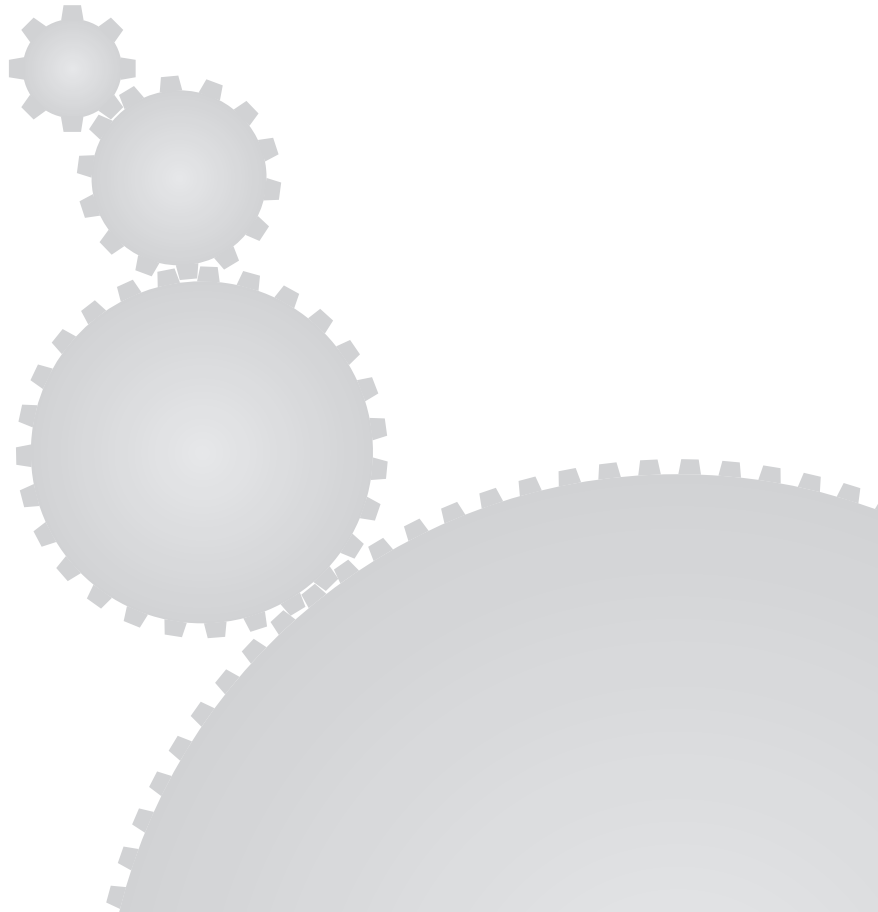
Chapter 4

Automated reconstruction of three-dimensional fish motion, forces, and torques

Cees J. Voesenek[1], Remco P. M. Pieters[1], Johan L. van Leeuwen[1]

[1] Experimental Zoology Group, Wageningen University & Research, Wageningen, The Netherlands

Abstract

Fish can move freely through the water column and make complex three-dimensional motions to explore their environment, escape or feed. Nevertheless, the majority of swimming studies is currently limited to two-dimensional analyses. Accurate experimental quantification of changes in body shape, position and orientation (swimming kinematics) in three dimensions is therefore essential to advance biomechanical research of fish swimming. Here, we present a validated method that automatically tracks a swimming fish in three dimensions from multi-camera high-speed video. We use an optimisation procedure to fit a parameterised, morphology-based fish model to each set of video images. This results in a time sequence of position, orientation and body curvature. We post-process this data to derive additional kinematic parameters (e.g. velocities, accelerations) and propose an inverse-dynamics method to compute the resultant forces and torques during swimming. The presented method for quantifying 3D fish motion paves the way for future analyses of swimming biomechanics.

4.1 Introduction

Quantification of swimming kinematics is essential to perform biomechanical analyses of fish locomotion. Kinematic parameters, such as tail-beat frequency or amplitude (Hunter, 1972; Eloy, 2012), are frequently used to express changes in swimming behaviour. More detailed descriptions of the fish motion are required to perform mechanism-oriented studies into propulsion and manoeuvring, using for example computational fluid dynamics techniques (Borazjani and Sotiropoulos, 2009; Li et al., 2012). Many types of fish motion are essentially three-dimensional, as fish are free to move through the water column to explore their environment, escape predators, or hunt for prey. Unless relatively rare cases of single-plane motion are considered, it is necessary to quantify swimming kinematics in three dimensions.

Experimental data on swimming motion are commonly obtained in the form of high-speed videographs (Liao et al., 2003; Müller and Van Leeuwen, 2004; Green et al., 2011), from which the motion and/or kinematic variables are extracted. Historically, this has often been done by manual digitisation (Müller and Van Leeuwen, 2004; Tytell and Lauder, 2002; MacIver and Nelson, 2000; Kasapi et al., 1993). This process is tedious, time consuming and may introduce a user-dependent bias, e.g. the results may differ consistently between individual digitisers. An automated approach is therefore preferred, allowing higher data throughput and consistency compared to manual digitisation.

Automated fish tracking methods have been proposed in 2D (Fontaine et al., 2008; Xiong and Lauder, 2014), but the assumption of two-dimensional motion restricts application to a narrow range of swimming behaviour. A method was developed (Butail and Paley, 2012) that allows tracking of multiple fish in three dimensions. However, it does not support rolling motion, and describes the fish centreline with relatively low accuracy using a quadratic polynomial in lateral direction, and a quartic polynomial in longitudinal direction. To our knowledge, an automated method to reconstruct arbitrary 3D motion

(translation, pitch, roll and yaw) and body curvature with sufficiently high accuracy in all variables to analyse dynamics (i.e. forces and torques) is still lacking.

Resultant forces and torques can be reconstructed from kinematic data, under specific assumptions. This approach, commonly known as inverse dynamics, has been used often for terrestrial and aerial locomotion (Koopman et al., 1995; Muijres et al., 2015), but it has rarely been applied to analyse fish swimming. Resultant forces and torques were computed for swimming zebrafish larvae in 2D (Van Leeuwen et al., 2015). Other studies (Hess and Videler, 1984; Cheng and Blickhan, 1994) compute swimming forces and bending moments along the fish body, assuming (simplified) fluid-dynamic models. This requires assumptions to be made on the fluid motion, that may not hold for low and intermediate Reynolds number flow regimes, or complex manoeuvres with strong vortex interactions (Li et al., 2014). We calculate the resultant 3D forces and torques on the body directly from the motion of the fish, only assuming a mass distribution based on its shape. To our knowledge, three-dimensional tracking has never been used to calculate resultant forces and torques to study the dynamics of fish swimming and manoeuvring.

In this article, we describe a method that allows accurate tracking of the fish's body position, orientation and deformation in 3D space, and reconstruction of resultant forces and torques from high-speed video sequences from two or more arbitrary viewpoints. We use an optimisation procedure to minimise differences between a parameterised model fish and fish silhouettes from segmented high-speed video frames. The method is validated using synthetically generated data, and demonstrated on three-camera synchronised high-speed video of a three day old zebrafish larva.

4.2   Materials and Methods

Our tracking method, outlined in Fig. 4.1 and implemented in MATLAB (R2013a; version 8.1, The Mathworks, Natick, Massachusetts, USA), is based on the creation of an *in silico* representation of the videography experiment: we create a virtual, parameterised fish and project it onto virtual cameras. We find the fish's position, orientation and deformation by minimising the difference between the virtual and the actual images using an optimisation algorithm. We post-process these kinematics to yield resultant forces and torques on the body, and other quantities of interest. For a full mathematical treatment of the methods, we refer to the Appendix.

4.2.1   Creating the parameterised fish model

To represent the fish *in silico*, we create a three-dimensional virtual representation of the fish. To this end, we construct a 3D model of the outer surface of the fish. The motion and deformation of this model is parameterised based on the typical motion of body and caudal fin swimmers.

We assume that: (1) The fish bends its body in lateral direction only (Hughes and Kelly, 1996; Butail and Paley, 2012; Van Leeuwen et al., 2015), resulting in a single deformation plane. (2) Transverse sections remain perpendicular to the deformed centre line; only pure
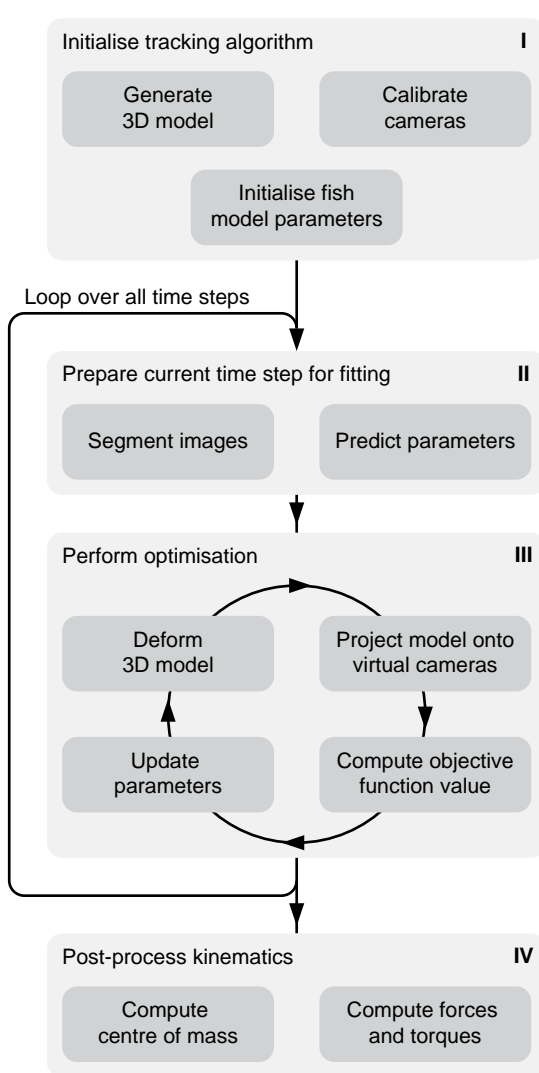
Figure 4.1: Schematic overview of the tracking method. We provide initial information by creating a 3D model of the fish, calibrating the cameras and initialising the fish position by clicking the snout and tail position in the images from every camera (I). For every time step, we segment the fish in the images from all cameras and predict the fish position, orientation and body curvature based on previous frames (II). The predicted parameters are then used to initialise an optimisation algorithm. This algorithm finds the set of parameters (body curvature, position and orientation) that minimises the difference with the high-speed video frames (III). Once the optimisation has been performed for all frames, we compute the centre of mass and, by inverse dynamics, the resultant forces and torques over time (IV).

bending is applied to the fish model. This allows us to describe the body deformation by a single parameter: the curvature along the centre line (Van Leeuwen et al., 2015). (3) There is no passive or active deformation of the medial fin fold relative to the body. Because the fin fold has a small mass compared to the trunk of the fish, its deformation will only be a minor contribution to the resultant forces and torques from inverse dynamics. (4) The motion of the pectoral fins is ignored in the present version of the 3D fish tracker. For zebrafish larvae, the pectoral fins have been suggested to play a minor role in propulsion during slow swimming (Green et al., 2011), and often remain adducted during fast swimming (Thorsen et al., 2004). (5) The 3D position and orientation (roll, pitch, yaw) of the head are completely unconstrained.
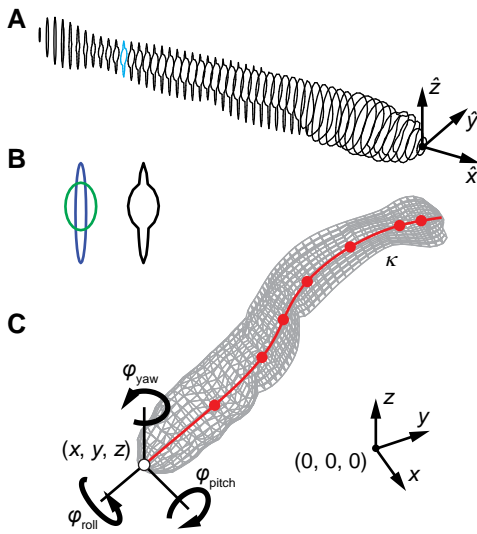
Figure 4.2: Construction of the *in silico* zebrafish. (A) A series of cross-sectional shapes is combined into a three-dimensional body model. The cross-section indicated in blue is shown in more detail in (B). (B) Generation of cross-section in the tail region: two 'components', body (green) and fin (blue), with different cross-sectional shapes are merged into a single cross-section (black). (C) Parameterisation (position, head orientation and body curvature) of the three-dimensional body model. The position of the tip of the snout is described by the coordinates x, y, z, and head orientation by the three Tait-Bryan angles $\varphi_{\text{roll}}, \varphi_{\text{pitch}}, \varphi_{\text{yaw}}$. Body deformation is parameterised by prescribing a curvature κ along the centreline (red) at a number of control points, indicated by the dots; the body surface is deformed along with the centreline, under the assumption that the transverse sections stay plane, and perpendicular to the centreline.

We describe the three-dimensional surface of the fish by a longitudinal series of transverse sections (Van Leeuwen et al., 2015) (see Fig. 4.2A). This approach allows large flexibility in the body shapes to be described, and makes it relatively easy to create new three-dimensional surface models. Furthermore, deforming the body model under the assumption of pure bending becomes a simple matter of rotating and translating cross-sections.

For our case of the larval zebrafish, we distinguish three 'components': trunk, eyes and medial fin fold. The cross-sectional shape of these components is described separately by respectively cubic splines, superellipses (generalised ellipses with an exponent $\neq 2$) and ordinary ellipses. To determine the parameters of each cross-sectional shape at different points along the body, we photograph zebrafish larvae laterally and dorsally using a digital camera (DP50, Olympus, Japan) mounted on a microscope (Stemi SV11, Zeiss, Germany), and then digitise these photos using a custom MATLAB R2013a program.

At each point along the fish, the three components are merged into a single cross-section by finding their outermost contour (see Fig. 4.2B). All merged cross-sectional shapes are generated with the same number of circumferential points, allowing us to connect them into quadrilateral faces and thus create a 3D surface model. Because we assume that cross-sections remain plane and perpendicular to the fish's centreline, we can easily deform the model based solely on the centreline position.

The head motion is described by its three-dimensional position and orientation (roll, pitch, yaw). This also prescribes the orientation of the plane in which the fish bends. The body deformation is described by the local body curvature along the centre line in this deformation plane. We reconstruct curvature rather than position or local angle to allow applications of the method to use higher order spatial derivatives. We prescribe the curvature to be zero in the stiff head region of the fish, where we expect no deformation (the anterior 10% of a larval zebrafish). We define a relatively small number of control points (7

for the model of the zebrafish larva) where curvature is prescribed, which we interpolate to all nodes of the high-resolution body model using a cubic spline. This reduces computational load during tracking, while enabling us to capture arbitrary curvature distributions along the fish.

We calculate the deformed surface of the fish from a set of parameters (i.e. head position and orientation, and body curvature) and the 3D model (see Fig. 4.2C). First, we calculate the deformed shape of the body based in a coordinate system attached to the head, with the x-coordinate in caudo-rostral direction. The interpolating spline fit describes the curvature along the body as a third-order piecewise polynomial, which we integrate analytically to obtain the local angle of the centreline. The shape of the centreline is constructed by rotating each subsequent segment by this local angle. Each cross-section is then translated with the centreline, and rotated by the local angle to create the deformed surface model.

This model is subsequently rotated in 3D space by multiplication with a rotation matrix, created using the roll, pitch and yaw angles. Finally, it is translated to the specified snout position. The result is a three-dimensional surface representing the fish shape for the prescribed set of parameters.

4.2.2 Pre-processing video frames

The main input for the tracking algorithm is a set of high-speed video images of a swimming fish from two or more cameras. In order to track the fish, these images must be segmented into fish silhouette pixels and background pixels. The result of this procedure is a binary image, with background pixels set to 0 and fish pixels set to 1.

The specific implementation of the segmentation procedure is strongly dependent on the video setup. We shortly outline the procedure for our example case of larval zebrafish, which was implemented in MATLAB R2013a. First, we correct the video sequence for intensity fluctuations originating from the incandescent light sources. We obtain a correction factor for these fluctuations by calculating the average background intensity, and normalising it by its maximum value. Because the zebrafish larvae have translucent fins with low greyscale contrast to the background, we cannot use intensity thresholding. Instead, we calculate the magnitude of the spatial gradient, threshold this at a specified value and fill all holes; this results in a white silhouette of the fish on a black background.

4.2.3 Fitting the body model

The goal of the tracking algorithm is to find the set of fish model parameters that corresponds best to the set of video frames. To assess how well a set of parameters matches a set of video frames, we compare a simulated image of the fish to the segmented video frames. This comparison can be expressed in a single scalar, that is low for a good fit, and high for a bad fit.

To find the set of fish parameters that minimises this number at every time step, we use an optimisation algorithm. However, we cannot directly apply the optimisation to

the goodness-of-fit term, because the problem of reconstructing a three-dimensional shape from a small number of viewpoints is ill-posed. A unique solution may not exist and the optimal solution may vary strongly with small changes in the projections. We therefore introduce a regularising term that ensures smoothness of the body curvature, and thus reduces the risk of local minima with unrealistic body curvature. The regularised objective function f_{tot} is therefore given by

$$f_{\text{tot}}(\mathbf{\Omega}) = f_{\text{GoF}}(\mathbf{\Omega}) + f_{\text{reg}}(\mathbf{\Omega}), \tag{4.1}$$

where $\mathbf{\Omega}$ is the set of fish parameters, f_{GoF} is the term expressing the goodness of fit and f_{reg} is the regularising term. The solution that minimises this function is selected to represent the state of the fish in the current time step.

The goodness-of-fit term is computed by determining the overlap between projections of the virtual fish and the segmented high-speed video images in the current time step. We generate these projections with virtual cameras at calibrated positions and orientations of the experimental cameras (using a bundle adjustment approach for the zebrafish experiment). The projections of the three-dimensional body model onto the virtual image planes are overlayed onto the segmented video images. We count all non-zero pixels in this combined image, and subtract the number of overlapping non-zero pixels. The total number of pixels that differ between all virtual-actual image pairs is our goodness-of-fit term.

The regularising term is defined to become larger if the body curvature is less 'smooth'; this suppresses sets of parameters with unrealistically steep curvature gradients. We compute this term by integrating the squared curvature gradient along the fish, weighted with a function that is high near the head and small near the tail:

$$f_{\text{reg}} = \int_0^1 w(s) \left(\frac{\mathrm{d}\kappa(s)}{\mathrm{d}s} \right)^2 \mathrm{d}s, \tag{4.2}$$

where s is a normalised parameter along the fish midline, $w(s)$ is the weighting function of the form $c_0\, e^{-c_1 s}$ with constants c_0 and c_1, and $\kappa(s)$ is the local curvature. Due to the weighting function, the regularisation penalises curvature gradients near the head more strongly than near the tail, corresponding to the expected deformation of the fish. The final objective function is computed by summing the goodness-of-fit term and the regularising term.

The objective function (Equation 4.1) is minimised using the Nelder-Mead (or downhill simplex) algorithm (Nelder and Mead, 1965; Lagarias et al., 1998), which marches an N-dimensional simplex with $N+1$ vertices through optimisation space to find an optimal set of parameters. We initialise the algorithm by extrapolating from the solution in previous time steps, or from a manual indication of the snout and tail tip in the first time step. A rough optimisation is performed from this initial solution, after which we restart the optimisation with ten-fold reduced tolerances. If the objective function differs more than a threshold value from the value in the previous frame, additional optimisations are

performed from a randomised initial condition near the previous solution, until the difference is sufficiently small. Applying this procedure to all time steps, we get a description of the state of the fish in terms of the model parameters for the complete video sequence.

4.2.4 Post-processing and inverse dynamics

The result from the fish tracker is a time series of head positions, head orientations and body curvatures, sampled at every frame in the high-speed video. These data can be post-processed to compute derived quantities of interest (velocities, accelerations, forces, and torques) to answer biological questions on the mechanics of swimming.

Computing these derived quantities involves the computation of (second) derivatives, requiring smoothing of the solution to ensure accurate results. We apply a penalised least squares approach (Eilers, 2003) to the raw model parameters—no further smoothing is applied to the derived quantities. A fourth order derivative regularisation term is used, ensuring that all second time derivatives are smooth (Stickel, 2010). The smoothing parameter is chosen by visual evaluation of the resulting derived quantities, such that unrealistic high-frequency components disappear and relevant low-frequency information is retained. The derivatives are computed of the smoothed data using second order finite differences.

The resultant force on the fish body can be computed from the centre of mass (CoM) acceleration and total fish mass. Computation of both quantities requires knowledge of the mass distribution. By assuming a constant density (of water) of the fish volume, the surface description can be used as a mass distribution. We triangulate the optimised surface, and compute the CoM position and fish mass with a method for general polyhedra (Dobrovolskis, 1996). We calculate the acceleration of the CoM by double differentiation of its 3D position, yielding the resultant force vector by multiplication with the fish mass according to Newton's second law. This approach reconstructs the resultant of all external fluid forces acting on the body. Note that the added mass of the surrounding water contributes to these fluid forces, and does not have to be implemented explicitly.

Calculating the resultant torque on a rigid body can be done in a similar manner to the force reconstruction: it is equal to the moment of inertia multiplied by the angular acceleration. However, for the case of a swimming fish this is not applicable, since a significant portion of its mass is moving over distances of the same order of magnitude as its body size, causing the moment of inertia to vary significantly (Van Leeuwen et al., 2015). We have developed an alternative approach, where we calculate the total angular momentum of the body by an extension of a previously developed method for calculation of moments of inertia (Dobrovolskis, 1996); see the Appendix for the mathematical background. Taking the time derivative of the total angular momentum $\mathbf{L}$ yields the resultant torque $\boldsymbol{\tau}$ of a three-dimensional, arbitrarily shaped, deforming body:

$$\boldsymbol{\tau} = \rho \, \frac{\mathrm{d}}{\mathrm{d}t} \left\{ \iiint_V \mathbf{r}^*(\mathbf{x}) \times \mathbf{v}^*(\mathbf{x}) \, \mathrm{d}V \right\}, \tag{4.3}$$

where ρ is the fish's mass density, $\mathbf{r}^*$ is the distance vector from the CoM and $\mathbf{v}^*$ is the velocity vector relative to the CoM.

To simplify interpretation of the calculated forces and torques, we express them in a local coordinate system $(x_{\text{fish}}, y_{\text{fish}}, z_{\text{fish}})$, aligned with the deformation plane of the fish and moving with its CoM. In the deformation plane, x_{fish} is aligned with the resultant body angle (Van Leeuwen et al., 2015), which is defined as a local moment of inertia-weighted average angle. Torque vectors in this coordinate system can be interpreted as being respectively 'roll'-, 'pitch'-, 'yaw'-torques. To provide a more intuitive definition of the 'forward' force, we define it in the direction of the CoM velocity vector, in addition to the fish coordinate system.

4.2.5 Larval zebrafish kinematics setup

As an example, we created high-speed videography of a three days post fertilisation zebrafish larva (*Danio rerio* Hamilton 1822). We used a three-camera setup, with one vertical camera (pco.dimax HS4, PCO, Kelheim, Germany; 2000 × 2000 pixels, 75 μs exposure, 500 pixels along the 3.5 mm fish), and a left- and right-facing camera (respectively FASTCAM APX RS and FASTCAM SA5, Photron, Tokyo, Japan; 1024 × 1024 pixels, 33 μs exposure, 250 pixels along the 3.5 mm fish) at $30°$ to horizontal. A macro lens at f/2.8 (105 mm AF Micro-NIKKOR f/2.8D, Nikon, Tokyo, Japan) with 27.5 mm extension tubes was used on all three cameras. The cameras were synchronised with a digital delay pulse generator (9618+, Quantum Composers, Bozeman, Montana, USA), running at 2000 pulses (frames) per second. Approximately 50 larvae were placed in a regular-hexagonal tube (16 mm sides, 80 mm long), positioned such that the optical axes of all cameras were perpendicular to the air-glass-water interface. Parallel light, created by shining a fibre optic cold light source (KL 150 B, Schott AG, Mainz, Germany) through a 250 mm lens (52 mm 250D close-up lens, Canon, Tokyo, Japan), was aligned with the camera axis. This allows for the creation of high contrast shadow images with large depth-of-field (approximately 8 mm for 15×15 mm field of view) at shutter speeds in the order of 50 μs. These experiments were approved by the animal ethics committee of Wageningen University.

4.2.6 Test cases

Motion verification

In order to assess the motion tracking accuracy of the method, we generated a sequence of images simulating a swimming fish with an exactly known motion. We prescribed the snout motion, orientation and the body curvature analytically, such that it has comparable properties (i.e. spatiotemporal resolution, angle amplitudes, velocities, curvature amplitudes) to actual zebrafish swimming kinematics. A C-start-like motion is prescribed first, which then smoothly blends into a 'continuous' swimming mode with a travelling body wave along the body (see Fig. 4.3A).

A

Time [ms]

0   25   50   75   100   125   150

B

- **Reference**
- **Tracked, snout**
- **Tracked, centre of mass**

z [mm]

y [mm]

x [mm]

C

θ_z [°]

θ_y [°]

θ_x [°]

D

Reference

Tracked

Time [ms]

s [-]

s [-]

Curvature [rad mm⁻¹]

E

Head-tail angle [°]

- Reference
- Tracked

Time [ms]
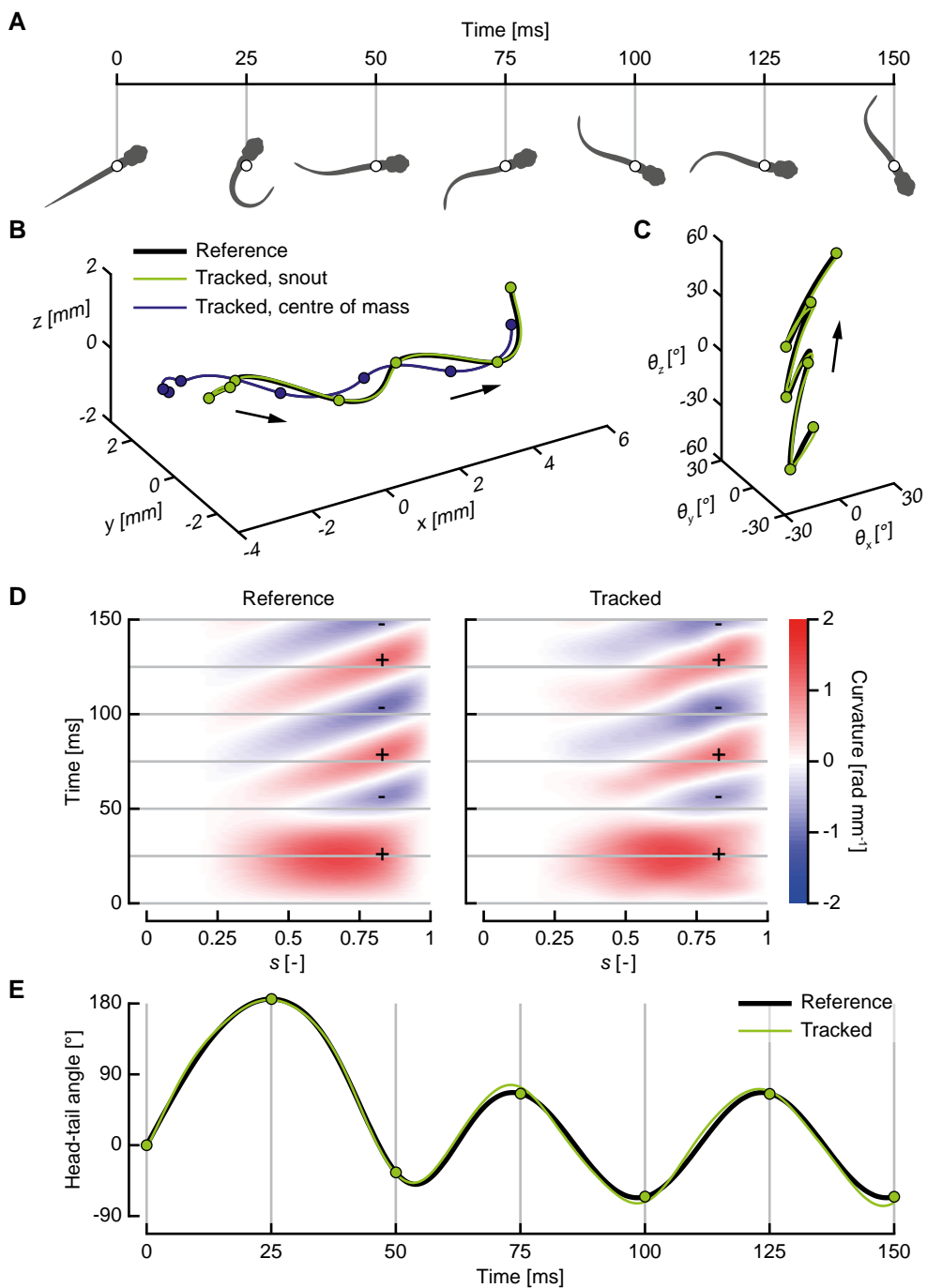
(Caption on the next page.)

Figure 4.3: Results of tracking a simulated swimming fish. (A) Projections in the world x, y-plane of the analytically prescribed simulated swimming motion. (B) Path of the snout and the centre of mass, reference (thick, black) and tracked (thin, respectively green and purple), the arrow indicates the direction in time. The dots correspond to the fish states depicted in A. (C) The rotation angle vector over time, reference (thick, black) and tracked (thin, green), the arrow indicates the direction in time. (D) Body curvature (colours) as a function of normalised position along the body s (horizontal axis) and time (vertical axis) for the reference (left) and tracked result (right), $s = 0$ corresponds to the head, $s = 1$ corresponds to the tail. The grey lines correspond to the fish states depicted in A. (E) Head-tail angle for the reference (thick, black) and tracked (thin, green) solution. This is effectively the difference in angle between the first and last point on the body, and is the net result of the curvature in every location along the body. The grey lines correspond to the fish states depicted in A.

We projected the prescribed shape of the body model onto three simulated cameras, oriented similarly to the set we used for the larval zebrafish. We simulated a frame rate of 2000 frames per second, and set all virtual cameras to have a field of view of 15×15 mm at 1024×1024 pixels, resulting in approximately 340 pixels along the simulated fish ($\ell = 5$ mm). The projections were then Gaussian blurred ($\sigma = 1$ pixel) and given a 45% decreased contrast. We generated normally distributed ($\sigma = 5\%$ of maximum intensity) additive noise at a $10\times$ lower resolution than the images (102×102 pixels), oversampled this to full resolution and Gaussian blurred it ($\sigma = 5$ pixels). This noise image was added to the generated images to simulate dirt and other disturbances in the background of the image. We created synthetic images at two other resolutions: 512×512, and 2048×2048 (respectively 170 and 680 pixels along the fish) with the same kinematics and camera settings as used for the motion verification.

Inverse dynamics verification

In order to verify the validity of the approach for computing forces and moments from a triangulated surface, we simulated a cylinder to which we applied prescribed forces and torques. We generated a cylinder with a diameter of 1.25 mm and a length of 5 mm and applied simple prescribed forces and torques. We integrated the forces over time using trapezoidal integration (MATLAB's `trapz`), we integrated the torques using the midpoint rule (Simo et al., 1995; Zupan and Saje, 2011). The resulting translation and rotation were applied to the three-dimensional, triangulated cylinder model and fed directly into the inverse dynamics module of the post-processor.

4.3 Results

4.3.1 Motion verification

We tracked the synthetically generated images (see §4.2.6) to assess how accurately the motion is reproduced by the tracker (see Figs 4.3 and 4.4). The snout position was tracked with an error smaller than 2% body length over the entire motion (see Figs 4.3B and 4.4A). The centre of mass position is reconstructed more accurately, with an error smaller than 0.5% over the image sequence. The snout rotation angle was reproduced with a magnitude of the error vector less than $6°$ (see Figs 4.3C and 4.4B). The curvature is shown in Fig. 4.3D: the

largest deviation of the tracked curvature from the reference values occurs near the head. We assess the accuracy of the body curvature reconstruction by computing the integrated value over the entire body—effectively the difference in angle between the first point on the head and the last point on the tail. This head–tail angle is reconstructed with an error smaller than $11°$, approximately 6% of its maximum value (see Figs 4.3E and 4.4C).

4.3.2 Inverse dynamics verification

The results in Figs 4.5B and C verify that our inverse dynamics method functions correctly in principle—all components of the reconstructed forces and torques are practically identical to the prescribed reference values.

A final step in the verification is the reproducibility of forces and torques from kinematics sequences tracked from video. We fed the prescribed three-dimensional body shape directly into the inverse dynamics module to compute reference forces and torques. We also tracked the generated images and computed the forces and torques from these results (see Fig. 4.6). Having verified the inverse dynamics method with the moving cylinder, we consider the first as our reference and compare it to the latter.

In general, there is strong agreement between the reference and tracked solutions, with a maximum error of approximately $0.5\ \mu N$ in force and $0.5\ \mu N$ mm in torque for the solution with a resolution of 1024×1024. The dependency on resolution is as expected: higher resolutions will give more accurate results since the body mass distribution can be reconstructed with higher fidelity. The largest deviations occur in the first and last frames, due to edge effects in the smoothing and numerical differentation. Fish swimming data will generally consist of two types of sequences: starts and 'continuous' swimming. Edge effects for starts can be eliminated by assuming zero time derivative for all kinematic parameters in the first frame, and cutting off the last few frames. Edge effects for 'continuous' swimming can be eliminated by cutting off a few frames from the start and end of the movie sequence during post-processing. Hence, for fish swimming in general, edge effects should not present a major problem for solution accuracy.

4.3.3 Analysis of three-dimensional fast start of a larval zebrafish

Fig. 4.7 shows an example tracked result of a fast-start of a zebrafish larva three days post fertilisation (see also the Supplementary Movie). The difference between the fish model and the high-speed images is small in all three views, also in the presence of optical occlusions in the form of other fish (around 29 ms). Deviations occur mostly near the head, where the body curvature is underestimated.

The post-processed result for the same movie is shown in Fig. 4.8. During the preparatory stroke, the CoM moves very little, after which it increases its speed and moves along a waving path (Fig. 4.8A). The motion is not confined to a single plane: the fish moves downward by approximately 1.4 mm over a total distance of 8.3 mm. The curvature (Fig. 4.8B) shows clear waves along the body after the start, moving from approximately $0.25\ \ell$ to close
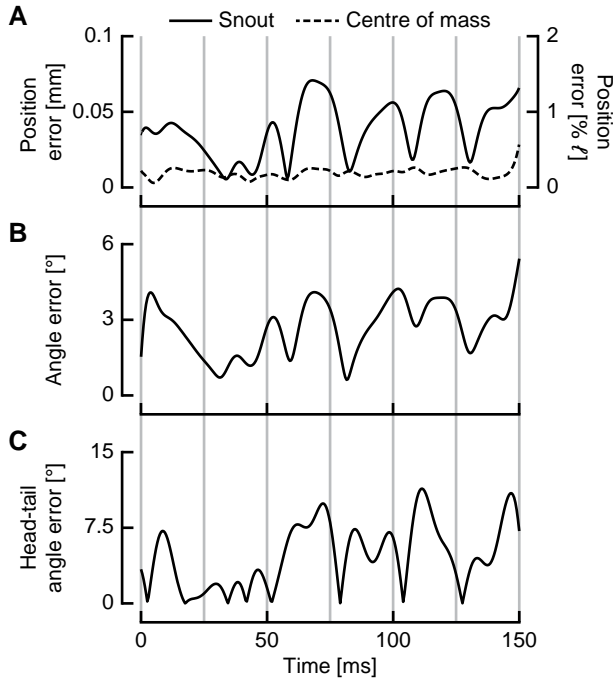
Figure 4.4: Errors in tracking of a simulated swimming fish, corresponding to the results shown in Fig. 4.3. The grey lines correspond to the time points indicated in Fig. 4.3A. (A) Magnitude of the error in snout (solid line) and centre of mass (dashed line) position, expressed by the Euclidean distance between the reference and tracked points. (B) Magnitude of the angle error vector of the head, expressed by the distance between the tips of the reference and the tracked rotation axis-angle representation. (C) Error in head–tail angle.
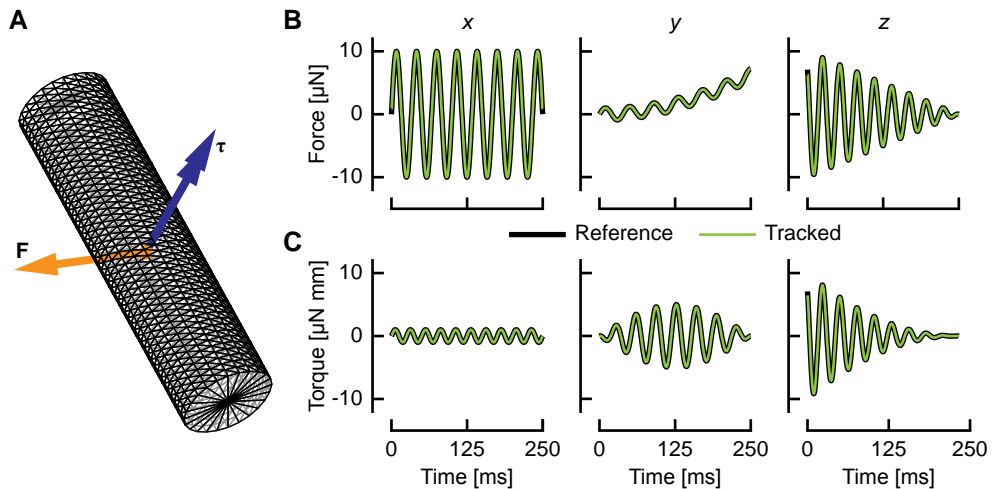
Figure 4.5: Results of the inverse dynamics algorithm on a simulated rigid body. (A) Triangulated cylinder surface with prescribed time-dependent force and torque. (B) Applied force: reference (thick, black) and computed (thin, green), from left to right x-, y- and z-components. (C) Applied torque: reference (thick, black) and computed (thin, green), from left to right x-, y- and z-components.)
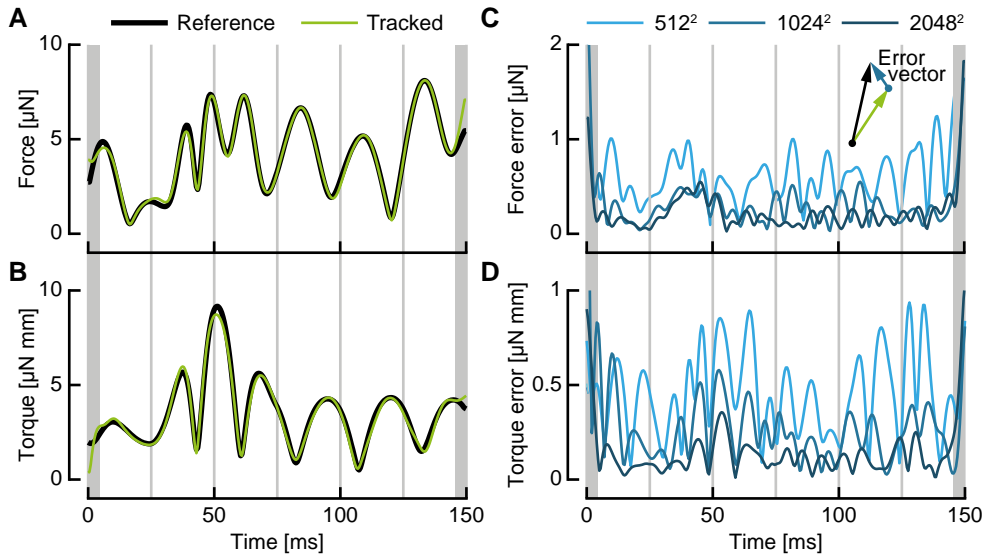
Figure 4.6: Inverse dynamics results of the simulated fish from Fig. 4.3. The reference forces and torques were computed by applying our inverse dynamics method to the prescribed triangulated body shape. The grey lines correspond to the time points indicated in Fig. 4.3A. (A) Resultant force on the fish, reference (thick, black) and tracked (thin, green) at a resolution of 1024×1024 pixels. (B) Resultant torque on the fish, reference (thick, black) and tracked (thin, green) at a resolution of 1024×1024 pixels. (C) Magnitude of the force error vector $||\mathbf{F}_{ref} - \mathbf{F}_{calc}||$ and (D) the torque error vector for three resolutions of the generated images: 512×512 (light blue), 1024×1024 (medium blue) and 2048×2048 (dark blue) pixels, respectively approximately 170, 340 and 680 pixels along the fish. The grey bands indicate the first and last 5 frames that have reduced accuracy due to edge effects and may be cut off.

to the tail. The curvature of the highly flexible tail is mainly caused by a strong interaction with the surrounding fluid, resulting in a complex pattern.

The resultant three-dimensional forces and torques (Figs 4.8C,D) start at low amplitudes until the tail starts moving at high speed at the end of the preparatory phase. The forces in sideward and upward direction oscillate around zero, resulting in a path that is approximately straight. In forward direction, there is a mainly positive force during the start, indicating that the fish is accelerating. After the start, the average force per cycle is around zero, indicating an approximately constant cycle-averaged speed. The pattern of produced force looks non-periodic, similar to earlier results for zebrafish larvae (Van Leeuwen et al., 2015). Slight differences from periodicity at the level of position will result in large differences in the force time series.

The torque about the upward axis ('yaw') is largest over most of the motion compared to the 'roll'-torque and 'pitch'-torque, because most of the fish's mass is rotating in its deformation plane. For the examined tail beats, the yaw torque shows a double-peaked pattern, similar to earlier observations for zebrafish larvae (Van Leeuwen et al., 2015). Though smaller than the yaw torque, the roll and pitch torques are considerable, mainly causing pitch (up to approximately $15°$) and an oscillating roll angle (up to approximately $30°$ during the start).
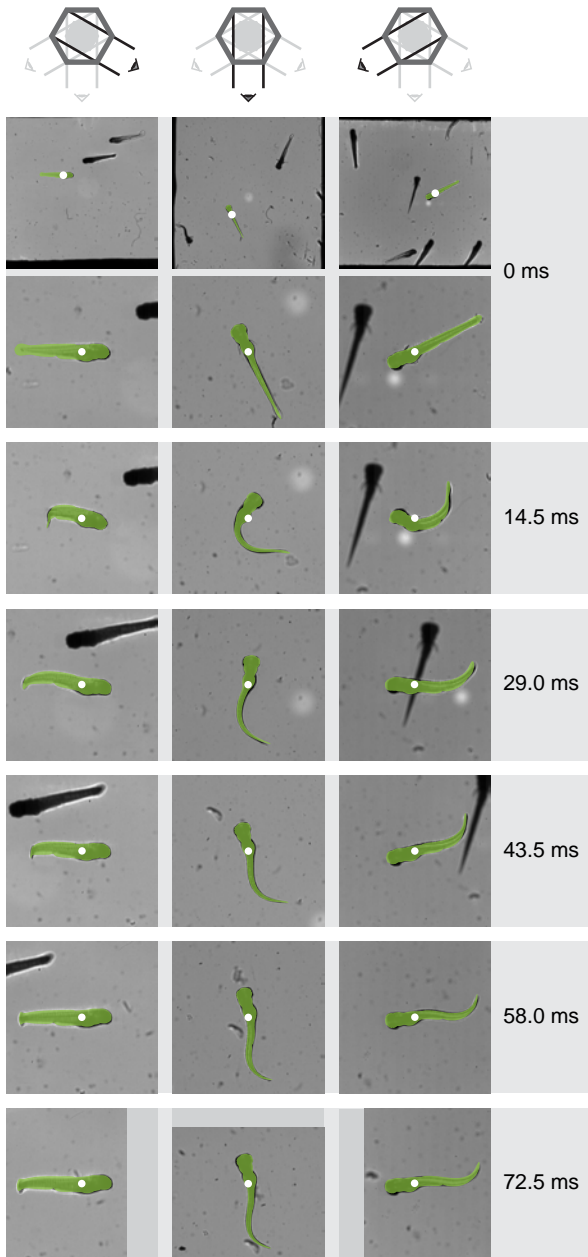
Figure 4.7: Overlap between the tracked fish and the video images of a three days post fertilisation zebrafish larva. The tracked fish (green) is overlayed over high-speed shadow images for a fast-start of a three days post fertilisation zebrafish larva, with its centre of mass indicated by white dots. Each column shows data from a different camera, from left to right oriented at: 30° to horizontal from the left, vertical, and 30° to horizontal from the right, as illustrated on the top of each column. The first frame (0 ms) is shown in full, and zoomed in to the fish to illustrate the field of view size; the rest of the frames are only shown zoomed in.

113

A

○— Preparatory stroke
●— Other strokes

z_{fish}
yaw

y_{fish}
pitch

x_{fish}
roll

B

Time [ms]

Normalised curvature [-]

s [-]

C

Force [µN]

Force [µN]

— forward   — x_{fish} — y_{fish} — z_{fish}

D

Torque [µN mm]

— roll   — pitch   — yaw

Time [ms]

E
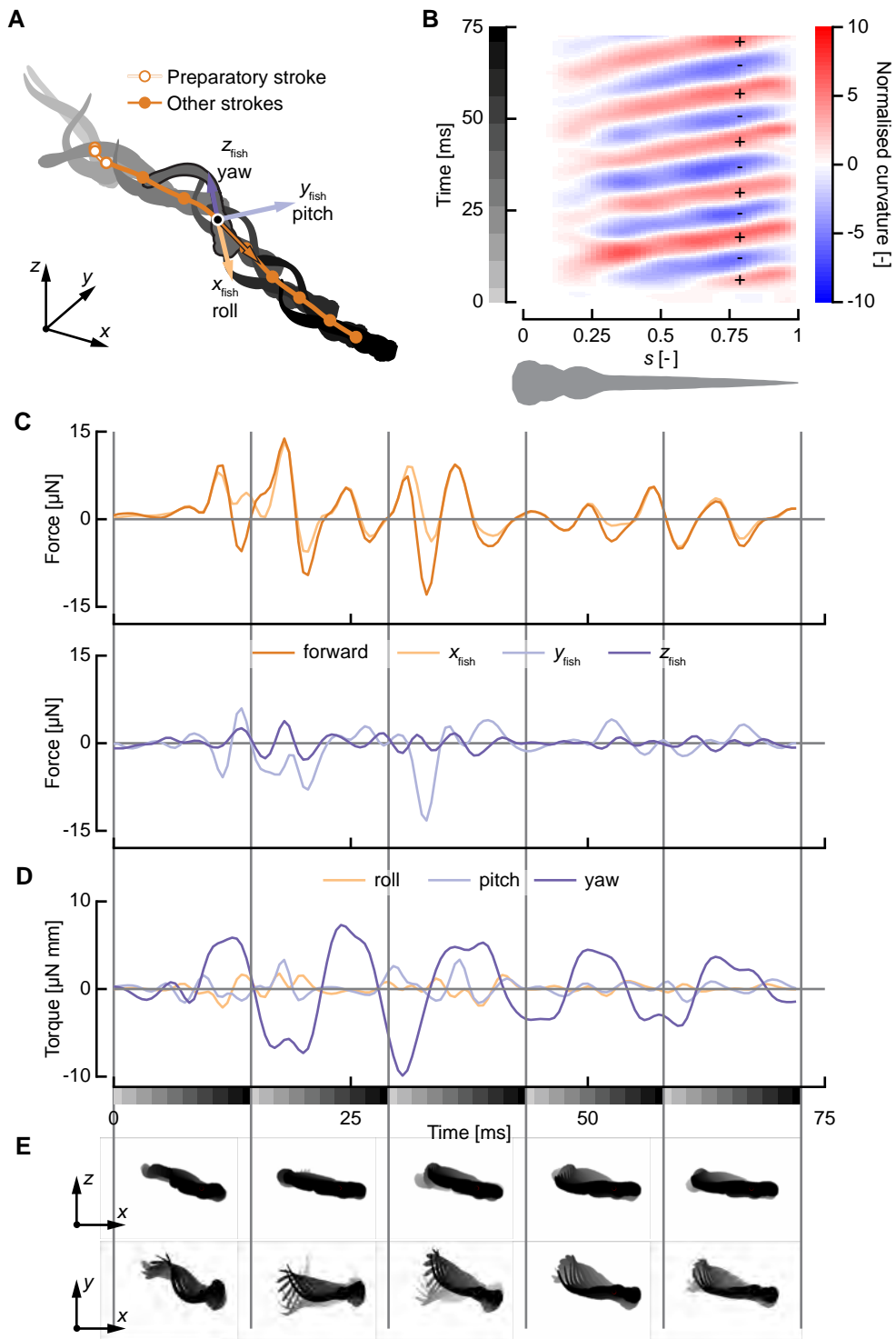
(Caption on the next page.)

Figure 4.8: Post-processing result for a fast-start of a three days post fertilisation zebrafish larva.
(A) Tracked fish model, time is shown by fill colour (from light grey to black), the path of the centre of mass is indicated by the orange line, with circles corresponding to each of the depicted fish shapes. The preparatory stroke is indicated by a narrow white line. The axes (x, y, z) define the world coordinate system, the axes $(x_\text{fish}, y_\text{fish}, z_\text{fish})$ define an instantaneous local coordinate system for the highlighted fish shape, defined in the deformation plane of the fish aligned with an inertia-weighted average of the local deformation angle. (B) Local body curvature (colours) along the fish length (horizontal) and time (vertical). The grays on the time axes correspond to the fish shapes in A. (C) Resultant force on the body in 'forward', x_fish-, y_fish- and z_fish-direction, in respectively dark orange, light orange, light purple and dark purple. The 'forward', x_fish- and y_fish-, z_fish-components are shown separately for reasons of clarity. (D) Resultant torque on the body in x_fish-, y_fish- and z_fish-direction, in respectively light orange, light purple and dark purple. The grayscale boxes on the time axes correspond to the fish shapes in each section in E. (E) Time trace of the body shape in the world x, y- and x, z-plane (from light grey to black) for each of the 5 time-slices in D and E, every second frame is shown.

This example demonstrates that the tracker performs well on high-speed video images of swimming fish. Furthermore, it illustrates that swimming behaviour is essentially three-dimensional, and needs to be analysed as such.

4.4 Discussion and perspectives

Testing of the method using synthetically generated data shows that our tracking method reconstructs position, orientation, curvature, and forces and torques accurately. The example data with a three day old zebrafish demonstrate that it is applicable to real-world high-speed videography.

The accuracy of the extraction of the fish silhouette from the high-speed images strongly determines the fidelity of the result. The quality of segmentation is influenced by image contrast and spatial resolution. Higher image resolution will in general lead to a higher fidelity of reconstruction, both in motion and forces and torques. Higher contrast between fish and background will lead to a sharper silhouette, resulting in smaller tracking errors.

An important source of error is the regularising term that we use to suppress non-physical solutions. It cannot distinguish between spurious and physical curvature gradients, and will suppress any strong gradient, regardless of its source. Most importantly, this leads to an underestimation of curvature in the region near the stiff head section. However, reducing the penalty below a certain threshold may lead to unrealistically steep changes in curvature in the same region. These errors have a limited effect on the reconstructed mass distribution, since the local error can be compensated by changing body curvature elsewhere. Therefore, resultant forces and torques will still be accurate.

For some cases, our assumptions on the fish deformation may not hold; the fish body may twist, the medial fin fold may deform in a more complex way (Van den Boogaart et al., 2012), and subtle out of plane movements may be used to generate the fluid dynamic torques that roll and pitch the animal. Furthermore, the assumption that transverse cross-sections remain perpendicular to the centreline may be invalid for fish with a low aspect ratio body shape, unlike the slender zebrafish larvae. These effects may influence hydrodynamic force generation, but will have a minor influence on the accuracy of the mass distribution of the fish. Since we use the mass distribution directly to calculate forces and

torques, they are sufficiently accurate under the present assumptions.

The assumed morphology may not match perfectly with the measured fish and will therefore result in errors. We generate body models separately from the experiments, as opposed to previous approaches (Fontaine et al., 2008; Butail and Paley, 2012), which generated a body model from the images themselves. We chose our morphology-based approach to maximise use of *a priori* information on the 3D shape of the fish, which cannot be perfectly reconstructed from only three camera views. To prevent tracking errors, care should be taken that the chosen body model corresponds well to the target fish by e.g. generating separate shape models for each individual fish. In our case, we assume that fish of a similar developmental stage are highly similar (Parichy et al., 2009), so we will generate body models for different individuals than the tracked fish.

To calculate forces and torques, we assume that the fish has a constant density over its entire volume. In general, this is not the case—the presence of different types of tissue and a swim bladder cause an inhomogeneous mass distribution. The swim bladder causes the largest density difference within the body, since it is filled with gas. However, because it is located close to the fish's centre of mass, it will have a small influence on the reconstructed torques. If necessary, density differences can be taken into account by creating a high-resolution tetrahedral mesh in the complete volume, on which a density distribution can be prescribed.

If needed, the current tracking method can be extended to track the complex deformation of the medial fin fold and the motion and deformation of the pectoral fins. This will require the addition of parameterised models of the medial and pectoral fins to the overall shape model. These parameters can be optimised simultaneously with the body deformation and motion. The image resolution of the data in the present work is insufficient to reliably perform this tracking, because we chose a large field of view to film extended swimming motions.

The method presented in this article is able to track a fish in three-dimensions by reconstructing its position, orientation (yaw, pitch and roll) and body curvature from high-speed video, with sufficient accuracy to compute resultant forces and torques. Body kinematics and dynamics at this high level of detail will help to pave the way for in-depth mechanistic analyses of the biomechanics of locomotion and manoeuvring in swimming fish.

Acknowledgments

Supplementary movie

The supplementary movie can be found at:

`https://doi.org/10.1371/journal.pone.0146682.s002`

References

Borazjani, I. and Sotiropoulos, F. (2009). Numerical investigation of the hydrodynamics of anguilliform swimming in the transitional and inertial flow regimes. *J. Exp. Biol.* **212**, 576–592.

Butail, S. and Paley, D. A. (2012). Three-dimensional reconstruction of the fast-start swimming kinematics of densely schooling fish. *J. R. Soc., Interface* **9**, 77–88.

Cheng, J.-Y. and Blickhan, R. (1994). Bending moment distribution along swimming fish. *J. Theor. Biol.* **168**, 337–348.

Dobrovolskis, A. R. (1996). Inertia of any polyhedron. *Icarus* **124**, 698–704.

Eilers, P. H. C. (2003). A perfect smoother. *Anal. Chem.* **75**, 3631–3636.

Eloy, C. (2012). Optimal Strouhal number for swimming animals. *J. Fluids Struct.* **30**, 205–218.

Fontaine, E., Lentink, D., Kranenbarg, S., Muller, U. K., Van Leeuwen, J. L., Barr, A. H. and Burdick, J. W. (2008). Automated visual tracking for studying the ontogeny of zebrafish swimming. *J. Exp. Biol.* **211**, 1305–1316.

Green, M. H., Ho, R. K. and Hale, M. E. (2011). Movement and function of the pectoral fins of the larval zebrafish (*Danio rerio*) during slow swimming. *J. Exp. Biol.* **214**, 3111–3123.

Hess, F. and Videler, J. J. (1984). Fast continuous swimming of saithe (*Pollachius virens*): a dynamic analysis of bending moments and muscle power. *J. Exp. Biol.* **109**, 229–251.

Hughes, N. F. and Kelly, L. H. (1996). New techniques for 3-D video tracking of fish swimming movements in still or flowing water. *Can. J. Fish. Aquat. Sci.* **53**, 2473–2483.

Hunter, J. R. (1972). Swimming and feeding behavior of larval anchovy *Engraulis mordax*. *Fish. Bull.* **70**, 821–838.

Kasapi, M. A., Domenici, P., Blake, R. W. and Harper, D. (1993). The kinematics and performance of escape responses of the knifefish *Xenomystus nigri*. *Can. J. Zool.* **71**, 189–195.

Koopman, B., Grootenboer, H. J. and De Jongh, H. J. (1995). An inverse dynamics model for the analysis, reconstruction and prediction of bipedal walking. *J. Biomech.* **28**, 1369–1376.

Lagarias, J. C., Reeds, J. A., Wright, M. H. and Wright, P. E. (1998). Convergence properties of the Nelder-Mead simplex method in low dimensions. *SIAM J. Optim.* **9**, 112–147.

4

Li, G., Müller, U. K., Van Leeuwen, J. L. and Liu, H. (2012). Body dynamics and hydrodynamics of swimming fish larvae: a computational study. *J. Exp. Biol.* **215**, 4015–4033.

Li, G., Müller, U. K., Van Leeuwen, J. L. and Liu, H. (2014). Escape trajectories are deflected when fish larvae intercept their own C-start wake. *J. R. Soc., Interface* **11**, 20140848–20140848.

Liao, J. C., Beal, D. N., Lauder, G. V. and Triantafyllou, M. S. (2003). The Kármán gait: novel body kinematics of rainbow trout swimming in a vortex street. *J. Exp. Biol.* **206**, 1059–1073.

MacIver, M. A. and Nelson, M. E. (2000). Body modeling and model-based tracking for neuroethology. *J. Neurosci. Methods* **95**, 133–143.

Muijres, F. T., Elzinga, M. J., Iwasaki, N. A. and Dickinson, M. H. (2015). Body saccades of *Drosophila* consist of stereotyped banked turns. *J. Exp. Biol.* **218**, 864–875.

Müller, U. K. and Van Leeuwen, J. L. (2004). Swimming of larval zebrafish: ontogeny of body waves and implications for locomotory development. *J. Exp. Biol.* **207**, 853–868.

Nelder, J. A. and Mead, R. (1965). A simplex method for function minimization. *Comput. J.* **8**, 308–313.

Parichy, D. M., Elizondo, M. R., Mills, M. G., Gordon, T. N. and Engeszer, R. E. (2009). Normal table of postembryonic zebrafish development: staging by externally visible anatomy of the living fish. *Dev. Dyn.* **238**, 2975–3015.

Simo, J. C., Tarnow, N. and Doblare, M. (1995). Non-linear dynamics of three-dimensional rods: exact energy and momentum conserving algorithms. *Int. J. Numer. Methods Eng.* **38**, 1431–1473.

Stickel, J. J. (2010). Data smoothing and numerical differentiation by a regularization method. *Comput. Chem. Eng.* **34**, 467–475.

Thorsen, D. H., Cassidy, J. J. and Hale, M. E. (2004). Swimming of larval zebrafish: fin-axis coordination and implications for function and neural control. *J. Exp. Biol.* **207**, 4175–4183.

Tytell, E. D. and Lauder, G. V. (2002). The C-start escape response of *Polypterus senegalus*: bilateral muscle activity and variation during stage 1 and 2. *J. Exp. Biol.* **205**, 2591–2603.

Van den Boogaart, J. G. M., Muller, M. and Osse, J. W. M. (2012). Structure and function of the median finfold in larval teleosts. *J. Exp. Biol.* **215**, 2359–2368.

Van Leeuwen, J. L., Voesenek, C. J. and Müller, U. K. (2015). How body torque and Strouhal number change with swimming speed and developmental stage in larval zebrafish. *J. R. Soc., Interface* **12**, 20150479.

Xiong, G. and Lauder, G. V. (2014). Center of mass motion in swimming fish: effects of speed and locomotor mode during undulatory propulsion. *Zoology* **117**, 269–281.

Zupan, E. and Saje, M. (2011). Integrating rotation from angular velocity. *Adv. Eng. Softw.* **42**, 723–733.

4

Appendix

S4.1 Creating the parameterised fish model

S4.1.1 Shape

We describe the fish in its undeformed state in a coordinate system $(\hat{x}, \hat{y}, \hat{z})$ attached to the snout of the fish, with $\hat{x}$ in caudal-rostral direction, $\hat{y}$ in lateral direction and $\hat{z}$ in ventral-dorsal direction such that they form a right-handed coordinate system.

A (super-)elliptic cross-sectional shape is used for the eyes, the fin fold and the region of the body without yolk sack is given by:

$$
\begin{cases}
\hat{y}(\psi) = r_{\hat{y}} \cos(\psi); \\
\hat{z}(\psi) = \hat{z}_0 \pm r_{\hat{z}} \left[1 - \left(\frac{|\hat{y}(\psi)|}{r_{\hat{y}}} \right)^n \right]^{\frac{1}{n}},
\end{cases}
\tag{S4.1}
$$

with $r_{\hat{y}}$ and $r_{\hat{z}}$ the radii in respectively $\hat{y}$- and $\hat{z}$-direction and $\psi = [0, 2\pi]$ where the sign in the equation for $\hat{z}$ depends on the considered quadrant: $+$ in the positive $\hat{z}$-quadrant, $-$ in the negative $\hat{z}$-quadrant. For the fin fold and body cross-sections in the tail, the exponent $n = 2$, making it a regular ellipse. The elliptic exponent for the eyes is 2.3.

The slices of the body with a bulging yolk sack have their egg-like cross-sectional shape defined by a cubic spline fit (using MATLAB's `spline`) through 4 points: $(\hat{x}_0, r_{\hat{y}}, \hat{z}_0 + h_{\text{shift}})$, $(\hat{x}_0, 0, \hat{z}_0 + r_{\hat{z}})$, $(\hat{x}_0, -r_{\hat{y}}, \hat{z}_0 + h_{\text{shift}})$, $(\hat{x}_0, 0, \hat{z}_0 - r_{\hat{z}})$. To prevent edge effects of the spline, we perform the fit on three repetitions of the points, and only use the middle section as a cross-section.

We build up the body with N_{lon} cross-sections and N_{circ} points along the circumference of each cross-section. We can connect each set of two cross-sections with $(N_{\text{lon}} - 1)N_{\text{circ}}$ quadrilateral faces, or $2(N_{\text{lon}} - 1)N_{\text{circ}}$ triangular faces. To close the surface, we cap the front- and aftmost cross-sections with N_{circ} triangular faces each.

S4.1.2 Parameterisation

The body curvature κ is prescribed in a small number ($< N_{\text{lon}}$, 7 for the zebrafish larva) of control points along the length of the fish. We define a normalised parameter along the fish length $s = [0, 1]$ and use it to create a cubic spline (MATLAB's `spline`) that interpolates the curvature control points. We analytically integrate each piecewise polynomial of the curvature spline to obtain the local deformation angle:

$$
\theta(s) = \ell \int_0^s \kappa(s) \, \mathrm{d}s,
\tag{S4.2}
$$

with ℓ the body length. We model the fish's centreline as a sequence of straight segments i of length $\Delta\ell = \ell/(N_{\mathrm{lon}} - 1)$, and apply the local deformation angle to each:

$$\hat{x}_{\mathrm{centre},i} = \begin{cases} 0 & i = 1 \\ \hat{x}_{i-1} - \Delta\ell\cos\left(\frac{\theta_{i-1}+\theta_i}{2}\right) & \text{otherwise} \end{cases}$$
$$\hat{y}_{\mathrm{centre},i} = \begin{cases} 0 & i = 1 \\ \hat{y}_{i-1} + \Delta\ell\sin\left(\frac{\theta_{i-1}+\theta_i}{2}\right) & \text{otherwise} \end{cases} \tag{S4.3}$$

in coordinates relative to the fish's head. Every cross-section i consists of N_{circ} circumferential points to which we assign the index j. We rotate every point i, j on the cross-section with the rotation of the centreline, such that it remains perpendicular:

$$\hat{\mathbf{x}}_{\mathrm{def},i,j} = \begin{pmatrix} \hat{x}_{\mathrm{def},i,j} \\ \hat{y}_{\mathrm{def},i,j} \\ \hat{z}_{\mathrm{def},i,j} \end{pmatrix} = \begin{pmatrix} \hat{x}_{\mathrm{centre},i} + \hat{y}_{i,j}\sin\theta_i \\ \hat{y}_{\mathrm{centre},i} + \hat{y}_{i,j}\cos\theta_i \\ \hat{z}_{i,j} \end{pmatrix} \tag{S4.4}$$

We now have a deformed fish in the $(\hat{x}, \hat{y}, \hat{z})$ coordinate system, which we place in world coordinates with the position $\mathbf{x}_{\mathrm{snout}}$ and rotation $\boldsymbol{\varphi}$ at the snout. The angles φ_{roll}, φ_{pitch}, φ_{yaw} (abbreviated as φ_{r}, φ_{p}, φ_{y} for reasons of clarity) specifying the rotation are converted to a rotation matrix:

$$\mathrm{R} = \begin{bmatrix} \cos\varphi_{\mathrm{p}}\cos\varphi_{\mathrm{y}} & -\cos\varphi_{\mathrm{p}}\sin\varphi_{\mathrm{y}} & \sin\varphi_{\mathrm{p}} \\ \begin{pmatrix} \sin\varphi_{\mathrm{r}}\sin\varphi_{\mathrm{p}}\cos\varphi_{\mathrm{y}}+ \\ \cos\varphi_{\mathrm{r}}\sin\varphi_{\mathrm{y}} \end{pmatrix} & \begin{pmatrix} -\sin\varphi_{\mathrm{r}}\sin\varphi_{\mathrm{p}}\sin\varphi_{\mathrm{y}}+ \\ \cos\varphi_{\mathrm{r}}\cos\varphi_{\mathrm{y}} \end{pmatrix} & -\sin\varphi_{\mathrm{r}}\cos\varphi_{\mathrm{p}} \\ \begin{pmatrix} -\cos\varphi_{\mathrm{r}}\sin\varphi_{\mathrm{p}}\cos\varphi_{\mathrm{y}}+ \\ \sin\varphi_{\mathrm{r}}\sin\varphi_{\mathrm{y}} \end{pmatrix} & \begin{pmatrix} \cos\varphi_{\mathrm{r}}\sin\varphi_{\mathrm{p}}\sin\varphi_{\mathrm{y}}+ \\ \sin\varphi_{\mathrm{r}}\cos\varphi_{\mathrm{y}} \end{pmatrix} & \cos\varphi_{\mathrm{r}}\cos\varphi_{\mathrm{p}} \end{bmatrix} \tag{S4.5}$$

We compute the final position of each point on the fish with:

$$\mathbf{x}_{\mathrm{def},i,j} = \mathrm{R}\hat{\mathbf{x}}_{\mathrm{def},i,j} + \mathbf{x}_{\mathrm{snout}}. \tag{S4.6}$$

Finally, all points are reassembled into a three-dimensional surface of quadrilaterals during tracking and of triangles during post-processing.

S4.2 Fitting the body model

S4.2.1 Objective function

The objective function that we aim to minimise in order to achieve an optimal fit is defined as follows:

$$f_{\mathrm{tot}}(\boldsymbol{\Omega}) = f_{\mathrm{GoF}}(\boldsymbol{\Omega}) + f_{\mathrm{reg}}(\boldsymbol{\Omega}). \tag{S4.7}$$

Here, $\boldsymbol{\Omega}$ is the list of optimised parameters, $f_{\mathrm{GoF}}(\boldsymbol{\Omega})$ is a term indicating how accurately the fish model approaches the high-speed video images, and $f_{\mathrm{reg}}(\boldsymbol{\Omega})$ is a term that penalises 'unsmoothness'. The two terms are discussed in detail below.

Goodness of fit

To compare the virtual images to the segmented high-speed video images, we project the three-dimensional shape of the fish onto virtual cameras. We define a left-handed camera coordinate system (ξ, η, ϑ), respectively rows, columns, and a coordinate perpendicular to the image plane in the viewing direction of the camera. A transformation matrix from camera to world coordinate system is given by:

$$
\mathrm{T}_{\mathrm{cam}} = \begin{bmatrix} \omega_{x,\xi} & \omega_{x,\eta} & \omega_{x,\vartheta} \\ \omega_{y,\xi} & \omega_{y,\eta} & \omega_{y,\vartheta} \\ \omega_{z,\xi} & \omega_{z,\eta} & \omega_{z,\vartheta} \end{bmatrix} \tag{S4.8}
$$

Since we are considering a camera system with parallel light, the distance of an object from the camera has no influence on its projected size. The light is collimated to within 10° divergence, so perspective effects are negligible at the millimetre scales of zebrafish motion. Projecting objects onto the camera is therefore only a coordinate transformation to camera coordinates (i.e., a rotation, translation and rescaling):

$$
\boldsymbol{\xi} = \frac{1}{d_{\mathrm{scale}}} \mathrm{T}_{\mathrm{cam}}^{\mathrm{T}} (\mathbf{x}_{\mathrm{obj}} - \mathbf{x}_{\mathrm{cam}}) + 1, \tag{S4.9}
$$

where $\mathbf{x}_{\mathrm{object}}$ are the object coordinates, $\mathbf{x}_{\mathrm{cam}}$ the camera coordinate system origin (i.e., the top left corner of the image), d_{scale} a scaling factor in unit distance per pixel. The 1 is added because by convention, the top left corner is denoted as having row-column (i.e., ξ, η) coordinates $(1, 1)$. Because the transformation matrix $\mathrm{T}_{\mathrm{cam}}$ is orthogonal, we can invert the matrix by taking its transpose. The image plane coordinates of the projected point are given by (ξ, η); the third coordinate ϑ can be ignored.

When considering cases with significant magnification effects (e.g., when no collimated light setup is used), we use a simple linear pinhole model, where image magnification is linear with distance from the camera. In that case, we use the ϑ coordinate to determine the scaling factor for the current projected point and thus compute its projection on the image plane.

To compute the goodness of fit, we project the three-dimensional surface of the fish onto the camera plane using the procedure outlined above. We then overlay the fish silhouette in image coordinates onto the segmented high-speed video frames. All pixels in the combined image are counted, and the pixels that overlap between the model fish and the actual fish are subtracted from this number. The final result is the number of mismatching pixels – an expression for the goodness of fit.

Penalty function

The regularising term in the objective function is of the form

$$
f_{\mathrm{reg}} = \int_0^1 w(s) \left(\frac{\mathrm{d}\kappa(s)}{\mathrm{d}s} \right)^2 \mathrm{d}s, \tag{S4.10}
$$

where $w(s)$ is a weighting function that allows stronger suppression of curvature near the head than near the tail. For the zebrafish, we prescribe $w(s)$ as a cubic spline fit (MATLAB's `spline`) in logarithmic space of control points along the body. In our case of the larval zebrafish, we prescribe two points at $s = \{0, 1\}$. Since a cubic spline fit of two points is linear, the result is a function of the form $w(s) = c_0 \, e^{-c_1 s}$.

S4.2.2 Initialisation

The initial set of model parameters for the first frame $\boldsymbol{\omega_0}$ is computed from two user-clicked points per camera: the snout and the tail. Rewriting Eqn. S4.9 gives, for every camera,

$$\frac{1}{d_{\text{scale}}} \text{T}_{\text{cam}}^{\text{T}} \mathbf{x}_{\text{obj}} = \boldsymbol{\xi} + \frac{1}{d_{\text{scale}}} \text{T}_{\text{cam}}^{\text{T}} \mathbf{x}_{\text{cam}} - 1. \tag{S4.11}$$

Manually indicating a point in an image will give us the first two components of $\boldsymbol{\xi}$, so we can use the first two equations of this system for each camera. This results in an overdetermined linear system (for $N_{\text{cam}} > 2$): we have 3 unknowns (x, y, z) and $2N_{\text{cam}}$ equations. We solve this system with least-squares (MATLAB's \ operator) to obtain the snout and tail positions in 3D.

The snout position can be directly used to initialise the position parameter for the optimisation. We set the initial roll angle to 0, the pitch angle to

$$\varphi_{\text{pitch}} = \arctan\left(\frac{z_{\text{snout}} - z_{\text{tail}}}{\left[(x_{\text{snout}} - x_{\text{tail}})^2 + (y_{\text{snout}} - y_{\text{tail}})^2\right]^{\frac{1}{2}}}\right) \tag{S4.12}$$

and the yaw angle to

$$\varphi_{\text{yaw}} = \arctan\left(\frac{y_{\text{snout}} - y_{\text{tail}}}{x_{\text{snout}} - x_{\text{tail}}}\right). \tag{S4.13}$$

The arctangents are computed using MATLAB's `atan2` function, that takes into account the sign of the nominator and denominator to compute the angle in the correct quadrant.

We approximate the fish length ℓ as follows:

$$\ell_{\text{init}} = \sqrt{(x_{\text{snout}} - x_{\text{tail}})^2 + (y_{\text{snout}} - y_{\text{tail}})^2 + (z_{\text{snout}} - z_{\text{tail}})^2} \tag{S4.14}$$

This approximation is used as an initial condition for an optimisation in the first frame of the sequence, where we allow the fish length to vary. The final, optimised fish length ℓ is then kept fixed in the rest of the video sequence.

S4.2.3 Solution extrapolation

We extrapolate the solution from previous time steps to initialise the next time step. We use the following:

$$
\boldsymbol{\Omega}_{\mathrm{init},i_t} =
\begin{cases}
\boldsymbol{\Omega}_0 & i_t = 1 \\
\boldsymbol{\Omega}_{\mathrm{opt},i_t-1} & i_t = 2 \\
-\boldsymbol{\Omega}_{\mathrm{opt},i_t-2} + 2\boldsymbol{\Omega}_{\mathrm{opt},i_t-1} & i_t = 3 \\
\boldsymbol{\Omega}_{\mathrm{opt},i_t-3} - 3\boldsymbol{\Omega}_{\mathrm{opt},i_t-2} + 3\boldsymbol{\Omega}_{\mathrm{opt},i_t-1} & i_t > 3
\end{cases}
\tag{S4.15}
$$

where $i_t \in \mathbb{N}$ denotes the time step, $\boldsymbol{\Omega}_{\mathrm{init},i_t}$ is the set of parameters used to initialise the optimisation at time step i_t and $\boldsymbol{\Omega}_{\mathrm{init},i_t}$ is the final, optimised set of parameters at time step i_t.

S4.3 Post-processing and inverse dynamics

S4.3.1 Smoothing

In general, the solution from the optimisation procedure is insufficiently smooth in time to accurately compute (second) derivatives. We perform *post hoc* smoothing to remove spurious high-frequency components, but retain (most of) the physical signal. We use a regularised data fit similar to (Stickel, 2010), where smoothing is presented as a minimisation problem:

$$
\underset{\phi_{\mathrm{sm}}}{\mathrm{argmin}} \left\{ \int_0^{t_{\max}} \left| \phi_{\mathrm{data}}(t) - \phi_{\mathrm{sm}}(t) \right|^2 \mathrm{d}t + \lambda_{\mathrm{sm}} \int_0^{t_{\max}} \left| \frac{\mathrm{d}^n \phi_{\mathrm{sm}}(t)}{\mathrm{d}t^n} \right|^2 \mathrm{d}t \right\}, \tag{S4.16}
$$

where ϕ_{sm} are the smoothed data points, ϕ_{data} are the measured data points, λ_{sm} is a parameter controlling the amount of regularisation and n is the order of the derivative used for the penalty function. It has been shown (Stickel, 2010) that the solution for a discrete number of points is given by

$$
\phi_{\mathrm{sm}} = (\mathrm{I} + \lambda_{\mathrm{sm}} \mathrm{D}^{\mathrm{T}} \mathrm{D})^{-1} \phi_{\mathrm{data}}, \tag{S4.17}
$$

where D is a matrix that approximates the required n^{th}-order derivative. We assume here that our fitted points are located at the same time instants as the data points. For the D matrix, we use 4 subsequent one-sided differences (using MATLAB's `diff`) to approximate the fourth order derivative, ensuring that our second derivatives are smooth.

To combat edge effects of the smoothing, we separate two cases: starts, where the animal accelerates from a stationary position, and 'continuous' swimming, where it enters and exits the field of view while swimming. In the case of starts, we know that the animal is stationary before the time series starts. We therefore add 25 time points before $t = 0$ which all have the value at $t = 0$, thus forcing the solution to have a realistic zero gradient at the start. In the case of 'continuous' swimming, we can simply cut off the first few (in our case 5) points, where the edge effects are strongest. For both cases, we cut off the same number of points off the end of the time series.

S4.3.2 Derivatives

Differentiation is required to compute velocity and acceleration from the centre of mass position, and torque from the angular momentum vector. We use the same procedure for any time series, for first derivatives:

$$\frac{\partial \phi}{\partial t} \approx \begin{cases} \frac{-3\phi_1 + 4\phi_2 - \phi_3}{2\Delta t} & i_t = 1 \\ \frac{-\phi_{i_t-1} + \phi_{i_t+1}}{2\Delta t} & 1 < i_t < N_t \\ \frac{\phi_{N_t-2} - 4\phi_{N_t-1} + 3\phi_{N_t}}{2\Delta t} & i_t = N_t \end{cases} \tag{S4.18}$$

for second derivatives:

$$\frac{\partial^2 \phi}{\partial t^2} \approx \begin{cases} \frac{\phi_1 - 2\phi_2 + \phi_3}{\Delta t^2} & i_t = 1 \\ \frac{\phi_{i_t-1} - 2\phi_{i_t} + \phi_{i_t+1}}{\Delta t^2} & 1 < i_t < N_t \\ \frac{\phi_{N_t-2} - 2\phi_{N_t-1} + \phi_{N_t}}{\Delta t^2} & i_t = N_t \end{cases} \tag{S4.19}$$

S4.3.3 Resultant forces and torques

The resultant force $\mathbf{F}_{\text{net}}$ on the fish can be computed from Newton's second law:

$$\mathbf{F}_{\text{net}} = m\, \mathbf{a}_{\text{CoM}} = \rho V \frac{\mathrm{d}^2 \mathbf{r}_{\text{CoM}}}{\mathrm{d}t^2}, \tag{S4.20}$$

where m is fish mass, ρ is fish density, and $\mathbf{a}_{\text{CoM}}$ denotes the acceleration of the centre of mass; the volume V and position of the centre of mass $\mathbf{r}_{\text{CoM}}$ can be computed using the method by Dobrovolskis (1996) from the triangulated surface of the body model. Every triangular face is made into a tetrahedron by taking the coordinate system origin as a fourth vertex, see Fig S4.1A. Calculations can be performed separately on each of these tetrahedra, and subsequently summed to yield the result for the complete fish.
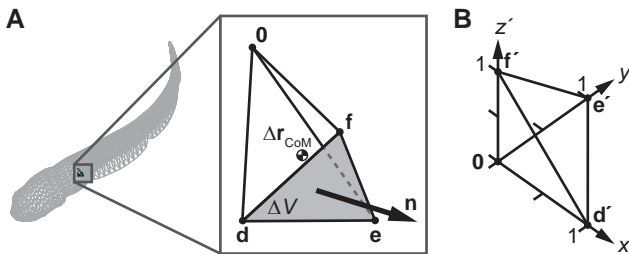
Figure S4.1: Tetrahedra used for computation of derived quantities: centre of mass position and instantaneous forces and torques. (A) To compute volume properties from a surface description, a tetrahedron is created for each surface triangle **d e f**, with a volume ΔV and a centre of mass position $\Delta \mathbf{r}_{\text{CoM}}$. The sign of its contribution is determined by the direction of the normal **n**. (B) The same tetrahedron is transformed into a unit tetrahedron for easier interpolation and integration, allowing us to compute the contribution of each tetrahedron to the angular momentum separately with a single analytical expression as a function of the values at the vertices.

The method by Dobrovolskis (1996) only computes the centre of mass and the moment of inertia matrix; we extend their method to compute angular momentum for an arbitrary triangulated polyhedron of constant density. Angular momentum is defined as:

$$\mathbf{L} = \rho \iiint\limits_{V} \mathbf{r}^*(\mathbf{x}) \times \mathbf{v}^*(\mathbf{x}) \, dV, \qquad (S4.21)$$

where the asterisks denotes quantities measured with respect to the centre of mass. The integrand is linear, so we can evaluate Equation S4.21 for each tetrahedron separately and then sum the results. To simplify this computation, we transform every tetrahedron into a unit tetrahedron in the origin of a new coordinate system (x', y', z'), see Fig S4.1B. This is a linear transformation, with the following transformation matrix from unit to world tetrahedron:

$$\mathrm{T_{tet}} = \begin{bmatrix} x^*_{d,k} & x^*_{e,k} & x^*_{f,k} \\ y^*_{d,k} & y^*_{e,k} & y^*_{f,k} \\ z^*_{d,k} & z^*_{e,k} & z^*_{f,k} \end{bmatrix} \qquad (S4.22)$$

The transformed integral for every tetrahedron becomes

$$\Delta\mathbf{L} = \rho \det \mathrm{T_{tet}} \int\limits_{0}^{1} \int\limits_{0}^{1-x'} \int\limits_{0}^{1-x'-y'} \mathbf{r}^*(\mathbf{x}') \times \mathbf{v}^*(\mathbf{x}') \, dz' dy' dx', \qquad (S4.23)$$

Transformed to a unit tetrahedron, linear interpolation of quantities known at its vertices reduces to a single matrix multiplication. The interpolating matrices for the position and velocity are given by:

$$\Gamma_r = \begin{bmatrix} x^*_{d,k} & x^*_{e,k} & x^*_{f,k} \\ y^*_{d,k} & y^*_{e,k} & y^*_{f,k} \\ z^*_{d,k} & z^*_{e,k} & z^*_{f,k} \end{bmatrix} \qquad (S4.24)$$

$$\Gamma_v = \begin{bmatrix} v^*_{x,d,k} & v^*_{x,e,k} & v^*_{x,f,k} \\ v^*_{y,d,k} & v^*_{y,e,k} & v^*_{y,f,k} \\ v^*_{z,d,k} & v^*_{z,e,k} & v^*_{z,f,k} \end{bmatrix} \qquad (S4.25)$$

With interpolation, Equation S4.23 can be written as:

$$\Delta\mathbf{L}_k = \rho \det \mathrm{T_{tet}} \int\limits_{0}^{1} \int\limits_{0}^{1-x'} \int\limits_{0}^{1-x'-y'} \Gamma_r\mathbf{x}' \times \Gamma_v\mathbf{x}' \, dz' dy' dx'. \qquad (S4.26)$$

Evaluating this integral (using Maple 18, Maplesoft, Waterloo, Ontario, Canada) gives the following expressions for the x-, y- and z-components of the angular momentum vector:

$$
\begin{aligned}
\Delta L_{x,k} = \frac{\rho \Delta V_k}{20} \big[&+ y_{d,k}^* \, (2v_{z,d,k}^* + v_{z,e,k}^* + v_{z,f,k}^*) \\
&+ y_{e,k}^* \, (v_{z,d,k}^* + 2v_{z,e,k}^* + v_{z,f,k}^*) \\
&+ y_{f,k}^* \, (v_{z,d,k}^* + v_{z,e,k}^* + 2v_{z,f,k}^*) \\
&- z_{d,k}^* \, (2v_{y,d,k}^* + v_{y,e,k}^* + v_{y,f,k}^*) \\
&- z_{e,k}^* \, (v_{y,d,k}^* + 2v_{y,e,k}^* + v_{y,f,k}^*) \\
&- z_{f,k}^* \, (v_{y,d,k}^* + v_{y,e,k}^* + 2v_{y,f,k}^*) \big];
\end{aligned}
$$

(S4.27)

$$
\begin{aligned}
\Delta L_{y,k} = \frac{\rho \Delta V_k}{20} \big[&- x_{d,k}^* \, (2v_{z,d,k}^* + v_{z,e,k}^* + v_{z,f,k}^*) \\
&- x_{e,k}^* \, (v_{z,d,k}^* + 2v_{z,e,k}^* + v_{z,f,k}^*) \\
&- x_{f,k}^* \, (v_{z,d,k}^* + v_{z,e,k}^* + 2v_{z,f,k}^*) \\
&+ z_{d,k}^* \, (2v_{x,d,k}^* + v_{x,e,k}^* + v_{x,f,k}^*) \\
&+ z_{e,k}^* \, (v_{x,d,k}^* + 2v_{x,e,k}^* + v_{x,f,k}^*) \\
&+ z_{f,k}^* \, (v_{x,d,k}^* + v_{x,e,k}^* + 2v_{x,f,k}^*) \big];
\end{aligned}
$$

(S4.28)

$$
\begin{aligned}
\Delta L_{z,k} = \frac{\rho \Delta V_k}{20} \big[&+ x_{d,k}^* \, (2v_{y,d,k}^* + v_{y,e,k}^* + v_{y,f,k}^*) \\
&+ x_{e,k}^* \, (v_{y,d,k}^* + 2v_{y,e,k}^* + v_{y,f,k}^*) \\
&+ x_{f,k}^* \, (v_{y,d,k}^* + v_{y,e,k}^* + 2v_{y,f,k}^*) \\
&- y_{d,k}^* \, (2v_{x,d,k}^* + v_{x,e,k}^* + v_{x,f,k}^*) \\
&- y_{e,k}^* \, (v_{x,d,k}^* + 2v_{x,e,k}^* + v_{x,f,k}^*) \\
&- y_{f,k}^* \, (v_{x,d,k}^* + v_{x,e,k}^* + 2v_{x,f,k}^*) \big].
\end{aligned}
$$

(S4.29)

The total angular momentum is then given by the sum over all tetrahedra k:

$$
\mathbf{L} = \sum_k \Delta \mathbf{L}_k.
$$

(S4.30)

With the angular momentum known in each time step, we can compute the net torque by taking its time derivative:

$$
\boldsymbol{\tau}_{\text{net}} = \frac{d\mathbf{L}}{dt}.
$$

(S4.31)

S4.3.4 Fish reference system

To make interpretation of the forces and torques more intuitive, we transform them to a local fish coordinate system $(x_{\text{fish}}, y_{\text{fish}}, z_{\text{fish}})$ that rotates with the changing orientation of the fish. To create this fish axis system, we first rotate the world coordinate system so it is aligned with the fish's head, using the rotation matrix in Equation S4.5. This transforms

the fish to the $(\hat{x}, \hat{y}, \hat{z})$ coordinate system defined in §S4.1, where the $\hat{x}, \hat{y}$-plane is aligned with the deformation plane of the fish, and $\hat{z}$ is perpendicular to it. The $\hat{x}$-coordinate is aligned with the head, which rotates with a large amplitude and makes interpretation of the time-variation of the forces and torques difficult.

In order to define an angle that is related to the entire body, we use a 'body angle' (Van Leeuwen et al., 2015), defined as:

$$\varphi_{\text{body}} = \frac{\int_0^1 I_{\text{CoM},i}(s)\alpha(s)\,\mathrm{d}s}{\int_0^1 I_{\text{CoM},i}(s)\,\mathrm{d}s}, \tag{S4.32}$$

where $I_{\text{CoM},i}(s)$ is the moment of inertia about the centre of mass per unit length of the cross-section at s and $\alpha(s)$ is the angle between a line projected from the centre of mass to the centre of segment and horizontal. The body angle is effectively a moment of inertia-weighted average of the local angles of each segment.

We can express the local moment of inertia per unit length as the contribution of the cross-section about its own vertical centre axis $I_{\text{cross},i}$ and its contribution with respect to the centre of mass

$$I_{\text{CoM},i} = I_{\text{cross},i} + \mu r_{\text{CoM},i}^2, \tag{S4.33}$$

where μ is a mass per unit length and $r_{\text{CoM},i}$ the distance between the centre of mass in the $x_{\text{fish}}, y_{\text{fish}}$-plane and the cross-section centre. We compute the moment of inertia per unit length and area, and thus mass, assuming constant density, of each cross-section with the expressions for arbitrary polygons (Liggett, 1988). The local segment angle α is computed by projecting a line from the centre of mass to the segment centre in the deformation plane (i.e., in $\hat{x}, \hat{y}, \hat{z}$-coordinates), and computing the angle it makes with respect to the head:

$$\alpha_i = \arctan\left(\frac{\hat{y}_{\text{centre},i} - \hat{y}_{\text{CoM}}}{\hat{x}_{\text{centre},i} - \hat{x}_{\text{CoM}}}\right), \tag{S4.34}$$

making sure we get the correct sign depending on the quadrant we are in by using MAT-LAB's `atan2` function.

We compute the body angle by evaluating the integral from Equation S4.32 using MAT-LAB's `trapz` function. This results in a series of body angles over time that may still have discontinuities where the centre of mass crosses the centreline; in these points, the angle 'reflects' around an unknown line since all the projected lines flip direction. To remove these discontinuities, we average a one-sided derivative left and right of the discontinuity. We then extrapolate the solution from the point left of the discontinuity:

$$\alpha_i = \alpha_{i-1} + \frac{1}{2}\left(\frac{\alpha_{i-3} - 4\alpha_{i-2} + 3\alpha_{i-1}}{2} + \frac{-3\alpha_i + 4\alpha_{i+1} - \alpha_{i+2}}{2}\right), \tag{S4.35}$$

where i is the index of the point just right of the discontinuity. The entire sequence to the right of the discontinuity is shifted, retaining gradient information. We iterate over

all discontinuities in the sequence, yielding a body angle that is continuous from the first angle onwards. Since we start with a straight fish in the $\hat{x}, \hat{y}, \hat{z}$-coordinates, we define this first angle as 0.

We rotate the head-aligned coordinate system along its vertical axis by the computed body angle. We represent the rotation as an axis and angle: respectively $\boldsymbol{\omega}_{z_{\text{head}}}$ (abbreviated in Equation S4.36 as $\boldsymbol{\omega}$), the unit orientation vector of the z_{head}-axis and φ_{body} (abbreviated in Equation S4.36 as φ). This results in a rotation matrix of the following form:

$$
R_{\text{body}} = \left[\begin{array}{ccc}
\left(\begin{array}{c} \cos\varphi \\ +\omega_x^2(1-\cos\varphi) \end{array} \right) & \left(\begin{array}{c} \omega_x\omega_y(1-\cos\varphi) \\ -\omega_z\sin\varphi \end{array} \right) & \left(\begin{array}{c} \omega_x\omega_z(1-\cos\varphi) \\ +\omega_y\sin\varphi \end{array} \right) \\
\left(\begin{array}{c} \omega_x\omega_y(1-\cos\varphi) \\ +\omega_z\sin\varphi \end{array} \right) & \left(\begin{array}{c} \cos\varphi \\ +\omega_y^2(1-\cos\varphi) \end{array} \right) & \left(\begin{array}{c} \omega_y\omega_z(1-\cos\varphi) \\ -\omega_x\sin\varphi \end{array} \right) \\
\left(\begin{array}{c} \omega_x\omega_z(1-\cos\varphi) \\ -\omega_y\sin\varphi \end{array} \right) & \left(\begin{array}{c} \omega_y\omega_z(1-\cos\varphi) \\ +\omega_x\sin\varphi \end{array} \right) & \left(\begin{array}{c} \cos\varphi \\ +\omega_z^2(1-\cos\varphi) \end{array} \right)
\end{array} \right] \tag{S4.36}
$$

Applying this rotation matrix to the axes of the head coordinate system yields our final fish coordinate system $(x_{\text{fish}}, y_{\text{fish}}, z_{\text{fish}})$, in which we express our forces and torques. We transform the force vector by projecting it onto each unit orientation vector of the axes, e.g.,

$$
F_{x,\text{fish}} = \mathbf{F} \cdot \boldsymbol{\omega}_{x_{\text{fish}}}. \tag{S4.37}
$$

We define an additional axis in the direction of the velocity vector:

$$
\boldsymbol{\omega}_{\text{fwd}} = \mathbf{v}_{\text{CoM}}/||\mathbf{v}_{\text{CoM}}||, \tag{S4.38}
$$

where $\mathbf{v}_{\text{CoM}}$ is the instantaneous velocity vector of the centre of mass. We project the force to this axis to have an indication of the effective force propelling the fish.

References

Dobrovolskis, A. R. (1996). Inertia of any polyhedron. *Icarus* **124**, 698–704.

Liggett, J. A. (1988). Exact formulae for areas, volumes and moments of polygons and polyhedra. *Commun. Appl. Numer. Methods* **4**, 815–820.

Stickel, J. J. (2010). Data smoothing and numerical differentiation by a regularization method. *Comput. Chem. Eng.* **34**, 467–475.

Van Leeuwen, J. L., Voesenek, C. J. and Müller, U. K. (2015). How body torque and Strouhal number change with swimming speed and developmental stage in larval zebrafish. *J. R. Soc., Interface* **12**, 20150479.

5
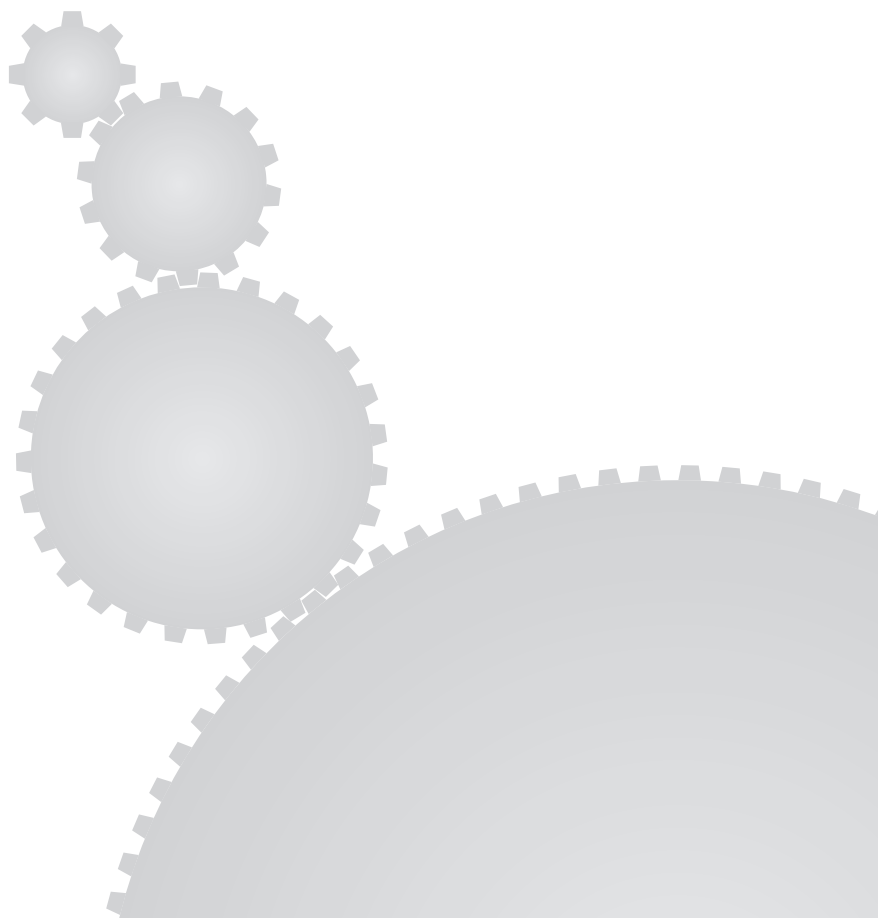
Chapter 5

Reorientation and propulsion in fast-starting zebrafish larvae: an inverse dynamics analysis

Cees J. Voesenek[1], Remco P. M. Pieters[1], Florian T. Muijres[1], Johan L. van Leeuwen[1]

[1] Experimental Zoology Group, Wageningen University & Research, Wageningen, The Netherlands

Abstract

Most fish species use fast starts to escape from predators. Zebrafish larvae perform effective fast starts immediately after hatching. They use a C-start, where the body curls into a C-shape, and then unfolds to accelerate. These escape responses need to fulfil a number of functional demands, under the constraints of the fluid environment and the larva's body shape. Primarily, the larvae need to generate sufficient escape speed in a wide range of possible directions, in a short-enough time. In this study, we examined how the larvae meet these demands. We filmed fast starts of zebrafish larvae with a unique five-camera setup with high spatiotemporal resolution. From these videos, we reconstructed the three-dimensional swimming motion with an automated method and from these data calculated resultant hydrodynamic forces and, for the first time, 3D torques. We show that zebrafish larvae reorient mostly in the first stage of the start by producing a strong yaw torque, often without using the pectoral fins. This reorientation is expressed as the body angle, a measure that represents the rotation of the complete body, rather than the commonly used head angle. The fish accelerates its centre of mass mostly in stage 2 by generating a considerable force peak while the fish 'unfolds'. The escape direction of the fishs correlates strongly with the amount of body curvature in stage 1, while the escape speed correlates strongly with the duration of the start. This may allow the fish to independently control the direction and speed of the escape.

5.1   Introduction

The fast start is an important manoeuvre in the motion repertoire of many fish species across developmental stages (Domenici and Blake, 1997; Hale et al., 2002). Fast starts are commonly divided into two types by the shape changes of the fish during the motion: the S-start and the C-start. This article concerns the C-start, which is mainly used to escape from (potential) threats (Walker et al., 2005), and in some species for prey capture (Wöhl and Schuster, 2007). It involves the fish bending itself into a C-shape, and then unfolding to produce a strong acceleration and a change of direction (Hertel, 1966; Weihs, 1973). This motion is often considered to consist of three stages (Domenici and Blake, 1997; Hertel, 1966; Weihs, 1973): stage 1, where the fish bends into a C-shape; stage 2, where the fish unfolds; and stage 3, the remainder of the motion—continuous swimming or coasting. In this study, we look at the first two stages of the C-start—we do not consider the highly variable third stage.

 For the fast start to contribute to the survival of the larvae, the stages need to satisfy a number of functional demands (Voesenek et al., 2018). The primary demand on a start is to escape from a predator (Domenici and Blake, 1997). This requires strong accelerations to create sufficient distance in a short time between the predator and the larvae (Walker et al., 2005). In addition, it requires control over the escape angle, as the relative heading with respect to the predator often determines escape success (Domenici et al., 2011). Since predators may approach from all sides, it is necessary that the larvae can produce a large range of possible escape directions, both horizontally and vertically. Finally, the threat should be de-

tected early, and the response needs to be well-timed for the escape to be effective (Stewart et al., 2013).

These functional demands should be fulfilled within physical constraints on the body of the larva and the hydrodynamics. Fish larvae need to be able to escape immediately after hatching (Voesenek et al., 2018), while their muscles (Van Raamsdonk et al., 1978), sensory system, and motor control (Fetcho and McLean, 2010) are not fully developed—even within these limits, the larvae need to respond appropriately, quickly, and produce effective motion. Furthermore, to perform effective propulsion as an undulatory swimmer, the larva needs to prepare its body for a propulsive tail-beat by bending into a C (Foreman and Eaton, 1993). To produce thrust, the fish also needs to 'prepare' the surrounding water by generating (precursors to) vortices and jets that will contribute to the hydrodynamic forces in stage 2 (Ahlborn et al., 1991; Tytell and Lauder, 2008). In addition, stage 1 prepares the axial muscle for maximum power production by active lengthening of the contralateral side during bending (James and Johnston, 1998).

To meet the functional demands of the fast start, the fish larvae must generate hydrodynamic forces and torques, producing linear and angular accelerations. Different methods have been used to quantify these forces and torques. The motion of the fish and the flow can be quantified with high-speed video images and particle image velocimetry, allowing estimation of momentum changes of the fish and flow (Tytell and Lauder, 2008), or estimation of forces via a reconstructed pressure (Lucas et al., 2017). The reconstructed motion can also be used as input to a computational fluid dynamics method to estimate the forces (Borazjani et al., 2012). Alternatively, the net forces and torques can be reconstructed from kinematics without requiring flow visualisation or fluid-dynamic models, based on inverse dynamics (Van Leeuwen et al., 2015; Voesenek et al., 2016). Since the hydrodynamics are the only source of external forces and torques acting on the fish, we can use the net accelerations of the fish—both linear and angular—to calculate the hydrodynamic forces and torques directly from the kinematics.

The kinematics of the fast start have been characterised in many species (Domenici and Blake, 1993; Fleuren et al., 2018; Kasapi et al., 1993; Müller and Van Leeuwen, 2004). Fast starts have been stated to occur mostly in the horizontal plane (Domenici and Blake, 1997), and most studies investigate two-dimensional kinematics from single-camera high-speed video (e.g. Domenici and Blake, 1993; Harper and Blake, 1990; Hertel, 1966). However, three-dimensional kinematics studies show a vertical motion component in adults (Butail and Paley, 2012; Fleuren et al., 2018; Kasapi et al., 1993) and larval fish (Nair et al., 2015; Stewart et al., 2014). This vertical component is ecologically relevant, since it may influence the effectiveness of predator evasion with the escape response (Stewart et al., 2014).

In this article, we analyse fast starts of zebrafish larvae at 5 days after fertilisation. We filmed fast-start behaviour with a synchronised five-camera setup with high spatial and temporal resolution (Fig. 5.1A). From these videos, we reconstructed the kinematics in 3D (Fig. 5.1B,C) and used these data to calculate resultant hydrodynamic forces and torques. Based on the three-dimensional dynamics, we examined how zebrafish larvae meet the functional demands on the fast start. We show that zebrafish larvae produce torques in
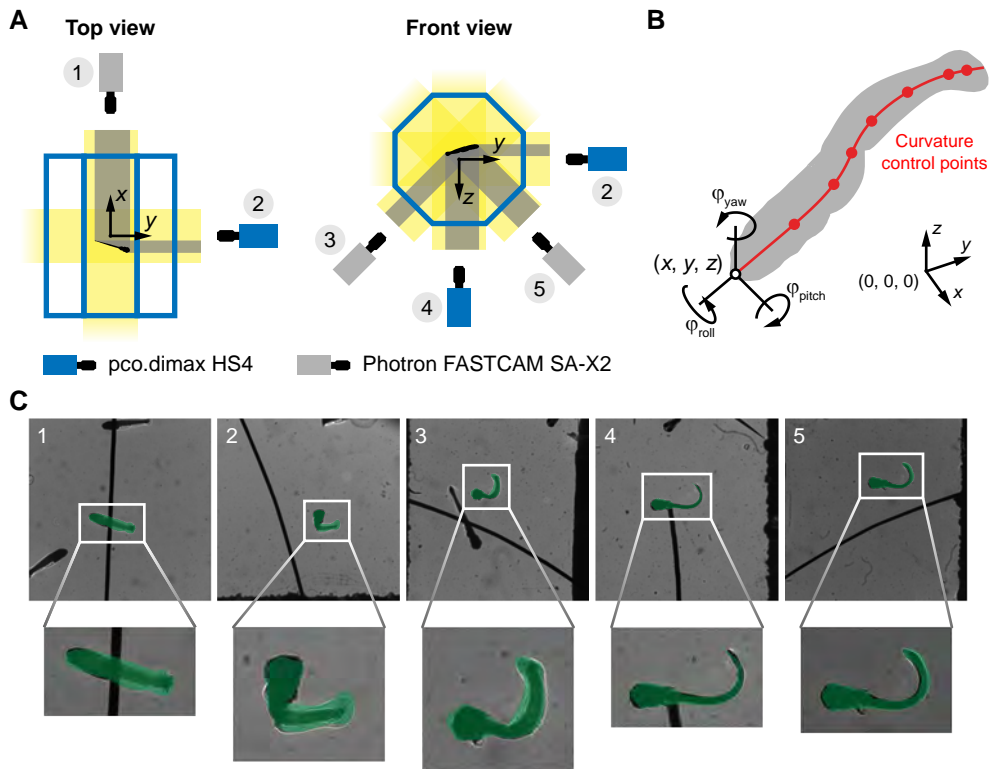
Figure 5.1: Multi-camera setup and automated tracking method. (A) Sketch of the five-camera setup, top view (left) and front view (right). (B) Parameterised fish model used in the automated tracking method. The model parameters are the 3D position of the snout, the 3D orientation of the head as expressed by the Tait-Bryan angles (roll, pitch, and yaw), and a series of control points for the curvature along the body. Adapted from Voesenek et al. (2016) (C) Overlap between the high-speed video images (grayscale background) and projections of the body model (transparent green). The numbers in the top left corner correspond to the camera numbers in A.

stage 1 that provide most of the reorientation of the body, while limited propulsion is produced. This is followed by a peak in propulsive force in stage 2, resulting in a strong acceleration of the centre of mass. The turn angle of a start is mostly determined by the amount of body curvature, while the speed at the end of stage 2 is mostly determined by the duration of the start. This allows early-development larvae to perform appropriate escape responses for threats approaching from different directions and at different speeds.

5.2 Results

5.2.1 Example of a fast start

We used an automated video-tracking method (Fig. 5.1) to reconstruct the fast-start motion of a zebrafish larva of 5 days after fertilisation, showing a change in direction of 83 deg, and a maximum speed of 0.15 m s^{-1}. The larva curls into a C-shape in stage 1, then unfolds

itself in stage 2 followed by a tail beat in opposite direction (Fig. 5.2A). Over the course of the start, the larva reorients itself from being approximately aligned with the negative x-axis of the world reference frame, to swimming in the direction of the positive y-axis. In addition, it changes its pitch angle from a nose-down stance to an upward motion.

The reconstructed forces vary around 0 in stage 1 of the start, in x-, y-, and z-direction (Fig. 5.2B). Around the halfway point of stage 2 the force peaks, mainly in 'forward' direction (i.e. the direction of the instantaneous velocity vector)—the larva pushes off and produces the largest acceleration resulting in a velocity peak approximately 2 ms later (Fig. 5.2C). At the same time as the forward peak, an upward (i.e. positive z-direction) force peak also occurs, causing an upward velocity of the centre of mass (Fig. 5.2C). This is followed by a force peak in opposite direction to the velocity, thus decelerating the larva.

The resultant x- and y-torques are limited in stage 1, but the z-torque is considerable (Fig. 5.2D). The yaw torque is similar to the z-torque since the deformation plane is approximately aligned with the x–y plane for most of the motion. The first peak of the yaw torque in stage 1 reorients the fish, and is produced while the fish is bending into a C-shape. Later in stage 1, a counter-torque is produced that brakes the reorientation. In stage 2, a higher peak in the same direction as the counter-torque is produced to reorient the fish in the opposite direction during the push-off tail beat.

We determined body angles (Fig. 5.2E) by integrating the angular velocity that we calculated from the angular momentum and instantaneous moment of inertia. The head angles are defined with the orientation of the stiff head region of the fish. The roll and pitch angle show different dynamics for the head than the body, because the coordinate systems are not aligned so their relative contribution to the out-of-plane orientation changes. The yaw angle is different due to the deformation of the larva—the head angle is not a good indicator for the orientation of the whole larva. The head angle shows large-amplitude variation across the start, while the body angle changes close to monotonously throughout the start, in the direction of reorientation.

5.2.2 Reorientation and speed

We determined the turn angle of the start by calculating the angle between the initial orientation of the larva and the heading at the end of stage 2. The initial orientation was defined as the unit vector pointing from tail tip to snout, while the heading was defined as the direction of the velocity vector of the centre of mass at the end of stage 2. The 'final speed' of the start is defined as the speed of the centre of mass at the end of stage 2. We show the turn angle (Fig. 5.3A,B) and final speed (Fig. 5.3C,D) as a function of the head-to-tail angle and start duration. The head-to-tail angle is defined as the angle between the head and the tail at the transition point from stage 1 to stage 2, an indication of the whole-body curvature at the most-curved point. The start duration is computed as the time interval between start initiation and the end of stage 2.

More strongly curved starts show a higher turn angle—the turn angle is strongly correlated to the head-to-tail angle, with a correlation coefficient of 0.83 ($P < 0.001$, $N = 33$;

5

A
2 mm   0.1 m s⁻¹   10 µN

Top view

Side view

B — Magnitude — Forward — Yaw — x — y — z

Force [µN] / Acceleration [m s⁻¹]

C

Velocity [m s⁻¹]

D

Torque [µN mm]

E — Body - - - Head — Roll — Pitch — Yaw

Angle [deg]

Stage 1   Stage 2

Time [ms]
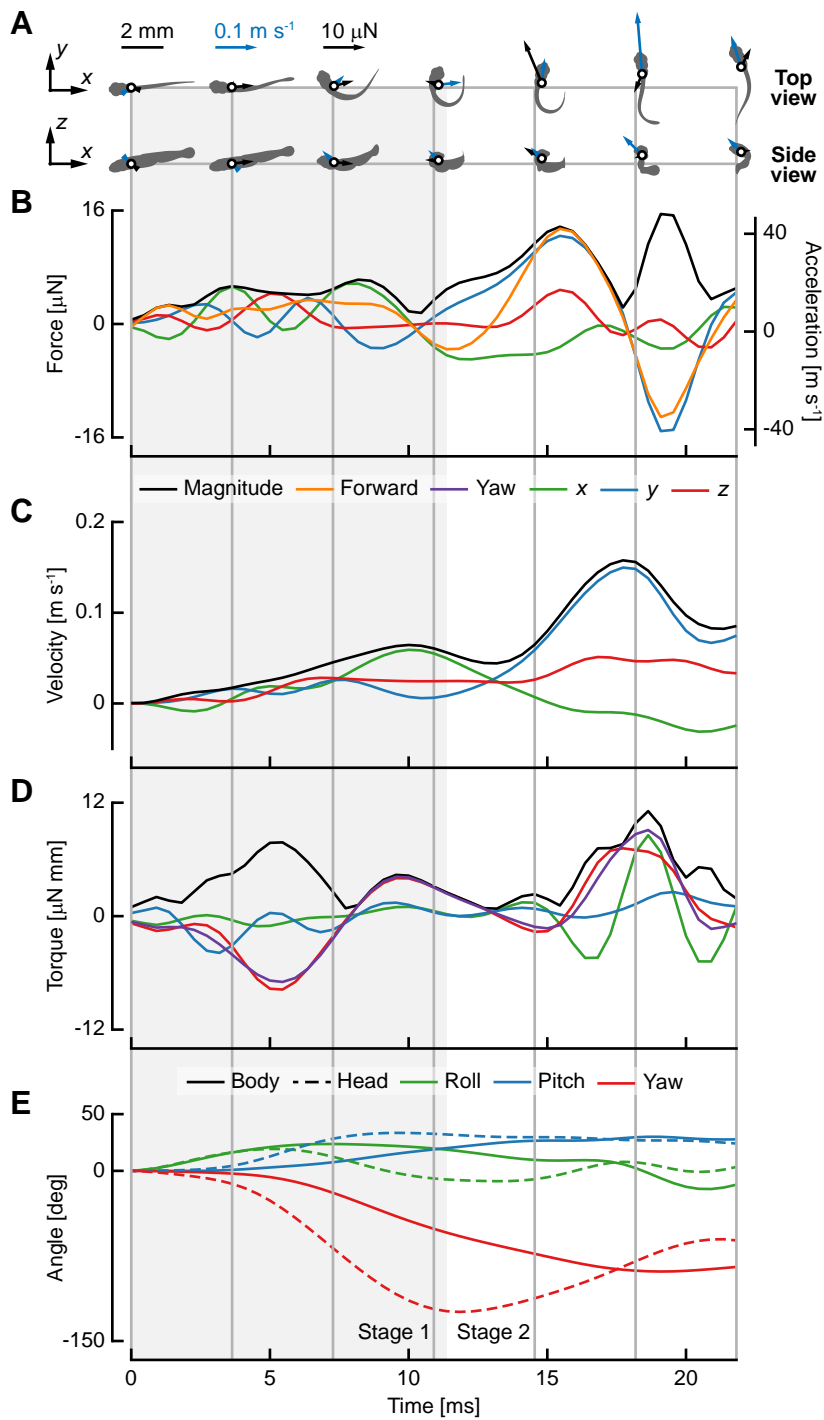
(Caption on the next page.)

Figure 5.2: Individual example of a fast-starting zebrafish larvae. Across all sub-panels, the light grey rectangle indicates stage 1, and the vertical dark grey lines connect the fish shapes in A to the time series in B–E. (A) Projections of the reconstructed fish model in the x–y (top) and x–z (bottom) plane. The white dot indicates the centre of mass, the blue arrow indicates the instantaneous velocity, and the black arrow represents the instantaneous resultant force. (B) The instantaneous resultant force in x (green), y (blue), z (red), and forward (orange) direction, and the force magnitude (black). The forward direction is defined as the vector pointing in the direction of the instantaneous velocity of the centre of mass. (C) The velocity of the centre of mass in x (green), y (blue, and z (red) direction. (D) The instantaneous resultant torque in x (green), y (blue), z (red), and yaw (purple) direction, and the torque magnitude (black). The yaw torque is defined as perpendicular to the deformation plane of the centre line. (E) The body (solid) angle and head (dashed) Tait-Bryan angles, roll (green), pitch (blue), and yaw (red).

bootstrapped 95% confidence interval ($\mathrm{CI}_{95\%}$): $[0.71, 0.92]$). The slope of the correlation is 0.59 ($\mathrm{CI}_{95\%}$: $[0.50, 0.65]$) deg of turn angle per deg of head-to-tail angle. In contrast, the turn angle is weakly correlated with the start duration, with a correlation coefficient of 0.19 ($P = 0.032$, $N = 33$; $\mathrm{CI}_{95\%}$: $[0.028, 0.36]$). A longer start duration tends to result in a slightly larger turn angle, at a rate of 0.84 ($\mathrm{CI}_{95\%}$: $[0.125, 1.61]$) deg ms^{-1}.

Shorter starts have a higher final speed—the final speed is strongly negatively correlated with the duration of the start, with a correlation coefficient of -0.77 ($P < 0.001$, $N = 33$; $\mathrm{CI}_{95\%}$: $[-0.89, -0.63]$). The slope of the correlation is -0.0061 (m s^{-1}) ms^{-1}— every millisecond shorter duration will result in a speed increase of 0.0061 m s^{-1}. We also fitted a power law to the final speed as a function of start duration, resulting in an exponent of -1.42 ($\mathrm{CI}_{95\%}$: $[-1.87, -1.05]$). The final speed is shows a weaker correlation with the head-to-tail angle, with a correlation coefficient of 0.38 ($P = 0.0033$, $N = 33$; $\mathrm{CI}_{95\%}$: $[0.11, 0.64]$). The slope is $4.88 \cdot 10^{-4}$ (m s^{-1}) deg^{-1} ($\mathrm{CI}_{95\%}$: $[1.33 \cdot 10^{-4}, 0.82 \cdot 10^{-4}]$); an increase in head-to-tail angle of 90 deg would result in an increase in final speed of 0.044 m s^{-1}.

The centrelines of the fish at the transition from stage 1 to stage 2 are shown in Fig. 5.3E, transformed to the coordinate system attached to the head of the fish in its initial orientation. The larvae curl up while the centre of mass remains in approximately the same position. The more strongly curved motions show a larger reorientation of the head, as well as a larger turn angle. In general, the head angle at the end of stage 2 is larger than the turn angle at the end of stage 2: the head turns further than the final heading at the end of stage 1, and then turns back over the course of stage 2.

We can divide the total angle change of the body during the start in an elevation angle change (vertical reorientation) and an azimuth angle change (horizontal reorientation), see Fig. 5.3F,G. The elevation change ranges from -35.0 deg to 34.2 deg (Fig. 5.3F); the azimuth change ranges from 3.9 deg to 102.7 deg (Fig. 5.3G). There is no significant correlation between the final speed and the azimuth change ($P = 0.77$, $N = 33$) or final speed and the elevation change ($P = 0.13$, $N = 33$).
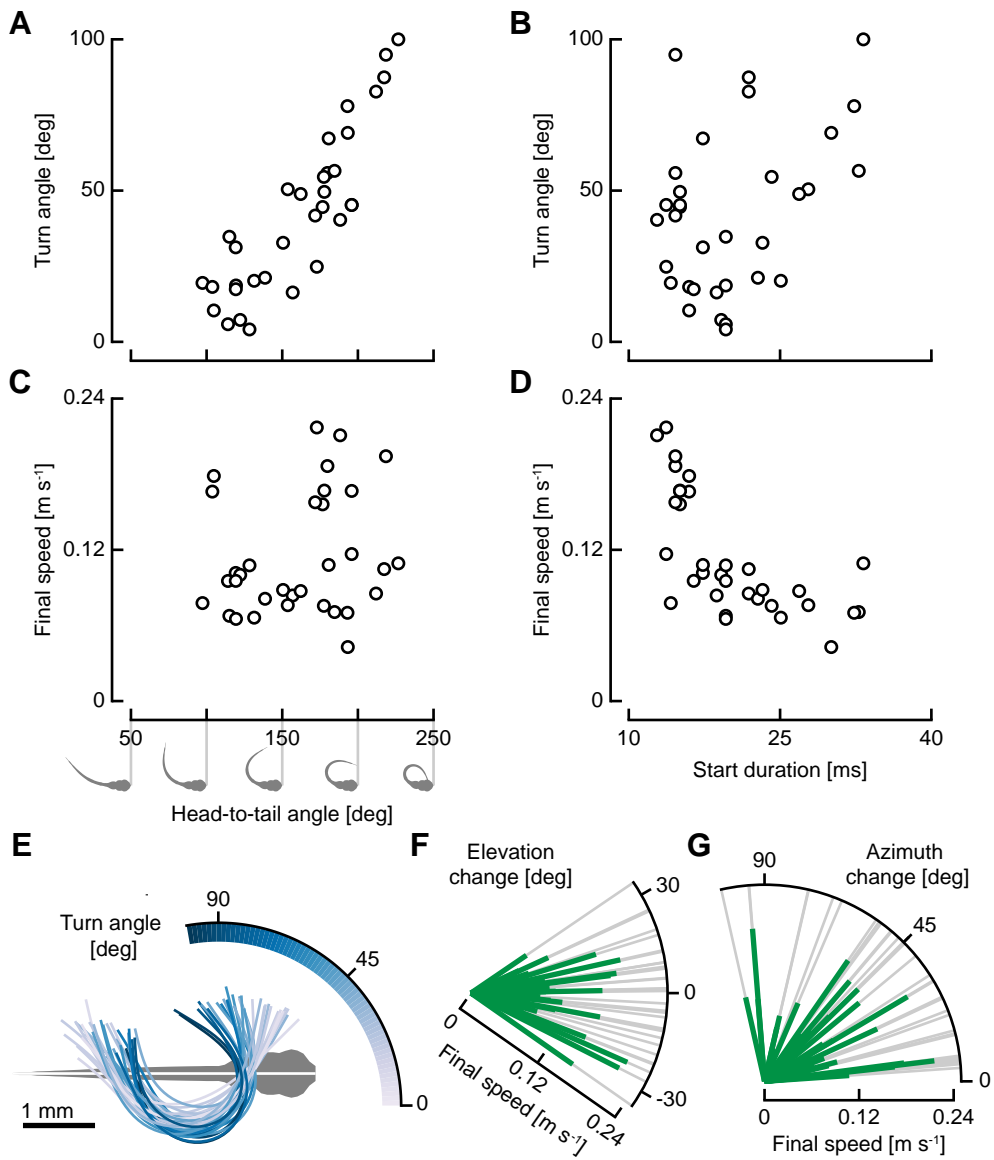
Figure 5.3: Higher start curvatures increase turn angle, while shorter start durations increase final speed. (A,C) The turn angle (A) and the final speed at the end of stage 2 (C) as a function of the maximum head-to-tail angle, an indication for the total amount of curvature of the body as illustrated below the horizontal axis of C. (B, D) The turn angle (B) and the final speed at the end of stage 2 (D) as a function of the start duration (computed as the time interval between start initiation and the end of stage 2). (E) The shape of the centreline at the transition from stage 1 to stage 2, coloured by the turn angle of the start. (F) The elevation change (curved axis) and final speed at the end of stage 2 (green radial lines) for all analysed starts. (G) The azimuth change (curved axis) and final speed at the end of stage 2 (green radial lines) for all analysed starts.

5.2.3 Stages of the fast start

We divided the fast start in stages with the same method as Fleuren et al. (2018), and analysed the first two stages. The durations of stage 1 and stage 2 are significantly correlated ($P <$ 0.001, $N = 33$; correlation coefficient 0.79, $CI_{95\%}$: $[0.70, 0.89]$). Stage 1 takes on average $52 \pm 4.6\%$ of the start until the end of stage 2 (Fig. 5.4A)—slightly over half of the first two stages is spent bending into a C-shape. No starts were recorded where stage 1 took less than 42% or more than 64% of the start duration. The larvae show a displacement between 3.3–$21.1\times$ larger in stage 2 compared to stage 1 (Fig. 5.4B). Also the speed is larger, both total speed (Fig. 5.4C; 1.5–$5.6\times$) and speed in the direction of the final heading (Fig. 5.4C, 'forward'; 1.7–$23.6\times$). The total speed in stage 1 is higher than the 'forward' speed—the centre of mass moves slightly in stage 1, but not much in 'forward' direction (i.e. in the direction of the velocity at the end of stage 2).

In all cases, the peak linear momentum is larger in stage 2 than in stage 1 (Fig. 5.4D; 1.5–$5.6\times$), while the peak angular momentum is often smaller in stage 2 than in stage 1 (Fig. 5.4E; 0.58–$1.9\times$). Stage 1 therefore often shows higher angular velocities than stage 2. In most cases, the peak force is higher in stage 2 than in stage 1 (Fig. 5.4F), this holds for both the total force (0.80–$4.6\times$) and the 'forward' force (i.e. in the direction of the velocity at the end of stage 2; 0.82–$10.3\times$). Not much force is produced in stage 1, especially in the direction of the start—the acceleration is mostly visible as an undirected wiggling of the centre of mass. In most cases, the torque is also higher in stage 2 than in stage 1 (Fig. 5.4G; 0.78–$3.9\times$), but the ratio is smaller than that of the speed and forces; some sequences even show higher torques in stage 1 than stage 2. The higher torques in stage 2 are presumably produced by the higher forces during the push-off.

5.2.4 Reorientation

Stage 1 has a significantly higher contribution to the yaw angle change than stage 2 (Fig. 5.5A; t-test, $P < 0.001$, $N = 33$); on average the contribution of stage 1 is 28.7 ± 13.7 deg higher than the contribution of stage 2. For smaller total yaw changes, stage 2 might have a negative contribution, undoing part of the reorientation of stage 1. Phase plots of the yaw angle (Fig. 5.5B) show that starts with relatively small turn angles generally have a negative contribution of stage 2 to the body yaw angle, while for large turn angles the body yaw angle changes almost monotonously. In contrast, the head yaw angle shows considerably larger variation over the fast start than the body angle, reaching a maximum near the end of stage one, before rotating in opposite direction in stage 2.

For all fast starts, we averaged the linear momentum, angular momentum, and change in moment of inertia normalised by their maximum value (Fig. 5.5C–E). The linear momentum (Fig. 5.5C) reaches a small peak in stage 1, followed by a much larger peak in stage 2, where peak speed is reached. In contrast, the angular momentum (Fig. 5.5D) shows its largest peak in stage 1, followed by a lower peak in stage 2. The large peak in angular momentum just proceeds to the dip in moment of inertia (Fig. 5.5E). A combination of large

A

Frequency [%]

Stage 1 relative duration [-]

B **Displacement** [mm]

Stage 2

Stage 1

C **Peak speed** [m s⁻¹]

Stage 2

Total ○
Forward ●

Stage 1

D **Peak linear momentum** [μg m s⁻¹]

Stage 2

Stage 1

E **Peak angular momentum** [μg m² ms⁻¹]

Stage 2

Stage 1

Ratio of stage 2 to stage 1: 1–2 2–4 >4

F **Peak force** [μN]

Stage 2

Total ○
Forward ●

Stage 1

G **Peak torque** [μN mm]
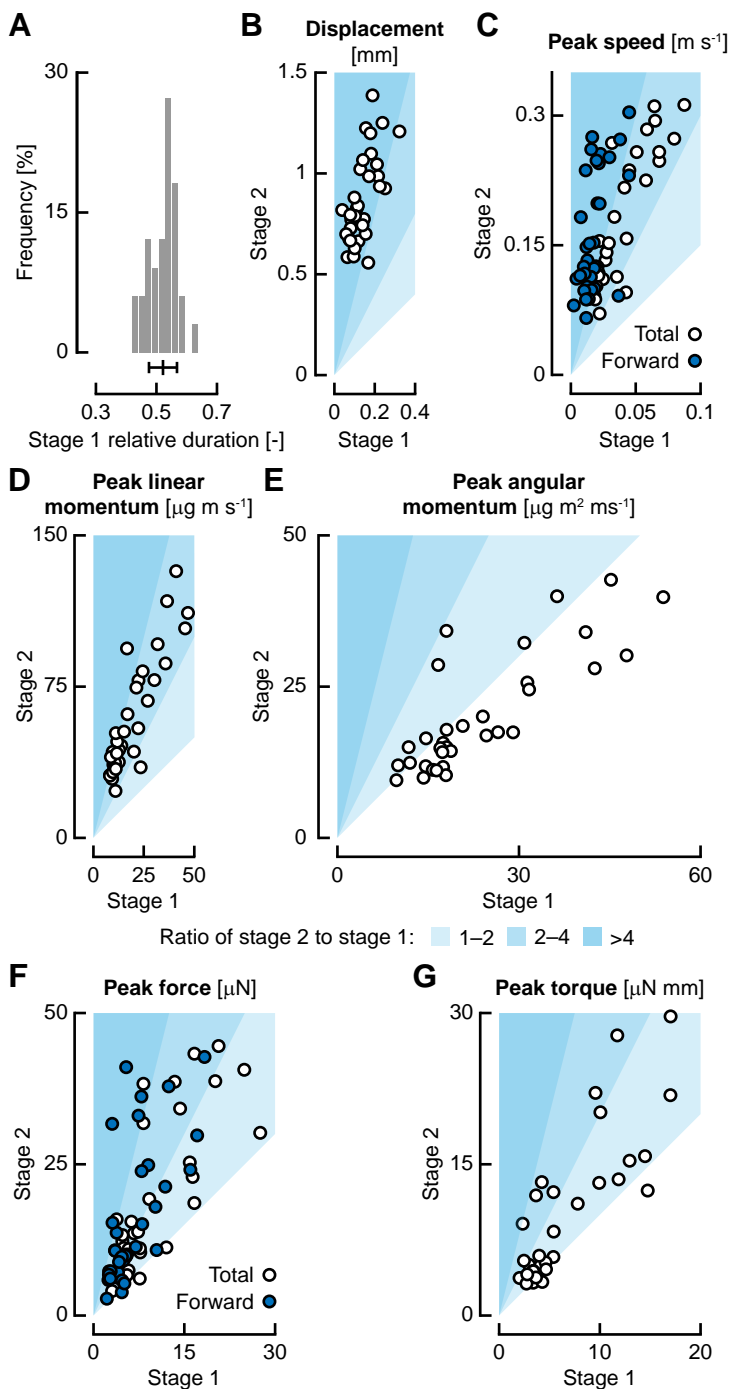
Stage 2

Stage 1

(Caption on the next page.)

Figure 5.4: Stages of the fast start: highest speeds, forces, and torques occur in stage 2. (A) The duration of stage 1 with respect to the duration of the start (computed as the time interval between start initiation and the end of stage 2), the histogram indicates the frequency of each bin as a percentage of all starts. The bar below the histogram shows the mean and one standard deviation. (B–G) The white region indicates where the values in stage 2 are lower than stage 1, in the light blue region, the values for stage 2 are 1–2× higher, in the medium blue region 2–4×, and in the dark blue region > 4×. The contribution of stage 1 is on the horizontal axis, the contribution of stage 2 on the vertical axis. (B) Net displacement, i.e. the reduction in distance to the final position of the centre of mass at the end of stage 2. (C) Peak speed; white dots indicate the total speed, blue dots indicate the speed in the direction of the final heading. (D) Peak linear momentum. (E) Peak angular momentum. (F) Peak force; white dots indicate the total force, blue dots indicate the force in the direction of the final heading. (G) Peak torque.

angular momentum and low moment of inertia leads to a high angular velocity, indicating a strong reorientation in stage 1. After the peak, the angular momentum reduces, indicating that the yaw rotation is braked by a counter-torque before rising again as the fish beats its tail in the opposite direction.

5.2.5 Propulsion in stage 2

We calculated the speed of the tail as the speed averaged over the posterior 10% of the body, relative to the speed of the centre of mass. The peak tail speed over the fast starts tends to increase with decreasing duration of the motion (Fig. 5.6A), with a correlation coefficient of -0.67 ($P < 0.001$, $N = 33$; $\text{CI}_{95\%}$: $[-0.79, -0.54]$). For every millisecond of decrease in duration, the peak tail speed increases by 20.3 m s^{-1} ($\text{CI}_{95\%}$: $[16.3, 23.9]$). In addition, we fitted a power law to the tail speed as a function of start duration, resulting in an exponent of -1.27 ($\text{CI}_{95\%}$: $[-1.68, -0.96]$). Since much of the propulsive force is produced at the tail, which moves in opposite direction to the velocity of the centre of mass (Fig. 5.1A), the peak force tends to increase with increasing peak tail speed (Fig. 5.6B), with a correlation coefficient of 0.85 ($P < 0.001$, $N = 33$; $\text{CI}_{95\%}$: $[0.70, 0.94]$). The slope of the correlation is 58.4 μN (m s^{-1})$^{-1}$ ($\text{CI}_{95\%}$: $[48.3, 64.7]$). In this way, a decrease in duration leads to an increase in tail speed, and hence a corresponding increase in propulsive force, and therefore leads to an increase in escape acceleration.

5.2.6 Pectoral fin use during the fast start

For each time point in the fast start, we manually indicated whether or not the pectoral fins were abducted. During high-speed starts, the pectoral fins remain adducted for the entire duration of the start, while during slower starts, they are abducted for part of the start (Fig. 5.7A). Whether the pectoral fins are abducted during a start does not depend on the turn angle (Fig. 5.7A). In starts where the fins were used, they were first abducted in stage 1 after $8.2 \pm 6.0\%$ of the start duration (Fig. 5.7B). They were then adducted in stage two, after $75 \pm 8.3\%$ of the start duration, resulting in an average duration of pectoral fin abduction of $67 \pm 8.6\%$ of the start.

In starts where the fins are used, the fraction of the start that they are abducted correlates significantly with the change in elevation ($P = 0.0252$, $N = 17$), with a correl-
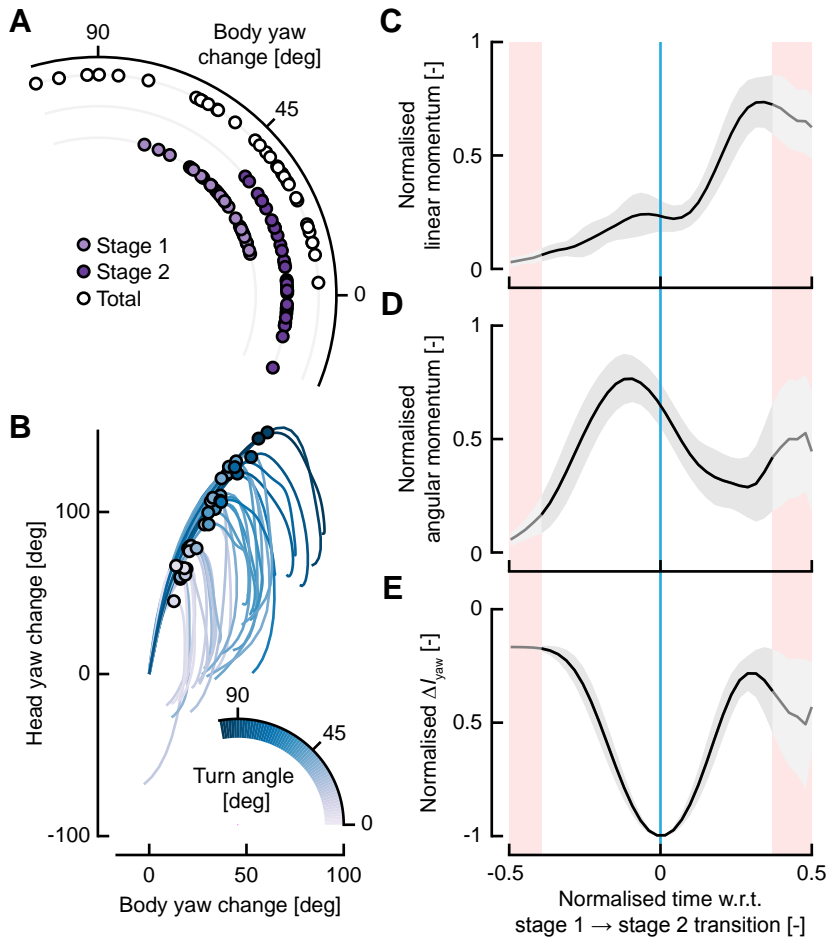
Figure 5.5: Reorientation during the fast start. (A) Change in yaw angle in stage 1 (light purple), stage 2 (dark purple), and the complete start (white). (B) Phase plots of the change in head yaw angle to the change in body yaw angle, coloured by the turn angle of the start (the angle between the initial orientation of the fish and the direction of the velocity vector at the end of stage 2). The dots indicate the transition point from stage 1 to stage 2. (C–E) The black line indicates the mean, with ± 1 standard deviation shown by the grey area. The red bands at the left and right indicate time points for which not all data is present due to differences in the relative length of stage 1 and 2. The blue line indicates the transition point from stage 1 to stage 2. (C) The linear momentum profile over the start, normalised by its maximum value and aligned to the transition from stage 1 to stage 2 before averaging over all starts. (D) The angular momentum profile over the start, normalised by its maximum value and aligned to the transition from stage 1 to stage 2 before averaging over all starts. (E) Changes in moment of inertia in the deformation plane (ΔI_{yaw}), normalised by its minimum value and aligned to the transition from stage 1 to stage 2 before averaging over all starts.

ation coefficient of 0.54 (CI$_{95\%}$: $[0.15, 0.83]$). In starts where the fins are not used, large elevation changes could also be produced—the mean elevation change between starts with and without fins are not significantly different (two-sample t-test, $P = 0.82$, $N_1 = 17$, $N_2 = 16$).
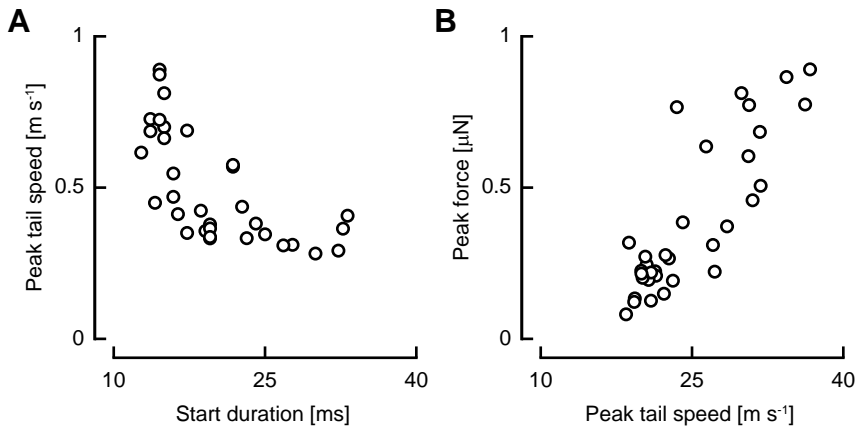
Figure 5.6: Higher tail speeds with shorter durations lead to higher forces. (A) The peak tail speed in stage 2 as a function of the start duration. (B) The peak force in stage 2 as a function of the peak tail speed in stage 2.

5.3 Discussion

We reconstructed the three-dimensional motion of zebrafish larvae of 5 days after fertilisation during C-start escape responses and reconstructed linear and angular momentum, and forces and torques. We consider the results of the analysis in the context of the functional demands of the start, as outlined in the introduction.

5.3.1 Producing acceleration

The primary demand of a fast start is to accelerate the body, both linearly and rotationally. This acceleration is produced by a large force peak in stage 2 (Fig. 5.2B, Fig. 5.4F), causing an increase in linear momentum, and hence speed (Fig. 5.2C, Fig. 5.4D, Fig. 5.5C). Although the body is prepared for the propulsive stroke by curling up in stage 1, the body curvature (as expressed with the head-to-tail angle) correlates with the speed relatively weakly (Fig. 5.3C). In contrast, the speed shows a strong inverse correlation with the duration of the start, with a power law exponent of -1.42: shorter starts lead to higher speeds (Fig. 5.3D). The durations of the stage 1 and stage 2 do not vary independently (Fig. 5.4A). Hence, shorter start durations lead to shorter durations of stage 2, resulting in an increase in tail speed (Fig. 5.6A) with a power law exponent of -1.27, and a resulting increase in force (Fig. 5.6B).

   To produce these forces, fish produce fluid-dynamic jets. During stage 1, fish larvae produce a jet flow into the C-shape (Li et al., 2014; Müller et al., 2008). A CFD simulation of a single zebrafish larva swimming sequence (Li et al., 2012) showed that initially this mainly produces a torque that reorients the fish. The jet is then reoriented along the body in stage 2, where it produces propulsive force, in agreement with our reconstructed resultant forces (Fig. 5.2B). Adult bluegill sunfish show a similar flow pattern in velocity field measurements (Tytell and Lauder, 2008).
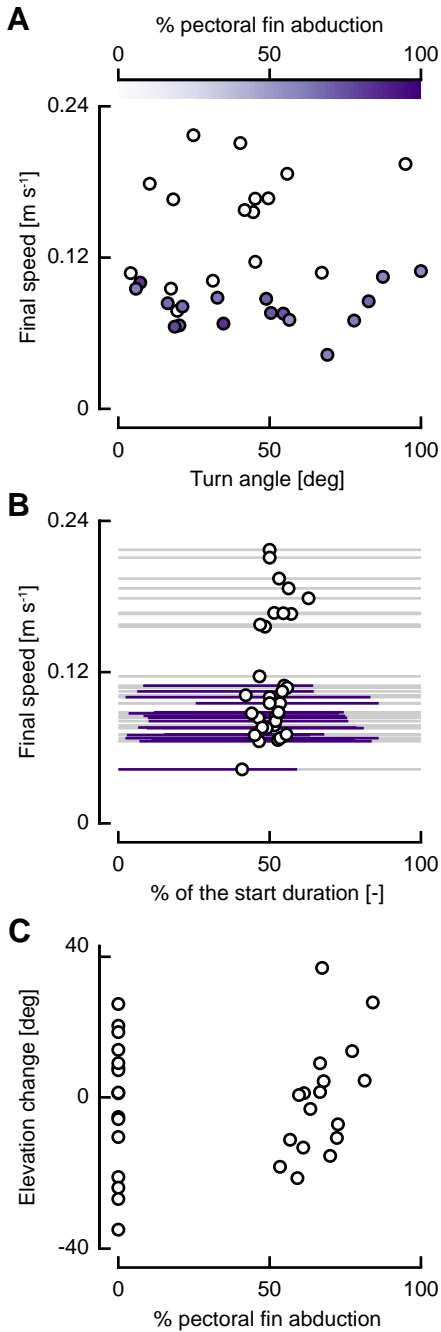
Figure 5.7: Pectoral fins are only abducted during low-speed starts and help produce elevation change. (A) The percentage of the start duration (computed as the time interval between start initiation and the end of stage 2) that the pectoral fins are abducted (colours) in the turn angle–final speed landscape. (B) The relative time as a fraction of the start that the pectoral fins are abducted (purple lines) as a function of the speed. Each grey line indicates a start, with the transition point between stage 1 and 2 indicated by the dot. (C) The elevation change as a function of the percentage of the start that the pectoral fins are abducted.

Based on numerical simulations it has been found that the motion of the larval C-start was near-optimal for maximising escape distance in a given time (Gazzola et al., 2012)—a measure that corresponds to maximising the mean acceleration during a start from a standstill. They also found that a higher curvature could result in a higher escape distance, given a start duration; this corresponds to the weak correlation that we find for speed with head-to-tail angle. For (near-)cyclic swimming of larval fish, the swimming speed was found to increase with increasing tail-beat frequency and to a lesser extent amplitude (Van Leeuwen et al., 2015). The fast start duration is the equivalent of the frequency, while the head-to-tail angle is connected to the tail-beat amplitude. Hence, we see similar effects on the speed in cyclic swimming as in fast starts.

5.3.2 Reorienting the body

The larvae produce a wide range of escape directions (Fig. 5.3F,G), both in azimuth and, to a lesser extent, in elevation. The turn angle of a start correlates strongly with the head-to-tail angle: more strongly curved starts tend to show a larger turn angle (Fig. 5.3A,E). The turn angle correlates weakly with the duration of the start (Fig. 5.3B), where longer starts show a slightly larger turn angle. Hence, large turn angles do not take much more time to produce than small turn angles. In adult fish, the start duration correlates more strongly to the escape angle (angelfish: Domenici and Blake, 1991; goldfish: Eaton et al., 1988). This suggests a difference in reorientation between adults and zebrafish larvae: adults seem to use an approximately fixed turn rate, while larval zebrafish increase turn rates with increasing turn angles.

The changes in escape angle are mostly produced in stage 1 (Fig. 5.5A), despite lower peak torques (Fig. 5.4G). The yaw torque is consistently in the direction of turning during the first part of stage 1 (Fig. 5.2D), causing the angular momentum to show its largest peak in stage 1 (Fig. 5.5D), while the moment of inertia is close to its minimum (Fig. 5.5E). The high angular momentum combined with a low moment of inertia leads to a high angular speed, allowing large turn angles. At the end of stage 1, the torque reverses sign (Fig. 5.2D), thus reducing the angular momentum. Together with the increase in moment of inertia (Fig. 5.5E), this decreases the angular speed. The torque then decreases until the end of stage 2, where the torque increases again, rotating the fish in opposite direction (Fig. 5.2D). This reorienting torque and the following counter-torque were shown to be caused mainly by pressure forces, while the largest shear forces were found at the head, and counteracted the initial reorienting torque (Li et al., 2012).

Previous studies of adult fish have shown that the turn angle of the head in stage 1 correlates with the turn angle during the complete fast start (Domenici and Blake, 1993; Eaton et al., 1988; Fleuren et al., 2018). This has also been found for fast starts of zebrafish larvae (Nair et al., 2015). Danos and Lauder (2007) analysed routine turns of zebrafish larvae, for which they created a model where only the body bending caused a change in head angle, resulting in a large underprediction of the escape angle. They suggested that the additional effect is caused by fins. In fast starts, however, the pectoral fins cannot explain the reori-

entation torque as they are adducted at high speeds, even for large turn angles (Fig. 5.7A). Without fins, fish have been shown to produce a yaw torque in the first stage of the start (Li et al., 2012; Song et al., 2018). This torque is mainly produced by pressure forces at the tail, which has a much larger lever arm with respect to the centre of mass than the pectoral fins.

5.3.3 Alternatives to the head angle

The head angle change after stage 1 is connected to the head-to-tail angle of the fish due to the stereotypical nature of the C-bend (Fig. 5.3E). The tail excursion of zebrafish larvae was found to correlate with the head yaw angle (Nair et al., 2015), so the head-to-tail angle correlates with the head yaw angle. Rather than use the head angle to indirectly indicate the curvature of the start, we use the head-to-tail angle as a more direct indicator of the whole-body curvature. Since the posterior part of the fish produces much of the reorienting torque (Li et al., 2012; Song et al., 2018), it is useful to consider the complete body when analysing at escape direction.

Furthermore, rather than using the head angle as an indicator for orientation (Domenici and Blake, 1993; Eaton and Emberly, 1991; Nair et al., 2015), we use the 'body angle', that we calculate from the mass distribution. The head angle is not representative of the heading of the fish: they differ considerably across most of the fast start (Fig. 5.2E, Fig. 5.5B). The body angle is more difficult to quantify than the head angle, as it requires a three-dimensional mass distribution model of the fish, and reconstructed kinematics of high accuracy (Van Leeuwen et al., 2015). Nonetheless, it is worth calculating when analysing reorientations, as it gives a much more accurate representation of the reorientation of the fish mass. In the absence of body angles, the head angle cannot be used to replace it, as it shows completely different dynamics.

5.3.4 Control of the fast start

The turn angle and final speed seem to be adjusted mostly independently for C-starts of zebrafish larvae. The turn angle can be adjusted with the head-to-tail angle (i.e. body curvature), having relatively limited effect on the escape speed (Fig. 5.3A,C). The escape speed can be adjusted with the start duration, having a limited effect on the escape angle (Fig. 5.3B,D). In adult goldfish, the escape trajectory was found to be controlled by the relative size of the initial and second contractions and the timing between them with minimal feedback from sensors (Foreman and Eaton, 1993). Assuming that starts are controlled similarly in larval zebrafish, the head-to-tail angle and start duration are presumably a direct result of these parameters, and might be used as proxies for them.

The duration of stage 1 and stage 2 vary concomitantly (Fig. 5.4A), also previously found for two species of adult fish (Webb, 1975) and zebrafish larvae (Nair et al., 2015). The larvae do not individually tune the duration of stage 1 and stage 2 to adjust the angle and speed of their escape. At a given escape speed, smaller head-to-tail angles are produced

by turning more slowly, rather than turning at the same rate but shorter. Furthermore, the duration of stage 2 is not shortened independently of stage 1 to increase the tail speed, and hence propulsive force. This might suggest a limitation on how quickly the tail-beat duration can be changed from one tail-beat to the next.

The elevation of the start has been found to be controlled by dorsoventral excursions of the midline (Nair et al., 2015). In the slow starts where the pectoral fins were used, the amount of time that the pectoral fins were abducted correlates with the elevation change (Fig. 5.7C). Larvae of 5 dpf naturally show a nose-down pitch moment (Ehrlich and Schoppik, 2017), so a hydrodynamic torque must be produced to counteract this for positive, or perhaps even less-negative elevation changes. The action of the pectoral fins is an additional effect to the dorsoventral tail excursion, since starts without pectoral fin abduction do not produce significantly different elevation changes. The pectoral fins are only used during relatively slow C-starts (Fig. 5.7A). At lower speeds, perhaps the required pitch torques cannot be produced by the body alone, requiring help of the pectoral fins. In contrast, at high speeds, the body is able to produce sufficient pitch torque, and can adduct the fins to reduce drag to achieve a higher escape speed.

5.3.5 Timing the start

The importance of fine-tuning the speed and direction of the escape depends on speed of the predator relative to the prey. When the speed of the predator is close to the speed of the prey, faster starts will result in greater survival probability (Walker et al., 2005). However, for a much faster or much slower predator than prey, the speed and direction are less important than for intermediate predator speeds (Soto et al., 2015). Zebrafish larvae have been stated to be mostly in the 'slow predator' regime, where escape timing is the dominant parameter (Stewart et al., 2013) influencing escape performance, although below strong reductions ($> 50\%$) in escape speed, the probability of escape from the predator's suction flow drops rapidly (Nair et al., 2017).

Zebrafish larvae show a relatively long stage 1 (Fig. 5.4A), in which hardly any propulsion is produced (Fig. 5.4B,C,F), reducing the mean acceleration of the start. However, if the zebrafish detects the threat sufficiently early, it can initiate stage 1 of the fast start to begin stage 2 at the optimal moment. Hence, the relatively long duration of stage 1 without significant propulsion might not be a disadvantage in escaping predators for zebrafish larvae.

5.3.6 Contributions of stage 1 and stage 2

Zebrafish larvae show a relatively long stage 1 (Fig. 5.4A), in which hardly any propulsion is produced (Fig. 5.4B,C,F), reducing the mean acceleration of the start. However, if the zebrafish detects the threat sufficiently early, it can initiate stage 1 of the fast start to begin stage 2 at the optimal moment. Hence, the relatively long duration of stage 1 without significant propulsion might not be a disadvantage in escaping predators for zebrafish larvae.

The role of stage 1 and stage 2 in the fast start has been the subject of on-going debate. The first stage has often been called purely preparatory (Domenici and Blake, 1997; Hertel, 1966; Weihs, 1973). Stage 1 prepares the body for stage 2: its preparatory role is clear (Fleuren et al., 2018). In addition to the preparatory function, it has also been argued that stage 1 may contribute significantly to propulsion (Fleuren et al., 2018; Tytell and Lauder, 2008; Wakeling, 2006). For bluegill sunfish, $37.2 \pm 0.6\%$ of linear momentum is produced after stage 1 (Tytell and Lauder, 2008); for the larval zebrafish this is somewhat lower at $27.8 \pm 8.2\%$ (Fig. 5.5C). Based on the linear momentum, there is some propulsion component in stage 1, but the displacement, speed, peak linear momentum, and peak forces are all considerably lower compared to stage 2 (Fig. 5.4). Arguably, the preparatory role of the start, including reorientation, is more important for zebrafish larvae than the propulsive role.

5.3.7 Conclusions

In this article, we analysed the dynamics of the fast start of zebrafish larvae at five days post fertilization. We confirm that early-development larvae can produce effective escape response in a wide range of directions (both azimuth and elevation) and speeds. The larvae seem to be able to adjust the direction and speed of their escape close to independently. They adjust the escape angle mostly with the extent of body curvature, while the escape speed is adjusted mostly with the duration of the start. Apart from its preparatory role, stage 1 is used to produce most of the reorientation, while stage 2 produces most of the acceleration of the centre of mass. This shows that despite their early stage of development, zebrafish larvae meet the functional demands for producing effective escape responses.

5.4 Materials and methods

5.4.1 Animals

We used two batches (from different parents) of 50 wild type zebrafish larvae (*Danio rerio*, Hamilton 1822), bred at the Carus animal facilities of Wageningen University. All fast start sequences were filmed for fish of 5 days post fertilisation, with a body length of 4.2 ± 0.14 mm. We housed each batch in a separate tank, kept at a constant temperature of $27°$C. The experimental aquarium was also maintained at $27°$C by heating the experimental room. We placed 50 larvae at the same time in the aquarium. The fish were stimulated to perform fast start manoeuvres by approaching them with a horse hair. Sequences where the hair touched the fish were eliminated from analysis, because the resultant forces would not only be from the hydrodynamics, but also from the hair. The influence of the flow induced by the hair is limited: the centre of mass of the larvae hardly moves before the initiation of the start. All experiments were approved by the Wageningen University animal ethics committee.

5.4.2 Experimental setup

The swimming of larval zebrafish was recorded with a synchronised high-speed video setup with five cameras with different orientations (Fig. 5.1A). Zebrafish larvae were placed in a glass aquarium in the shape of an octagonal prism (12 mm sides). To limit refraction effects, the cameras were placed perpendicular to the glass from five angles. From the bottom and the right side, we used pco.dimax HS4 cameras (PCO AG, Kelheim, Germany; 2000×2000 pixels). From the back, bottom left, and bottom right side, we used Photron FASTCAM SA-X2 cameras (Photron, Tokyo, Japan; 1024×1024 pixels). All cameras were equipped with 105 mm $f/2.8$ macro lenses (105 mm $f/2.8$ FX AF MICRO-NIKKOR and AF-S 105 mm $f/2.8$G VR Micro, Nikon, Tokyo, Japan) with +5 diopter close-up lenses (DHG Achromat Macro 200(+5), Marumi, Nagano, Japan), mounted on 27.5 mm extension tubes (PK-13, Nikon, Tokyo, Japan). All cameras were recording at 2200 frames per second, synchronised with a pulse generator (9618+, Quantum Composers, Bozeman, Massachusetts, USA). By using a collimated light setup, we created high-contrast shadow images with large depth of field. Collimated light was produced by shining an LED light source (MNWHL4/MWWHL4, Thorlabs Inc., Newton, New Jersey, USA) placed in the focus of a 250 mm lens (250D, Canon, Tokyo, Japan). The light setup was aligned such that the collimated light was parallel with the optical axis of the camera. Since the fish larvae were in an aquarium between the light source and the camera, they projected deep shadows on a brightly lit background image at short shutter speeds ($\approx 10\ \mu s$).

5.4.3 Camera calibration and modelling

We generated calibration points visible in all cameras by moving a sharp-tipped needle through the measurement volume with a computer-controlled micromanipulator (MCL-3, LANG GmbH & Co. KG, Hüttenberg, Germany). The needle was moved through a cuboid volume, at $5 \times 5 \times 5$ uniformly spaced points along each dimension. This resulted in 125 images per camera with a known position of the needle tip. In each of these images, we indicated the needle tip manually with a custom Python 3 program.

Camera projections were modelled by a simple affine transform, where we ignored perspective effects. For our camera setup, this is a valid assumption, as the shadows projected onto the sensor by the fish are (theoretically) independent of the distance from the sensor, owing to the collimated light. The affine transform for each camera was parameterised by a 3D translation and the orthonormal basis of the image plane coordinate system (i.e. one outward and two in-plane vectors). From an initial estimate of the camera parameters, we started a constrained optimisation procedure in MATLAB (interior-point algorithm as implemented in `fmincon`; R2016a, The Mathworks, Natick, Massachusetts, USA). Using this procedure, we minimised the sum of squared differences between the clicked image coordinates and the reprojected image coordinates, while maintaining orthonormality (i.e. all vectors perpendicular and of unit length) of the image plane basis vectors.

5.4.4   Motion reconstruction

The motion of the larvae was reconstructed from the synchronised high-speed video with the method described in Voesenek et al. (2016); it was originally developed in MATLAB, but converted to Python 3. We will briefly summarise the method here, but refer the reader to the original article for more details.

The method is based on a virtual representation of the camera setup and the fish larva. The virtual camera setup was created from the results of the calibration procedure described above. It transforms a point in world coordinates to image plane coordinates for each camera. The fish was represented by a three-dimensional surface model. The shape, position, and orientation of this model were determined by 14 parameters (3 for position, 3 for orientation, 8 for body curvature control points; Fig. 5.1B)—we ignore dorsoventral curvature, deformation of the median fin fold, and motion of the pectoral fins. For every point in time, we applied the Nelder-Mead optimisation algorithm to these parameters to minimise the difference between virtual images, for which the 3D model was projected onto the virtual cameras, and the real high-speed video images, from which the fish was segmented. The result was a time series of body curvature along the body, position, and orientation that described a three-dimensional surface with optimal overlap (Fig. 5.1C). We smoothed each of these time series with regularised least squares (Eilers, 2003; Stickel, 2010), with derivatives of order 4, and a smoothing parameter of 100.

The reconstructed time series of parameters uniquely described the 3D shape of the fish. Under the assumption of a constant density across the fish, the mass distribution is known at every point in time. This allowed us to calculate its linear and angular momentum, and therefore the resultant fluid-dynamic forces and torques (Voesenek et al., 2016). In addition, for each frame in each tracked sequence, we determined visually from the bottom camera whether the pectoral fins were abducted or adducted.

5.4.5   Body angle calculation

We calculated the body angle by integrating angular velocity obtained from the angular momentum. We calculated the angular velocity as $\boldsymbol{\omega} = \mathrm{I}^{-1}\mathbf{L}$, where $\boldsymbol{\omega}$ is the angular velocity vector in rad s^{-1}, I is the moment of inertia tensor, and $\mathbf{L}$ is the angular momentum vector. We integrated this angular velocity vector with the midpoint rule (Simo and Wong, 1991; Zupan and Saje, 2011) to obtain rotation matrices, with the rotation matrix of the head at the beginning of the start as the initial condition. Finally, we reconstructed the body roll, pitch, and yaw Tait-Bryan angles from these rotation matrices.

5.4.6   Statistics

For all statistical tests, we used a significance threshold of 0.05. We performed all statistics with MATLAB (R2018b, The Mathworks, Natick, Massachusetts, USA) and the associated Statistics and Machine Learning Toolbox (R2018b, The Mathworks, Natick, Massachusetts, USA). We verified normality of the data with a Kolomogorov-Smirnov test

(MATLAB's `kstest`). To calculate correlation coefficients, we fitted linear models (MAT-LAB's `fitlm`). We standardised all data before fitting the model by subtracting its mean and dividing by its standard deviation, which allowed us to use the fit coefficients as correlation coefficients (Schielzeth, 2010). To calculate confidence intervals of the correlation coefficients, we used bootstrapping with $10,000$ repetitions, then calculated the 2.5^{th} and 97.5^{th} percentile. The correlation coefficients and their confidence intervals were converted back into slopes by multiplying with σ_x/σ_y, the ratio of standard deviations.

For the models of the turn angle and speed as a function of the head-to-tail angle and duration, we initially fitted models with interaction terms between head-to-tail angle and duration. For both models, the correlation coefficients of the interaction terms were not significantly different from 0 (head-to-tail angle: $P = 0.069$, $N = 33$; speed: $P = 0.37$, $N = 33$), so we eliminated them from the model.

For selected pairs of variables, we performed total-least-squares curve fits with an optimisation method (MATLAB's `fminsearch`). We normalised both variables to a range of $[0, 1]$. We fit functions of the form $y = c_1 x^{c_2}$, since we expect a negative power law with an asymptote $y = 0$ when $x \rightarrow \infty$. For each set of trial coefficients, we calculated the perpendicular distance to the curve for all data points. The squared sum of these distances was used as the objective function of the optimisation, resulting in a set of best-fitting coefficients c_1 and c_2. By bootstrapping with $10,000$ repetitions and computing the 2.5^{th} and 97.5^{th} percentile, we calculated 95% confidence intervals of the coefficients.

Acknowledgements

References

Ahlborn, B., Harper, D. G., Blake, R. W., Ahlborn, D. and Cam, M. (1991). Fish without footprints. *J. Theor. Biol.* **148**, 521–533.

Borazjani, I., Sotiropoulos, F., Tytell, E. D. and Lauder, G. V. (2012). Hydrodynamics of the bluegill sunfish C-start escape response: three-dimensional simulations and comparison with experimental data. *J. Exp. Biol.* **215**, 671–684.

Butail, S. and Paley, D. A. (2012). Three-dimensional reconstruction of the fast-start swimming kinematics of densely schooling fish. *J. R. Soc., Interface* **9**, 77–88.

Danos, N. and Lauder, G. V. (2007). The ontogeny of fin function during routine turns in zebrafish *Danio rerio*. *J. Exp. Biol.* **210**, 3374–3386.

Domenici, P., Blagburn, J. M. and Bacon, J. P. (2011). Animal escapology I: theoretical issues and emerging trends in escape trajectories. *J. Exp. Biol.* **214**, 2463–2473.

Domenici, P. and Blake, R. W. (1991). The kinematics and performance of the escape response in the angelfish (*Pterophyllum eimekei*). *J. Exp. Biol.* **205**, 187–205.

Domenici, P. and Blake, R. W. (1993). The effect of size on the kinematics and performance of Angelfish (*Pterophyllum eimekei*) escape responses. *Can. J. Zool.* **71**, 2319–2326.

Domenici, P. and Blake, R. W. (1997). The kinematics and performance of fish fast-start swimming. *J. Exp. Biol.* **200**, 1165–1178.

Eaton, R. C., DiDomenico, R. and Nissanov, J. (1988). Flexible body dynamics of the goldfish C-start: implications for reticulospinal command mechanisms. *J. Neurosci.* **8**, 2758–2768.

Eaton, R. C. and Emberly, D. S. (1991). How stimulus direction determines the trajectory of the Mauthner-initiated escape response in a teleost fish. *J. Exp. Biol.* **161**, 469–487.

Ehrlich, D. E. and Schoppik, D. (2017). Control of movement initiation underlies the development of balance. *Curr. Biol.* **27**, 334–344.

Eilers, P. H. C. (2003). A perfect smoother. *Anal. Chem.* **75**, 3631–3636.

Fetcho, J. R. and McLean, D. L. (2010). Some principles of organization of spinal neurons underlying locomotion in zebrafish and their implications. *Ann. N. Y. Acad. Sci.* **1198**, 94–104.

Fleuren, M., Van Leeuwen, J. L., Quicazan-Rubio, E. M., Pieters, R. P. M., Pollux, B. J. A. and Voesenek, C. J. (2018). Three-dimensional analysis of the fast-start escape response of the least killifish, *Heterandria formosa*. *J. Exp. Biol.* **221**, jeb168609.

Foreman, M. B. and Eaton, R. C. (1993). The direction change concept for reticulospinal control of goldfish escape. *J. Neurosci.* **13**, 4101–4113.

Gazzola, M., Van Rees, W. M. and Koumoutsakos, P. (2012). C-start: optimal start of larval fish. *J. Fluid Mech.* **698**, 5–18.

Hale, M. E., Long Jr., J. H., McHenry, M. J. and Westneat, M. W. (2002). Evolution

of behavior and neural control of the fast-start escape response. *Evolution (N. Y)*. **56**, 993–1007.

Harper, D. G. and Blake, R. W. (1990). Fast-start performance of rainbow trout *Salmo gairdneri* and northern pike *Esox lucius*. *J. Exp. Biol.* **150**, 321–342.

Hertel, H. (1966). Fast Start—Trout. In *Structure, Form, Movement*, pp. 160–162. New York City, NY, USA: Reinhold Publishing Company.

James, R. S. and Johnston, I. A. (1998). Scaling of muscle performance during escape responses in the fish *Myoxocephalus scorpius* L. *J. Exp. Biol.* **201**, 913–923.

Kasapi, M. A., Domenici, P., Blake, R. W. and Harper, D. (1993). The kinematics and performance of escape responses of the knifefish *Xenomystus nigri*. *Can. J. Zool.* **71**, 189–195.

Li, G., Müller, U. K., Van Leeuwen, J. L. and Liu, H. (2012). Body dynamics and hydrodynamics of swimming fish larvae: a computational study. *J. Exp. Biol.* **215**, 4015–4033.

Li, G., Müller, U. K., Van Leeuwen, J. L. and Liu, H. (2014). Escape trajectories are deflected when fish larvae intercept their own C-start wake. *J. R. Soc., Interface* **11**, 20140848–20140848.

Lucas, K. N., Dabiri, J. O. and Lauder, G. V. (2017). A pressure-based force and torque prediction technique for the study of fish-like swimming. *PLoS One* **12**, e0189225.

Müller, U. K., Van den Boogaart, J. G. M. and Van Leeuwen, J. L. (2008). Flow patterns of larval fish: undulatory swimming in the intermediate flow regime. *J. Exp. Biol.* **211**, 196–205.

Müller, U. K. and Van Leeuwen, J. L. (2004). Swimming of larval zebrafish: ontogeny of body waves and implications for locomotory development. *J. Exp. Biol.* **207**, 853–868.

Nair, A., Azatian, G. and McHenry, M. J. (2015). The kinematics of directional control in the fast start of zebrafish larvae. *J. Exp. Biol.* **218**, 3996–4004.

Nair, A., Changsing, K., Stewart, W. J. and McHenry, M. J. (2017). Fish prey change strategy with the direction of a threat. *Proc. R. Soc. B* **284**, 20170393.

Schielzeth, H. (2010). Simple means to improve the interpretability of regression coefficients. *Methods Ecol. Evol.* **1**, 103–113.

Simo, J. C. and Wong, K. K. (1991). Unconditionally stable algorithms for rigid body dynamics that exactly preserve energy and momentum. *Int. J. Numer. Methods Eng.* **31**, 19–52.

Song, J., Zhong, Y., Luo, H., Ding, Y. and Du, R. (2018). Hydrodynamics of larval fish quick turning: A computational study. *Proc. Inst. Mech. Eng. Part C J. Mech. Eng. Sci.* **232**, 2515–2523.

Soto, A., Stewart, W. J. and McHenry, M. J. (2015). When optimal strategy matters to prey fish. *Integr. Comp. Biol.* **55**, 110–120.

Stewart, W. J., Cardenas, G. S. and McHenry, M. J. (2013). Zebrafish larvae evade predators by sensing water flow. *J. Exp. Biol.* **216**, 388–398.

Stewart, W. J., Nair, A., Jiang, H. and McHenry, M. J. (2014). Prey fish escape by sensing the bow wave of a predator. *J. Exp. Biol.* **217**, 4328–4336.

Stickel, J. J. (2010). Data smoothing and numerical differentiation by a regularization method. *Comput. Chem. Eng.* **34**, 467–475.

Tytell, E. D. and Lauder, G. V. (2008). Hydrodynamics of the escape response in bluegill sunfish, *Lepomis macrochirus*. *J. Exp. Biol.* **211**, 3359–3369.

Van Leeuwen, J. L., Voesenek, C. J. and Müller, U. K. (2015). How body torque and Strouhal number change with swimming speed and developmental stage in larval zebrafish. *J. R. Soc., Interface* **12**, 20150479.

Van Raamsdonk, W., Pool, C. W. and Te Kronnie, G. (1978). Differentiation of muscle fiber types in the teleost *Brachydanio rerio*. *Anat. Embryol.* **153**, 137–155.

Voesenek, C. J., Muijres, F. T. and Van Leeuwen, J. L. (2018). Biomechanics of swimming in developing larval fish. *J. Exp. Biol.* **221**, jeb149583.

Voesenek, C. J., Pieters, R. P. M. and Van Leeuwen, J. L. (2016). Automated reconstruction of three-dimensional fish motion, forces, and torques. *PLoS One* **11**, e0146682.

Wakeling, J. M. (2006). Fast-start Mechanics. In *Fish Biomechanics* (eds. R. E. Shadwick and G. V. Lauder), volume 23, pp. 333–368. Cambridge, MA, USA: Academic Press.

Walker, J. A., Ghalambor, C. K., Griset, O. L., McKenney, D. and Reznick, D. N. (2005). Do faster starts increase the probability of evading predators? *Funct. Ecol.* **19**, 808–815.

Webb, P. W. (1975). Acceleration performance of rainbow trout *Salmo gairdneri* and green sunfish *Lepomis cyanellus*. *J. Exp. Biol.* **63**, 451–465.

Weihs, D. (1973). The mechanism of rapid starting of slender fish. *Biorheology* **10**, 343–350.

Wöhl, S. and Schuster, S. (2007). The predictive start of hunting archer fish: a flexible and precise motor pattern performed with the kinematics of an escape C-start. *J. Exp. Biol.* **210**, 311–324.

Zupan, E. and Saje, M. (2011). Integrating rotation from angular velocity. *Adv. Eng. Softw.* **42**, 723–733.

6
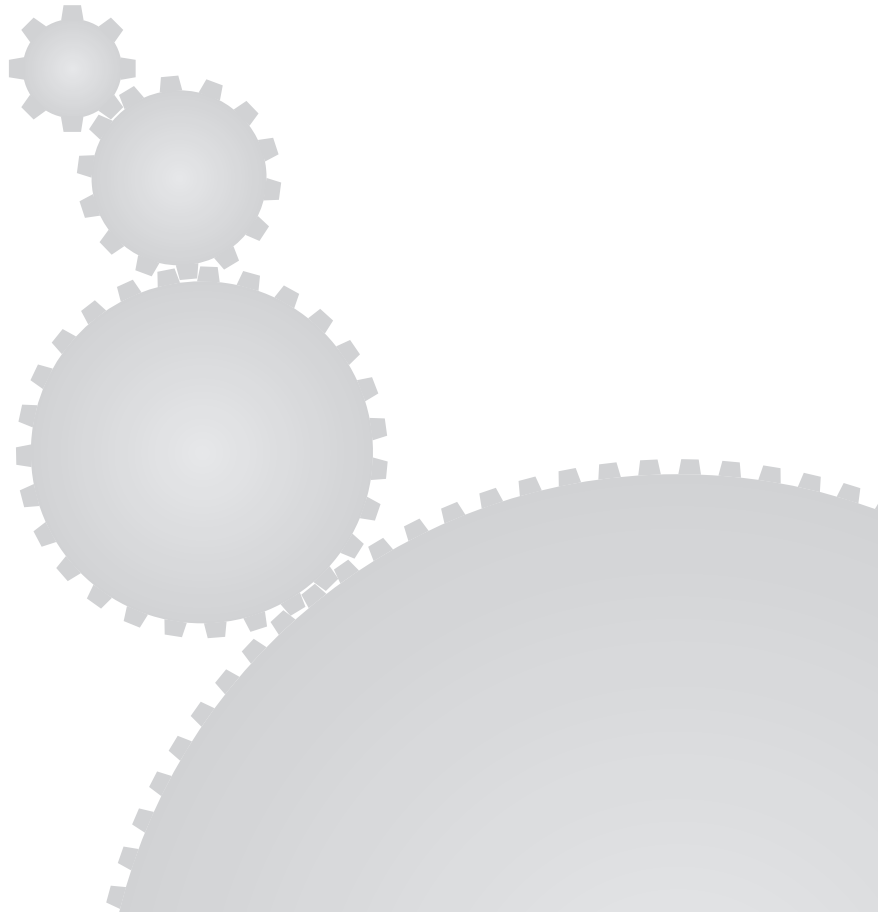
Chapter 6

Fish larvae use similar bending moment patterns across early development and speed

Cees J. Voesenek[1], Gen Li[2], Florian T. Muijres[1], Johan L. van Leeuwen[1]

[1] Experimental Zoology Group, Wageningen University & Research, Wageningen, The Netherlands
[2] Department of Mathematical Science and Advanced Technology, JAMSTEC, Yokohama, Japan.

Significance

Thousands of fish species swim with body undulations. The physics of undulatory swimming are complex, involving strongly-coupled interactions between the body of the fish and the water. Given this complexity, one would expect that fish require considerable neural processing capacity to control swimming effectively. However, just-hatched fish larvae without fully developed brains can already swim. With an advanced inverse-dynamics approach, we show that fish larvae use similar bending-moment patterns across early development, speeds, and accelerations. This suggests muscle activation in simple patterns, with the kinematics emerging from the body-water interaction. This 'offloading' of complexity to passive systems enables just-hatched larvae to swim successfully. The principle is of interest as bio-inspiration for simple control of complex systems.

Abstract

Most fish swim by undulating their bodies. These undulations result from an interaction between the fish's internal tissues and the surrounding water. Despite the complex physics and therefore expected need for advanced control, just-hatched larvae can swim effectively without fully developed brains. To gain insight into the mechanisms of larval swimming, we calculated the spatiotemporal distributions of bending moments along the body of free-swimming larval zebrafish (3–12 days after fertilisation), based on reconstructed 3D kinematics of 113 swimming events, a large-amplitude beam model, and 3D computational fluid dynamics. The bending moment varies over time and along the central axis of the fish due to the muscles, passive tissues, inertia, and fluid dynamics. We show that zebrafish larvae use similar bending moment patterns for each half tail-beat as previously reported for adults for near-cyclic swimming. Furthermore, we show that this pattern is qualitatively similar across development, swimming speed, and acceleration. Changes are mostly restricted to the amplitude and duration of the bending moments of the half tail-beat. The envelope of possible bending moment amplitudes grows as the fish develops, allowing it to reach higher speeds and accelerations with a similar bending moment pattern. The similarity in bending moments suggests that muscle activation patterns are similar too, which would allow fish larvae to use relatively simple control for the complex physics of swimming.

6.1 Introduction

Swimming is a vital component of the fitness of a fish—it needs for instance to search for food, hunt prey, escape from predators, migrate and disperse, and manoeuvre through complex environments. Many fish species swim by performing body undulations that result from an interaction between body tissues and the surrounding water (e.g. McMillen and Holmes, 2006; Tytell et al., 2010). Understanding these complex fluid-structure interactions is crucial to gain insight into the mechanics and control behind fish swimming (Voesenek et al., 2018).

  To analyse the fluid-structure interactions during swimming, we need to understand

the external fluid mechanics (water), the internal solid mechanics (skin, muscle, skeleton), and their coupling. During swimming, the fish's body moves through the water, inducing a flow around the fish (Borazjani et al., 2012; Müller et al., 2008). The resulting fluid dynamic forces interact with the fish's body tissues, resulting in a change in body deformation. This deformation will change the motion of the surface of the body, which influences the fluid dynamic forces, thus forming a loop of tight coupling between the fluid mechanics and the internal solid mechanics (Jordan, 1996; Tyson et al., 2008; Tytell et al., 2010). The complex two-way fluid-structure interaction creates the typical travelling wave pattern observed in swimming fish (Gray, 1933; Wakeling and Johnston, 1999).

The complexity of the physics would suggest that fish need a sophisticated control system to produce swimming motions reliably. Zebrafish (*Danio rerio*, Hamilton 1822) larvae, the subject of this study, would seem to contradict this: they can swim immediately after hatching, at considerable speed and tail beat frequency (Müller and Van Leeuwen, 2004; Van Leeuwen et al., 2015; for a review, see Voesenek et al., 2018). Furthermore, the spinal cord can produce swimming motions even when severed from the brain (Downes and Granato, 2006). This suggests that a relatively simple system can produce reliable undulatory swimming, despite the non-linear governing physics. Over the first days of development, the larvae refine their control of swimming (Borla et al., 2002; Ehrlich and Schoppik, 2017; Müller and Van Leeuwen, 2004) and improve swimming performance (Müller and Van Leeuwen, 2004; Van Leeuwen et al., 2015). These improvements raise the question: do control patterns change across early development, and at different swimming speeds and accelerations?

To study the mechanics of control of swimming, we need insight into the internal mechanics of the axial muscles and passive tissues. Muscle activation patterns can be measured directly with electromyography, where electrodes are inserted in the muscles to measure potential differences (Blight, 1976; Jayne and Lauder, 1995; Van Leeuwen et al., 1990). However, this technique may incur considerable changes in swimming behaviour. Especially for fish larvae, it requires them to be paralysed (Buss and Drapeau, 2002) or fixed in place (Cho et al., 2015), thus changing the fluid-structure interaction that produces the body wave (Bowtell and Williams, 1991). Furthermore, the resolution along the body is limited by the number of inserted electrodes.

An alternative is an inverse dynamics approach (Knudson, 2007), where we calculate internal forces and moments from measured kinematics. Hess and Videler (1984) used a simplified small-amplitude fluid and internal body model to estimate bending moments along the central axis of saithe from the motion of its centreline. The bending moment is defined for each transversal slice along the fish's body as the sum of the moments produced by the muscles and passive tissues, counteracting the moments due to inertia and water (Cheng and Blickhan, 1994; Cheng et al., 1998; Hess and Videler, 1984). Because the muscles are the only component in the system that produce net positive work over a cycle, bending moment distributions hint towards properties of the muscle activation pattern.

In this study, we examined bending moments calculated from measured swimming motion across early developmental stages in zebrafish larvae. Previous pioneering studies

A

B

z

x

1 mm

Time [ms]

0   40   80

C

z

y

Vorticity magnitude [s⁻¹]

500

250

0

1 mm

D

Stress [N m⁻²]

20

10

0

z

x

y

E

10 mN m⁻¹

1 mm

F

Bending moment [μN mm]

-16   0   16

Time [ms]

80

40

0

0   0.5ℓ   ℓ

G

Length [mm]

3.5   4.5   5.5

Acceleration [m s⁻²]

25

0

-15

0   0.15   0.3

Speed [m s⁻¹]
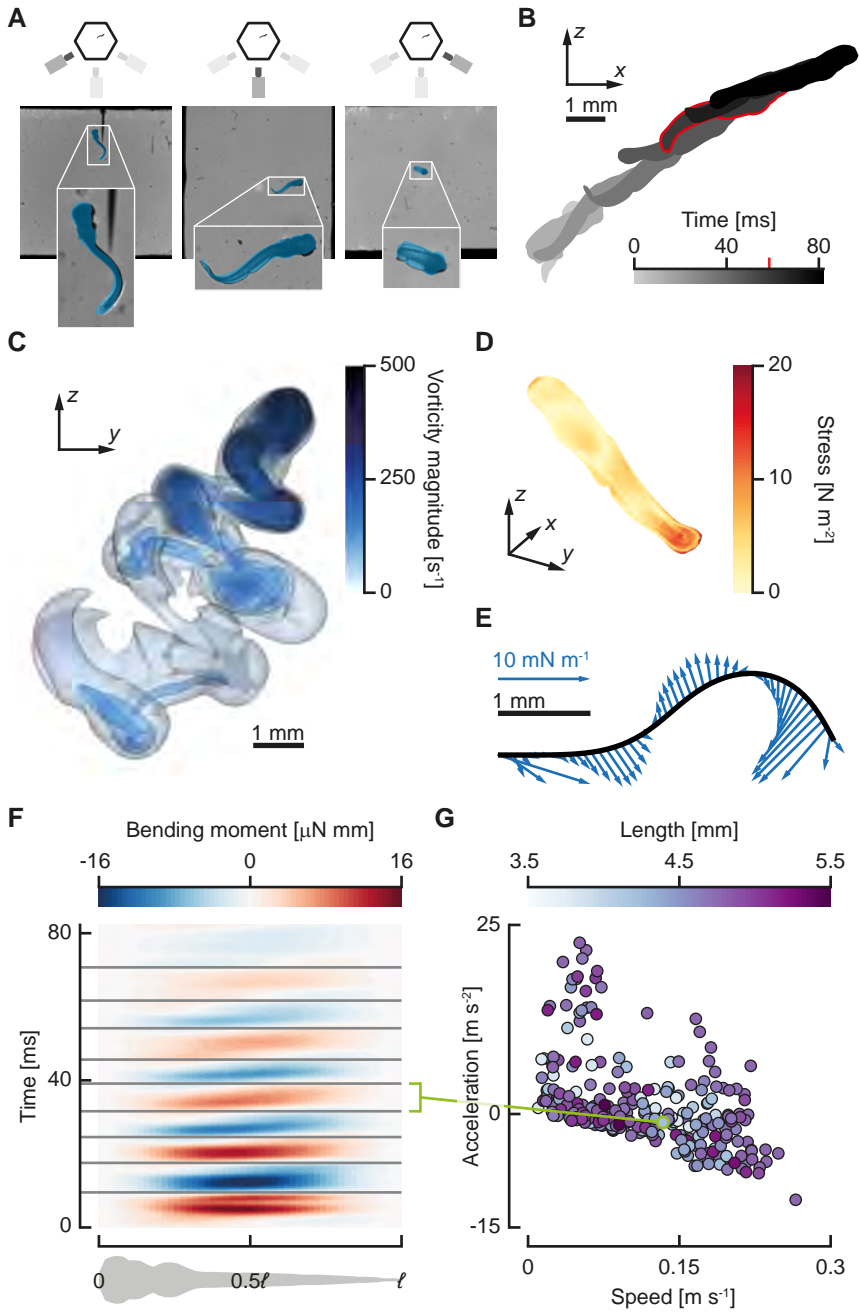
(Caption on the next page.)

Figure 6.1: Procedure to calculate bending moments. (A) Larval zebrafish motion is reconstructed from synchronised three-camera high-speed video. Video frames (background) from the three-camera-setup overlaid with projections (blue) of the reconstructed model fish. The legend at the top indicates which camera produced the video frame. (B) Reconstructed three-dimensional motion from the video, projected onto the $x–z$ plane, the highlighted time instant is shown in A and C–E. (C) Transparent vorticity isosurfaces for the same motion as (B), calculated with computational fluid dynamics (CFD). (D) Total fluid dynamic stress distribution on the skin, the sum of the pressure and shear stress magnitude contributions, calculated from the flow field from CFD. (E) Fluid dynamic force distribution transformed to the 2D coordinate system attached to the deformation plane. This distribution is used as input to reconstruct internal moments and forces. (F) Reconstructed bending moment distributions (colour) along the fish (horizontal) and over time (vertical). The horizontal lines separate the half-phases in which the bending moment was divided. The green line links a single half phase to a data point in G. (G) The mean speed (horizontal), mean acceleration (vertical), and body length (colours) for all individual half-beats in the data set. The green data point corresponds to the highlighted half-beat in F.

(Cheng and Blickhan, 1994; Hess and Videler, 1984) used a low-amplitude model and simplified fluid-dynamics to compute bending moments for only a few cases of periodic swimming in the inertial regime. We refined and extended these previous approaches by removing previous simplifying assumptions and analysing an extensive data set. We use three-dimensional reconstructed kinematics (Voesenek et al., 2016), beam theory supporting arbitrarily large amplitudes, and full numerical solutions of the Navier-Stokes equations to calculate fluid-dynamic forces (Fig. 6.1). With this method, we examine the question: do fish larvae use similar bending moment patterns across early development, speeds, and accelerations? We calculated bending moments for 113 periodic and aperiodic swimming sequences, across early development from 3–12 days after fertilisation. The reconstructed bending moment patterns are qualitatively similar across development, speed, and acceleration. Rather than change the spatiotemporal distribution of bending moments, fish larvae control speed and acceleration with only the amplitude and duration of the bending moment patterns. This suggests that fish larvae use the same simple control mechanism across early development, despite complex physics determining the resulting motion.

6.2 Results

6.2.1 Overview of an individual swimming sequence

We performed phase-averaging on a periodic section of a swimming sequence of a 3 days post fertilisation (dpf) zebrafish larva to illustrate how bending moments and bending powers vary along the body during swimming. We selected four half tail-beats (Fig. 6.2A) based on the periodicity of the body curvature. We averaged body curvature, bending moment, kinetic power, and fluid power over these half-beats.

Body curvature (Fig. 6.2B,C) shows a travelling wave pattern behind the stiff head with one positive and one negative peak per cycle. The highest curvatures are reached near the tail, at around 0.8 of the body length (ℓ), where body width is relatively small. Curvature waves originate from around $0.25\,\ell$, close to where the most anterior axial muscle is located. They then travel at approximately constant speed ($3.3\,\ell$ per tail beat) posteriorly, growing in amplitude until close to the tail, and finally dropping to zero amplitude at the tail tip.

A

Half beat
4
3
2
1

1 mm

B

% of tail beat

0   25   50   75   100

C Curvature [rad ℓ^{-1}]

-2π 0 2π

100

50
% of tail beat

0

0   0.5ℓ ℓ

D Bending moment [μN mm]

-12 0   12

100

50
% of tail beat

0

0   0.5ℓ ℓ

E

$\times10^{-3}$

10

5
Muscle area [mm^2]

0

0   0.5ℓ ℓ

F Fluid power [μW ℓ^{-1}]

-20 0   20

100

50
% of tail beat

0

0   0.5ℓ ℓ

G Kinetic power [μW ℓ^{-1}]

-2 0   2

100

50
% of tail beat

0

0   0.5ℓ ℓ

H Resultant power [μW ℓ^{-1}]

-20 0   20

100

50
% of tail beat

0

0   0.5ℓ ℓ
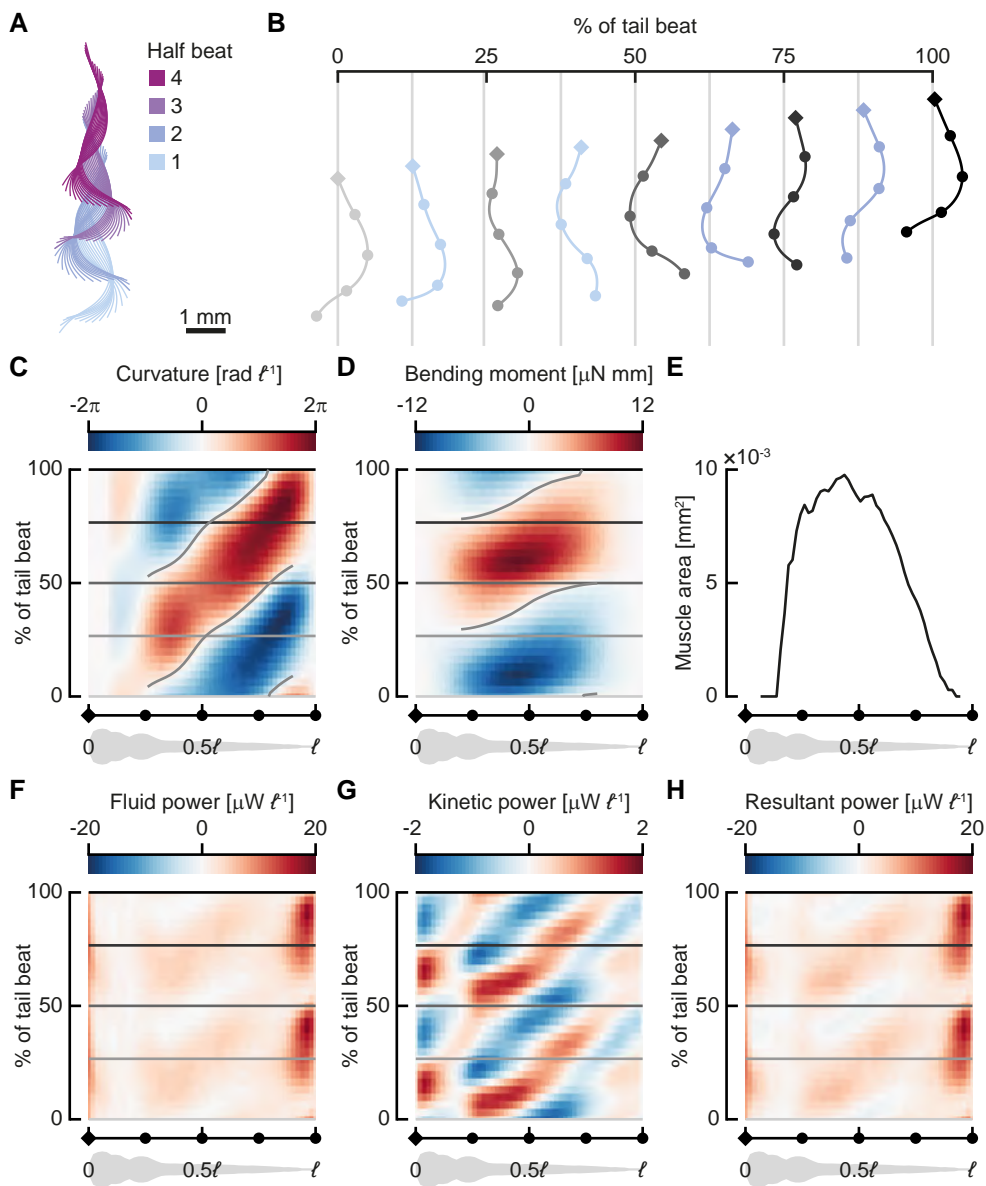
(Caption on the next page.)

Figure 6.2: Near-periodic sequence of a 3 **days post fertilisation zebrafish larva.** The larva swam at $31\,\ell\,\mathrm{s}^{-1}$ with a tail-beat frequency of 69 Hz. (A) Centreline motion throughout the sequence. The colours indicate half-phases. The coordinates were transformed to a best-fit plane through all points along the centreline throughout the motion. (B) Motion during a single full tail-beat (half-beat 1 and 2) of the motion; the grey centrelines correspond to the time points shown with horizontal lines in C,D,F–H. The diamond (head) and dots on the centrelines correspond to points on the x-axis for C–H. (C,D,F–H) Heat maps of distributions (colours) along the fish (horizontal) and over the phase over the tail beat (vertical); all quantities are averaged over separate half-beats; 'negative' half-beats are mirrored for the curvature and bending moment. (C) Body curvature normalised by body length. (D) Bending moment. (E) Muscle area distribution along the fish. (F) Fluid power per unit body length (power exerted by the fish to move the fluid). (G) Kinetic power per unit body length (rate of change in kinetic energy). (H) Resultant power, the sum of the fluid and kinetic power.

Bending moments (Fig. 6.2D) show a positive and a negative peak during swimming, corresponding to the direction of the tail beat, but preceding it in phase along most of the body. The peak amplitude occurs around $0.4\,\ell$, corresponding to the area with the highest muscle cross-section (Fig. 6.2E). Bending moments in the head and tail regions are low due to the free-end boundary conditions, where the bending moment must be zero, the absence of muscle, and in the tail region, the limited cross-sectional area. Also the bending moment shows a travelling wave pattern, but its wave speed is more than twice as high as the curvature wave speed ($7.1\,\ell$ per tail beat).

The power used by the body to move the fluid (Fig. 6.2F) shows a large peak close to the tip of the tail. The motion amplitude is large here (Fig. 6.2A,B), a well as the lateral velocities, therefore fluid forces are large. Since power is the product of velocity and forces, most power is expected to be transferred to the fluid here. The kinetic power, defined as the time rate of change in kinetic energy, is smaller in magnitude compared to the fluid power (Fig. 6.2G). The head shows considerable variation in kinetic energy over a tail-beat cycle, owing to its relatively large mass and side-to-side motion. There is a dip in kinetic energy fluctuations in the anterior region of the yolk sac. In the remainder of the body, the kinetic power shows a travelling-wave pattern, caused by the travelling-wave character of the body motion, and hence its speed. The resultant power (Fig. 6.2H), defined as the sum of the fluid and kinetic power, is dominated by the fluid power.

6.2.2 Swimming effort and vigour

We reconstructed 3D kinematics from 113 video sequences of fast-start responses followed by swimming, calculated flow fields throughout the sequence with CFD, and fitted distributions of internal forces and moments. These swimming sequences hardly contain periodic swimming. To analyse the data despite its aperiodicity, we subdivided it into half-beats based on zero-crossings of the bending moment in the mid-point along the centreline (Fig. 6.1F,G). For each of these 285 half-beats, we calculated the period length, mean speed, mean acceleration of the centre of mass to the next half-beat, and peak (95th percentile) bending moment.

To reduce the number of parameters for the analysis, we identified combinations of parameters with high explanatory capacity. To control swimming, the fish has two main

A

Mean resultant power [mW]

Effort [μN mm s⁻¹]

B

Vigour [μN]

Effort [μN mm s⁻¹]

C

Acceleration [m s⁻²]

Speed [m s⁻¹]

Effort [μN mm s⁻¹]

D

Speed [m s⁻¹]

Acceleration [m s⁻²]

Effort [μN mm s⁻¹]
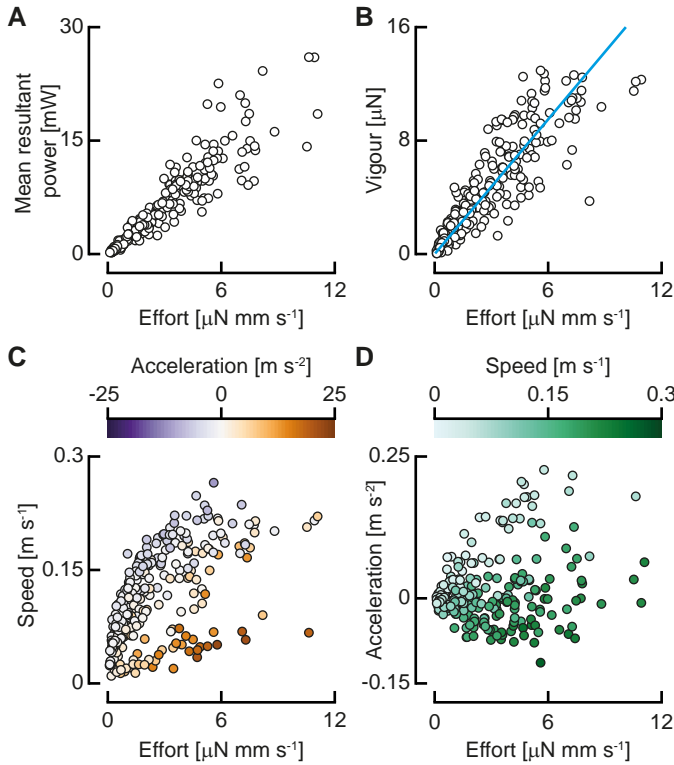
Figure 6.3: Swimming effort and vigour. (A) The mean resultant power as a function of swimming effort. (B) Swimming vigour as a function of effort, and the optimal linear fit. (C) Mean speed as a function of swimming effort, coloured by the mean acceleration. (D) Mean acceleration as a function of swimming effort, coloured by speed.

parameters to change the bending moment (see section below): its amplitude and the duration of each half-beat. We define the swimming effort as $E = M_{\text{peak}}\, t_{\text{half}}^{-1}$ —higher bending moments and shorter periods increase E. We fitted a generalised linear model (gamma distribution, log link function) with MATLAB (`fitglm`; R2018b, The Mathworks) and the Statistics and Machine Learning Toolbox (R2018b, The Mathworks). This showed that the swimming effort correlates significantly with the mean resultant power (Fig. 6.3A; $P < 0.0001$), with an exponent of 1.06—close to linear.

We expect the net propulsive force to scale with the mass of the fish, its acceleration, and its squared speed (from the dynamic pressure). Based on this, we define swimming vigour as $V = m(cv^2 + a)$, where m is body mass, v is swimming speed, and a is mean acceleration (i.e. change of speed to the next half-beat per unit of time). The coefficient c is calculated with an optimisation algorithm that minimises the sum of squared errors of a linear fit of vigour to effort with total least squares. The fitted value of $517.7\,\mathrm{m}^{-1}$ results in a clear trend of vigour as a function of effort (Fig. 6.3B; generalised linear model fit with gamma distribution and log link function: $P < 0.0001$), collapsing the broad clouds of speed and acceleration (Fig. 6.3C,D).

6.2.3 Bending moment distributions are similar across swimming vigour and development

To assess how bending moment patterns differ across vigour and development (indicated by body length; Parichy et al., 2009), we compared bending moment patterns normalised by their amplitude. We normalised the bending moment distribution of each half-beat by dividing by the peak bending moment. We then calculated the mean and standard deviation (Fig. 6.4A,B) of the normalised distributions of all half-beats. The standard deviation (Fig. 6.4B) is relatively small, locally peaking at 0.24, caused primarily by variation in the peak phase (Fig. 6.4E,F). For each half-beat, we calculated the mean absolute difference of each point in the distribution to the corresponding point in the mean distribution. The mean of these differences across half-beats is 0.091 ± 0.028—the differences are relatively low, and of similar magnitude across half-beats. Thus, the patterns look similar across different developmental stages and swimming vigour. Note that the peak value is smaller than 1, since the peak location shows variation in both phase and location along the body (Fig. 6.4C–F).

    The centre of volume of the individual bending moment patterns (Fig. 6.4C–F) lies around $0.5\,\ell$ along the body length and 25% of the tail beat (i.e. 50% of the half-beat). The location along the body varies little across length (i.e. developmental stage) and swimming vigour. The phase (i.e. time relative to the tail-beat duration) shows more variation over length and vigour but shows no clear pattern. We fitted linear models with MATLAB (`fitlm`; R2018b, The Mathworks) with the centre of volume location along the body and in phase as response variable, and the length and vigour as predictors. The slopes for the centre of volume position along the body are not significantly different from 0 for length ($P = 0.071$), vigour ($P = 0.78$) or their interaction ($P = 0.78$). The slopes for the phase of the centre of volume is not significantly different from zero for length ($P = 0.32$) and the interaction between length and vigour ($P = 0.065$), but marginally significant for vigour ($P = 0.049$).

    Although the spatiotemporal distributions of the bending moments are similar across lengths (i.e. developmental stage), the duration and amplitude vary (Fig. 6.4G,H). As the fish develop, the range of half-period durations increases (Fig. 6.4G)—young larvae use mostly short durations, while larger larvae use a broad range of durations. The maximum peak bending moment increases substantially over development (Fig. 6.4H). Older fish can generate higher peak bending moments and can reach higher swimming vigour values, but do not always do so.

6.2.4 Control parameters of swimming vigour

Because the bending moment patterns are similar across swimming styles and developmental stage, the parameters left for controlling swimming vigour are the amplitude of the bending moment and the duration of the tail beat. All experimental points lie on a broad cloud around a curve through the effort landscape, a function of peak bending mo-
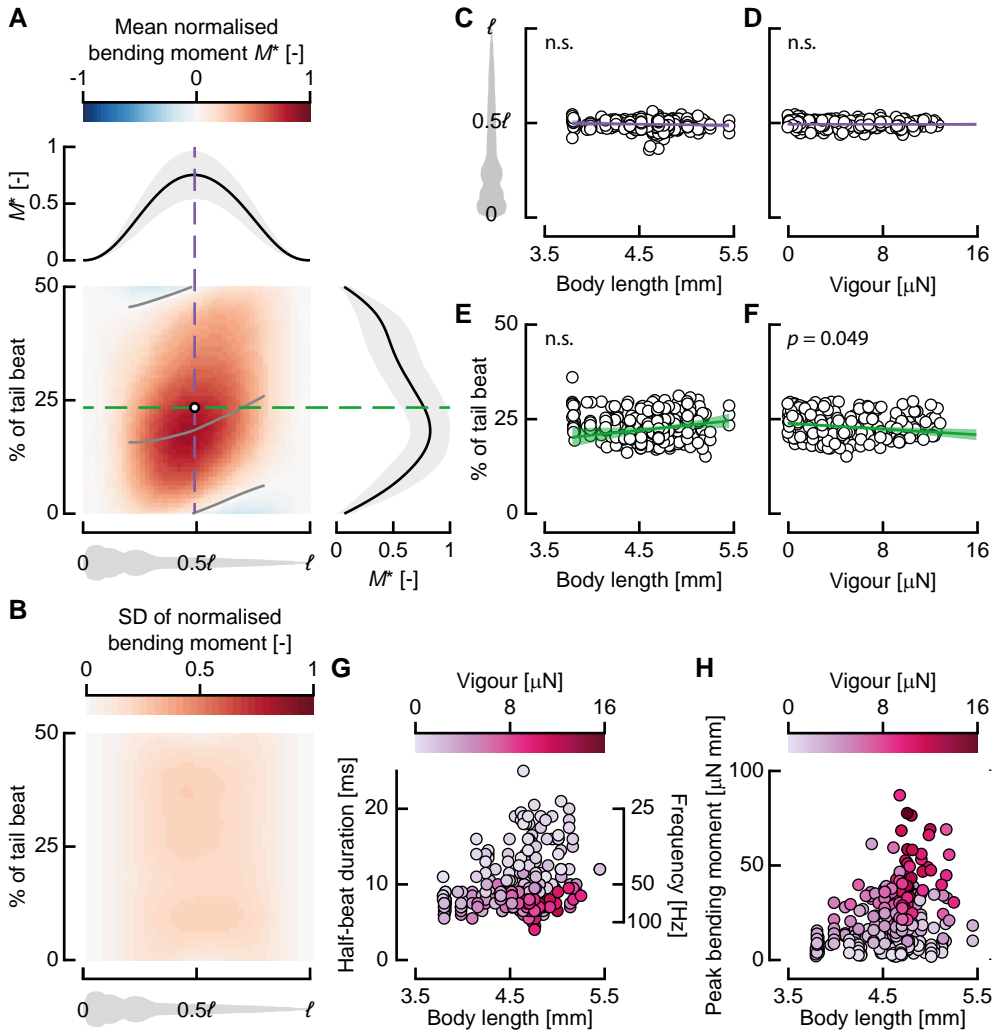
Figure 6.4: Bending moment patterns are similar across swimming vigour and development. (A) Normalised bending moment pattern along the fish (horizontal) and over normalised time (vertical), averaged over all half-beats ($N = 398$). The dashed lines indicate slices through the pattern in time (green) and location (purple) of the centre of volume of the distribution, shown respectively at the top and right of the heat map, along with their standard deviation. The grey lines over the heat map show the zero and maximum contour line. (B) The standard deviation (SD) of the normalised bending moment along the fish (horizontal) and over normalised time (vertical). (C,D) The location along the body of the centre of volume of the bending moment as a function of body length (C) and swimming vigour (D). (E,F) Normalised time of the centre of volume of the bending moment as a function of body length (E) and swimming vigour (F). (G) Half-beat duration as a function of length (i.e. developmental stage), coloured by swimming vigour. (H) Peak bending moment as a function of length, coloured by swimming vigour.
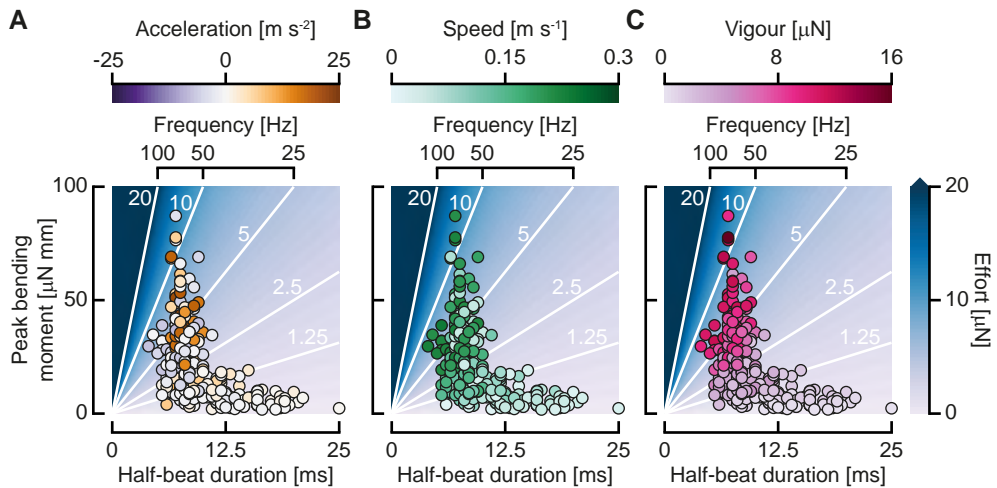
Figure 6.5: Swimming control parameters. (A,B,C) Individual half-beats in the duration–peak bending moment landscape, the coloured background with white contour lines shows the swimming effort. (A) Dots coloured by acceleration. (B) Dots coloured by speed. (C) Dots coloured by swimming vigour.

ment and half-beat duration (Fig. 6.5). In general, high peak bending moments are only produced for tail beats of short duration. As the duration decreases (i.e. frequency increases), the bending moment amplitude decreases. Higher efforts generally lead to higher speeds (Fig. 6.5B), unless the larva is accelerating strongly. Strong accelerations are mostly found with slow-swimming larvae using short half-beat durations and high peak bending moments (Fig. 6.5A). For high-effort tail beats, the larvae are generally either swimming fast, or accelerating: high-effort, low-speed tail beats show high accelerations, while high-effort, low acceleration tail beats show high speeds. Swimming vigour tends to increase with increasing effort (Fig. 6.5C).

6.3 Discussion

In this study, we analysed bending moment distributions of developing zebrafish larvae with inverse dynamics. We found that larvae use similar bending moment patterns across development. They control their swimming vigour, a combination of speed and acceleration, by adjusting the peak bending moment and tail-beat duration. At higher speeds and accelerations, the larvae produce the required fluid-dynamic forces by increasing bending moment amplitude and/or decreasing tail-beat duration.

Previous inverse-dynamics approaches for the internal mechanics of swimming used simplified models for both the fluid and the structure. The structure was modelled with linear bending theory, assuming small deformations of the centreline (Cheng and Blickhan, 1994; Hess and Videler, 1984). The effects of a large-amplitude correction to these was expected to be small for adult fish that swim periodically (Pedley and Hill, 1999). However, zebrafish larvae beat their tails often at $> 90°$ with the head (Van Leeuwen et al., 2015), violating the small-amplitude assumption. The beam theory underlying our bending moment

calculations allows arbitrarily large deformation, under the assumption of pure bending. Our beam model ignores the effect of shear deformation that is expected to occur close to the medial plane (Van Leeuwen et al., 2008), but we expect it to be of small influence to the bending moments due to its proximity to the axis and hence small moment arm.

In addition, we used 3D CFD to calculate fluid-dynamic forces, dropping previous assumptions of inviscid flow (Lighthill, 1960; Wu, 1961) and the necessity to model the boundary layer separately (Pedley and Hill, 1999). The assumption of inviscid flow does not hold for fish swimming in the intermediate regime (Li et al., 2012; Voesenek et al., 2018)—full solution of the Navier-Stokes equations is necessary to obtain sufficiently accurate fluid-dynamic force distributions. The intermediate Reynolds number of the zebrafish larvae allows us to solve the Navier-Stokes equations accurately, without requiring turbulence modelling (Li et al., 2012).

In our analysis of swimming sequences across development, we do not assume periodicity. Periodic motion is a common assumption in the analysis of fish swimming (e.g. Van Leeuwen et al., 2015; Videler and Hess, 1984). For zebrafish, cyclic swimming occurs most often after a fast start, and rarely spontaneously (Budick and O'Malley, 2000; Müller and Van Leeuwen, 2004), and generally only for a few tail beats. To analyse aperiodic motion, we subdivided each swimming sequence in tail beats based on zero-crossings of the bending moment in the middle of the body. During aperiodic swimming, the speed is generally non-constant. For this reason, we define a parameter 'swimming vigour', that combines the effects of acceleration and swimming speed as $V = m(cv^2 + a)$. This approach for analysing aperiodic swimming could be of general use in swimming research. The subdivision in half-beats can also be done with quantities other than the bending moment, for example body curvature. This enables similar analyses of aperiodic swimming from pure kinematics without inverse dynamics.

We define the swimming effort exerted by the fish based on the amplitude of the bending moment and the duration of the tail-beat, as $E = M_{\text{peak}} t_{\text{half}}^{-1}$. This quantity correlates with resultant power, indicating that it is indeed an indicator of swimming effort (Fig. 6.3A). The speed and acceleration fall on broad clouds as a function of effort (Fig. 6.3C,D), since they interact in determining the required effort for the fish. The effort-speed landscape (Fig. 6.3C) shows a two-pronged distribution, one branch showing high effort but low speed, and the other, broader branch showing increased effort with speed. This distribution is mainly explained by the acceleration, showing high values in the lower branch—fish only accelerate strongly from low speeds and use high effort to do so. This is reflected in the effort-acceleration landscape (Fig. 6.3D), low (including negative) acceleration are found at high speeds, and vice versa.

When speed and acceleration are combined into the swimming vigour, these clouds collapse into a narrower curve (Fig. 6.3B). Variation in this curve may be partly caused by turning behaviour and contributions of the pectoral fins. We can estimate the relative contribution of the speed and acceleration to the swimming vigour, giving an indication of their relative cost. If we assume force production to maintain speed and to accelerate are equally costly, we can estimate a drag coefficient from the coefficient in the vigour equation

as $c_{D,\text{estimated}} = mc\left(\frac{1}{2}\rho S\right)^{-1}$, where ρ is the fluid density, and S is the wetted area. Its value is 0.061, which is considerably lower than the value of 0.26 calculated from a previous CFD study on larval zebrafish (Li et al., 2016). This means our equal-cost assumption does not hold: the contribution of the speed term is relatively low compared to the acceleration term. Since swimming vigour correlates with swimming effort, this indicates that acceleration is more costly to achieve compared to maintaining swimming speed—the larvae need to invest more effort to produce force to accelerate than to swim steadily.

Most of the resultant power produced by the fish is used to increase the energy in the fluid, rather than the kinetic energy of the body (Fig. 6.2H). The energy spent on the water is likely lost on lateral velocity: larvae swim at high Strouhal number, associated with large tail-beat amplitudes and relatively high energy consumption (Borazjani and Sotiropoulos, 2009; Van Leeuwen et al., 2015). Most of this fluid power is produced at the tail, where the largest fluid-dynamic forces are produced (Li et al., 2016), even though no muscles are present here. This suggests a transfer mechanism by passive tissues from the muscles to the tail (Altringham and Ellerby, 1999; Blickhan and Cheng, 1994; Long et al., 2002).

The bending moment does not correspond directly to muscle action, as it also includes the effects of passive structures inside the body (Hess and Videler, 1984). We do not know the contribution of the muscles to the total bending moment, nor the specific distribution of stresses inside the body. Cheng et al. (1998) modelled the elastic and visco-elastic properties of the passive tissue, and thus estimated the contribution of the muscle bending moment. The amplitude of the muscle bending moment was found to be higher than the overall bending moment, while the wave speed was found to be lower. However, the overall dynamics look reasonably similar. If we assume similar distributions of passive tissues inside the fish across the considered developmental stages (Parichy et al., 2009), similar total bending moment patterns will require a similar muscle contribution. Furthermore, the difference in amplitude between similar bending moment patterns must originate from the muscle moment, since it is the only net source of power in the system—the work done by the fluid and passive tissues indirectly comes from the muscles.

We found that the bending moments follow a similar pattern across development and swimming vigour (i.e. speed and acceleration). The only significant coefficient in the linear models is the phase of the centre of volume of the bending moment patterns as a function of swimming vigour (Fig. 6.4F), but the effect is limited. More vigorously swimming fish generate the peak bending moment slightly earlier in the half-beat. The mean pattern looks qualitatively similar to earlier calculations done for adult fish (Cheng and Blickhan, 1994). It is a single-peaked distribution, with the maximum around the bulk of the muscle (Fig. 6.2E, Fig. 6.4A), and a fast-travelling wave character. Muscle electromyograms (EMG) done on paralysed zebrafish also looked similar to adult activation patterns (Buss and Drapeau, 2002). This suggests that this simple pattern of bending moments is common to fish across species and developmental stage. Even though fish larvae swim in the intermediate regime (Voesenek et al., 2018), and adult fish often swim in the inertial regime (Müller and Videler, 1996), the differences in fluid dynamics do not seem to require

fundamentally different bending moment patterns.

Since the bending moments look similar along the body and over the phase for each half-beat, the two control parameters left for the larvae to adjust are the amplitude and duration of the half-beat. Young larvae use a relatively narrow range of amplitudes and durations (Fig. 6.4G), which broadens as the fish develop. Older larvae are able to generate higher peak bending moments, likely correlated to development of their muscle system (Van Raamsdonk et al., 1978). While younger larvae only use a combination of short duration and relatively low bending moment amplitude (Fig. 6.4G,H), older fish often use longer-duration tail beats than young fish, suggesting that they have more freedom to control their swimming vigour.

Swimming kinematics emerge from simple bending moment patterns. These patterns presumably stem from simple muscle activation input—their quantification is an interesting avenue for future research. The arrangement and properties of the muscles, passive tissues and propulsive surface causes simple inputs to translate into complex kinematics and flow fields. Thus, handling the non-linear coupling between the body and flow becomes is simplified for the larvae. This has profound consequences for the survival of larvae that need to swim to survive (Walker et al., 2005). Straight from the egg, they can produce swimming behaviour to escape threats, despite relatively limited neural processing capacity. This concept of designing passive systems to allow complex systems to be controlled simply is of broad interest in engineering and biology (Degallier et al., 2011; Full and Koditschek, 1999; Liu et al., 2011).

6.4 Materials and methods

An in-depth mathematical treatment of the methods is given in the Supplemental Information.

6.4.1 Reconstructing 3D motion from multi-camera high-speed video

We made high-speed video recordings of fast starts of three separate batches of 50 zebrafish larvae from 3–12 days post fertilisation (dpf). The camera setup was identical to the setup described in Voesenek et al. (2016), with three synchronised high-speed video cameras, recording free-swimming larvae at 2000 frames per second. To reconstruct the swimming kinematics from the recorded high-speed video, we used in-house developed automated 3D tracking software (Voesenek et al., 2016) in MATLAB (R2013a, The Mathworks). For every time point in a multi-camera video sequence, the software calculates the best fit for the larva's 3D position, orientation and body curvature to the video frames. These parameters are then used to calculate the position of the larva's central axis and the motion of its outer surface (Fig. 6.1A,B).

6.4.2 Subdividing motion

We calculated phase-averaged quantities for an individual swimming sequence to look in detail at the generated bending moments and powers. We determined whether a (subset of a) sequence is periodic with a similar approach to Van Leeuwen et al. (2015). For every possible subset of a swimming sequence, we calculated the sum of absolute difference with a time-shifted version of the curvature, similar to an autocorrelation. We then calculated extrema in this function—if extrema are detected, their maximum value determines the 'periodicity' of the sequence. We then selected the longest possible subsequence that has a periodicity value higher than a threshold of 35—this is a swimming sequence for a 3 dpf fish. We divided this sequence in half-phases based on peaks in the body angle (Van Leeuwen et al., 2015; Voesenek et al., 2016). The curvature, bending moment, fluid power, kinetic power, and resultant power were then phase-averaged based on these subdivisions.

Most of the swimming of larval zebrafish is aperiodic, but there is an alternating pattern in the bending moments. For this reason, we analysed swimming per half-beat, based on the bending moment. We found the zero-crossings of the bending moment at $0.5\,\ell$. Since some of these points are related to noise, we evaluated every possible permutation of zero-crossings per sequence on several criteria with a custom MATLAB (R2018b, The Mathworks) program. We eliminated zero-crossings with neighbouring sections with an amplitude of less than 5% of the peak half-beat amplitude in the sequence, as they are most probably noise. We required more than three zero-crossings to have at least two half-beats to be able to calculate a mean acceleration. Extreme values in each half-beat should alternate direction to eliminate noisy zero-crossings: the larva beats its tail left and right, so therefore bending moment must alternate. Finally, we eliminated half-beats with a duration shorter than 2.5 ms (equivalent to 200 Hz tail-beat frequency)—the maximum tail-beat frequency observed for zebrafish larvae is 95 Hz (Van Leeuwen et al., 2015). From all permutations that met the criteria, we selected the permutation with the smallest standard deviation in half-period length across the sequence. This left the longest possible, least noisy sequence of half-beats for every swimming bout.

Out of 113 swimming sequences, we selected 398 half-beats with this procedure. For each of these half-beats, we calculated the duration, mean speed, and peak bending moment. We determined the mean acceleration by calculating the difference in speed between the following and current half-beat. Since we could not calculate mean acceleration for the last half-beat in each sequence, 285 half-beats remained for which we computed all quantities.

6.4.3 Calculating fluid force distributions

To calculate fluid-force distributions, we used the adaptive multigrid, immersed boundary method solver IBAMR (Griffith et al., 2007). We converted the tracked video data into a three-dimensional point cloud model in the fluid solver. We exclusively used swimming sequences where the larvae start from rest in quiescent water, so we do not need to consider

history in the wake. The solver time step was much smaller than the time step between video frames, so we interpolated the reconstructed kinematics with a quintic spline (Guennebaud et al., 2010). Using this interpolated state, we updated the location of the point cloud representing the surface of the fish. This resulted in a three-dimensional velocity and pressure field at every point in time (Fig. 6.1C). To verify the accuracy of the method, we compared reconstructed bending moments from IBAMR to an experimentally validated CFD solver (Li et al., 2012, 2014, 2016), showing only small differences, see the Supplemental Information.

We extracted force distributions by interpolating the pressure and velocity gradient tensor components to the centre of each face of an offset triangulated representation of the fish surface. We then integrated these values into contributions to the pressure force and the shear force at every face of the surface (Fig. 6.1D). By further integration, we calculated the force at every point along the centreline in a coordinate system attached to the larva's head (Fig. 6.1E).

6.4.4 Calculating bending moments

To calculate bending moments, we represented the fish by its central axis only. Effects of muscles, spine, and other tissues were combined for every transversal slice along this axis. This simplification allowed us to describe the fish as a non-linear, one-dimensional beam in two-dimensional space. We derived the equations of motion for this beam (see Supplemental Information) in an accelerating and rotating coordinate system attached to the fish's head (Török, 2000).

We obtained the motion of the fish from the tracked video, and the fluid forces from the fluid model. This left the normal forces, shear forces, and the bending moment as the only unknowns in the equations. We described the distributions of these unknowns with a quintic spline (Guennebaud et al., 2010) with uniformly spaced control points along the axis.

To determine the control point values of the normal force, shear force and bending moment, we minimised the residuals of the equations of motion. For every trial combination of control points, we calculated the residuals of equations at all points along the fish. The squared sum of these normalised residuals was minimised with a Levenberg-Marquardt algorithm (Jones et al., 2001) to obtain the best-fitting control point values that meet the boundary conditions for both free ends (internal forces and moments are zero). When the residuals of the equations are equal to zero, the optimised distributions satisfy the governing equations and boundary conditions exactly. Therefore, this procedure ensured that the computed internal force and moment distributions (Fig. 6.1F) were as close to physically valid as possible within the measurement error. From the motion of the centreline and fluid dynamic forces, we derived a local resultant power.

This optimisation procedure was validated with reference data obtained by integrating the equations of motion with a known external force distribution and internal moment distribution. We then reconstructed the bending moments, shear force, and normal

force from the integrated motion and the prescribed external force distribution, resulting in near-identical values (see Supplemental Information).

6.4.5 Calculating muscle cross-sectional area

We performed micro-computed-tomography (μCT) images of a 3 dpf zebrafish larva at the TOMCAT beamline at the Paul Scherrer Institut (Stampanoni et al., 2007). The larva was fixed in Bouin's solution and stained with phosphotungstic acid (PTA). The complete fish was imaged by stitching three scans with a resolution of $650 \times 650 \times 650$ nm per voxel. From these data, a centreline was extracted by finding the centre of area of each slice, segmented with simple thresholding. Finally, the muscle area was manually digitised in 51 planes, for which the image data was interpolated in a plane perpendicular to the centreline.

Acknowledgements

6

References

Altringham, J. D. and Ellerby, D. J. (1999). Fish swimming: patterns in muscle function. *J. Exp. Biol.* **202**, 3397–3403.

Blickhan, R. and Cheng, J.-Y. (1994). Energy storage by elastic mechanisms in the tail of large swimmers—a re-evaluation. *J. Theor. Biol.* **168**, 315–321.

Blight, A. R. (1976). Undulatory swimming with and without waves of contraction. *Nature* **264**, 352–354.

Borazjani, I. and Sotiropoulos, F. (2009). Vortex-induced vibrations of two cylinders in tandem arrangement in the proximity-wake interference region. *J. Fluid Mech.* **621**, 321–364.

Borazjani, I., Sotiropoulos, F., Tytell, E. D. and Lauder, G. V. (2012). Hydrodynamics of the bluegill sunfish C-start escape response: three-dimensional simulations and comparison with experimental data. *J. Exp. Biol.* **215**, 671–684.

Borla, M. A., Palecek, B., Budick, S. and O'Malley, D. M. (2002). Prey capture by larval zebrafish: evidence for fine axial motor control. *Brain. Behav. Evol.* **60**, 207–229.

Bowtell, G. and Williams, T. L. (1991). Anguilliform body dynamics: modelling the interaction between muscle activation and body curvature. *Philos. Trans. R. Soc., B* **334**, 385–390.

Budick, S. A. and O'Malley, D. M. (2000). Locomotor repertoire of the larval zebrafish: swimming, turning and prey capture. *J. Exp. Biol.* **203**, 2565–2579.

Buss, R. R. and Drapeau, P. (2002). Activation of embryonic red and white muscle fibers during fictive swimming in the developing zebrafish. *J. Neurophysiol.* **87**, 1244–1251.

Cheng, J.-Y. and Blickhan, R. (1994). Bending moment distribution along swimming fish. *J. Theor. Biol.* **168**, 337–348.

Cheng, J.-Y., Pedley, T. J. and Altringham, J. D. (1998). A continuous dynamic beam model for swimming fish. *Philos. Trans. R. Soc., B* **353**, 981–997.

Cho, S.-J., Nam, T.-S., Byun, D., Choi, S.-Y., Kim, M.-K. and Kim, S. (2015). Zebrafish needle EMG: a new tool for high-throughput drug screens. *J. Neurophysiol.* **114**, 2065–2070.

Degallier, S., Righetti, L., Gay, S. and Ijspeert, A. (2011). Toward simple control for complex, autonomous robotic applications: combining discrete and rhythmic motor primitives. *Auton. Robots* **31**, 155–181.

Downes, G. B. and Granato, M. (2006). Supraspinal input is dispensable to generate glycine-mediated locomotive behaviors in the zebrafish embryo. *J. Neurobiol.* **66**, 437–451.

Ehrlich, D. E. and Schoppik, D. (2017). Control of movement initiation underlies the development of balance. *Curr. Biol.* **27**, 334–344.

Full, R. J. and Koditschek, D. E. (1999). Templates and anchors: neuromechanical hypotheses of legged locomotion on land. *J. Exp. Biol.* **202**, 3325–3332.

Gray, J. (1933). Studies in animal locomotion — I. The movement of fish with special reference to the eel. *J. Exp. Biol.* **10**, 88–104.

Griffith, B. E., Hornung, R. D., McQueen, D. M. and Peskin, C. S. (2007). An adaptive, formally second order accurate version of the immersed boundary method. *J. Comput. Phys.* **223**, 10–49.

Guennebaud, G., Benoît, J. and Others. Eigen. http://eigen.tuxfamily.org.

Hess, F. and Videler, J. J. (1984). Fast continuous swimming of saithe (*Pollachius virens*): a dynamic analysis of bending moments and muscle power. *J. Exp. Biol.* **109**, 229–251.

Jayne, B. C. and Lauder, G. V. (1995). Are muscle fibers within fish myotomes activated synchronously? Patterns of recruitment within deep myomeric musculature during swimming in largemouth bass. *J. Exp. Biol.* **815**, 805–815.

Jones, E., Oliphant, T., Peterson, P. and Others. SciPy: Open source scientific tools for

Python. http://www.scipy.org.

Jordan, C. E. (1996). Coupling internal and external mechanics to predict swimming behavior: a general approach. *Am. Zool.* **36**, 710–722.

Knudson, D. (2007). *Fundamentals of Biomechanics*. Berlin, Germany: Springer.

Li, G., Müller, U. K., Van Leeuwen, J. L. and Liu, H. (2012). Body dynamics and hydrodynamics of swimming fish larvae: a computational study. *J. Exp. Biol.* **215**, 4015–4033.

Li, G., Müller, U. K., Van Leeuwen, J. L. and Liu, H. (2014). Escape trajectories are deflected when fish larvae intercept their own C-start wake. *J. R. Soc., Interface* **11**, 20140848–20140848.

Li, G., Müller, U. K., Van Leeuwen, J. L. and Liu, H. (2016). Fish larvae exploit edge vortices along their dorsal and ventral fin folds to propel themselves. *J. R. Soc., Interface* **13**, 20160068.

Lighthill, M. J. (1960). Note on the swimming of slender fish. *J. Fluid Mech.* **9**, 305–317.

Liu, Y.-Y., Slotine, J.-J. and Barabási, A.-L. (2011). Controllability of complex networks. *Nature* **473**, 167–173.

Long, J. H. J., Koob-Emunds, M., Sinwell, B. and Koob, T. J. (2002). The notochord of hagfish *Myxine glutinosa*: visco-elastic properties and mechanical functions during steady swimming. *J. Exp. Biol.* **205**, 3819–3831.

McMillen, T. and Holmes, P. (2006). An elastic rod model for anguilliform swimming. *J. Math. Biol.* **53**, 843–886.

Müller, U. K., Van den Boogaart, J. G. M. and Van Leeuwen, J. L. (2008). Flow patterns of larval fish: undulatory swimming in the intermediate flow regime. *J. Exp. Biol.* **211**, 196–205.

Müller, U. K. and Van Leeuwen, J. L. (2004). Swimming of larval zebrafish: ontogeny of body waves and implications for locomotory development. *J. Exp. Biol.* **207**, 853–868.

Müller, U. K. and Videler, J. J. (1996). Inertia as a 'safe harbour': do fish larvae increase length growth to escape viscous drag? *Rev. Fish Biol. Fish.* **6**, 353–360.

Parichy, D. M., Elizondo, M. R., Mills, M. G., Gordon, T. N. and Engeszer, R. E. (2009). Normal table of postembryonic zebrafish development: staging by externally visible anatomy of the living fish. *Dev. Dyn.* **238**, 2975–3015.

Pedley, T. J. and Hill, S. J. (1999). Large-amplitude undulatory fish swimming: fluid mechanics coupled to internal mechanics. *J. Exp. Biol.* **202**, 3431–3438.

Stampanoni, M., Groso, A., Isenegger, A., Mikuljan, G., Chen, Q., Meister, D., Lange, M., Betemps, R., Henein, S. and Abela, R. (2007). TOMCAT: A beamline for TOmographic microscopy and coherent rAdiology experimenTs. In *AIP Conference Proceedings*, volume 879, pp. 848–851.

Török, J. S. (2000). *Analytical Mechanics*. New York City, NY, USA: Wiley.

6

Tyson, R., Jordan, C. E. and Hebert, J. (2008). Modelling anguilliform swimming at intermediate Reynolds number: a review and a novel extension of immersed boundary method applications. *Comput. Methods Appl. Mech. Eng.* **197**, 2105–2118.

Tytell, E. D., Borazjani, I., Sotiropoulos, F., Baker, T. V., Anderson, E. J. and Lauder, G. V. (2010). Disentangling the functional roles of morphology and motion in the swimming of fish. *Integr. Comp. Biol.* **50**, 1140–1154.

Van Leeuwen, J. L., Lankheet, M. J. M., Akster, H. A. and Osse, J. W. M. (1990). Function of red axial muscles of carp (*Cyprinus carpio*): recruitment and normalized power output during swimming in different modes. *J. Zool.* **220**, 123–145.

Van Leeuwen, J. L., Van der Meulen, T., Schipper, H. and Kranenbarg, S. (2008). A functional analysis of myotomal muscle-fibre reorientation in developing zebrafish *Danio rerio*. *J. Exp. Biol.* **211**, 1289–1304.

Van Leeuwen, J. L., Voesenek, C. J. and Müller, U. K. (2015). How body torque and Strouhal number change with swimming speed and developmental stage in larval zebrafish. *J. R. Soc., Interface* **12**, 20150479.

Van Raamsdonk, W., Pool, C. W. and Te Kronnie, G. (1978). Differentiation of muscle fiber types in the teleost *Brachydanio rerio*. *Anat. Embryol.* **153**, 137–155.

Videler, J. J. and Hess, F. (1984). Fast continuous swimming of two pelagic predators, saithe (*Pollachius virens*) and mackerel (*Scomber scombrus*): a kinematic analysis. *J. Exp. Biol.* **109**, 209–228.

Voesenek, C. J., Muijres, F. T. and Van Leeuwen, J. L. (2018). Biomechanics of swimming in developing larval fish. *J. Exp. Biol.* **221**, jeb149583.

Voesenek, C. J., Pieters, R. P. M. and Van Leeuwen, J. L. (2016). Automated reconstruction of three-dimensional fish motion, forces, and torques. *PLoS One* **11**, e0146682.

Wakeling, J. M. and Johnston, I. A. (1999). Body bending during fast-starts in fish can be explained in terms of muscle torque and hydrodynamic resistance. *J. Exp. Biol.* **202**, 675–682.

Walker, J. A., Ghalambor, C. K., Griset, O. L., McKenney, D. and Reznick, D. N. (2005). Do faster starts increase the probability of evading predators? *Funct. Ecol.* **19**, 808–815.

Wu, T. Y.-T. (1961). Swimming of a waving plate. *J. Fluid Mech.* **10**, 321–344.

Supplemental Information

In this Supplemental Information, we provide the detailed mathematical background of the methods used in the article "Fish larvae use similar bending moment patterns across early development and speed". In addition, we show the results of the validation performed on these methods.

S6.1 Equations of motion

In this study, we calculated internal forces and moments for swimming zebrafish larvae. The three-dimensional motion of the larvae was obtained from multi-camera high-speed video with an automated tracking method (Voesenek et al., 2016). From this motion, we calculated the internal forces and moments by modelling the fish as a bending 'beam'. In this section, we show the derivation of the equations of motion for this large-deformation beam representation of the fish.

S6.1.1 Deriving the equations of motion

We model the fish as a beam with varying cross-sections, undergoing arbitrarily large deformation. Plane cross-sections are assumed to remain plane and perpendicular to the neutral line (no shear deformation), but axial deformation is allowed. Although the motion we tracked from the video is three-dimensional, we assume that the fish deforms in a single plane. Therefore, we can use a two-dimensional beam model to represent the deformation of the fish, under a suitable coordinate transformation. In summary, we model the fish as a beam undergoing large bending deformations in two dimensions.

We describe the deformation of the beam with the displacement of each infinitesimal beam element with respect to the reference configuration (Fig. S6.1A). It is defined as a function $\boldsymbol{\xi}(s,t) = \big(\xi(s,t), \eta(s,t)\big)$ of a parameter s along the length of the beam, and the time t. The position of the central axis at each point s is given by:

$$\big(x(s,t), y(s,t)\big) = \big(x_0(s) + \xi(s,t), y_0(s) + \eta(s,t)\big), \tag{S6.1}$$

where $(x_0(s), y_0(s))$ is the reference configuration of the beam. We define the reference configuration as a straight beam aligned with the positive x-axis, so the position becomes:

$$\big(x(s,t), y(s,t)\big) = \big(s + \xi(s,t), \eta(s,t)\big), \tag{S6.2}$$

This displacement results in a local deformation angle $\theta(s,t)$ for each beam element (Fig. S6.1A). It can be calculated from the displacements with:

$$\theta = \arctan\left(\frac{\frac{\partial \eta}{\partial s}}{1 + \frac{\partial \xi}{\partial s}}\right). \tag{S6.3}$$
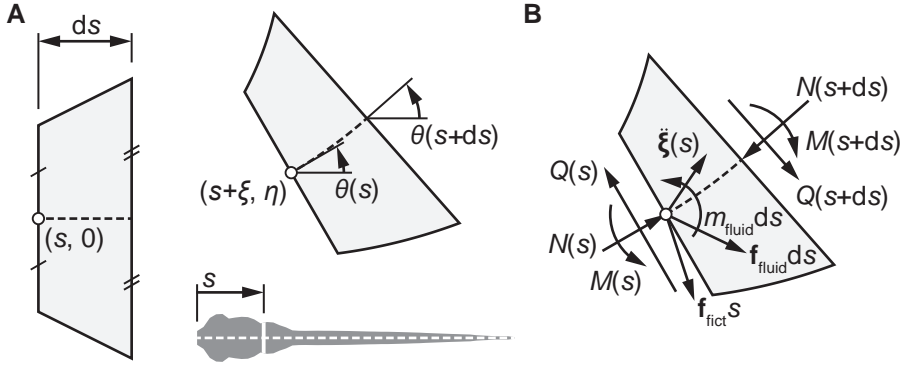
Figure S6.1: Beam representation of the fish body for computation of bending moments. (A) Geometric definitions of a beam element ds at a position s along the body, in reference (left) and deformed (right) configuration. We consider an infinitesimal element at $(s, 0)$ in the reference configuration, that is displaced by (ξ, η), and rotated by an angle θ. (B) Free body diagram of a beam element ds, with axial force N, shear force Q, bending moment M, net fictitious force distribution $\mathbf{f}_{\text{fict}}$, net fluid force distribution $\mathbf{f}_{\text{fluid}}$, net in-plane fluid moment distribution m_{fluid}, and acceleration $\frac{\partial^2 \xi}{\partial t^2}$.

To derive the equations of motion, we consider a free body diagram of an infinitesimal beam element of length ds (Fig. S6.1B). The force balance in x- and y-direction for a beam element ds can be expressed as:

$$
\begin{aligned}
\rho_{\text{fish}} A(s)\, \mathrm{d}s\, \frac{\partial^2 \xi}{\partial t^2}(s, t)\ =\ & \\
& N(s, t) \cos\big(\theta(s, t)\big) - N(s + \mathrm{d}s, t) \cos\big(\theta(s + \mathrm{d}s, t)\big) \\
& -\ Q(s, t) \sin\big(\theta(s, t)\big) + Q(s + \mathrm{d}s, t) \sin\big(\theta(s + \mathrm{d}s, t)\big) \\
& +\ f_{x,\text{muscle}}(s, t)\, \mathrm{d}s + f_{x,\text{fluid}}(s, t)\, \mathrm{d}s + f_{x,\text{fict}}(s, t)\, \mathrm{d}s;
\end{aligned}
\tag{S6.4}
$$

$$
\begin{aligned}
\rho_{\text{fish}} A(s)\, \mathrm{d}s\, \frac{\partial^2 \eta}{\partial t^2}(s, t)\ =\ & \\
& +\ N(s, t) \sin\big(\theta(s, t)\big) - N(s + \mathrm{d}s, t) \sin\big(\theta(s + \mathrm{d}s, t)\big) \\
& +\ Q(s) \cos\big(\theta(s, t)\big) - Q(s + \mathrm{d}s, t) \cos\big(\theta(s + \mathrm{d}s, t)\big) \\
& +\ f_{y,\text{muscle}}(s, t)\, \mathrm{d}s + f_{y,\text{fluid}}(s, t)\, \mathrm{d}s + f_{y,\text{fict}}(s, t)\, \mathrm{d}s,
\end{aligned}
\tag{S6.5}
$$

where ρ_{fish} is the beam density, A is the beam cross-sectional area, N is the internal normal force, Q is the internal shear force, $f_{x,\text{muscle}}$, $f_{y,\text{muscle}}$ are the muscle forces in x- and y-direction, $f_{x,\text{fluid}}$, $f_{y,\text{fluid}}$ are the external fluid forces in x- and y-direction, and $f_{x,\text{fict}}$, $f_{y,\text{fict}}$ are the fictitious forces in x- and y-direction (from the non-inertial reference frame, see section S6.1.2).

The moment balance (counter-clockwise positive) about the point on the neutral line

at $s + \mathrm{d}s$ is given by:

$$\rho_{\text{fish}} I(s)\,\mathrm{d}s\,\frac{\partial^2 \theta}{\partial t^2}(s,t) =$$
$$M(s,t) - M(s+\mathrm{d}s,t) - Q(s,t)\mathrm{d}s \qquad \text{(S6.6)}$$
$$+\ m_{\text{muscle}}(s,t)\,\mathrm{d}s + m_{\text{fluid}}(s,t)\,\mathrm{d}s + m_{\text{fict}}(s,t)\,\mathrm{d}s,$$

where I is the distribution of the second moment of area, M is the internal moment, m_{muscle} is the muscle moment, m_{fluid} is the external fluid moment, and m_{fict} is the fictitious moment (see section S6.1.2).

Dividing equations S6.4, S6.5, and S6.6 by the infinitesimal length $\mathrm{d}s$, applying the definition of a derivative $\frac{\partial \varphi}{\partial s}(s,t) = \frac{\varphi(s+\mathrm{d}s,t)-\varphi(s,t)}{\mathrm{d}s}$, and dropping the explicit $f(s,t)$ notation, yields the equations of motion:

$$\rho_{\text{fish}} A\,\frac{\partial^2 \xi}{\partial t^2} = -\frac{\partial}{\partial s}\left(N\cos\theta\right) + \frac{\partial}{\partial s}\left(Q\sin\theta\right) + f_{x,\text{muscle}} + f_{x,\text{fluid}} + f_{x,\text{fict}}; \quad \text{(S6.7)}$$

$$\rho_{\text{fish}} A\,\frac{\partial^2 \eta}{\partial t^2} = -\frac{\partial}{\partial s}\left(N\sin\theta\right) - \frac{\partial}{\partial s}\left(Q\cos\theta\right) + f_{y,\text{muscle}} + f_{y,\text{fluid}} + f_{y,\text{fict}}; \quad \text{(S6.8)}$$

$$\rho_{\text{fish}} I\,\frac{\partial^2 \theta}{\partial t^2} = -\frac{\partial M}{\partial s} - Q + m_{\text{muscle}} + m_{\text{fluid}} + m_{\text{fict}}. \qquad \text{(S6.9)}$$

S6.1.2 Fictitious forces

We reconstructed the motion of the fish from video in three-dimensional space, but described the equations of motion in a two-dimensional plane. However, in the video-tracking method, we assumed that the fish deforms in a single plane. Hence, we can create a coordinate system aligned to this plane and obtain the equations in two dimensions only. We define this head reference frame as fixed to the snout of the fish and rotating along with the stiff head region in the deformation plane. Any point $\hat{\mathbf{x}}$ in world coordinates (denoted with a circumflex) can be expressed in the fish coordinate system at time t as:

$$\mathbf{x} = \mathrm{R}^{\mathrm{T}}(t)\,(\hat{\mathbf{x}} - \hat{\mathbf{x}}_{\text{snout}}), \qquad \text{(S6.10)}$$

where $\mathrm{R}(t)$ is the time-dependent rotation matrix expressing the orientation of the snout and $\hat{\mathbf{x}}_{\text{snout}}$ is the position of the snout.

When we transform the motion to the non-inertial fish reference frame, additional equation terms accounting for the effect of the translation and rotation of the frame must be considered. These additional acceleration terms for any point $\mathbf{x}$ in the rotating reference frame are given by (Török, 2000):

$$\mathbf{a}_{\text{add}} = -\hat{\mathbf{a}}_{\text{head}} - 2\hat{\boldsymbol{\omega}} \times \mathbf{v} - \hat{\boldsymbol{\omega}} \times (\hat{\boldsymbol{\omega}} \times \mathbf{x}) - \hat{\boldsymbol{\alpha}} \times \mathbf{x}, \qquad \text{(S6.11)}$$

where $\hat{\mathbf{a}}_{\text{head}}$ is the acceleration of the origin, $\hat{\boldsymbol{\omega}}$ is the angular velocity of the rotating co-ordinate system, $\mathbf{v}$ is the velocity of the considered point, and $\hat{\boldsymbol{\alpha}}$ is the angular velocity of the rotating coordinate system. Note that the quantities $\hat{\mathbf{a}}_{\text{head}}$, $\hat{\boldsymbol{\omega}}$, and $\hat{\boldsymbol{\alpha}}$ are calculated with respect to the world reference frame, but expressed in the basis vectors of the moving reference frame. The position $\mathbf{x}$ and velocity $\mathbf{v}$ are expressed with respect to the moving reference frame.

These accelerations can be considered as an additional 'fictitious' external force distribution in the moving reference frame. This force distributions is given by

$$\mathbf{f}_{\text{fict}} = \rho A \, \mathbf{a}_{\text{add}}. \tag{S6.12}$$

These fictitious forces are added to the fluid-dynamic forces to calculate the total external force distribution acting on each beam element.

S6.2   Calculating fluid forces from kinematics

The equations of motion include an external force distribution, produced by the water on the skin. Since this is exceedingly difficult to measure directly and non-invasively, we modelled the fluid dynamics numerically. We used two independent computational fluid dynamics (CFD) methods to calculate fluid-dynamic forces. We used an experimentally validated method to validate the second method to assess its accuracy when calculating internal forces and moments.

We performed computational fluid dynamics using a Navier-Stokes solver based on overset meshes (Li et al., 2012, 2014, 2016), coupled to a body dynamics solver to simulate free swimming. Simulations were performed with swimming kinematics based on a travelling wave with a known curvature amplitude at a frequency of 50 Hz. The same motion was used in a second, independent Navier-Stokes solver based on the immersed boundary method, the open-source code IBAMR (Griffith et al., 2007).

The Navier-Stokes equations were solved on a rectangular domain, with extents determined by the bounding box around the complete motion with an additional margin of 2 fish lengths. The immersed boundary solver used an adaptive mesh refinement approach, in which the computational mesh can be locally refined depending on the flow conditions. In our case, the mesh consisted of four levels of refinement. Each level was a simple rectangular Cartesian mesh with 4 times the number of subdivision in all dimensions compared to the coarser level. The choice of mesh refinement level depended on the local value of the vorticity, we chose thresholds of 1, 25, and $250\,\text{s}^{-1}$ to switch to the second, third, and fourth refinement level respectively. We used a fixed time step of $0.5\,\mu\text{s}$ (see section S6.5.2), where the CFL-number is always much smaller than 1. We saved the fluid solution every 0.25 ms—at these points we reconstruct the internal forces and moments.

The surface of the fish was described as a cloud of Lagrangian points, moving over the Eulerian fluid solution mesh. The motion of these points was prescribed based on quintic spline interpolation (Guennebaud et al., 2010) of the tracked kinematics, with a custom-developed add-on to IBAMR. The density of the point cloud was chosen such that the

mean distance between the points is $0.75\times$ the smallest mesh level. This ensured that each cell inside the fish body will have at least one point in it, and not much more.

The resulting flow fields were post-processed to extract the fluid force distribution on the skin of the fish with a custom Python 3 program. In this program, we interpolated (Jones et al., 2001) the pressure and velocity gradients to a triangulated surface slightly offset from the fish skin. These were then used to calculate the local stress on each triangular face as:

$$\sigma_{\text{pressure}} = -p\mathbf{n}; \tag{S6.13}$$

$$\sigma_{\text{friction}} = \tau\mathbf{n}, \tag{S6.14}$$

where p is the pressure, τ is the shear stress tensor, and $\mathbf{n}$ is the outward facing normal of the face. Under the assumption of a Newtonian fluid, the shear stress tensor is defined as:

$$\tau = \mu \begin{bmatrix} 2\frac{\partial u}{\partial x} & \frac{\partial u}{\partial y} + \frac{\partial v}{\partial x} & \frac{\partial u}{\partial z} + \frac{\partial w}{\partial x} \\ \frac{\partial u}{\partial y} + \frac{\partial v}{\partial x} & 2\frac{\partial v}{\partial y} & \frac{\partial v}{\partial z} + \frac{\partial w}{\partial y} \\ \frac{\partial u}{\partial z} + \frac{\partial w}{\partial x} & \frac{\partial v}{\partial z} + \frac{\partial w}{\partial y} & 2\frac{\partial w}{\partial z} \end{bmatrix}, \tag{S6.15}$$

where μ is the dynamic viscosity, and u, v, w are the velocity components in respectively x-, y-, and z-direction. These surface stress distributions were then grouped into segments along the fish to calculate the local net fluid force in the moving reference frame.

S6.3 Reconstructing internal forces and moments with inverse dynamics

We reconstructed bending moments from the motion of the fish and its simulated external fluid force distribution, an approach commonly called inverse dynamics. This section describes the optimisation procedure we used to reconstruct the internal forces and moments.

In our inverse dynamics approach, we cannot separate the effects of the active and passive tissues inside the fish: the internal forces and moments that we compute include the effects of both. Considering this, the moment equation becomes:

$$\rho_{\text{fish}}I\frac{\partial^2\theta}{\partial t^2} = -\frac{\partial M^*}{\partial s} - Q + m_{\text{fluid}} + m_{\text{fict}}, \tag{S6.16}$$

where $\frac{\partial M^*}{\partial s} = \frac{\partial M}{\partial s} - m_{\text{muscle}}$. This combined moment is what we reconstruct from the motion with our optimisation procedure. From here onwards, we drop the asterisk notation and refer to the combined active and passive internal bending moment as the 'bending moment'.

S6.3.1 Optimising internal forces and moments

To calculate the normal force, shear force, and bending moment, we used an optimisation algorithm that determines the best-fitting distributions in space and time. At every point in time, we described the internal forces and moments with a quintic spline (Jones et al., 2001) along the length of the fish. Values were prescribed at 12 uniformly spaced control points, between which the values were interpolated with the spline. The first and last control point, at respectively $s = 0$ and $s = \ell$, were fixed at a value of 0, to satisfy the boundary conditions of $N(0) = Q(0) = M(0) = 0$, and $N(\ell) = Q(\ell) = M(\ell) = 0$, that should hold for the free ends of a beam.

At a each time step, we optimised the moment-, shear-, and normal distributions to minimise the deviation from equations S6.7, S6.8, S6.9 at every point along the fish. This deviation was quantified by the residual value that is needed to balance the left- and right-hand side of the equations. We optimised the distributions with the Levenberg-Marquardt algorithm (Jones et al., 2001), that minimises the squares of the residuals. At every time step, this resulted in a series of control point values describing the internal forces and moments that best satisfy the equations.

S6.3.2 Calculating resultant power

We calculated the resultant power on the fish from two source: the power exerted on the fluid, and the changes in kinetic energy. Both quantities are computed in the inertial reference frame. We calculated the power per unit length that the fish exerts on the water as:

$$\hat{p}_{\text{fluid}} = -\hat{\mathbf{f}}_{\text{fluid}} \cdot \hat{\mathbf{v}}, \tag{S6.17}$$

where $\hat{\mathbf{v}}$ is the velocity of the centreline in world coordinates. We negated the power since we are considering the power that the fish exerts on the water, rather than the inverse.

The kinetic energy at any point in time was calculated as:

$$\hat{e}_{\text{kinetic}} = \frac{1}{2}\rho A||\hat{\mathbf{v}}||^2. \tag{S6.18}$$

The kinetic power per unit length is the time derivative of the kinetic energy:

$$\hat{p}_{\text{kinetic}} = \frac{\partial \hat{e}_{\text{kinetic}}}{\partial t}. \tag{S6.19}$$

S6.4 Integrating the equations of motion to generate reference data

We integrated the equations of motion to determine whether the derived equations are physically valid, and to generate reference data to test our algorithm for reconstructing bending moments.

S6.4.1 Constitutive and kinematic relations

The normal forces and moments can be calculated from the displacements using constitutive equations. To generate the reference data, we assumed a Hookean material, resulting in the following equations:

$$N = -YA\varepsilon; \tag{S6.20}$$

$$M = -YI\frac{\partial\theta}{\partial s}, \tag{S6.21}$$

where Y is the Young's modulus. The strain ε can be computed from the displacements as follows:

$$\varepsilon = \sqrt{\left(1 + \frac{\partial\xi}{\partial s}\right)^2 + \left(\frac{\partial\eta}{\partial s}\right)^2} - 1. \tag{S6.22}$$

These relations complete the set of equations required to calculate the accelerations of each point on the beam with equations S6.7 and S6.8.

S6.4.2 Temporal integration

We used the backward Euler method to integrate the beam accelerations to velocities, and velocities to displacements. To calculate the velocities and displacements in x-direction at the time step i, we used:

$$\left(\frac{\partial\xi}{\partial t}\right)_i = \left(\frac{\partial\xi}{\partial t}\right)_{i-1} + \Delta t\left(\frac{\partial^2\xi}{\partial t^2}\right)_i; \tag{S6.23}$$

$$\xi_i = \xi_{i-1} + \Delta t\left(\frac{\partial\xi}{\partial t}\right)_i; \tag{S6.24}$$

and analogous expressions for η.

S6.4.3 Equation scaling

The governing equations resulted in an ill-conditioned system, caused by large scale differences in the matrix coefficients. This makes a system difficult to solve numerically. To improve the condition number, we scaled variables such that all coefficients were close to 1. We used the following scaling coefficients, where an asterisk denotes a scaled quantity:

$$s^* = \frac{1}{\Delta s}s; \quad t^* = \frac{1}{\Delta t}t;$$

$$\xi^* = \frac{1}{\Delta s}\xi; \quad \eta^* = \frac{1}{\Delta s}\eta; \quad \theta^* = \theta; \tag{S6.25}$$

$$N^* = \frac{\Delta t^2}{\rho A\Delta s^2}N; \quad Q^* = \frac{\Delta t^2}{\rho A\Delta s^2}Q; \quad M^* = \frac{\Delta t^2}{\rho I\Delta s}M.$$

The scaled equations for temporal integration of ξ then become:

$$\xi_i^* - \xi_{i-1}^* - \left(\frac{\partial \xi^*}{\partial t^*}\right)_i = 0, \tag{S6.26}$$

and analogously for the other three equations related to integration of ξ and η.

Scaling the force balance in x-direction yields:

$$\frac{\partial^2 \xi^*}{\partial t^{*2}} + \frac{\partial N^*}{\partial s^*}\cos\theta^* - N^*\frac{\partial \theta^*}{\partial s^*}\sin\theta$$
$$- \frac{\partial Q^*}{\partial s^*}\sin\theta^* - Q^*\frac{\partial \theta^*}{\partial s^*}\cos\theta - \frac{\Delta t^2}{\rho A \Delta s}f_x = 0. \tag{S6.27}$$

Equivalently, for the force balance in y-direction:

$$\frac{\partial^2 \eta^*}{\partial t^{*2}} + \frac{\partial N^*}{\partial s^*}\sin\theta^* + N^*\frac{\partial \theta^*}{\partial s^*}\cos\theta^*$$
$$+ \frac{\partial Q^*}{\partial s^*}\cos\theta^* - Q^*\frac{\partial \theta^*}{\partial s^*}\sin\theta^* - \frac{\Delta t^2}{\rho A \Delta s}f_y = 0. \tag{S6.28}$$

The scaled moment balance becomes:

$$\frac{\partial^2 \theta^*}{\partial t^{*2}} + \frac{\partial M^*}{\partial s^*} + \frac{A\Delta s^2}{I}Q^* - \frac{\Delta t^2}{\rho I}m = 0 \tag{S6.29}$$

Finally, the constitutive and kinematic relations become:

$$N^* + \frac{Y\Delta t^2}{\rho \Delta s^2}\left[\sqrt{\left(1 + \frac{d\xi^*}{ds^*}\right)^2 + \left(\frac{d\eta^*}{ds^*}\right)^2} - 1\right] = 0 \tag{S6.30}$$

$$M^* + \frac{Y\Delta t^2}{\rho \Delta s}\frac{\partial \theta^*}{\partial s^*} = 0 \tag{S6.31}$$

$$\theta^* - \arctan\left(\frac{\frac{\partial \eta^*}{\partial s^*}}{1 + \frac{\partial \xi^*}{\partial s^*}}\right) = 0 \tag{S6.32}$$

S6.4.4 Solution method

We integrated the scaled equations of motion with multivariate Newton-Raphson, an iterative solution method for non-linear partial differential equations. Based on the solution at the previous time step, we calculated the vector of residuals for each of the 4 temporal

integration relations, 3 force and moment balances, and 3 constitutive and kinematics relations per point along the beam. This led to a vector of $10\,n_{\mathrm{lon}}$ residuals, with n_{lon} the number of longitudinal points in the beam. To calculate the value for the next iteration, we solved:

$$\mathcal{J}_F(\boldsymbol{\varphi}_i)\big(\boldsymbol{\varphi}_{i+1} - \boldsymbol{\varphi}_i\big) = -F(\boldsymbol{\varphi}_i), \tag{S6.33}$$

where the subscripts i and $i+1$ denote the current and next iteration, $\mathcal{J}_F$ is the Jacobian of the residuals, F is the vector of residuals, and $\boldsymbol{\varphi}$ is the vector of variables.

We calculated the Jacobian numerically by perturbing each variable with a fixed-step size and then calculating one-sided finite-differences. We solved the system with a direct solver (Oliphant, 2006).

S6.5 Validating the inverse dynamics methods

This section describes the validation of the internal forces and moments reconstruction, based on reference data, and based on a reference CFD simulation.

S6.5.1 Internal forces and moment reconstruction

We assessed the validity of the equations of motion by comparing a simulated beam to experimental results (Beléndez et al., 2002). We then tested the reconstruction of internal forces and moments based on reference data produced by integrating the equations of motion (see section S6.4).

Equations of motion

To assess the validity of the derived beam equations, we compared experimental results from Beléndez et al. (2002) with our simulation of a cantilever beam. In their study, a 300 mm steel ruler ($Y = 200\,\mathrm{GPa}$) with rectangular cross-section (width $\times$ height $= 30.4$ mm $\times\, 0.78$ mm) was clamped at one end. The beam was loaded with a point force of 3.92 N in negative y-direction at the unclamped tip, in addition to the distributed gravity load of $1.85\,\mathrm{N\,m^{-1}}$ (total $0.554\,\mathrm{N}$ over 300 mm).

We simulated a beam with the same geometry and loading, but in a time-dependent manner. We started with the beam in undeformed configuration, then smoothly ramped the loading from 0 to the reference amplitudes over a period of 5 seconds, and continued simulating for 5 more seconds. The resulting deformation was compared to the experimental reference in Fig. S6.2A—it overlaps strikingly, providing confidence in the physical validity of the derived equations of motion.

Calculating internal forces and moments

To check the correctness of the algorithm for reconstructing forces and moments, we generated a simple model of a 'swimmer' by prescribing analytical external forces and moments

A

1.85 N m⁻¹

5 mm

— Simulation
○ Beléndez *et al.* 2002

B

— "head"
— "tail"
— centreline

2 mm

3.92 N

C

Phase angle [rad]

0    $\frac{1}{2}\pi$ π $\frac{3}{2}\pi$ 2π

2 mm

D Elastic
bending moment [μN mm]

-50   0   50

100

% of tail beat

50

0

0   0.5   1.0
s [-]

E "Muscle"
bending moment [μN mm]

-50   0   50

0   0.5   1.0
s [-]
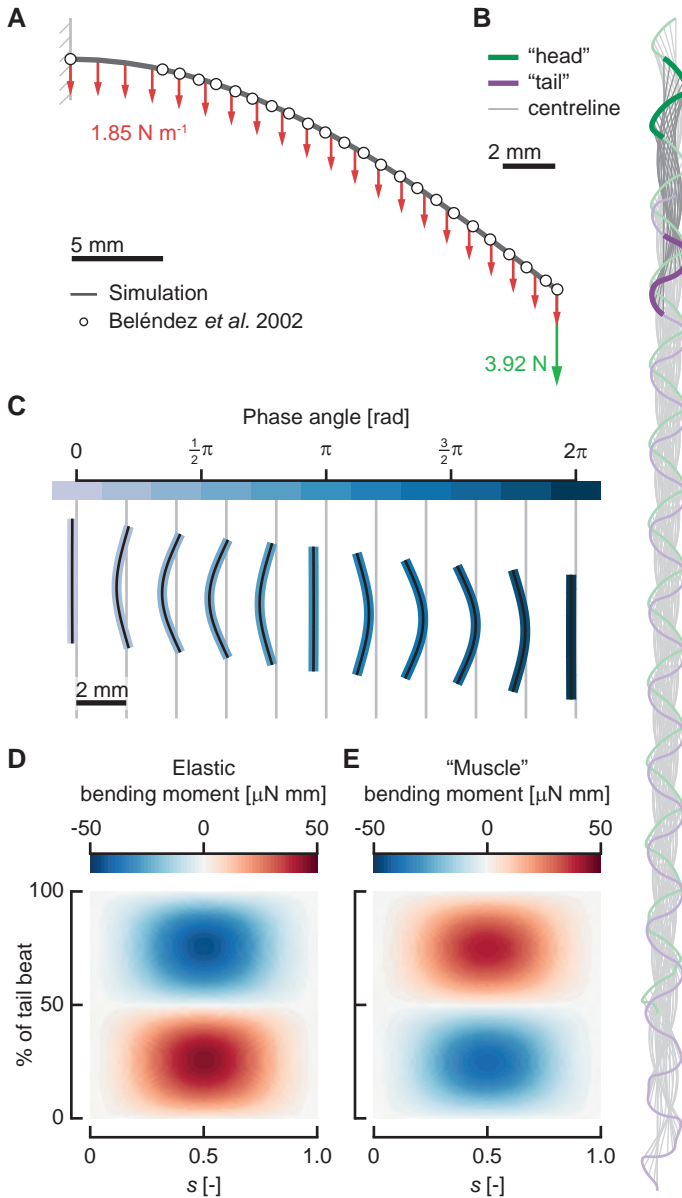
Figure S6.2: Reference data for the internal forces and moments reconstruction. (A) Comparison of our simulated beam (solid grey line) with experimental results (Beléndez et al., 2002, dots), under a distributed and point load (resp. red and green arrows). (B) Motion of the simulated reference 'swimmer', with the beam centrelines (grey), path the 'head' (green) and of the 'tail' (purple). The dark grey, green, and purple indicate the cycle selected for further analysis. (C) The motion of the reference 'swimmer' over the selected cycle, centreline (black), beam coloured by phase angle. (D–E) The elastic contribution (D) and the 'muscle' contribution (E) to the internal bending moment for the reference 'swimmer'.

to a simulated beam of a Hookean material (see section S6.4). We prescribed the fluid forces as:

$$f_{x,\text{fluid}}(s,t) = A_x \sin(2\pi f t); \tag{S6.34}$$
$$f_{y,\text{fluid}}(s,t) = A_y \cos(2\pi f t), \tag{S6.35}$$

and the muscle moment by:

$$m_{\text{muscle}} = A_m \sin(2\pi f t)\left[1 + \sin\left(2\pi\frac{s}{\ell} - \frac{\pi}{2}\right)\right]. \tag{S6.36}$$

The resulting motion is shown in Fig. S6.2B, demonstrating a swimming-like motion. We selected a single cycle from the motion (Fig. S6.2C), after the motion had become reliably periodic after 11 cycles. The total internal bending moment, which is what we reconstruct, consisted of an elastic contribution (Fig. S6.2D), and a contribution from the 'muscle' moment (Fig. S6.2E).

We reconstructed the total internal forces and moments of the reference 'swimmer' with the method described in section S6.3, see Fig. S6.3. The results match well, both qualitatively and quantitatively. Qualitatively, the patterns are similar, showing the same dynamics between the reference and the reconstruction. The shear force and normal force show relatively the largest errors (respectively maximum 9.7% and 7.0% of the peak value), while the error in bending moment is low (maximum 0.9% of the peak value). This shows that our main quantity of interest, the bending moment, can be reliably reconstructed with the proposed method.

S6.5.2 Computational fluid dynamics

As a reference to compare the computational fluid dynamics (CFD) results of IBAMR, we used an extensively validated numerical method for fish free swimming (Li et al., 2012, 2014, 2016). The curvature of the fish was prescribed similar to Li et al. (2014), by a travelling curvature wave (rather than an amplitude wave in the original reference) with an experimental curvature amplitude envelope of a 3 days post fertilisation zebrafish larva. The frequency was 50 Hz, the fish length 3.8 mm, the water density 1000 kg m^{-3}, and the dynamic viscosity 0.8301 mPa s. The motion of the fish was calculated based on the fluid dynamic forces, resulting in a free-swimming fish. We used the resulting fluid force distributions and motion to calculate internal forces and moments.

We prescribed the same motion with a custom-developed add-on to the open-source immersed boundary method IBAMR (Griffith et al., 2007), see section S6.2. Note that we did not integrate the motion of the fish, but prescribed the position of the fish surface directly at all time points. For the results from IBAMR, we also calculated the internal forces and moments to compare to the reference from the validated solver.
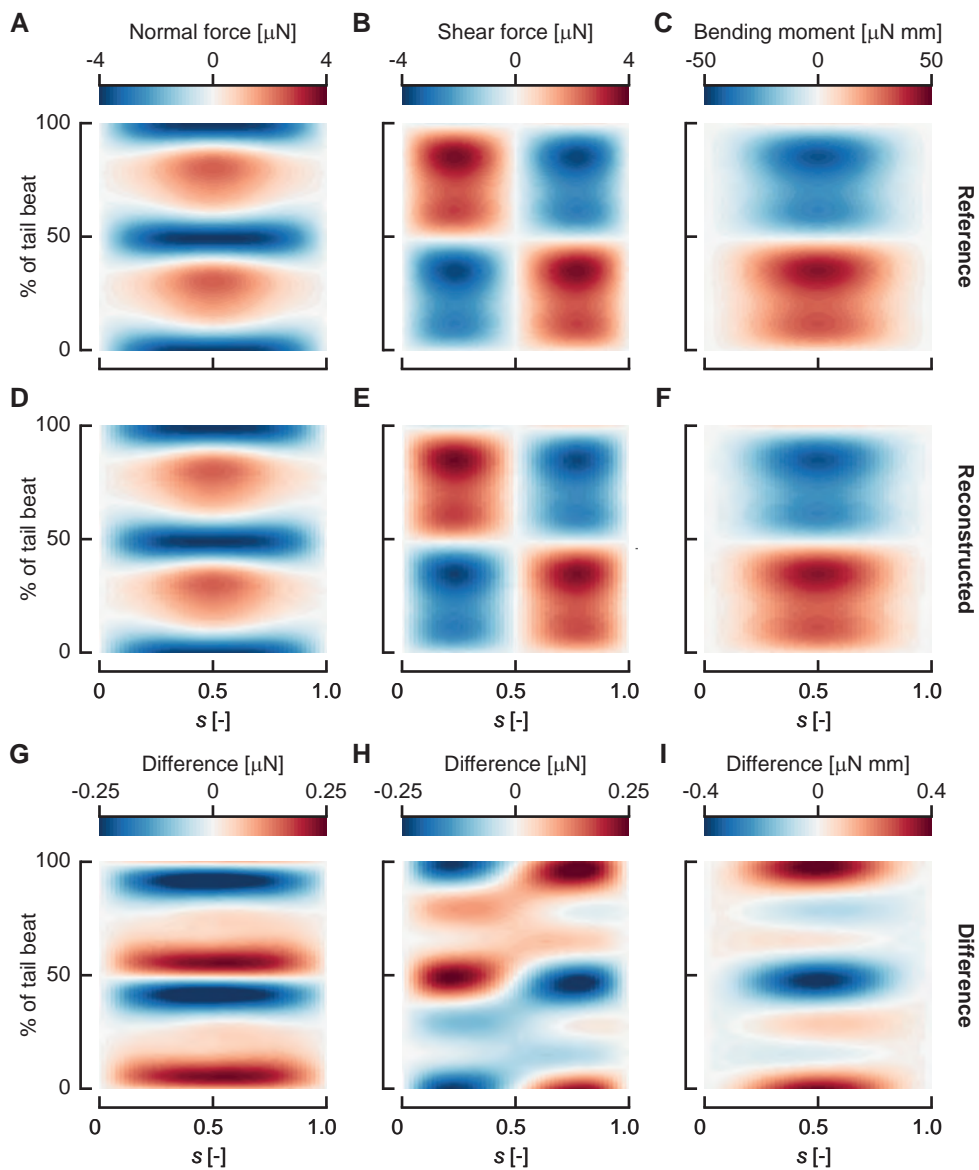
Figure S6.3: Comparison between reference and reconstructed internal forces and moments. (A–C) Reference normal force (A), shear force (B), and bending moment (C). (D–F) Reconstructed normal force (D), shear force (E), and bending moment (F). (G–I) Difference between the reference and the reconstructed normal force (G), shear force (H), and bending moment (I).

Influence of the surface offset

We calculated the force distributions on the fish by interpolating quantities from the CFD flow field to a triangulated surface of slightly offset from the skin of the fish. The amplitude of these forces is dependent on this offset, related to the accuracy of the interpolation of the pressure and velocity gradients. Due to the immersed boundary approach, there is also a flow field inside the fish, but this is not physically relevant for the force calculations. If this is taken into account in the interpolation, errors in the force distribution will occur.

Fig. S6.4A shows the effect of the surface offset on the accuracy of the bending moment reconstruction. The optimal distance for the offset surface for a simulation with a finest mesh size of 15 μm (the final selected mesh size) was found to be 20 μm. This distance guaranteed that the flow field was interpolated from only cells outside the body, but was close enough to accurately reconstruct the frictional forces.
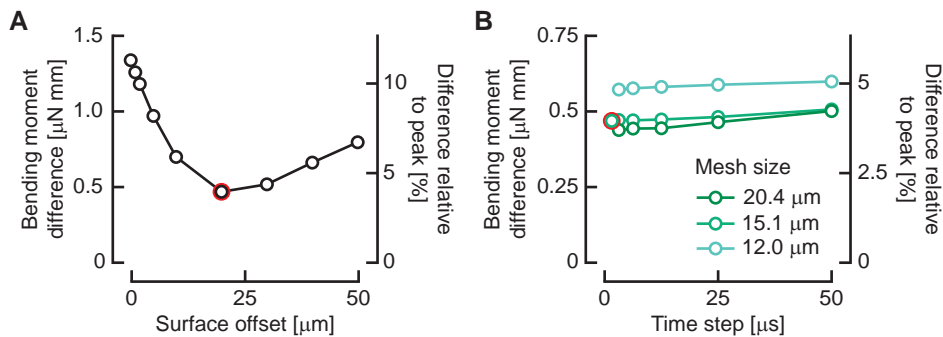
Figure S6.4: Convergence of the immersed boundary solver. (A–B) The difference in reconstructed bending moment compared to the reference solution as a function of the offset of the surface used for force calculations (A), and the mesh size and time step (B). The final choices of surface offset, mesh size, and time step size are highlighted with a red circle.

Influence of the mesh size and time step

To assess the dependency of the solution on the mesh size and time step, we simulated the reference case from the validated solver on three different mesh sizes (finest level size 20.4, 15.1, 12.0 μm), and 5–6 different time steps. The time steps were chosen such that the coarsest step always led to a maximum CFL number close to (but below) 1. In the tested range, mesh size nor time step had a large influence on the solution.

For mesh size, the largest step in accuracy is from 20.4 μm to 15.1 μm, the step to 12.0 μm is smaller. We chose a mesh size of 15.1 μm, as it allows reasonable accuracy while remaining computationally feasible—memory usage is a limiting factor on our computational facilities as the meshes get larger. For the time step, smaller time steps lead to marginally smaller errors. Computation times are at most linearly affected by the time step, so the trade-off for computational feasiblity is less relevant. Hence, to be on the safe side, we chose a time step of 0.5 μs for solving the fluid dynamics.

A comparison of the reference simulation with the final choice of mesh size 15.1 μm and time step 0.5 μs is shown in Fig. S6.5. The bending moments show qualitatively similar patterns, in time and space. The magnitude is slightly underestimated in IBAMR compared to the reference solution.
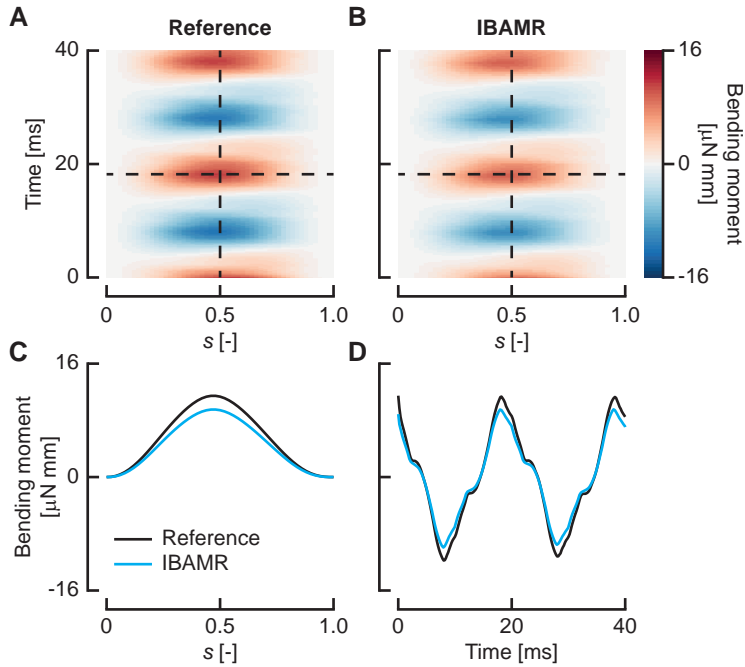
Figure S6.5: Comparison between the validated solver and the final choice of immersed boundary solver settings. (A–B) The reconstructed bending moment for the fluid dynamic forces from the reference solver (A) and IBAMR (B). The dashed lines indicate the two slices shown in C and D, at a single time step, and a single position along the fish.

References

Beléndez, T., Neipp, C. and Beléndez, A. (2002). Large and small deflections of a cantilever beam. *Eur. J. Phys.* **23**, 317.

Griffith, B. E., Hornung, R. D., McQueen, D. M. and Peskin, C. S. (2007). An adaptive, formally second order accurate version of the immersed boundary method. *J. Comput. Phys.* **223**, 10–49.

Guennebaud, G., Benoît, J. and Others. Eigen. http://eigen.tuxfamily.org.

Jones, E., Oliphant, T., Peterson, P. and Others. SciPy: Open source scientific tools for Python. http://www.scipy.org.

Li, G., Müller, U. K., Van Leeuwen, J. L. and Liu, H. (2012). Body dynamics and hydrodynamics of swimming fish larvae: a computational study. *J. Exp. Biol.* **215**, 4015–4033.

Li, G., Müller, U. K., Van Leeuwen, J. L. and Liu, H. (2014). Escape trajectories are deflected when fish larvae intercept their own C-start wake. *J. R. Soc., Interface* **11**, 20140848–20140848.

Li, G., Müller, U. K., Van Leeuwen, J. L. and Liu, H. (2016). Fish larvae exploit edge vortices along their dorsal and ventral fin folds to propel themselves. *J. R. Soc., Interface* **13**, 20160068.

Oliphant, T. E. (2006). *A guide to NumPy*. USA: Trelgol Publishing.

Török, J. S. (2000). *Analytical Mechanics*. New York City, NY, USA: Wiley.

Voesenek, C. J., Pieters, R. P. M. and Van Leeuwen, J. L. (2016). Automated reconstruction of three-dimensional fish motion, forces, and torques. *PLoS One* **11**, e0146682.

6
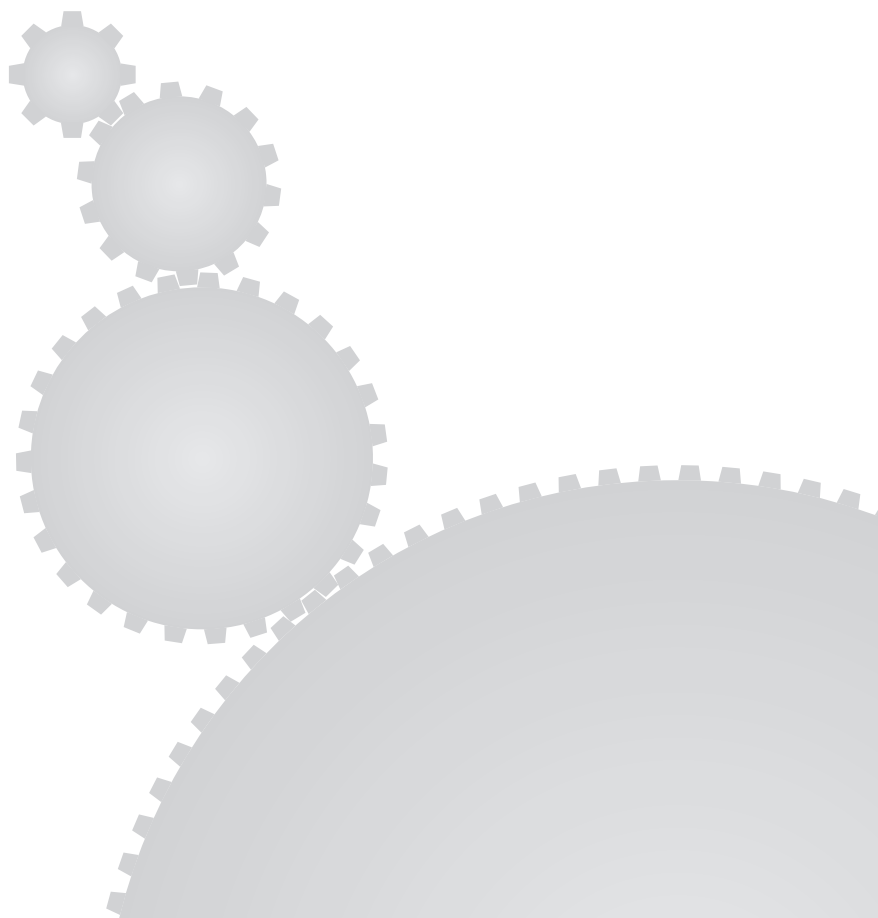
Chapter 7
General discussion

In this thesis, we aimed to understand the biomechanics behind the swimming of fish larvae in their early stages of development. To this end, we explored different aspects of the swimming of larval fish. In **chapter 2**, we reviewed the functional demands of larval swimming, and what solutions have evolved to meet these demands. In **chapter 3**, we used two-dimensional kinematics to analyse the effects of the intermediate hydrodynamic regime on the mechanics of near-periodic swimming of zebrafish larvae at different developmental stages. In **chapter 4**, a method is outlined to reconstruct three-dimensional kinematics, as well as forces and torques from multi-camera high-speed video. This method is applied in **chapter 5**, where we investigate how zebrafish larvae produce reorientation and propulsion during fast starts. Finally, in **chapter 6**, we show that zebrafish larvae seem to use similar muscle activation patterns across development and swimming speeds and accelerations with an advanced inverse-dynamics approach to reconstruct internal bending moments.

We focussed on the swimming mechanics of the zebrafish in its early stages of development. The swimming of fish larvae is highly relevant to fish biology. Fish larvae are orders of magnitude more numerous than adult fish (Houde, 2002): most larvae die before they become juveniles (Hjort, 1914). For fish larvae, swimming is a deciding factor in their survival: they need to hunt to eat, disperse, and escape threats (**chapter 2**). Understanding how larvae can swim effectively will therefore give crucial insight into the ecology of fish. Since many fish larvae are similar in early developmental stages (**chapter 2**; Kendall Jr. et al., 1984), our results for the larval zebrafish are likely applicable to larvae of other species, and perhaps also to some extent for adult fish.

In this general discussion, I place the knowledge on swimming gained in this thesis in a broader framework of fish swimming. We use several novel methods to analyse swimming in three dimensions, the strengths and limitations of which I address. Next, I discuss the seemingly simple way that fish larvae exploit complex physics to swim. I then speculate on how the results from this thesis could be generalised to adult fish, also of other species. Based a simple scaling analysis, I ponder how different contributions to the bending moment might change with fish size. I propose a direction for future research with forward dynamics, rather than inverse dynamics used in this thesis. Finally, I discuss how this rather fundamental work might inspire engineering applications.

7.1 The end of the two-dimensional era?

Historically, fish swimming has been analysed mostly in the two-dimensional plane (e.g. **chapter 3**; Bainbridge, 1958; Domenici and Blake, 1993; Gray, 1933; Müller and Van Leeuwen, 2004). This simplification has made it possible to perform research on undulatory swimming over the past 100 years, despite technical limitations in e.g. number of cameras. However, in ignoring the third dimension, potentially important effects are neglected (Tytell et al., 2008). Many fish swim three-dimensionally, exhibiting considerable pitch and roll angles (**chapter 4**, **5**; Fleuren et al., 2018; Kasapi et al., 1993). Analysing this motion in two dimensions will often result in underestimated speeds, since the third component of the velocity vector is ignored. Furthermore, the three-dimensionality of the motion may be of

ecological relevance. For example, during fast starts, fish may increase escape probability by escaping in the vertical direction (Stewart et al., 2014). Analyses in 2D will miss this fundamentally 3D information; they might draw incomplete or even incorrect conclusions.

Not only kinematics have been simplified to two-dimensions, also flow fields around swimming fish have often been examined in 2D (Carling et al., 1998; Lighthill, 1971; Liu et al., 1996; Müller et al., 2008). Fluid-dynamic phenomena in general behave fundamentally different in 2D compared to 3D (Boffetta and Ecke, 2012; Mittal and Balachandar, 1995). In addition, when measuring or calculating fish swimming in a single plane, the 3D shape of the fish is not taken into account—often only the mid-frontal plane of the fish is considered. This will cause important effects to be ignored, such as edge vortices on the tail or fin fold (Borazjani and Daghooghi, 2013; Li et al., 2016). Hence, the fluid dynamics might be even more important to analyse in 3D than the kinematics.

Technical advances in the past decade, especially in terms of computing power, have opened previously locked doors for the 3D analysis of swimming. Multi-camera video setups with high spatial and temporal resolution have become technologically feasible, as cameras have gotten higher resolutions and sensitivity at lower prices than before. In the past, researchers would labour for many hours digitising movie frames (e.g. **chapter 3**; Drost et al., 1987; Van Leeuwen et al., 1990); computers can now take this load off our shoulders (**chapter 4**). The increased computer power has made it feasible to automatically track fish in 3D from high-speed images with minimal input, realising significantly higher throughput and consistency compared with manual digitisation.

In the field of fluid mechanics of swimming, the third dimension has also become less elusive. Over the past two decades, considerable advances have been made in quantification of 3D flow fields with tomo-particle image velocimetry (Elsinga et al., 2006) and shake-the-box particle tracking velocimetry (Schanz et al., 2013). These methods are currently still challenging to set up for swimming fish, requiring high light intensities and optimally controlled seeding density. However, within the next decade(s) they should presumably become widely (and inexpensively) available, similar to the rise in availability of particle image velocimetry for biological research (Stamhuis, 2006).

For a long time, Computational Fluid Dynamics (CFD), especially in 3D, was unavailable to the biological researcher in terms of technical difficulty and cost. Fish swimming is particularly complex to analyse with CFD, due to the large-amplitude deformation of the complete body of the fish. Calculations on this complex, deforming geometry requires advanced numerical techniques that have not been available until relatively recently, especially in readily available CFD codes (commercial or open-source). A pioneering CFD analysis of swimming of a tadpole was done by Liu et al. (1996, 1997), who used two sets of meshes between which was interpolated: a static background mesh, and a moving, deforming mesh, conforming around the animal. This code was extensively used in the analysis of swimming and flying (e.g. Li et al., 2016; Liu et al., 1998; Nakata and Liu, 2012).

An alternative approach to deforming meshes are immersed boundary methods (Mittal and Iaccarino, 2005; Peskin, 1972), where the computational mesh does not conform to the shape of the simulated object. Instead, the deforming object is represented by a moving

cloud of points. Based on the motion of these points, a source term is added to the Navier-Stokes equation to enforce the no-slip condition in cells overlapping the object. This approach allows relatively straightforward modelling of complex, deforming 3D shapes that are difficult to model with a conforming mesh. An open-source implementation of the immersed boundary method, IBAMR, is easily accessible (used in **chapter 6**; Griffith et al., 2007). Although using this program still requires knowledge on high-performance computing and the C++ programming language, specific expertise to implement efficient CFD methods is no longer required of a researcher. This reduces the effort to perform good CFD significantly, perhaps making it more common in future swimming research.

In conclusion, I think that the era of two-dimensional analyses of fish swimming is nearing its end—at this stage of swimming research, with current and future technical possibilities, the third dimension is open for exploration.

7.2 Fins and out-of-plane deformation

Although we analyse three-dimensional motion of the fish (**chapter 4**, **5**, **6**), we ignore some deformation contributions that might have influence on the swimming motion. There are three main contributions that we ignore in our analyses (Fig. 7.1): out-of-plane deformation, pectoral fin motion, and deformation of the median fin fold.

We assumed that the larvae deform their bodies in a single plane, perpendicular to the medial plane. It has been shown that zebrafish larvae show dorsoventral excursion of the tail of over $30°$ during fast starts (Nair et al., 2015). Although considerably smaller than the lateral excursion, it influences the fluid-dynamic forces and torques. Furthermore, it has been shown that the body and caudal fin of adult fish twist during swimming (Donatelli

A

B

C
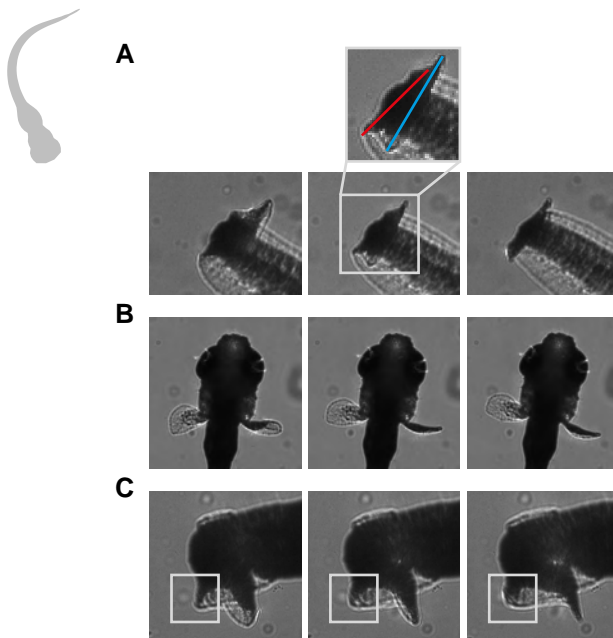
Figure 7.1: Complex, out-of-plane motion components of swimming of zebrafish larvae (8 days post fertilisation). (A) Twisting of the tail, successive frames are 0.45 ms apart. (B) Pectoral fin use, successive frames are 2.3 ms apart. (C) Deformation of the median fin fold, successive frames are 0.45 ms apart.

et al., 2017; Lauder, 2000). This is also visible in our high-speed video images (Fig. 7.1A). These out-of-plane deformations may be important for producing roll and pitch torques.

We also ignored the motion of the pectoral fins. Larval zebrafish develop functional pectoral fins before hatching (Grandel and Schulte-Merker, 1998). The larvae beat their pectoral fins during feeding (**chapter 2**), slow swimming (Thorsen et al., 2004), and during slow C-starts (**chapter 5**). The motion of these fins is complex: they deform considerably while they are beaten (Fig. 7.1B). The pectoral fins have been suggested to play a purely respiratory role during slow swimming, rather than a locomotory one (Green et al., 2011; Hale, 2014). These researchers proposed that the larvae mainly beat their pectoral fins to refresh the oxygen-deprived water around their gills, rather than provide additional thrust. However, during feeding they appear to fulfil a propulsive role (**chapter 2**), as for example in juveniles of metallic livebearers (Lankheet et al., 2016). Furthermore, we show in **chapter 5** that the elevation change correlates with the amount of time that the pectoral fins are used during the start. Hence, the motion of the pectoral fins may be instrumental in controlling key swimming manoeuvres.

Finally, we do not consider the deformation of the medial fin fold. The fin fold is a thin structure surrounding the body, present as a precursor to median fins in the larvae of many species of bony fish (Kendall Jr. et al., 1984). In zebrafish larvae, it surrounds the body behind the yolk sac, and is much taller at the ventral side than the dorsal side (Parichy et al., 2009). It deforms during swimming, especially on the ventral side (Fig. 7.1C; Van den Boogaart et al., 2012), caused by the fluid-dynamic forces and fin tissue architecture. This fin deformation changes the angle of incidence of the fin fold edge as it moves through the flow, which is likely to have influence on the fluid-dynamic forces and torques.

Dorsoventral excursions are important for producing pitch torques during fast starts (Nair et al., 2015). The deformation of the fin fold will likely also contribute to pitch and roll torques. The ventral part of the fin deforms more strongly than the dorsal part, causing an asymmetry in the local incidence angles—the resulting differences in pressure will result in roll and pitch torques. In a similar manner, axial twist of the body will influence the produced torques. The effects of out-of-plane deformation may be the cause of the considerable variation in roll angle during near-cyclic swimming of young zebrafish larvae (**chapter 4**, **5**); as the fish beats its tail, the medial fin fold will deform and the tail will twist, resulting in periodic variation of the roll (and pitch) torque. Since the mass moment of inertia of the fish is relatively small around its roll axis, relatively small torque variations may result in considerable angle changes.

Because we considered only single-plane deformation, we also model the bending moment only in this plane (**chapter 6**). The bending moment in the yaw plane is the dominant term: the axial muscles produce moments mostly in this plane, leading to a much larger motion amplitude than both dorsoventral excursions and tail twist. However, calculating the distributions of the dorsoventral bending moment and torsion moment might give additional insight. For example, one could examine how fish use dorsoventral tail excursion to produce pitch torques (Nair et al., 2015). The reconstruction of these additional terms from motion is possible, but would require the additional deformation contributions to

be reconstructed with high accuracy.

For future, more accurate automated tracking approaches of fish in general, and zebra-fish larvae in particular, I recommend introducing the additional deformation modes to the fish model. A dorsoventral curvature and axial twist can be added along the centreline of the fish, in addition to the lateral curvature. Furthermore, a model of the pectoral fins should also be added to analyse their contribution to motions that involve beating of the paired fins, e.g. feeding and slow C-starts. This will make the automated tracker more applicable to fish swimming in general; for many fish species, the paired fins are important during swimming and manoeuvring (Drucker and Lauder, 2003; Westneat, 1996).

Adding deformation parameters to the fish model requires more information to be extracted from the high-speed video images. This places more stringent demands on their spatial and temporal resolution, and the number of viewing angles. With the current number of parameters, the tracking problem is already ill-posed: many different wrong solutions (i.e. local minima) will fit the images almost as well as the real solution. This is caused by the limited information present in black-and-white silhouettes; only a projection of a 3D model is made. To overcome the ill-posedness, we introduce regularising terms that penalise physically invalid solutions (**chapter 4**; Tikhonov, 1963). This works up to a limit: as the number of parameters is increased, the number of 'local minimum' solutions increases rapidly.

The required extra information can be added by filming from more angles. However, using more cameras requires more complex, expensive setups. Alternatively, light conditions can be changed to highlight different parts of the fish (Lankheet et al., 2016)—rather than just a silhouette, individual body parts, such as the pectoral and median fins, can be identified. This may make it feasible to extract the missing motion components, even from a limited number of cameras.

7.3 The inverse dynamics approach: strengths and limitations

The main methodological approach in this thesis is inverse dynamics: the calculation of dynamics (external and internal) from motion. This method has advantages, but also limitations and drawbacks. The main strength of the inverse dynamics approach is that it can reconstruct properties of actual motion (**chapter 4, 5, 6**). The amount and type of information that we extract from the motion depends on the models that we introduce.

With an appropriate model, we can use the kinematics of the fish as a basis to fit or reconstruct its dynamics. For the reconstruction of hydrodynamic forces and torques, we used the kinematics in combination with a mass distribution model (**chapter 4**). Since this is a relatively simple model, the amount of additional information we extracted was limited: only two extra vectors per time step. For our bending moments analysis (**chapter 6**), the models are more complex. We solved the full Navier-Stokes equations, and introduced a large-amplitude beam model for the fish. This allowed us to reconstruct considerably more information from the motion: we analysed internal mechanics based solely on the kinemat-

ics. The approach of **chapter 6** can be considered a form of data assimilation (Bengtsson et al., 1981), in which a model is optimised to best take into account the data while satisfying governing equations. This is a powerful approach, with which even sensitive models (such as meteorological predictions, or internal mechanics of a fish) can produce reliable results, under the right conditions.

To reconstruct dynamics reliably, the accuracy of the input data should be sufficiently high, as relatively small errors in the motion can lead to large errors in acceleration, in turn causing bad estimates of forces (Cahouët et al., 2002). These errors generally do not propagate to other time steps or locations, although this depends on the applied model (Silva and Ambrósio, 2004). In our case of resultant forces and torques (**chapter 4**, **5**), propagation through time is minimal—the method depends only on the neighbouring time points. However, for the internal moment reconstruction (**chapter 6**), fluid forces depend also on the history of the flow, allowing errors to propagate forward in time.

The results we obtain with the inverse dynamics depend on the smoothing applied (**chapter 4**). To assess the reduction in error depending on the smoothing, consider a simplified one-dimensional example of force reconstruction of a point mass:

$$F = m\frac{\mathrm{d}^2 x}{\mathrm{d}t^2},\tag{7.1}$$

where F is the resultant force, m is the mass, x is the position, and t is the time. I assume that the mass is known with high accuracy, but that the position is measured with a certain error ε:

$$\hat{x} = x + \varepsilon,\tag{7.2}$$

where $\hat{x}$ is the measured position. We calculated the second derivative with a numerical method on data sampled with finite resolution. Consider a (numerical, linear) second derivative operator $\mathcal{D}_2$, our estimate for the second derivative then becomes:

$$\left(\frac{\mathrm{d}^2 x}{\mathrm{d}t^2}\right)_{\text{est}} = \mathcal{D}_2(\hat{x}),\tag{7.3}$$

leading to an error from the actual acceleration:

$$\frac{\mathrm{d}^2 x}{\mathrm{d}t^2} = \left(\frac{\mathrm{d}^2 x}{\mathrm{d}t^2}\right)_{\text{est}} + \mathcal{D}_2(\varepsilon) + \varepsilon,\tag{7.4}$$

where ε_D is the error originating from the derivative operator. With a sufficiently high time resolution, ε_D is limited (Harper and Blake, 1989); the main source of error is $\mathcal{D}_2(\varepsilon)$, the (numerical) second derivative of the position error.

In the case of the video tracking in this thesis (**chapter 4**, **5**), the errors in each frame were mostly independent—although the previous frame was used to initialise the optimisation, this mostly resulted in faster convergence rather than a different solution. This resulted in errors that are randomly distributed from frame to frame—differences between

frames may be large, so the (numerical) second derivative will be huge. Hence, when the position data remain unsmoothed, this error term will dominate the solution. As the solution is smoothed, high-frequency components disappear (Eilers, 2003; Stickel, 2010). Initially, this will mainly result in a reduction of error terms. At higher smoothing settings, the physical signal will be more strongly affected by smoothing, resulting in an increase in error. In other words: one must walk the line between over- and undersmoothing, trading reduction in errors for loss of high-frequency components. However, with sufficiently-high time resolution compared to the expected physically relevant frequencies, as is the case in this thesis (**chapter 3**, **5**, **6**), it is possible to filter out the noise while maintaining most of the physically relevant frequency content.

The error propagation is more complicated in **chapter 6**, where we calculated fluid-dynamic forces from the motion with computational fluid dynamics and used these to reconstruct internal force and moment distributions. Here, errors in the reconstructed bending moment depend non-linearly on position errors. The fluid flow itself has a damping effect due to the low Reynolds number and hence relatively high importance of viscosity (Conca et al., 1997)—high-frequency errors in position will be dampened and result in relatively small changes in forces. The optimisation approach that we used to calculate internal forces and moments will also tend to smooth errors, as it attempts to balance between satisfaction of the governing equations and minimal deviation from the data. Outlying points were mostly ignored, as they would otherwise cause large residuals of the equations of motion. In conclusion, despite the complex, potentially sensitive models, we can reliably reconstruct internal forces and moments from motion obtained from high-speed video.

7.4   Simplicity and complexity

Zebrafish larvae use relatively simple bending moment patterns for the complex process of swimming (**chapter 6**). The brains of young larvae are still underdeveloped (Mueller and Wullimann, 2016), and hence may not be able to reliably generate complex motor output. Despite these potential inaccuracies, when a predator appears, the larvae need to escape to survive to adulthood (Walker et al., 2005). These demands require the fish to effectively accelerate in an optimal direction and swim at a sufficiently high speed (**chapter 2**; Nair et al., 2017). This implies that the system (i.e. the fish interacting with the water) should be robust to inaccuracies in the motor input. I hypothesise that zebrafish larvae have evolved a finely-tuned combination of the muscle architecture, passive tissues arrangement and external morphology that makes the system robust to noisy inputs. As long as the larvae activate their muscles alternately on the left and right side, undulatory swimming motion or even starting motion is produced.

7.4.1   Undulatory swimming

To produce undulatory swimming, the stiffness distribution of the body might be such that a simple forcing will still lead to a travelling wave body pattern through the fluid-structure interaction of the body and the water. For example, (near-) standing wave muscle

activation patterns may result in a travelling wave curvature pattern, through interaction with the passive tissues and water (Blight, 1976). As demonstrated with a simplified model, relatively simple forcing may induce a complex motion in a stiffness-tuned body by causing higher-order deformation modes to be active (Bhalla et al., 2013). A similar mechanism might be present for the zebrafish, allowing it to produce complex motion along its body with simple forcing, mostly created by the interaction of the passive tissues in the body with the surrounding water.

If simple forcing is sufficient to produce body undulations, swimming may be controlled with relatively few parameters. In **chapter 6**, we show that across early development a similar bending moment pattern is produced, allowing the larvae to control its swimming speed and acceleration with two parameters: the amplitude of the bending moment and its duration. The duration could be controlled by modulating the central pattern generators to act at a different frequency (Harris-Warrick, 2011). The peak bending moment is presumably regulated by muscle recruitment. In adult fish, as the swimming speed—and hence the bending moment amplitude (**chapter 6**)—increases, the recruitment of red (aerobic) and white (anaerobic) muscle fibres changes. At slow speeds, only red muscle is recruited, with additional white muscle being recruited at higher speeds (Rome et al., 1984). At the highest speeds, the red muscle stops being active, leaving only white muscle to produce power (e.g. for Centrarchidae: Jayne and Lauder, 1996). The red and white muscle fibres have different properties in adult fish, but not in the early stages of larval development (Buss and Drapeau, 2000). Despite the similar properties, the recruitment pattern across speeds—from red, to red and white, to white—are similar to adults when measured in paralysed larvae (Buss and Drapeau, 2002). Muscle recruitment according to this pattern might controls the bending moment amplitudes in fish larvae too.

7.4.2 Beyond forward swimming

The system to control forward swimming may be relatively simple, but zebrafish larvae also produce more complex motion. At later developmental stages, zebrafish larvae show evidence of fine control over their motion in prey capture (Borla et al., 2002) and maintaining stability (Ehrlich and Schoppik, 2017). While just-hatched larvae appear to show little control over their orientation and the direction of swimming, older larvae seem much more able to direct their swimming (Müller and Van Leeuwen, 2004). This precise turning behaviour presumably requires subtle alterations of the bending moment patterns from tail-beat to tail-beat. I speculate that control of the turn rate is dependent on muscle activation strength in subsequent tail beats. For example, slightly stronger activation of the left axial muscle compared to the right may lead to a left turn, similar to how stronger body curvature during a fast start leads to larger turn angles (**chapter 5**). Manoeuvres further removed from simple body undulations, such as a J-turn, may requires different muscle activation patterns altogether, and hence specialised neural control. These motions are only shown later in development, several days after hatching (Fero et al., 2011).

Undulatory axial muscle activation in fish is controlled via motoneurons that lie along

the spine (Fetcho, 1987). In zebrafish larvae, the dorsal motoneurons are active at high frequencies, while more ventrally located motoneurons are active at low frequencies (McLean et al., 2007). The dorsal motoneurons develop before the ventral motoneurons, which reflects in the behaviour of fish larvae: they first swim fast and with coarse control, while later in development finer control and slow swimming becomes possible (Fetcho and McLean, 2010). This is also reflected by the fact that zebrafish larvae become better at maintaining balance across early development (Ehrlich and Schoppik, 2017). In zebrafish larvae 6 days post fertilisation, control over the swimming speed is highly localised to several neurons (Severi et al., 2014). Although these neurons appear before hatching (Kuwada et al., 1990), refined control over the swimming speed only becomes apparent later. This increase in control also fits with observations in **chapter 6**, where the just-hatched larvae swim at approximately one speed 'setting' to produce maximal performance, while older fish show much more variation in their swimming vigour. This could indicate that they become better at tailoring their swimming speed to the requirements of their situation.

7.4.3 Fast starts

The bending moments we computed in **chapter 6** also included starts: we did not base our selection of half-beats on the kinematics, but only on the bending moments. Since they are similar from tail-beat to tail-beat, the motion generated during a fast start (**chapter 5**) is produced with similar bending moments in the first and in the second stage. This means that the characteristic C-shape and subsequent propulsive tail beat motion primarily emerge from the fluid-structure interaction, and not necessarily from the specific motion activation pattern, as suspected before for adult fish (Foreman and Eaton, 1993). The difference in initial condition between a 'normal' tail beat and stage 1 of a C-start, both in terms of body shape and surrounding fluid, leads to the emergence of a different shape, but with similar bending moments.

   The generation of the C-shape has been measured to be generated by a synchronous unilateral muscle activation (Jayne and Lauder, 1993). The kinematics of following tail beats emerge from similar activation of the opposite side (Foreman and Eaton, 1993). This means that the escape angle and speed can probably be controlled with the same parameters used in forward swimming (**chapter 5, 6**): escape angle correlates strongly with the overall body curvature, which is probably related to the peak bending moment and the duration. The escape speed correlates strongly to the duration of the first two tail beats, which is related to the duration of the bending moment waves. This corresponds with earlier observations on adult fish, where the start direction was found to be influenced by the relative strength of the first and second tail beat, and the timing between them (Foreman and Eaton, 1993). Hence, it appears that even a seemingly complex, aperiodic motion such as the fast start can be controlled similarly to regular, near-periodic swimming.

7.4.4 Simple control in larvae across species

I expect that straightforward and reliable control over swimming is a valuable property of fish larvae across species. Many fish larvae look similar (Kendall Jr. et al., 1984), while they have a wide diversity of body shapes as juveniles and adults (**chapter 2**). I hypothesise that the larvae of many fish species have similar control of swimming to zebrafish larvae, which use simple bending moment patterns to produce effective swimming (**chapter 6**). This would enable any larvae to swim soon after hatching, allowing them for example to escape predators, hunt for food, or disperse (**chapter 2**). The universal body shape and presumably muscle activation patterns of larvae might have evolved early in the history of fish, and is common across a wide range of species. As the larvae develop into juveniles, they may develop the neural processing capacity to perform the more complex locomotion patterns required by some of their adult swimming styles (e.g. with pectoral fins), or they might adapt the pattern to their adult morphology (see below). To test whether all fish larvae indeed swim similarly, it would be interesting to compare bending moment patterns reconstructed for larvae of several fish species across taxa, and follow how these patterns change as the larvae develop into juveniles.

7.5 Generalisation of across species and developmental stage

Adult fish often differ considerably in morphology, swimming mode, and size from fish larvae (**chapter 2**). Understanding the swimming mechanics of adult fish is also of considerable interest. The fish that survive the larval stage spend most of their lives in the adult stage, during which they need to swim to survive and eventually reproduce. Furthermore, adult fish have historically been researched much more than larvae. We would like to compare our results for larvae to this broad base of previous studies, so in this section, I attempt to answer the question: can the knowledge on the swimming mechanics of larval fish be generalised to adult fish?

7.5.1 Bending moment patterns and muscle activation

The bending moments (Hess and Videler, 1984) that we reconstructed are qualitatively similar to results obtained for a near-periodically swimming adult saithe (Cheng and Blickhan, 1994). This similarity is interesting considering the differences between saithe and larval zebrafish in morphology and scale. This causes larvae and adults swim in a different hydrodynamic regime, resulting in changes in the fluid-structure interaction that produces their motion (**chapter 2**). Furthermore, their swimming style is different: while in saithe body deformation is largest in the tail, in zebrafish larvae almost the entire body deforms (**chapter 3**). In addition, there are methodological differences between this thesis and previous studies reconstructing bending moments: previous approaches assume small-amplitude motion (Cheng and Blickhan, 1994; Hess and Videler, 1984), and use a simplified, inviscid fluid model (Lighthill, 1971; Wu, 1961) rather than a large-amplitude model

and full solution of the 3D Navier-Stokes equations (**chapter 6**). Despite these differences, the bending moment patterns look similar.

The shared pattern of adult saithe and larval zebrafish is a fast-travelling wave in posterior direction that alternates between left and right with each tail beat, with an amplitude peak in the middle of the fish and limited high-frequency content (**chapter 6**; Cheng and Blickhan, 1994). I expect the bending moment to alternate direction, in accordance with the tail beats—bending moments that do not change sign cannot produce alternating swimming motion. Furthermore, since both ends of the fish are free, boundary conditions (Hibbeler, 2005) dictate that the internal bending moments are zero at the snout and tail. Hence, we expect the bending moment to have the largest amplitude away from the edges of the fish. These physical constraints may explain the overall similarity of the patterns. However, the precise characteristics of the travelling wave differ between our results for the larvae and the previously found results (Cheng and Blickhan, 1994). This might be caused by changes in the fluid-structure interaction due to the size effects (see below), due to dissimilar morphology and tissue properties, or due to methodological differences.

Rather than analysing bending moments by themselves, we would ideally want to compare muscle activation patterns. The bending moment patterns that we calculate cannot be straightforwardly translated to muscle activation patterns (**chapter 6**). This requires additional modelling, where the passive and active contribution to the bending moment need to be teased apart (Cheng and Blickhan, 1994; Pedley and Hill, 1999). However, when bending moment patterns are similar with the same morphology, it is likely that muscle activation patterns are similar too (**chapter 6**). When comparing larvae to adults, similar bending moments might not necessarily originate from the same muscle activation pattern for various reasons: scaling effects might be important (see below), the morphology often changes considerably from larvae to adult (**chapter 2**), and passive tissue and muscle properties are likely to be different. Hence, based on the bending moment patterns, it cannot be stated confidently that the similar bending moment patterns between larvae and adults stem from similar muscle activation patterns.

However, for both adults (Wardle et al., 1995) and larvae (Buss and Drapeau, 2002), muscle activation patterns are superficially similar: they alternate between left and right and show a phase delay along the body in posterior direction. Furthermore, like what the similar bending moment patterns suggest might happen in the zebrafish larva (**chapter 6**), timing of the onset and end of the muscle EMG signals is independent of the swimming speed in mackerel and saithe: these fish show similar patterns across all speeds (Wardle and Videler, 1993). Newt larvae, which look and swim like fish larvae, have been shown to have variable rostrocaudal activation delay: during their fastest swimming the muscles contract simultaneously, while during slower swimming the delay increases (Blight, 1976). In adult fish, anguilliform swimmers show a relatively slow activation wave, in contrast to carangiform swimmers, where the activation wave is much faster (Wardle et al., 1995). Perhaps the rostrocaudal delay of muscle activation is a suitable parameter to adapt a relatively simple common muscle activation pattern to the specific demands of swimming with a certain morphology at a certain speed. This could be tested by performing a parameter study with

a forward-dynamics model of the fish (see below), varying for example body flexural stiffness and the rostrocaudal delay of muscle activation.

In any case, it seems that having a consistent, adaptable muscle activation pattern across development and species is a good strategy. Across evolution, the control system might not have needed much change to keep on swimming effectively as fish were radiating across niches with large morphological changes. This would allow drastic adaptations in morphology to remain viable, which might partly explain the enormous evolutionary success of the fishes over a long period of time.

7.5.2 Scaling of the bending moment

The changes in body length between zebrafish larvae and adults may affect the bending moment, since the contributions to fluid-structure interaction may scale differently with length. The bending moment consists of four main contributions: passive tissues, muscles, fluid-dynamic forces, and inertia. To assess how these contributions change with respect to each other across length scales, and what consequences this might have, I propose a scaling analysis. Since the bending moment shows similar patterns between larvae and adults (**chapter 6**), I expect each contribution to the bending moment to scale similarly with the body length. To highlight where we can expect differences in scaling, I initially assume that there are no differences between the properties of the passive tissues and muscles of larvae and adults. The resulting scaling relations based on this assumption will then indicate which assumptions are likely to be invalid, and hence what might be different between adults and larvae.

I assume that the passive tissues scale like a Hookean material, with similar Young's modulus across lengths. The passive contribution is then proportional to the moment of inertia ($\propto \ell^4$) and the curvature ($\propto \ell^{-1}$). Therefore, the passive tissue contribution to the bending moment scales as $M_{\text{passive}} \propto \ell^3$ Assuming that muscle properties remain constant across lengths, the muscle forces should scale with cross-sectional area ($\propto \ell^2$), and the lever arm ($\propto \ell$). Hence, the contribution of the muscles to the bending moment scales as $M_{\text{muscle}} \propto \ell^3$.

Lateral fluid-dynamic drag forces are an important factor to determine the body deformation (Godoy-Diana and Thiria, 2018). I expect these forces to scale with the dynamic pressure ($\propto v^2$), the surface area of the fish ($\propto \ell^2$) and the lever arm ($\propto \ell$). Hence, expressed in terms of speed and length of the fish, the fluid contribution to the bending moment scales as $M_{\text{fluid}} \propto v^2\ell^3$. The inertial contribution scales with body mass ($\propto \ell^3$), acceleration due to deformation ($\propto \ell f^2$), and lever arm ($\propto \ell$), so $M_{\text{inertia}} \propto \ell^5 f^2$. Based on data of 27 fish species, compiled by Van Weerden et al. (2014), I performed linear least-squares fits in logarithmic coordinates for the dependency of the speed and frequency with body length. I found that speed scales with $\ell^{0.55}$—large fish swim faster in an absolute sense, but not when normalised by body length; this is in approximate agreement with earlier found values (Sambilay, 1990; Ware, 1978). The frequency scales with $\ell^{-0.52}$—larger fish beat their tails at lower frequencies; the exponent is in agreement with a study on cod

(Altringham and Johnston, 1990). Rounding off both exponents to 0.5, bringing the coefficients in line with a general locomotion scaling study by Bejan and Marden (2006), the scaling relations for the fluid and inertial contributions become respectively $M_{\text{fluid}} \propto \ell^4$ and $M_{\text{inertia}} \propto \ell^4$.

Summarising, if I assume constant tissue properties across scales, the contributions to the bending moment scale with length as:

$$M_{\text{passive}} \propto \ell^3; \tag{7.5}$$
$$M_{\text{muscle}} \propto \ell^3; \tag{7.6}$$
$$M_{\text{fluid}} \propto \ell^4; \tag{7.7}$$
$$M_{\text{inertia}} \propto \ell^4; \tag{7.8}$$

The passive and muscle tissue contributions scale with ℓ^3, but the fluid and inertia contribution scale with ℓ^4. Under these assumptions, for larger fish, the fluid and inertia are expected to have a relatively larger contribution to the bending moment balance than the internal tissues. Because we see a qualitatively similar pattern of bending moments, and probably also muscle activation (see above), these assumptions apparently do not hold: I expect that passive and muscle tissue properties change from larvae to adults.

For the bending-moment contribution of the passive tissues to remain similar across scales, I would expect the tissues of larger fish to be stiffer than smaller fish. A low stiffness tends to lead to more anguilliform swimming (Blight, 1977; Tytell et al., 2010a). However, adult fish in general show a more carangiform swimming style than larvae, suggesting a relatively higher body stiffness. So, what could be the origin of this increased stiffness? The zebrafish larvae that we consider in this thesis have not fully developed their skeletons, including the notochord (Bird and Mabee, 2003). The notochord/vertebral column has been suggested to play an important role in increasing body stiffness (Nowroozi and Brainerd, 2014), although it is not clear how ossification might influence stiffness. Furthermore, it was found that the relative skeletal mass in most cases does not increase further as the fish grow from juveniles to adults (Berrios-Lopez et al., 1996). Past the larval stages, I do not expect the skeleton to increase in stiffness contribution as fish become larger. The skin stiffness has also been shown to have an influence on swimming kinematics (Long et al., 1996). As it is located the furthest from the neutral line of bending, it will likely have a large contribution to the flexural stiffness. In zebrafish larvae, the skin shows considerable changes across development towards a juvenile (Parichy et al., 2009), perhaps causing an increased stiffness. Perhaps a forward dynamics model (see below) could be of help in elucidating the influence of the body stiffness on the bending moment patterns and motion across scales.

In addition to the increased stiffness, I expect the muscles of larger fish to produce higher forces per unit of cross-section than for smaller fish. Larval fish use high activation frequencies (**chapter 3**), which generally leads to relatively low forces (Rome et al., 1999). For optimal power output, larger fish use lower frequencies than smaller fish and hence relatively higher muscle forces (Altringham and Johnston, 1990). In short-horn sculpin,

the contractile properties of muscle change across lengths, causing a decrease in maximum shortening velocity (James et al., 1998), while specific muscle power remains the same (James and Johnston, 1998). This points to an increase in force generation capacity of muscle for larger fish.

The simple scaling analysis of the bending moments does not consider the changing requirements for producing propulsion. In the transition from the intermediate regime to the inertial regime, which happens as the larvae grow into adults, Strouhal numbers decrease (**chapter 3**; Eloy, 2012; Kayan et al., 1978). This effect is asymptotic: above a certain length, many undulatory swimmers (and fliers) use similar Strouhal numbers (Taylor et al., 2003). The Strouhal number has been associated with swimming efficiency, a range of 0.25–0.35 was suggested to lead to the most efficient swimming (Triantafyllou et al., 1993). However, this is not a sufficient condition for efficient locomotion. It has been suggested that the dimensionless tail-beat amplitude (Saadat et al., 2017) or a parameter based on the body wave properties (Wiens and Hosoi, 2018) determine the efficiency of swimming, with the Strouhal number following from the body morphology and swimming motion to a value where thrust and drag are balanced. The high Strouhal number of fish larvae (**chapter 3**) suggests that their drag, and hence required thrust, is relatively high (**chapter 2**). Therefore, the fluid-dynamic contribution to the bending moment might be larger for small fish than the scaling suggests. A high Strouhal number has similar implications for the inertial contribution: a high tail-beat frequency and relative amplitude will lead to a higher inertial bending moment. This might partly explain the similarity of the bending moments despite the different scaling of the fluid-dynamic and inertial contributions compared to the passive and muscle tissue contributions.

In summary, a scaling analysis suggests that larger fish have a higher tissue stiffness and higher muscle fibre stresses than larval fish. These effects might be somewhat reduced by the changes in hydrodynamics: the high required tail-beat amplitudes and -frequencies result in relatively stronger fluid-dynamic and inertial contributions to the bending moment for larvae. Finding the answers to these speculations requires new comparative experiments, both physical and numerical.

7.6 Forward with forward dynamics

This thesis has focussed on inverse dynamics, extracting information from existing motions. Interesting opportunities also present themselves in an alternative approach: forward-dynamics modelling. In a forward-dynamics approach, the model is built bottom-up: the motion follows from model parameters, rather than the other way around. The advantage of forward-dynamics modelling is that counterfactual inputs can be given, simulating what would happen if certain parameters would be varied outside their biological range.

Since the 90s, several forward dynamics models of swimming have been made that include the internal dynamics of the fish (e.g. Jordan, 1996; Tokić and Yue, 2012; Tytell et al., 2010b), with varying modelling assumptions. Due to a lack of computational power, these models often used simplified fluid-dynamics model (Jordan, 1996; Tokić and Yue, 2012),

such as Lighthill's elongated body theory (Lighthill, 1960, 1971). While other models used a computational fluid dynamics approach to solve the Navier-Stokes equation, but restricted themselves to two-dimensional flow, again due to computational limitations (Hamlet et al., 2015; Tytell et al., 2010b).

Despite their limitations, these valuable models have shown that well-tuned properties of the fish's tissues are crucial for producing effective swimming motion, for example body stiffness (Tytell et al., 2010b), or the muscle force-velocity relationship (Hamlet et al., 2015). Furthermore, the optimal external shape and muscle activation patterns determined with a multi-objective optimisation for maximum swimming speed and minimum cost of transport look similar to what is found in nature (Tokić and Yue, 2012). These studies illustrate the strength of forward dynamics modelling: by varying parameters outside the range found in nature, sensitivity of parameters and evidence of optimisation can be found. This will never be possible to the same extent by performing experiments—environmental factors can be modified, and perhaps the animal to some extent by genetic modification, but the freedom that computer simulations offer will never be achieved.

A fundamental drawback of forward-dynamics models is the necessity to approximate every component of the model. With an inverse-dynamics model, we can combine terms and thus forego the need to model them individually (**chapter 6**). With a forward-dynamics model, we generally need to model many individual components. This requires quantification of a considerable number of parameters—(visco-)elastic tissue properties, muscle force production properties, passive and muscle tissue architecture, etc. By performing reference experiments at a few different swimming speeds and frequency, the parameters may be tuned such that realistic swimming behaviour emerges, without requiring detailed measurement of each individual parameter. However, this should be done carefully: the swimming efficacy has been shown to depend sensitively on mechanical properties, particularly stiffness (Tytell et al., 2010b). Although the opposite has also been suggested: Bhalla et al. (2013) stated that swimming ability is relatively insensitive to variations in e.g. the stiffness. They argued that this makes sense from an evolutionary point of view: even as the individuals change across generations, swimming ability cannot be lost to remain viable.

The beam model we derive in **chapter 6** can serve as a basis for future three-dimensional forward-dynamics models. Rather than reconstruct internal forces and moments, the equations can be integrated to obtain the motion of the centreline. This simulation can then be coupled to the fluid solver, such that feedback from the fluid is implemented. The constitutive relations can be estimated to be representative for passive fish tissues from previous measurements on adult fish (e.g. Long et al., 1996, 2002). The effects of the muscles can be implemented via distributed muscle forces and moments, making it unnecessary to implement a complex muscle model initially.

Despite its relative simplicity, interesting numerical experiments could be performed with this initial model. With the current and future computational power, larger parameter studies become feasible. For example, the sensitivity of effective swimming to variations in the bending moment pattern can be examined. Robustness of the swimming

motion to inaccuracies in the bending moments, either due to neural noise or asymmetric development, is interesting to examine, as it is likely of large importance to just-hatched fish larvae. Furthermore, the origin of turning behaviour can be investigated—is it the case that left-right asymmetries in the bending moment generation lead to turning?

The holy grail of forward dynamics modelling of swimming would be a complete neuromechanical model of a fish, integrating neural models, tissue models, and fluid dynamics to provide a platform for numerical experiments: a true in silico fish. For example, coupling between the motor system and the lateral line could provide insight in the required sensory feedback for producing motion. In adult fish, head oscillations have been suggested to be important for controlling their motion by optimising a sensed pressure gradient to an expected profile (Akanyeti et al., 2016). Young fish larvae use their lateral line to sense flow for detecting predators (Stewart et al., 2014), perhaps it also plays a role in their motor control. A forward dynamics model is an ideal tool for this type of question: sensors could be turned on and off at will to observe what their influence would be.

An alternative to a completely numerical model would be a robotic fish. Rather than model the fluid-structure interaction numerically, an experimental model of the fish can be created (Gibouin et al., 2018; Wen et al., 2018), for example with multi-material 3D printing techniques (Porter et al., 2017). While it is feasible to create these robotic models on the scale of most adult fish, it is difficult to do for fish larvae. Careful scaling is necessary of for example the viscosity of the fluid, the material properties, and the actuation is required to be accurate. This is likely to be difficult to achieve for zebrafish larvae, due to their tiny scale. In this case, a numerical rather than physical model seems the most promising.

7.7 Inspiration for design

Nature has spent many millions of years evolving effective ways of swimming for a wide range of requirements: speed, acceleration, manoeuvrability, accuracy, etc. In designing underwater vehicles, engineers can take lessons from nature. For example, underwater vehicles for surveillance are often powered with propellers; although quiet (Griffiths et al., 2001), their unnatural noise spectrum might disturb the environment (Slabbekoorn et al., 2010). Designing an underwater surveillance vehicle that 'swims' with body undulations might be less disturbing to the underwater ecosystem for blending in better with the 'natural' background noise. In this thesis, we help to understand how undulatory swimming motion may be produced in a simple manner, so it may inspire future designs of swimming (miniature) robots.

Delegating complexity of systems to passive systems may be of interest in engineering applications as well. For example, research UAVs have flown with aeroelastic control, where small moving surfaces control a complex fluid-structure interaction that deforms the entire wing (Vos et al., 2007). Thus, small, relatively simple control inputs can lead to much larger outputs acting via complex physics. In engineering, the complexity can also be reduced with advanced control computer. For example, in fly-by-wire aircraft, the handling characteristics of an aircraft can be altered by the flight control computer to be more usable

for human pilots (Elliott, 1977). However, the development, and especially debugging, of safety-critical software systems is extremely costly (Blanchet et al., 2002). A system that is controllable passively is preferable, both in terms of cost and reliability: physics will never fail, while software might. Perhaps the tiny zebrafish larva can be an inspiration to engineers in the future development of passive control systems.

7.8 Epilogue

In this thesis, we set out to investigate how zebrafish larvae swim so soon after hatching. We gained understanding of the effects of the intermediate Reynolds regime on the swimming behaviour of the larvae (**chapter 2**, **3**). Furthermore, by analysing the motion in 3D (**chapter 4**, **5**), and with inverse dynamics (**chapter 5**, **6**), we conclude that swimming, although complex, seems to be controlled in a relatively simple manner. Of course, many open questions remain: how do the fish activate their muscles? How energetically efficient is their swimming, and does this change over development? How are the neural patterns that control swimming generated? How is sensory feedback used during swimming? The results from this thesis will hopefully help future researchers in their quest for answers to finally understand:

How do fish swim?

References

Akanyeti, O., Thornycroft, P. J. M., Lauder, G. V., Yanagitsuru, Y. R., Peterson, A. N. and Liao, J. C. (2016). Fish optimize sensing and respiration during undulatory swimming. *Nat. Commun.* **7**, 11044.

Altringham, J. D. and Johnston, I. A. (1990). Scaling effects on muscle function: power output of isolated fish muscle fibres performing oscillatory work. *J. Exp. Biol.* **151**, 453–467.

Bainbridge, R. (1958). The speed of swimming of fish as related to size and to the frequency and amplitude of the tail beat. *J. Exp. Biol.* **35**, 109–133.

Bejan, A. and Marden, J. H. (2006). Unifying constructal theory for scale effects in running, swimming and flying. *J. Exp. Biol.* **209**, 238–248.

Bengtsson, L., Ghil, M. and Källén, E. (1981). *Dynamic Meteorology: Data Assimilation Methods.* Berlin, Germany: Springer.

Berrios-Lopez, M., Lewis, A. R. and Hensley, D. A. (1996). Scaling of skeletal mass to body mass in fishes. *J. Morphol.* **227**, 87–92.

Bhalla, A. P. S., Griffith, B. E. and Patankar, N. A. (2013). A forced damped oscillation framework for undulatory swimming provides new insights into how propulsion arises in active and passive swimming. *PLoS Comput. Biol.* **9**, e1003097.

Bird, N. C. and Mabee, P. M. (2003). Developmental morphology of the axial skeleton of the zebrafish, *Danio rerio* (Ostariophysi: Cyprinidae). *Dev. Dyn.* **228**, 337–357.

Blanchet, B., Cousot, P., Cousot, R., Feret, J., Mauborgne, L., Miné, A., Monniaux, D. and Rival, X. (2002). Design and implementation of a special-purpose static program analyzer for safety-critical real-time embedded software. In *The Essence Of Computation: Complexity, Analysis, Transformation* (eds. T. Æ. Mogensen, D. A. Schmidt and I. H. Sudborough), pp. 85–108. Berlin, Germany: Springer.

Blight, A. R. (1976). Undulatory swimming with and without waves of contraction. *Nature* **264**, 352–354.

Blight, A. R. (1977). The muscular control of vertebrate swimming movements. *Biol. Rev.* **52**, 181–218.

Boffetta, G. and Ecke, R. E. (2012). Two-dimensional turbulence. *Annu. Rev. Fluid Mech.* **44**, 427–451.

Borazjani, I. and Daghooghi, M. (2013). The fish tail motion forms an attached leading edge vortex. *Proc. R. Soc. B* **280**, 20122071.

Borla, M. A., Palecek, B., Budick, S. and O'Malley, D. M. (2002). Prey capture by larval zebrafish: evidence for fine axial motor control. *Brain. Behav. Evol.* **60**, 207–229.

Buss, R. R. and Drapeau, P. (2000). Physiological properties of zebrafish embryonic red and white muscle fibers during early development. *J. Neurophysiol.* **84**, 1545–1557.

Buss, R. R. and Drapeau, P. (2002). Activation of embryonic red and white muscle fibers during fictive swimming in the developing zebrafish. *J. Neurophysiol.* **87**, 1244–1251.

Cahouët, V., Luc, M. and David, A. (2002). Static optimal estimation of joint accelerations for inverse dynamics problem solution. *J. Biomech.* **35**, 1507–1513.

Carling, J., Williams, T. L. and Bowtell, G. (1998). Self-propelled anguilliform swimming: simultaneous solution of the two-dimensional Navier-Stokes equations and Newton's laws of motion. *J. Exp. Biol.* **201**, 3143–3166.

Cheng, J.-Y. and Blickhan, R. (1994). Bending moment distribution along swimming fish. *J. Theor. Biol.* **168**, 337–348.

Conca, C., Osses, A. and Planchard, J. (1997). Added mass and damping in fluid-structure interaction. *Comput. Methods Appl. Mech. Eng.* **146**, 387–405.

Domenici, P. and Blake, R. W. (1993). The effect of size on the kinematics and performance of Angelfish (*Pterophyllum eimekei*) escape responses. *Can. J. Zool.* **71**, 2319–2326.

Donatelli, C. M., Summers, A. P. and Tytell, E. D. (2017). Long-axis twisting during locomotion of elongate fishes. *J. Exp. Biol.* **220**, 3632–3640.

Drost, M. R., Muller, M. and Osse, J. W. M. (1987). Prey capture by fish larvae, water flow patterns and the effect of escape movements of prey. *Neth. J. Zool.* **38**, 23–45.

Drucker, E. G. and Lauder, G. V. (2003). Function of pectoral fins in rainbow trout: behavioral repertoire and hydrodynamic forces. *J. Exp. Biol.* **206**, 813–826.

7

Ehrlich, D. E. and Schoppik, D. (2017). Control of movement initiation underlies the development of balance. *Curr. Biol.* **27**, 334–344.

Eilers, P. H. C. (2003). A perfect smoother. *Anal. Chem.* **75**, 3631–3636.

Elliott, J. R. (1977). NASA's advanced control law program for the F-8 digital fly-by-wire aircraft. *IEEE Trans. Automat. Contr.* **22**, 753–757.

Eloy, C. (2012). Optimal Strouhal number for swimming animals. *J. Fluids Struct.* **30**, 205–218.

Elsinga, G. E., Scarano, F., Wieneke, B. and Van Oudheusden, B. W. (2006). Tomographic particle image velocimetry. *Exp. Fluids* **41**, 933–947.

Fero, K., Yokogawa, T. and Burgess, H. A. (2011). The behavioral repertoire of larval zebrafish. In *Zebrafish Models in Neurobehavioral Research* (eds. A. V. Kalueff and J. M. Cachat), volume 52 of *Neuromethods*, chapter 12, pp. 249–291. Totowa, NJ, USA: Humana Press.

Fetcho, J. R. (1987). A review of the organization and evolution of motoneurons innervating the axial musculature of vertebrates. *Brain Res. Rev.* **12**, 243–280.

Fetcho, J. R. and McLean, D. L. (2010). Some principles of organization of spinal neurons underlying locomotion in zebrafish and their implications. *Ann. N. Y. Acad. Sci.* **1198**, 94–104.

Fleuren, M., Van Leeuwen, J. L., Quicazan-Rubio, E. M., Pieters, R. P. M., Pollux, B. J. A. and Voesenek, C. J. (2018). Three-dimensional analysis of the fast-start escape response of the least killifish, *Heterandria formosa*. *J. Exp. Biol.* **221**, jeb168609.

Foreman, M. B. and Eaton, R. C. (1993). The direction change concept for reticulospinal control of goldfish escape. *J. Neurosci.* **13**, 4101–4113.

Gibouin, F., Raufaste, C., Bouret, Y. and Argentina, M. (2018). Study of the thrust-drag balance with a swimming robotic fish. *Phys. Fluids* **30**.

Godoy-Diana, R. and Thiria, B. (2018). On the diverse roles of fluid dynamic drag in animal swimming and flying. *J. R. Soc., Interface* **15**, 20170715.

Grandel, H. and Schulte-Merker, S. (1998). The development of the paired fins in the zebrafish (*Danio rerio*). *Mech. Dev.* **79**, 99–120.

Gray, J. (1933). Studies in animal locomotion — I. The movement of fish with special reference to the eel. *J. Exp. Biol.* **10**, 88–104.

Green, M. H., Ho, R. K. and Hale, M. E. (2011). Movement and function of the pectoral fins of the larval zebrafish (*Danio rerio*) during slow swimming. *J. Exp. Biol.* **214**, 3111–3123.

Griffith, B. E., Hornung, R. D., McQueen, D. M. and Peskin, C. S. (2007). An adaptive, formally second order accurate version of the immersed boundary method. *J. Comput. Phys.* **223**, 10–49.

Griffiths, G., Enoch, P. and Millard, N. W. (2001). On the radiated noise of the Autosub

autonomous underwater vehicle. *ICES J. Mar. Sci.* **58**, 1195–1200.

Hale, M. E. (2014). Developmental change in the function of movement systems: transition of the pectoral fins between respiratory and locomotor roles in zebrafish. *Integr. Comp. Biol.* **54**, 238–249.

Hamlet, C., Fauci, L. J. and Tytell, E. D. (2015). The effect of intrinsic muscular nonlinearities on the energetics of locomotion in a computational model of an anguilliform swimmer. *J. Theor. Biol.* **385**, 119–129.

Harper, D. G. and Blake, R. W. (1989). A critical analysis of the use of high-speed film to determine maximum accelerations of fish. *J. Exp. Biol.* **471**, 465–471.

Harris-Warrick, R. M. (2011). Neuromodulation and flexibility in Central Pattern Generator networks. *Curr. Opin. Neurobiol.* **21**, 685–692.

Hess, F. and Videler, J. J. (1984). Fast continuous swimming of saithe (*Pollachius virens*): a dynamic analysis of bending moments and muscle power. *J. Exp. Biol.* **109**, 229–251.

Hibbeler, R. C. (2005). *Mechanics of Materials.* Upper Saddle River, NJ, USA: Pearson Prentice Hall.

Hjort, J. (1914). Fluctuations in the great fisheries of northern Europe, viewed in the light of biological research. *Rapp. P.-V. Cons. Perm. Int. Explor. Mer* **20**, 1–228.

Houde, E. D. (2002). Mortality. In *Fishery Science: the Unique Contributions of Early Life Stages* (eds. L. A. Fuiman and R. G. Werner), pp. 64–87. Hoboken, NJ, USA: Blackwell Science.

James, R. S., Cole, N. J., Davies, M. L. F. and Johnston, I. A. (1998). Scaling of intrinsic contractile properties and myofibrillar protein composition of fast muscle in the fish *Myoxocephalus scorpius* L. *J. Exp. Biol.* **201**, 901–912.

James, R. S. and Johnston, I. A. (1998). Scaling of muscle performance during escape responses in the fish *Myoxocephalus scorpius* L. *J. Exp. Biol.* **201**, 913–923.

Jayne, B. C. and Lauder, G. V. (1993). Red and white muscle activity and kinematics of the escape response of the bluegill sunfish during swimming. *J. Comp. Physiol., A* **173**, 495–508.

Jayne, B. C. and Lauder, G. V. (1996). New data on axial locomotion in fishes: how speed affects diversity of kinematics and motor patterns. *Am. Zool.* **36**, 642–655.

Jordan, C. E. (1996). Coupling internal and external mechanics to predict swimming behavior: a general approach. *Am. Zool.* **36**, 710–722.

Kasapi, M. A., Domenici, P., Blake, R. W. and Harper, D. (1993). The kinematics and performance of escape responses of the knifefish *Xenomystus nigri*. *Can. J. Zool.* **71**, 189–195.

Kayan, V. P., Kozlov, L. F. and Pyatetskii, V. E. (1978). Kinematic characteristics of the swimming of certain aquatic animals. *Fluid Dyn.* **13**, 641–646.

Kendall Jr., A. W., Ahlstrom, E. H. and Mose, H. G. (1984). Early life. In *Ontogeny*

and Systematics of Fishes (eds. H. G. Moser, W. J. Richards, D. M. Cohen, M. P. Fahay, J. A. W. Kendall and S. L. Richardson), pp. 11–22. Lawrence, KS, USA: American Society of Ichthyologists and Herpetologists.

Kuwada, J. Y., Bernhardt, R. R. and Nguyen, N. (1990). Development of spinal neurons and tracts in the zebrafish embryo. *J. Comp. Neurol.* **302**, 617–628.

Lankheet, M. J., Stoffers, T., Van Leeuwen, J. L. and Pollux, B. J. A. (2016). Acquired versus innate prey capturing skills in super-precocial live-bearing fish. *Proc. R. Soc. B* **283**, 20160972.

Lauder, G. V. (2000). Function of the caudal fin during locomotion in fishes: kinematics, flow visualisation, and evolutionary patterns. *Am. Zool.* **40**, 101–122.

Li, G., Müller, U. K., Van Leeuwen, J. L. and Liu, H. (2016). Fish larvae exploit edge vortices along their dorsal and ventral fin folds to propel themselves. *J. R. Soc., Interface* **13**, 20160068.

Lighthill, M. J. (1960). Note on the swimming of slender fish. *J. Fluid Mech.* **9**, 305–317.

Lighthill, M. J. (1971). Large-amplitude elongated-body theory of fish locomotion. *Proc. R. Soc. B* **179**, 125–138.

Liu, H., Ellington, C. P., Kawachi, K., Van den Berg, C. and Willmott, A. P. (1998). A computational fluid dynamic study of hawkmoth hovering. *J. Exp. Biol.* **201**, 461–477.

Liu, H., Wassersug, R. and Kawachi, K. (1997). The three-dimensional hydrodynamics of tadpole locomotion. *J. Exp. Biol.* **200**, 2807–2819.

Liu, H., Wassersug, R. J. and Kawachi, K. (1996). A computational fluid dynamics study of tadpole swimming. *J. Exp. Biol.* **199**, 1245–1260.

Long, J. H. J., Hale, M. E., McHenry, M. J. and Westneat, M. W. (1996). Functions of fish skin: Flexural stiffness and steady swimming of longnose gar *Lepisosteus osseus*. *J. Exp. Biol.* **199**, 2139–2151.

Long, J. H. J., Koob-Emunds, M., Sinwell, B. and Koob, T. J. (2002). The notochord of hagfish *Myxine glutinosa*: visco-elastic properties and mechanical functions during steady swimming. *J. Exp. Biol.* **205**, 3819–3831.

McLean, D. L., Fan, J., Higashijima, S., Hale, M. E. and Fetcho, J. R. (2007). A topographic map of recruitment in spinal cord. *Nature* **446**, 71–75.

Mittal, R. and Balachandar, S. (1995). Effect of three-dimensionality on the lift and drag of nominally two-dimensional cylinders. *Phys. Fluids* **7**, 1841–1865.

Mittal, R. and Iaccarino, G. (2005). Immersed boundary methods. *Annu. Rev. Fluid Mech.* **37**, 239–261.

Mueller, T. and Wullimann, M. F. (2016). *Atlas of Early Zebrafish Brain Development.* Amsterdam, The Netherlands: Elsevier.

Müller, U. K., Van den Boogaart, J. G. M. and Van Leeuwen, J. L. (2008). Flow patterns of larval fish: undulatory swimming in the intermediate flow regime. *J. Exp. Biol.* **211**,

196–205.

Müller, U. K. and Van Leeuwen, J. L. (2004). Swimming of larval zebrafish: ontogeny of body waves and implications for locomotory development. *J. Exp. Biol.* **207**, 853–868.

Nair, A., Azatian, G. and McHenry, M. J. (2015). The kinematics of directional control in the fast start of zebrafish larvae. *J. Exp. Biol.* **218**, 3996–4004.

Nair, A., Nguyen, C. and McHenry, M. J. (2017). A faster escape does not enhance survival in zebrafish larvae. *Proc. R. Soc. B* **284**, 20170359.

Nakata, T. and Liu, H. (2012). A fluid-structure interaction model of insect flight with flexible wings. *J. Comput. Phys.* **231**, 1822–1847.

Nowroozi, B. N. and Brainerd, E. L. (2014). Importance of mechanics and kinematics in determining the stiffness contribution of the vertebral column during body-caudal-fin swimming in fishes. *Zoology* **117**, 28–35.

Parichy, D. M., Elizondo, M. R., Mills, M. G., Gordon, T. N. and Engeszer, R. E. (2009). Normal table of postembryonic zebrafish development: staging by externally visible anatomy of the living fish. *Dev. Dyn.* **238**, 2975–3015.

Pedley, T. J. and Hill, S. J. (1999). Large-amplitude undulatory fish swimming: fluid mechanics coupled to internal mechanics. *J. Exp. Biol.* **202**, 3431–3438.

Peskin, C. S. (1972). *Flow Patterns Around Heart Valves: a Digital Computer Method for Solving the Equations of Motion*. PhD, Albert Einstein College of Medicine.

Porter, M. M., Ravikumar, N., Barthelat, F. and Martini, R. (2017). 3D-printing and mechanics of bio-inspired articulated and multi-material structures. *J. Mech. Behav. Biomed. Mater.* **73**, 114–126.

Rome, L. C., Cook, C., Syme, D. A., Connaughton, M. A., Ashley-Ross, M., Klimov, A., Tikunov, B. and Goldman, Y. E. (1999). Trading force for speed: why superfast crossbridge kinetics leads to superlow forces. *Proc. Natl. Acad. Sci. U. S. A.* **96**, 5826–5831.

Rome, L. C., Loughna, P. T. and Goldspink, G. (1984). Muscle fiber activity in carp as a function of swimming speed and muscle temperature. *Am. J. Physiol. - Regul. Integr. Comp. Physiol.* **247**, R272–R279.

Saadat, M., Fish, F. E., Domel, A. G., Di Santo, V., Lauder, G. V. and Haj-Hariri, H. (2017). On the rules for aquatic locomotion. *Phys. Rev. Fluids* **2**, 083102.

Sambilay, V. C. J. (1990). Interrelationships between swimming speed, caudal fin aspect ratio, and body length of fishes. *Fishbyte, WorldFish Cent.* **8**, 16–20.

Schanz, D., Schröder, A., Gesemann, S., Michaelis, D. and Wieneke, B. (2013). 'Shake The Box': A highly efficient and accurate Tomographic Particle Tracking Velocimetry (TOMO-PTV) method using prediction of particle positions. In *10th International Symposium on Particle Image Velocimetry — PIV13, Delft, The Netherlands, July 1–3, 2013*.

7

Severi, K. E., Portugues, R., Marques, J. C., O'Malley, D. M., Orger, M. B. and Engert, F. (2014). Neural control and modulation of swimming speed in the larval zebrafish. *Neuron* **83**, 692–707.

Silva, M. P. T. and Ambrósio, J. A. C. (2004). Sensitivity of the results produced by the inverse dynamic analysis of a human stride to perturbed input data. *Gait Posture* **19**, 35–49.

Slabbekoorn, H., Bouton, N., Van Opzeeland, I., Coers, A., Ten Cate, C. and Popper, A. N. (2010). A noisy spring: the impact of globally rising underwater sound levels on fish. *Trends Ecol. Evol.* **25**, 419–427.

Stamhuis, E. J. (2006). Basics and principles of particle image velocimetry (PIV) for mapping biogenic and biologically relevant flows. *Aquat. Ecol.* **40**, 463–479.

Stewart, W. J., Nair, A., Jiang, H. and McHenry, M. J. (2014). Prey fish escape by sensing the bow wave of a predator. *J. Exp. Biol.* **217**, 4328–4336.

Stickel, J. J. (2010). Data smoothing and numerical differentiation by a regularization method. *Comput. Chem. Eng.* **34**, 467–475.

Taylor, G. K., Nudds, R. L. and Thomas, A. L. R. (2003). Flying and swimming animals cruise at a Strouhal number tuned for high power efficiency. *Nature* **425**, 707–711.

Thorsen, D. H., Cassidy, J. J. and Hale, M. E. (2004). Swimming of larval zebrafish: fin-axis coordination and implications for function and neural control. *J. Exp. Biol.* **207**, 4175–4183.

Tikhonov, A. N. (1963). On the solution of ill-posed problems and the method of regularization. *Dokl. Akad. Nauk SSSR* **151**, 501–504.

Tokić, G. and Yue, D. K. P. (2012). Optimal shape and motion of undulatory swimming organisms. *Proc. R. Soc. B* **279**, 3065–3074.

Triantafyllou, G. S., Triantafyllou, M. S. and Grosenbaugh, M. A. (1993). Optimal thrust development in oscillating foils with application to fish propulsion. *J. Fluids Struct.* **7**, 205–224.

Tytell, E. D., Borazjani, I., Sotiropoulos, F., Baker, T. V., Anderson, E. J. and Lauder, G. V. (2010a). Disentangling the functional roles of morphology and motion in the swimming of fish. *Integr. Comp. Biol.* **50**, 1140–1154.

Tytell, E. D., Hsu, C.-Y., Williams, T. L., Cohen, A. H. and Fauci, L. J. (2010b). Interactions between internal forces, body stiffness, and fluid environment in a neuromechanical model of lamprey swimming. *Proc. Natl. Acad. Sci. U. S. A.* **107**, 19832–19837.

Tytell, E. D., Standen, E. M. and Lauder, G. V. (2008). Escaping Flatland: three-dimensional kinematics and hydrodynamics of median fins in fishes. *J. Exp. Biol.* **211**, 187–195.

Van den Boogaart, J. G. M., Muller, M. and Osse, J. W. M. (2012). Structure and function of the median finfold in larval teleosts. *J. Exp. Biol.* **215**, 2359–2368.

Van Leeuwen, J. L., Lankheet, M. J. M., Akster, H. A. and Osse, J. W. M. (1990). Function of red axial muscles of carp (*Cyprinus carpio*): recruitment and normalized power output during swimming in different modes. *J. Zool.* **220**, 123–145.

Van Weerden, J. F., Reid, D. A. P. and Hemelrijk, C. K. (2014). A meta-analysis of steady undulatory swimming. *Fish Fish.* **15**, 397–409.

Vos, R., De Breuker, R., Barrett, R. and Tiso, P. (2007). Morphing wing flight control via postbuckled precompressed piezoelectric actuators. *J. Aircr.* **44**, 1060–1068.

Walker, J. A., Ghalambor, C. K., Griset, O. L., McKenney, D. and Reznick, D. N. (2005). Do faster starts increase the probability of evading predators? *Funct. Ecol.* **19**, 808–815.

Wardle, C. S. and Videler, J. J. (1993). The timing of the electromyogram in the lateral myotomes of mackerel and saithe at different swimming speeds. *J. Fish Biol.* **42**, 347–359.

Wardle, C. S., Videler, J. J. and Altringham, J. D. (1995). Tuning in to fish swimming waves: body form, swimming mode and muscle function. *J. Exp. Biol.* **198**, 1629–1636.

Ware, D. M. (1978). Bioenergetics of pelagic fish: theoretical change in swimming speed and ration with body size. *J. Fish. Res. Board Canada* **35**, 220–228.

Wen, L., Ren, Z., Di Santo, V., Hu, K., Yuan, T., Wang, T. and Lauder, G. V. (2018). Understanding fish linear acceleration using an undulatory biorobotic model with soft fluidic elastomer actuated morphing median fins. *Soft Robot.* **5**, 375–388.

Westneat, M. W. (1996). Functional morphology of aquatic flight in fishes: kinematics, electromyography, and mechanical modeling of labriform locomotion. *Am. Zool.* **36**, 582–598.

Wiens, A. J. and Hosoi, A. E. (2018). Self-similar kinematics among efficient slender swimmers. *J. Fluid Mech.* **840**, 106–130.

Wu, T. Y.-T. (1961). Swimming of a waving plate. *J. Fluid Mech.* **10**, 321–344.

7

Summary

Most of the world's 34,000 known fish species are undulatory swimmers. Their body undulations are produced by fluid-structure interaction between water and the body of the fish, powered by its muscle system. Despite these complex physics, just-hatched fish larvae can already produce effective swimming motion. How they do this is not yet fully understood. With this thesis, we aim to contribute to answering this question by examining the biomechanics of swimming of early-development larval zebrafish. With novel experimental and computational techniques, we reconstructed the dynamics of the larvae from high-speed video. These analyses highlight the challenges that larval fish face during swimming, and how the larvae have evolved to solve these challenges.

In **chapter 2** we reviewed the mechanics of swimming of larval fish. We examined the functional demands on the locomotory system of fish larvae: immediately after hatching, fish need to escape predators, search and hunt for food, and migrate and disperse. These demands need to be fulfilled by the larvae while undergoing large changes in their bodies, both internal and external. Furthermore, the swimming speed and size of many larvae causes them to be in the intermediate flow regime, where the nature of the flow changes considerably with changes in size or speed. In this chapter, we integrated previous literature to gain insight into how these functional demands on the locomotory system are met with the advantages and limitations of their developing bodies and the changing hydrodynamic regime.

In **chapter 3**, we analysed near-periodic swimming of zebrafish larvae with two-dimensional inverse dynamics from motion that was manually tracked from high-speed video images. We used these data to show how the intermediate flow regime affects the swimming dynamics of fish larvae. We used the Reynolds number, which indicates the relative importance of viscous forces to inertial forces, to characterise the flow regime that the larvae swim in. Furthermore, we applied the Strouhal number, a measure of the ratio of the approximate lateral tail speed to the forward swimming speed, to express changes in swimming kinematics. We found that the Strouhal number depends inversely on the Reynolds number. Fish swimming at low Reynolds numbers tend to use relatively high Strouhal numbers, indicating that their tail-beat amplitude and frequency are high. Even the larvae swimming at the highest Reynolds numbers still use relatively high Strouhal numbers (around 0.72) compared to adult fish (typically 0.2–0.3). Swimming at intermediate Reynolds numbers is associated with high drag, requiring the larvae to use high tail-beat amplitudes and frequencies (and therefore Strouhal number) to produce sufficient thrust. This mode of swimming requires relatively high-amplitude yaw torques, resulting in large angular amplitudes and an expected high energetic cost of transport: the small size of the larvae is a burden to their swimming.

Most of the previous research on fish swimming, including our **chapter 3**, has been

S

done two-dimensionally. However, fish can perform complex, three-dimensional motions to escape predators, search or hunt for food, or manoeuvre through the environment. To expand our analyses to the third dimension, we developed a method to reconstruct the 3D motion of fish from multi-camera high-speed video, described in **chapter 4**. With an optimisation algorithm we find the 3D position, orientation, and body curvature that best fits the high-speed video frames. We demonstrated that the method allows us to reconstruct the swimming kinematics with high accuracy, while requiring minimal manual work. In addition, we developed a novel method to calculate resultant hydrodynamic forces and torques from the reconstructed motion. The described method is a valuable tool for analysing the biomechanics of swimming, providing data for future analyses of fish swimming.

In **chapter 5**, we apply this automated tracking method to analyse fast starts of zebrafish larvae five days after fertilisation. To be able to escape predators, the main functional demands on a fast start are producing sufficient speed within a narrow time frame and being able to generate a wide range of escape directions. To investigate how these demands are met, we used a five-camera high-speed video of fast-starting zebrafish larvae with unprecedented spatiotemporal resolution. From these videos, we reconstructed the 3D motion of the larvae and the resultant hydrodynamic forces and torques. Due to their undulatory swimming style, the larvae first need to bend into a C-shape before being able to produce a propulsive tail beat. For this reason, the first stage of the start is often considered 'preparatory'. Based on the reconstructed forces and torques, we show that the first stage of the start, in addition to its preparatory role, also serves to provide most of the reorientation of the start. After this stage, the larvae unfold their bodies, moving their tails at high speeds and thus producing large propulsive forces. The turn angle produced during a start mostly depends on the amount of body curvature in the first stage, while the escape speed mainly depends on the duration of the start. This suggests that larvae are able to independently adjust the direction and speed of their escape.

Fish larvae are able to produce these escape responses and the subsequent swimming bout immediately after hatching, despite their bodies and brains still undergoing development. To understand how this is possible, we use an advanced inverse-dynamics approach, with computational fluid dynamics and a large-amplitude beam model, to reconstruct internal mechanics from the motion of the fish in **chapter 6**. We compute the internal bending moments from more than 100 3D-recordings of swimming over a range of developmental stages. We show that larvae use similar bending moment patterns across development, speeds and accelerations. By varying the amplitude and duration of this pattern, the larvae can adjust their swimming speed and/or acceleration. This similarity suggests that their muscle activation patterns are also similar, which would help to explain how just-hatched larvae with limited neural capacity can produce effective swimming motion across a range of speeds and accelerations.

In this thesis, we demonstrated that larval fish swim in a challenging hydrodynamic regime. Despite the relatively high drag, they can produce effective swimming motions to help them survive to adulthood. We developed novel methods to quantify this motion in 3D, and from it reconstructed the external and internal mechanics. With these inverse-

dynamics approaches, we show that fish larvae can likely adjust their swimming in a relatively simple way, for both fast starts and continuous swimming. Thus, complex physics do not obstruct developing larvae from swimming effectively.

S

Samenvatting

De meeste van de 34.000 soorten vis zwemmen door hun lichaam te laten golven. Deze lichaamsgolven ontstaan door interactie tussen het lichaam van de vis en het water. Ondanks de complexe natuurkunde achter deze interacties kunnen vislarven onmiddellijk zwemmen nadat ze uit het ei gekomen zijn, terwijl hun zenuwstelsel en brein nog in ontwikkeling zijn. Het is nog niet volledig bekend hoe dit mogelijk is; het is doel van deze thesis is om bij te dragen aan het begrip van deze kwestie. Dit hebben we gedaan door de biomechanica van het zwemmen van zeer jonge zebravislarven te onderzoeken. Met vernieuwende experimentele en rekenkundige technieken hebben we inzicht verkregen in de dynamica van het zwemmen van de larven, gereconstrueerd uit beelden van hogesnelheidscamera's. Deze analyses laten zien wat voor problemen vislarven ondervinden tijdens het zwemmen, en hoe zij zijn geëvolueerd om deze problemen op te lossen.

In **hoofdstuk 2** geven we een overzicht van de literatuur over de mechanica van het zwemmen van larvale vissen. We bekijken daarvoor de functionele eisen die gesteld worden aan het voortbewegingsstelsel van de vislarven: onmiddelijk nadat ze uit het ei komen moeten ze ontsnappen aan roofdieren, foerageren en zich verspreiden. Dit stelt eisen aan het zwemsysteem van de larven die vervuld moeten worden terwijl hun lichaam volop in ontwikkeling is, zowel intern als extern. Het zwemmen wordt verder bemoeilijkt door het vloeistofmechanische regime waarin zij zich bevinden, waarin de vloeistofkrachten sterk variëren met veranderingen in lichaamsgrootte en zwemsnelheid. In dit hoofdstuk integreren we de kennis uit eerdere literatuur om inzicht te verwerven in hoe de functionele eisen op het voortbewegingssysteem van de larven ingevuld worden met de voor- en nadelen van hun ontwikkelende lichamen en de veranderende vloeistofkrachten.

In **hoofdstuk 3** hebben we gekeken naar het bijna-periodiek zwemmen van zebravislarven door de dynamica te reconstrueren uit zwembewegingen die handmatig zijn gedigitaliseerd uit hogesnelheidscamerabeelden. Met deze data laten we zien wat voor effecten het 'intermediaire' vloeistofmechanische regime heeft op de zwemdynamica van de larven. Hiervoor gebruiken het Reynolds-getal, dat de verhouding tussen de traagheids- en wrijvingskrachten in het water aangeeft. Ook gebruiken we het Strouhal-getal, een indicatie van de verhouding van de (geschatte) staartsnelheid en de voorwaartse snelheid. Uit onze data blijkt dat het Strouhal-getal omgekeerd afhangt van het Reynolds-getal: larven die met een laag Reynolds-getal zwemmen hebben doorgaans een relatief hoog Strouhal-getal (ongeveer 0.72) ten opzichte van volwassen vissen (meestal 0.2–0.3). Zwemmen op lage Reynolds-getallen gaat gepaard met hoge weerstanden, waardoor de larven alleen voldoende voortstuwing kunnen produceren door grote amplitudes en frequenties van de staartslag te gebruiken. Dit type zwembeweging veroorzaakt grote draaimomenten, resulterend in aanzienlijke hoekverdraaiingen en een hoog energieverbruik: het kleine formaat van de larven staat ze in de weg om efficiënt te zwemmen.

S

Het merendeel van eerder onderzoek aan viszwemmen is gedaan onder de aanname van tweedimensionaliteit, inclusief ons **hoofdstuk 3**. In veel gevallen voeren vissen echter complexe, driedimensionale bewegingen uit om bijvoorbeeld te ontsnappen aan een roofdier, voedsel te zoeken of te vangen of door hun omgeving te manoeuvreren. in **hoofdstuk 4** beschrijven we een methode om driedimensionale zwembewegingen te reconstrueren uit beelden van meerdere gesynchroniseerde hogesnelheidscamera's. Door middel van een optimalisatie-algoritme vinden we de combinatie van driedimensionale positie, oriëntatie en lichaamsvorm die het best overeenkomt met de camerabeelden. We laten zien dat deze methode met minimaal handwerk de zwembeweging accuraat uit de videobeelden kan volgen. Daarnaast hebben we een methode ontwikkeld om uit deze reconstructies de netto vloeistofmechanische krachten en momenten te berekenen. Deze methode kan van zeer nuttig zijn voor toekomstig onderzoek naar de biomechanica van zwemmen.

We passen de ontwikkelde reconstructiemethode toe in **hoofdstuk 5** op ontsnappingsreacties van zebravislarven vijf dagen na bevruchting. Om effectief te ontsnappen aan bedreigingen moet hun startbeweging voldoen aan twee primaire eisen: er moet voldoende snelheid opgebouwd worden in korte tijd, en de larven moeten over een breed bereik aan richtingen kunnen ontsnappen. Om te onderzoeken hoe de larven aan deze eisen voldoen hebben we de larven gefilmd met een geavanceerde vijfcamera-opstelling met zeer hoge resolutie in ruimte en tijd. Uit deze beelden reconstrueren we de driedimensionale zwembewegingen en de resultante hydrodynamische krachten en momenten. De larven buigen zich eerst in een C-vorm en produceren daarna een voortstuwende staartslag. De eerste buigingsfase van de startbeweging wordt vaak 'voorbereidend' genoemd. Op basis van de berekende krachten en momenten laten we zien dat de meeste heroriëntatie van de vis plaatsvindt in de eerste fase, naast de voorbereidende rol. Na deze fase ontvouwen de larven hun lichaam, waarbij hun staart met hoge snelheid door het water beweegt en daardoor grote voortstuwende krachten produceert. De draaihoek gedurende de start hangt sterk samen met de hoeveelheid kromming van het lichaam; de ontsnappingssnelheid hangt vooral samen met de duur van de manoeuvre. Dit wijst erop dat de larven hun ontsnappingsrichting en -snelheid onafhankelijk van elkaar kunnen bepalen.

Vislarven kunnen deze starts en de daaropvolgende zwembewegingen onmiddellijk maken nadat ze uit het ei gekomen zijn, ondanks het feit dat hun lichaam en zenuwstelsel nog niet volledig ontwikkeld zijn. Om te beantwoorden hoe dit mogelijk hebben we in **hoofdstuk 6** een nieuwe methode ontwikkeld om de netto interne krachten en momenten te berekenen uit de gereconstrueerde zwembeweging, met behulp van computersimulaties van de stroming en een vervormingsmodel voor het lichaam. We berekenen de interne krachten en momenten voor meer dan 100 driedimensionale zwembewegingen gedurende de eerste dagen van ontwikkeling. Hieruit blijkt dat vislarven vergelijkbare patronen van het interne moment vertonen voor verschillende ontwikkelingsstadia, en zwemsnelheden en -acceleraties. Ze variëren slechts de duur en amplitude van deze patronen om de zwemsnelheid of -acceleratie te bepalen. De vergelijkbaarheid van de momentpatronen wijst erop dat ook hun spieractivatiepatronen op elkaar lijken. Dit zou helpen verklaren hoe net-uitgekomen larven met een beperkte hersencapaciteit toch effectief kunnen zwemmen,

ondanks de complexe natuurkunde achter hun zwembewegingen.

In deze thesis hebben we laten zien dat larvale vissen in een problematisch vloeistof-mechanisch regime zwemmen. Ondanks de relatief hoge weerstand kunnen de larven effectieve zwembewegingen maken die ze helpen om het volwassen stadium te bereiken. We hebben nieuwe methodes ontwikkeld om de driedimensionale zwembewegingen te reconstrueren, en deze te gebruiken om externe en interne krachten en momenten te bereken. Uit data verzameld met deze nieuwe methodes blijkt dat vislarven waarschijnlijk op een relatief eenvoudige manier hun zwembewegingen kunnen aanpassen, voor zowel starts als continu zwemmen: de complexe natuurkunde staat vislarven niet in de weg om effectief te zwemmen.

S

Acknowledgements

The universal law of PhD-theses states that: "only the acknowledgements will ever be read". I abuse this knowledge by forcing some summarising sentences of this thesis onto you between the many thanks I have to express—promise me that you will not skip them!

Fish larvae of many species are similar in their early stages of development.

First of all, I am very grateful to Johan for his supervision, and of course the opportunity to start this project. Our cooperation was always productive and pleasant; I could not have wished for a better supervisor. Despite your (extremely) busy schedule, you always made time to discuss any manuscripts, presentations, problems, or ideas—and sometimes unrelated but interesting topics. Many thanks also to Florian, who joined the supervision team a bit later. Your different perspective as a flight researcher (and climber) was often very useful to nudge us fish-people towards different angles and clearer explanations. Thanks to all members of EZO for their useful feedback during my (admittedly rare) presentations for the group.

Thanks too for Ulrike and her great writing skills, also for the grant proposal. Together with her, Gen and Hao, we formed a truly global larval fish research team, making for some interesting, but somewhat challenging Skype sessions from Wageningen, Fresno and Tokyo simultaneously. Many thanks to Gen too for performing the simulations to validate our own simulations.

Because of their small size and low speed, water feels like syrup to fish larvae, requiring a relatively large effort to swim.

Many thanks are in order for the team of technicians who keep EZO running smoothly. Remco, you built and designed several amazing experimental setups and provided technical help on many fronts. Henk (`admu_schip001`), you were always willing to arrange a new hard-drive, screen, laptop, work station; type your administrator password; make microscope pictures; embed zebrafish; give lab advice; etc. Karen, if I needed lab-related advice or fish stimulation (even in the evening), you were always there. Kas, thanks for spending several days of your life poking fish with a horse hair. And of course, many thanks to our 'bureaucracy technician' Annemarie: you always manage to solve anything quickly and effectively, and oversee your EZO-children like a mother hen. Also thanks to the fish facilities team at Carus for providing zebrafish eggs, care for the fish larvae, and great Christmas parties!

I also got help with some of the work that remains unfinished, and is not represented in this thesis. Martin, thanks for your always sharp ideas and guidance on the injection experiments; Marcel, thanks for being of huge help with the practical work for these experiments

(among many other things, instructions on how to sterilise plastic bottles). Henk, thanks for taking over this work from Marcel, and for creating beautiful light sheet microscopy pictures. Sebastian: thanks for the opportunity to join you for the experiments at PSI, and allowing us to tag along to your beam time to scan zebrafish (some of those did make it in).

Swimming motion is produced by an interaction between the body of the fish and the water—without water, the fish does not produce a body wave. This type of problem is known as fluid-structure interaction, and often highly complex.

Over my long career as a PhD with EZO, I shared the office with a changing group of people, but it was always a joy. It started with the 'TU Wageningen' with Sebastian: just two people in the office, but junk for 10 (we once had >20 coffee cups standing around) and endless excellent live recordings over the speaker system. We were later joined by Uroš, Julian, and Wouter, requiring us to set the tables in a rather unconvential (and perhaps slightly impractical) manner, compensated by loudly playing AC/DC on Fridays and throwing styrofoam balls at each other's faces. And finally, the insect boys had to endure my endless expressions of frustration and my messy desk: Antoine ('le garçon maison'; 'the C-man'), Pulkit ('the G-unit'), and Wouter ('Gerben'); it was great to share the office, and thanks for all the useful (and useless) discussions! It's a shame that neither the cannon nor Tay-Tay have been ([never been]) heard for so long...

Fish motion is often three-dimensional; we developed a method for tracking this 3D motion in video from multiple high-speed video cameras.

For the vast majority of time I was happy to go to work, which was in no small part due to the great atmosphere in the E-wing. The weekends, activities, Friday afternoon drinks, etc. were always great (though sometimes slightly destructive) with you guys—Adrià, Andres, Annelieke, Ansa, Antoine, Bruno, Carmen, Christine, Edoardo, Elsa, Esther, Éva, Gauthier, Henri, Joeri, Jules, Julian, Lana, Lieke, Linda, Marcel, Marcela, Mark, Marloes, Maurijn, Mike, Mirelle, Mojtaba, Myrthe, Nadya, Nathalie, Olaf, Paulina, Pim, Pulkit, Remco, Sebastian, Sem, Uroš, Wouter: thanks for all the great times. The inspiring discussions over coffee and lunch were also essential to any work day; all the above people, Annemarie, Florian, Henk, Karen, Kees, Martin, Sander, Sander, and all the students: thanks for these moments (or hours) of relaxation. Special thanks to my two paranymphs Antoine and Remco: I'm glad to share the stage with you!

Fish usually escape with a C-start, where the body bends into a C-shape and subsequently unfolds to produce propulsion. Most of the reorientation during these starts takes place in the first phase, and adjusted with the curvature of the fish, while most of the propulsion is produced in the second phase, and is adjusted with the duration of the start.

The #PowerPof team (occasionally known as the 'Rouge Squadron') helped to reduce stress and improve my physique simultaneously. Andres, Annelieke, Antoine ('le beau parleur'),

Carmen, Florian, Marloes, Mike, Sander (and sometimes Irene), Uroš ('the cleaner'): it was very enjoyable to climb with you—let's keep it up on weekends!

Zebrafish larvae use similar patterns of bending moment, and probably muscle activation, across different developmental stages, speeds, and accelerations.

The time outside of work was greatly improved by hanging out with some lovely people. Many a Tuesday morning was ruined by a great Monday evening with the best cover band at the Lawickse Allee 166; Lenny, Pascal, Paulus, Rik, Thijs: thanks for all the fun, I'm sure we'll learn Halo of Flies at some point! Anne, Christine, Leonie, Linda, Marcel, Maurijn, Niek, Remco, Sebastian: thanks for a lot of great weekends and plenty of 'vormfouten'. In all my days at the Dijkstraat, I've had a lot of great house mates—Alex, Anna, Auke, Ferdy, Koen, Lennart, Lisa, Maria, Marie, Mónica, Philipp: thanks for making cheap living so nice. Dries, our Sporcling was essential to keep my non-fish-swimming related knowledge up to date, it's a shame we're now too old to let the taxpayers buy us concert tickets and fancy drinks. Finally, Eric-Jan, Maarten, Maarten-Jan, Mart: it's great that we're still friends after all these years, thanks for all the vacations, Mario Party, igloos, insults, Matadorenclub-tours, Carbage Runs, etc.—unfortunately, I will no longer be the professional scientist, but as a doctor I can also represent the current state of scientific knowledge.

Fish larvae evolved solutions to make swimming relatively simple, despite the complex physics.

Natuurlijk ook veel dank voor mijn ouders: jullie hebben ons leergierig en technisch opgevoed en altijd vrij gelaten in wat we wilden doen, wat in mijn geval uiteindelijk tot een boekje over viszwemmen heeft geleid! Dirk en Annette: als grote broer en zus hebben jullie daar zeker aan bijgedragen! Jet: jammer dat je niet in de zaal mag voor mijn verdediging, maar ik zal je later nog wel voorlezen uit mijn boekje.

Brownie and Fudge—although you can't read this, thanks for all the cuddles, especially while writing. Finally, many thanks to Carmen (me sgatje) for keeping me well-fed, sane, and loved during the final stages of my PhD—on to a life without theses (and sea kayaks)!

About the author

Cornelis Johannes Voesenek, more commonly known as Kees (jr.) or recently Cees, was born on the 11th of September 1987 in Breda (or, to be specific: Effen). His youth there was mainly spent building with LEGO, digging holes, and being fascinated by various mechanical and electronic devices and living organisms (including, but not limited to, cats, goats, horses, worms, pillbugs, ants—interestingly no fish or their larvae). In later developmental stages, when his parents bought their first PC, computers and their inner workings entered the equation. Quite early in high school, perhaps inspired by frequent flights in a small aeroplane with his dad, he decided to study Aerospace Engineering at Delft University of Technology.

Here, he got his BSc degree with a minor Aircraft Design and an MSc degree in Fluid Dynamics. As part the honours track belonging to this MSc degree, he did a project on magnetohydrodynamic flow at the department of Multiscale Physics at Delft University of Technology. This was followed by a short internship in the heavily industrial environment of Corus, where he performed fluid dynamics and chemical simulations on a waste-gas burning furnace. Finally, he performed the work for his MSc-thesis at the Experimental Zoology group at Wageningen University & Research, on a two-dimensional fluid-structure interaction problem. He was then kindly offered the opportunity to do a PhD on larval swimming with Johan van Leeuwen, the result of which you see before you.

After obtaining his PhD, he will say his goodbyes to academia and start working as a Scientific Software Engineer at VORtech in Delft.

List of publications

Fleuren, M. Van Leeuwen, J. L., Quicazan-Rubio, E. M., Pieters, R. P. M., Pollux, B. J. A., Voesenek, C. J. (2018). Three-dimensional analysis of the fast-start escape response of the least killifish, *Heterandria formosa*. *Journal of Experimental Biology* **221**, jeb168609.

Voesenek, C. J., Muijres, F. T., Van Leeuwen, J. L. (2018). Biomechanics of swimming in developing larval fish. *Journal of Experimental Biology* **221**, jeb149583.

Voesenek, C. J., Pieters, R. P. M., Van Leeuwen, J. L. (2016). Automated reconstruction of three-dimensional fish motion, forces, and torques. *PLOS ONE* **11**, e0146682.

Van Leeuwen, J. L., Voesenek, C. J., Müller, U. K. (2015). How body torque and Strouhal number change with swimming speed and developmental stage in larval zebrafish. *Journal of the Royal Society Interface* **12**, 20150479.

Kenjereš, S., Ten Cate, S., Voesenek, C. J. (2011). Vortical structures and turbulent bursts behind magnetic obstacles in transitional flow regimes. *International Journal of Heat and Fluid Flow* **32**, 510–528.

Educational activities

Course	Year	ECTS
The basic package		**3**
WIAS introduction course	2012	1.5
Ethics and Philosophy in Life Sciences	2014	1.5
Scientific exposure		**13**
International conferences		*6.6*
Society of Experimental Biology 2012, Salzburg, Austria	2012	1.2
Society of Experimental Biology 2013, València, Spain	2013	1.2
World Congress of Biomechanics 2014, Boston, USA	2014	1.8
Society of Experimental Biology 2015, Prague, Czech Republic	2015	1.2
Society of Experimental Biology 2016, Brighton, United Kingdom	2016	1.2
Seminars and workshops		*0.3*
MARIN natural propulsion seminar, Wageningen, the Netherlands	2014	0.3
Presentations		*6*
Society of Experimental Biology 2013; oral presentation. *Automated fish tracking from high-speed video*	2013	1
World Congress of Biomechanics 2014; oral presentation. *Inverse dynamics of larval zebrafish swimming*	2014	1
Society of Experimental Biology 2015; poster. *Three-dimensional dynamics of larval zebrafish swimming*	2015	1
Burgerssymposium 2016; oral presentation. *Three-dimensional tracking and inverse dynamics of larval zebrafish*	2016	1
Society of Experimental Biology 2016; oral presentation. *Bending moment dynamics during swimming of developing zebrafish larvae*	2016	1
WIAS Science Day 2017; oral presentation. *Bending moment dynamics during swimming of developing zebrafish larvae*	2017	1
In-depth studies		**6**
Locomorph Summer School	2012	1.5
Extensive training for CD-Adapco Star-CCM+	2013	0.9
EXCITE Summer School on Biomedical Imaging	2014	3.0
Data Assimilation & CFD Processing for PIV and Lagrangian Particle Tracking	2017	0.6

Professional skills support courses		**3**
High-Impact Writing in Science	2012	1.3
Surviving Peer Review	2016	0.3
Techniques for Scientific Writing	2016	1.8
The Final Touch: Writing the General Introduction and Discussion	2016	0.6

Research skills training		**12**
Co-writing an ALW Open Programma grant proposal (NWO/ALW-824-15-001)	2012	6
Assisting experiments with *in vivo* X-ray computed tomography of sea horse dorsal fin motion at the Paul Scherrer Institut in Switzerland (with Sebastian Henrion)	2013	6

Didactic skills training		**10**
Supervising practicals and excursions		*8*
Supervising Functional Zoology practicals	2013	0.5
Supervising Functional Zoology practicals	2014	0.5
Supervising Functional Zoology practicals	2015	0.5
Supervising Functional Zoology practicals	2016	0.5
Supervising Modelling Biological Systems practicals	2016	6
Supervising theses		*1*
Co-supervision of an internship	2015	1
Preparing course material		*1*
Developing tracking software and manual for Functional Zoology	2013	0.5

Total		**47**

Completion of the training activities is in fulfilment of the requirements for the education certificate of the Graduate School Wageningen Institute of Animal Sciences (WIAS). One ECTS equals a study load of 28 hours.